2-10-2022 2:30 PM

Assessment of Tropical Cyclone Wind and Wave Hazards and Their Effect on the Reliability of Wind Turbines

Chao Sheng, *The University of Western Ontario*

Supervisor: Han-Ping Hong, *The University of Western Ontario*

A thesis submitted in partial fulfillment of the requirements for the Doctor of Philosophy degree in Civil and Environmental Engineering

Abstract

Tropical cyclones (TC) induce strong winds, heavy rainfalls, and storm surge. They cause fatalities and property damage, especially in coastal regions that are prone to TC hazards. TC wind or wave assessments are reported in the literature. The assessment provides the required hazard characterizations for assessing the reliability and risk of structures such as onshore and offshore wind turbines (WTs). The present study considered sites near the coastline of mainland China. It is focused on 1) the assessment of using different historical best-track datasets on the development of stochastic TC track models and on the estimated TC wind hazard, 2) the establishment of a procedure to assess the joint TC wind and wave hazards, to assess their correlation, and the joint probabilistic model, 3) the development of a database-driven simulation-based (DDSB) framework to estimate the reliability of offshore WTs, and 4) the calibration of the design TC wind and wave loads and companion load factors for designing onshore and offshore monopile WTs for selected target reliability indices, and to recommend site-dependent and information-sensitive design TC wind and wave loads for such WTs.

For the analysis, both the historical best-track datasets from the China Meteorological Administration (CMA) and from the Joint Typhoon Warning Center (JTWC) are considered for developing the physical-based beta-advection model. The impact of using one or other track database on the TC wind hazard is quantified. Based on the stochastic TC track model, available TC wind and wave field models, the joint TC wind and wave hazard is assessed. The quantified TC hazard indicates that the correlation of the extreme (annual or event-based) TC wind speed and wave height should not be neglected. It is proposed that the joint TC wind and wave hazards used to assess the reliability of offshore WTs can be carried out according to a database-driven simulation-based procedure. This allows the combined use of synthetic tracks database, the prepared wind and wave fields database, and the structural response database of WTs subjected to combined wind and wave actions. The application of this procedure is shown for a semi-submersible WT. Moreover, the procedure is used to carry out reliability-based calibration of design TC wind and wave loads by considering monopile WTs that are placed in onshore or offshore locations that are near the coastline of

mainland China. Simple empirical equations are developed to evaluate the required return periods for evaluating the design TC wind and wave loads. These equations depend on the coefficient of variation of the annual maximum TC wind speed and significant wave height and the selected target reliability index. Also, maps of the required return periods, ranging from 50 to 500 years for two considered tolerable failure probability levels, are given for calculating the design wind load and wave load. The calibration analysis results also indicate that the companion load factor of 0.9 is to be considered for the wave load if the TC wind load is taken as the principal load and the wave force is dominated by the drag force component. This companion load factor becomes 0.85 if the TC wave load is dominated by the inertial force component. Also, the companion load factor of 0.85 for the wind load should be considered if the wave load acts as the principal load.

Keywords

Tropical cyclone, Stochastic track modeling, Typhoon wind and wave hazard, Probabilistic analysis, Wind turbine, Fragility, Reliability, Design code calibration, Simulation

Summary for Lay Audience

Tropical cyclones (TC) induce strong winds, heavy rainfalls, and storm surge, and also cause devastating damages to properties and fatalities. However, this thesis mainly focused on the TC hazard assessment and the reliability analysis for wind turbines (WTs). TC wind and wave assessment provides the wind speed and wave height for various return periods for offshore sites. To facilitate and inform the design of structures for civil engineers, structural reliability analysis needs to be carried out to examine the safety level implied in the current design codes or to recommend the safety factors for design code making.

The first topic of this thesis is about TC hazard modelling. In detail, chapter two presented a physical-based TC track model using environmental datasets. Furthermore, two historical best-track datasets are accessed and used to establish this track model. The differences between the historical and simulated tracks for statistics of the TC characteristics and *T*-return period wind values were compared; chapter three uses a popular wave model to assess TC wave hazard. This model is simple to use with only three input parameters. The marginal and joint probabilistic distributions for wind and wave were assessed, and the load combination analysis for offshore wind turbine design was carried out. Moreover, the analysis of identifying TC events contributing to a certain hazard level was performed, which is beneficial for TC risk mitigations.

The remaining topic is about the reliability analysis for wind turbines subjected to TC hazards. Chapter four developed a database-driven simulation-based (DDSB) framework, which was mainly based on several synthesized databases. This procedure was applied to evaluate the failure probability of a floating WT located in an offshore region in China; chapter five carried out the reliability-based design code calibration for the onshore and offshore monopile WT. The site-specified wind and wave return periods were identified and simple to use empirical equations were developed to evaluate such required return periods. The companion load combination factors for TC wind and wave loads are calibrated.

In short, this thesis established novel TC hazard wind and wave assessment approaches, developed a simulation-based framework for reliability assessment for offshore structures, and carried out the reliability-based design code calibration for WTs. This study could be valuable to enhance our understanding of TC risk for WT.

Co-Authorship Statement

The material presented in Chapter 2, 3, 4 and 5 of this thesis have been published or submitted for potential publication in peer-reviewed journals.

A version of Chapter 2 co-authored by C. Sheng and H.P. Hong is submitted for potential publication.

A version of Chapter 3 is published in the Structural Safety co-authored by C. Sheng and H.P. Hong.

A version of Chapter 4 is published in the Structural Safety co-authored by C. Sheng and H.P. Hong.

A version of Chapter 5 co-authored by H.P. Hong and C. Sheng is submitted for potential publication.

Dedication

To my parents, Mr. X.T. Sheng & Ms. X.Q. Cui

and old brother, Mr. G. Sheng

Acknowledgments

It is one of the meaningful and profound journeys in my life to have my Ph.D. program at Western University, Canada. I am impressed by the magnificent maple leaves, gorgeous natural lakes and mountains, and white snow. I truly like this peaceful and beautiful place that helped me grow and allowed me to concentrate on my research. At this moment, there are so many people to whom I would like to express my sincere thanks.

First and foremost, I would like to express my deep sense of gratitude to my supervisor, Professor Han-Ping Hong, who is a rigorous, insightful, and knowledgeable scholar as well as a thoughtful and supportive mentor. It is my privilege to be his Ph.D. student. I am deeply grateful for his intellectual guidance to foster my logical and critical thinking in research spirit, for his thought-provoking discussions and comments to broaden my horizon and deepen my understanding of knowledge and my thinking of research ideas, and for his consistent encouragement throughout the ups and downs toward the completion of this thesis. And I benefit tremendously from his mentorship for both academic research and life experience.

Many thanks go to my thesis committee members: Professor W. Zhou, Professor L. Jiang, Professor R. Carriveau for their constructive comments and suggestions on my comprehensive exam and this thesis. Special thanks go to Professor T. Newson for the course you taught me and the project we worked on.

I am grateful for the financial support from the Chinese Scholarship Council and the Natural Sciences and Engineering Research Council of Canada, which provided me with this precious opportunity to pursue my Ph.D. degree and work on these exciting research topics.

I would like to thank my office mates Minyu Xiao and Jungmyung Kim for the company and discussions we had for research and life. I also want to thank other colleagues, Chao Feng, Pengpeng He, Jiyang Gu, Qian Tang, Shucheng Yang, Qian Huang, Yongxu Liu, Xizhong Cui, and many others, for the discussion, collaboration, support, and joyful time we spent together. I also want to thank many relatives, friends in China and here for your help in my life and the joyful and memorable days we had.

I want to say thanks to my girlfriend, Yun, for your caring and love during this hardship. At last, I would like to express my deepest and most profound appreciation and gratitude to my parents and old brother. Your unwavering care and love have supported me from a little naïve boy to a well-developed man. It is my lifelong treasure to be your son and little brother. I am definitely indebted, and I will always be there for you for the rest of my life.

Thank you! Everyone.

Table of Contents

List of Tables

List of Figures

Nomenclature

Chapter 1

$\boldsymbol{s}_t$	vector consisting of the predicted TC track variables
$\boldsymbol{AR}$	autoregression function
$\boldsymbol{p}_{t-1}$	vector containing the selected model variables
$\boldsymbol{\varepsilon}_t$	independent residual random variables
$\mathbf{V}_{TC}$	TC translation velocity vector.
$\mathbf{V}_{steer}$	steering velocity
$\mathbf{V}_{\beta}$	beta drift vector
$V_g(r)$	gradient wind velocity in the tangential direction at a distance r from the TC center
ρ	air density
f	Coriolis parameter equal to $2\Omega\sin\psi$ at latitude ψ
Ω	the rotation of the earth
$p(r)$	pressure at a distance r from the TC center
$R_{\max}$	radius at which the maximum wind speed occurs
$V_{\max}$	maximum wind speed
Δp	central pressure difference
p_c	the minimum pressure in the storm's low centre
p_a	ambient pressure far from the storm

B	Holland B parameter
V_T	storm translation velocity
$H_{s,\max}$	maximum significant wave height within the TC
$V_{s,\max}$	surface maximum wind speed
g	gravitational acceleration
F_E	'equivalent' fetch distance
R'	scaling factor
H_s	spatially distributed significant wave height

Chapter 2

$\mathbf{V}_{TC}$	TC translation velocity vector
$\mathbf{V}_{steer}$	steering velocity
$\mathbf{V}_\beta$	beta drift
$\boldsymbol{v}_{GW}$	global wind field
P_u, P_l	upper and lower pressure levels
$\lvert \mathbf{V}_\beta \rvert$	magnitude of beta drift
θ_β	direction of beta drift
$m_{\lvert \mathbf{V} \rvert}$, $\varepsilon_{\lvert \mathbf{V} \rvert}$	mean and zero-mean residual of $\lvert \mathbf{V}_\beta \rvert$
m_θ, ε_θ	mean and zero-mean residual of θ_β
η, γ, δ, ζ	model parameters for Johnson S_B distribution

α, μ_i, σ_i	model parameters for binormal distribution
h_B	basic wind field
h_D	disturbance wind field
$h_{\text{non-TC}}$	vortex-removed disturbance wind field
I	relative intensity
p_{da}	ambient pressure
p_{c}	central pressure
e_s	saturation vapour pressure
T_{s}	sea surface temperature
p_{dc}	minimum sustainable surface value of central pressure
d_i	spatially varying model coefficients for intensity model
ε_I	zero-mean normally distributed residual
Δp	central pressure difference
a_i, b_i	model parameters for TC translation velocity and direction
c	TC translation velocity
θ	TC heading direction
R_{max}	radius to maximum wind speed
B	Holland's B parameter
ψ	latitude of the TC center
V_A	annual maximum TC wind velocity

$v_{A\text{-}T}$	T-year return period value of V_A
$R_{CMA/LH\text{-}T}$	ratio of $v_{A\text{-}T}$ obtained by using the beta-advection model derived based on the database from CMA to that obtained by using LH model
$R_{JTWC/CMA\text{-}T}$	ratio of $v_{A\text{-}T}$ obtained by using the beta-advection model derived based on the database from JTWC to that based on the database from CMA

Chapter 3

θ	orientation of the track
α	orientation of the site
$D_{\min}$	minimum distance to the track
$p(r)$	pressure at a distance r
B	Holland B parameter
$R_{\max}$	radius of maximum wind speed
Δp	central pressure difference
p_c	central pressure
p_a	ambient pressure far away from the storm center
$V_g(r,\alpha)$	gradient wind speed
ρ	air density
f	Coriolis parameter
ψ	latitude in degrees
Ω	rotation of the Earth
V_T	storm translation speed

$V_{s,\max}$	maximum surface 10-min mean wind speed
$\varepsilon_{ln\mathrm{Rmax}}$	residuals of $R_{\max}$
$\sigma_{\ln R_{\max}}$	standard deviation of $\varepsilon_{ln\mathrm{Rmax}}$
ε_{B}	residuals of B
$\sigma_{\ln B}$	standard deviation of ε_{B}
$\vec{u}_s$	wind velocity relative to the moving centre of the vortex
$\vec{u}_c$	TC translation velocity
$\vec{u}_g$	wind velocity resulting from the large-scale pressure field
$\hat{k}$	unit vector in the vertical direction
h	depth of the planetary boundary layer
C_D	surface drag coefficient
K_H	horizontal eddy viscosity coefficient
$V(z)$	surface mean wind speed at a height z above the ground surface
κ	von Karman coefficient
u^*	friction velocity
z_0	surface roughness
H^*	boundary layer height parameter
$H_s^{\max}$	maximum significant wave height within a storm
f_E	‘equivalent’ fetch distance

R'	scaling factor
H_s	surface significant wave height
$d_{\text{c-s}}$	distance from the storm center to the site
$V_{s\text{-maxA}}$	annual maximum wind speed
$H_{sW\text{A}}$	companion surface significant wave height along $V_{s\text{-maxA}}$
$H_{s\text{-maxA}}$	annual maximum significant wave height
$V_{sH\text{A}}$	companion surface wind speed along $H_{s\text{-maxA}}$
λ	average annual occurrence rate
x_{50}	0.98-quantile of annual maximum variables
$F_{GE}(x)$	cumulative density function for generalized extreme value distribution
u_0	model parameter for generalized extreme value distribution
a_0	model parameter for generalized extreme value distribution
k	model parameter for generalized extreme value distribution
$F_G(x)$	cumulative density function for Gumbel distribution
u_{10}	location parameter for Gumbel distribution
α_{10}	scale parameter for Gumbel distribution
u_{i}	standard uniformly distributed random variables
τ	Kendall's correlation coefficient
$Z(t)$	simultaneous wind and wave load actions
η_{i}	bilinear approximation parameters

Chapter 4

Δp	central pressure difference
$R_{\max}$	radius of maximum wind speed
V_s	surface mean wind speed
H_s	significant wave height,
$\boldsymbol{X}_L$	variables representing uncertainties associated with load effects
$\boldsymbol{X}_M$	variables representing uncertainties associated with material properties and geometric
$M_{Tow\text{-}L}()$	bending moment at the base of the tower,
$M_{flap\text{-}L}()$	flapwise bending moment at the root of the blade
$T_{M\text{-}L}()$	tension in mooring line
$M_{OM\text{-}L}()$	absolute values of the orientation-independent overturning moment
Y_{Li}	modelling errors associated with the loading
Y_{Mi}	modelling errors associated with material properties and geometric variable
t	time dimension in the stochastic process
μ_X	mean of $\boldsymbol{X}$, including $\boldsymbol{X}_L$ and $\boldsymbol{X}_M$
g_i	limit state functions
P_{fi}	failure probability for the i-th failure mode
P_{sys}	failure probability for WT system
N_m	number of 20 years of non-overlapping periods
N_m	total number of such tracks that passes within 250 km of the site

N_j	total number of such points for the track within the identified segment with a time increment of one hour between the two consecutive points
T_p	peak wave period
U_{10}	10-minute mean wind speed at 10 m height
g	gravitational acceleration
C_{LE}	correlation coefficient matrix
M_{cr}	critical bending moment capacity for local buckling
E	Young's Modulus
F_y	steel yield strength
$Y_{y,ss}$	model uncertainties that account for scale effects resulting from the differences between test specimens and full-scale structures for yield strength
$Y_{E,ss}$	model uncertainties that account for scale effects resulting from the differences between test specimens and full-scale structures for Young's Modulus
t_{tower}	tower wall thickness
X_{cr}	modelling error taking into account that the use of the numerical model
$\sigma_{b,f}$	blade tensile strength
$R_{b,r}$	radius of blade root section
$I_{b,r}$	second moment of blade root section,
Q	breaking load capacity
d	nominal diameter of mooring lines
ζ_a	maximum allowable pitch rotation

C_h	pitch rotational stiffness due to hydrostatic effect
V_{s50}	50-year return period values of annual maximum wind speed
H_{s50}	50-year return period values of significant wave height
V_{hub}	10-min mean wind speed at hub height
P_{fsys1}	annual failure probability
P_{fsys20}	failure probability for a service period of 20 years
V_d	design wind speed
H_d	design significant wave height

Chapter 5

L_a, L_{o}	latitude and longitude of TC center
u_c	TC translation velocity
Δp	central pressure difference
R_{max}	radius to the maximum wind speed
B	Holland's B parameters.
θ	TC translation direction
V_s	10-min mean surface wind speed
H_s	significant wave height
$V_{s\text{-}max}$	event-based maximum V_s,
$H_{s\text{-}max}$	event-based maximum H_s
H_{sW}	concurrent wave to $V_{s\text{-}max}$

V_{sH}	concurrent wind to $H_{s\text{-}max}$
$V_{s\text{-}maxA}$	annual maximum value of V_s
$H_{s\text{-}maxA}$	annual maximum value of H_s
H_{sWA}	concurrent value of H_s for $V_{s\text{-}maxA}$
V_{sHA}	concurrent value of V_s for $H_{s\text{-}maxA}$
$v_{s\text{-}maxA\text{-}p}$	(1-p)-quantiles of $V_{s\text{-}maxA}$
$h_{s\text{-}maxA\text{-}p}$	(1-p)-quantiles of $H_{s\text{-}maxA}$
$\boldsymbol{X}_L$	variables representing uncertainties associated with load effects
$\boldsymbol{X}_M$	variables representing uncertainties associated with material properties and geometric
$M_{Tow}()$	bending moment at the base of the tower,
$M_{flap}()$	flapwise bending moment at the root of the blade
t	time dimension in the stochastic process
μ_X	mean of $\boldsymbol{X}$, including $\boldsymbol{X}_L$ and $\boldsymbol{X}_M$
X_R	normalized resistance
γ	resistance factor
$Z_{WI,A,W\text{-}L}$	uncertain transformation factor for load effects
$b_{WI,A,W}$	variable related to bias factor
c_i	structural analysis coefficient
η_i	companion load combination factors
Y_{Li}	modelling errors associated with the loading

Y_{Mi}	modelling errors associated with material properties and geometric variable
g_i	limit state functions
M_{cr}	critical bending moment capacity for local buckling
E	Young's Modulus
F_y	steel yield strength
$Y_{y,ss}$	model uncertainties that account for scale effects resulting from the differences between test specimens and full-scale structures for yield strength
$Y_{E,ss}$	model uncertainties that account for scale effects resulting from the differences between test specimens and full-scale structures for Young's Modulus
D	diameter of a section of the tower
t_{tower}	tower wall thickness
X_{cr}	modelling error taking into account that the use of the numerical model
γ_M	overall resistance reduction factor due to the uncertainty in $Y_{y,ss}$ and X_{cr}
$\sigma_{b,f}$	blade tensile strength
$R_{b,r}$	radius of blade root section
$I_{b,r}$	second moment of blade root section,
b_{TOW}, b_{Flap}	conservatism factor for load effects
β_{T20}	target reliability index for 20-year service life
T	required return period for target β_{T20}
M_{crD}	design bending moment capacity for local buckling resistance

M_{FlapD}	design flapwise bending moment at the root of the blade
H_{SS}	adjusted significant wave height for the shallow water
d	water depth
R_0	ratio of the factored resistance to the factored load effect

Chapter 1

1 Introduction

Tropical cyclones (TCs) are large-scale meteorological phenomena that can cause fatalities and tremendous monetary loss. A TC is known as a typhoon if it occurs in the northwestern Pacific Ocean and the Indian Ocean and as a hurricane if it occurs in the Atlantic Ocean and the northeastern Pacific Ocean. The deadly typhoon Bhola that occurred in 1970 struck East Pakistan, resulting in a half-million death (https://en.wikipedia.org/wiki/1970_Bhola_cyclone). A typhoon that occurred in August 1956 with winds up to 243 kph killed 4,900 people in Zhejiang Province, China. A powerful typhoon named Winnie in 1997 struck the east coast of China, killing 250 people and causing $2.2 billion worth of damage (https://factsanddetails.com/china/cat10/sub64/item398.html). Since 1970, more than 1942 disasters have been attributed to TCs, which killed more than 779,000 people and caused the US $1,408 billion in economic losses (World Meteorological Organization 2020). TC-induced wind and waves can cause large responses and damages to the onshore and offshore wind turbine (WT) (Ishihara et al. 2005; Chen and Xu 2016). In September 2003, typhoon Maemi struck Miyakojima Island in Okinawa, Japan, with a central pressure of 912 hPa and a maximum 3-s gust of 86.6 m/s at 100-m above the sea surface. It caused the collapse of three out of six WTs, and the remaining three WTs suffered significant damages, including damage to blades and the nacelle cover. In September 2013, typhoon Usagi affected the wind farm in Shanwei city, China, with the observed maximum 3-s gust wind of 57 m/s measured by a nearby meteorological station. Usagi resulted in catastrophic damage to the wind farm with economic losses of approximate $16 million. More specifically, eight towers were collapsed; eleven blades were fractured, even the towers were still intact; around half of the total blades were broken; additionally, the mechanical parts, including the vanes and anemometers of the wind turbines, were damaged. These observed damages are mainly attributed to three characteristics of the TC wind: high wind speed, sudden change of direction, and high turbulence intensity (Li et al. 2013). Though these failures were mainly observed for

onshore WTs and the direct observations of damages for offshore WTs have rarely been reported. This may be due to that the offshore wind exploitation has a relatively short history, and the majority of offshore WTs are employed in non-hurricane-prone regions. However, it has been recognized that TCs pose a great challenge for the development of offshore wind. Many studies have been carried out for reliability and risk assessment of WTs due to TCs (Rose 2012; Hallowell et al. 2018) and have discussed reliability-based design code calibration (Tarp-Johansen and Clausen 2006; Jia et al. 2010). More information on reliability analysis for WTs subjected to the TC will be elaborated on in the subsequent sections.

A TC is a large-scale rotating system with a typical diameter between 100 and 2,000 km. It has well-defined inner and outer structures. It usually has a low-pressure center (i.e., eyewall) with a typical 30–65 km radius. The formation of a TC depends on several atmospheric conditions, including warm sea surface temperatures, low vertical wind shear, and enough Coriolis force. TC winds rotate counterclockwise in the Northern Hemisphere and clockwise in the Southern Hemisphere because of the Coriolis effect. The intensification of TCs depends on the availability of heat source that is primarily from the warm ocean waters, and also on the wind shear condition. Therefore, these storms are the strongest over water, resulting in the high winds and strong concurrent waves that can damage offshore structures, such as the oil and gas platforms and offshore wind turbines. After a TC makes landfall, its central pressure difference decays, and its TC intensity weakens (Vickery 2005). A landfalling TC also causes damages to infrastructure and lifeline networks that are located in the coastal regions.

Tropical cyclone wind hazard assessment has been investigated for different regions in the world (Vickery et al. 2009). If the multi-year TC wind speed records at the spatially distributed locations from the meteorological stations are available, the estimation of the extreme TC wind speed can be carried out based on statistical analysis and extreme value theory. However, the available surface wind speed records are often scarce, and the meteorological stations are only sparsely spatially distributed. To overcome this problem, simulation-based approaches can be considered. The simulation-based approach consists of using a wind field model and a track model. For example, Russell

(1971), Batts et al. (1980), Georgiou (1986), Ou et al. (2002), Xiao et al. (2011) and Hong et al. (2016) considered the use of segments of tracks, while Vickery et al. (2000), and Li and Hong (2016) considered stochastic full track models. In all cases, the segment tracks or full tracks are developed based on the historical TC tracks. The wind field model used to assess the TC wind field ranges from a simple gradient wind field model, height averaged 2-dimensional slab model, or a linear and nonlinear 3-dimensional model (Gu et al. 2020). More details on the review of the wind field model and track model are given in the following sections.

TCs induce not only strong winds but also large waves. TC-induced wave hazard was investigated by Ross (1976), King and Shemdin (1978), Young (1998), and Hwang (2016). Early studies provided a simple model to predict the TC-induced maximum wave height as a function of TC wind speed (Bretschneider 1959). Subsequent studies attempted to incorporate observations as well as physics in developing TC-induced wave field models (King and Shemdin 1978; Bowyer and MacAfee 2005; Young and Vinoth 2013). A well-recognized wave field model that can be directly applied for the TC wave hazard assessment was developed by Young (1988) and Young and Vinoth (2013), which will be discussed further in the subsequent sections in this chapter.

1.1 Review of TC track modelling

For some of the earlier hurricane wind hazard modelling assessments, the circle sub-region method (CSM) was developed (Russell 1971; Batts et al. 1980; Georgiou 1986; Vickery and Twisdale 1995). The idea of this approach is to extract the statistical characteristics of the historical tracks within a circle centered at the site of interest. The parameters defining the segment of track within the circle include the annual occurrence rate, TC translation direction and velocity, central pressure difference, and the minimum approaching distance. Each parameter is characterized by a probability distribution that is assigned based on samples of the historical track segments within the considered circle.

The drawbacks to using CSM include the samples within the circle may be insufficient for assigning the probability distribution of each parameter with confidence. Since the

probability distribution of each parameter may be site-dependent, the set of distributions developed for a site may not be applicable to another site of interest. These mentioned drawbacks may be overcome by using a stochastic model for the (full) TC track from genesis to lysis. There are several approaches for developing the stochastic model. For example, a model was developed by Vickery et al. (2000) based on the autoregressive type of approach. The model could be written in general as:

$$\boldsymbol{s}_t = \boldsymbol{AR}\left(\boldsymbol{p}_{t-1}, \boldsymbol{p}_{t-2}, ..., \boldsymbol{p}_{t-q}\right) + \boldsymbol{\varepsilon}_t \tag{1.1}$$

where $\boldsymbol{s}_t$ is the vector of variables defining TC track at instance *t*, which is a function of the values of the variables at earlier instances $\boldsymbol{p}_{t-1}$, …, $\boldsymbol{p}_{t-q}$; $\boldsymbol{AR}$ denotes the autoregressive model, and $\boldsymbol{\varepsilon}_t$ represents independent zero-mean normally distributed residual.

The full track model in Vickery et al. (2000) considered that the number of TC occurrences per year is randomly generated using the negative binomial distribution; the location, date, heading, and translation of each genesis is randomly drawn from the historical best-track datasets. The track is simulated using the stochastic model schematically represented by Eq. (1), in which the change of TC translation speed and translation direction are the dependent variables, and location parameters, translation speed, and translation direction in previous steps are used as the independent variables. The intensity is modelled as a function of the sea surface temperature using the approach given in Darling (1991). The coefficients in the models are estimated considering a 5°×5° grid system over the whole basin of interest, and the refined coefficients, especially for the intensity model, can be established depending on the data availability. Once the track makes landfalling, the geographical-dependent filling rate model is used to evaluate the decay of central pressure difference. The lysis of the track is determined based on the thresholds of the central pressure difference. Li and Hong (2015) noted that the number of model parameters for the model given in Vickery et al. (2000) could be reduced because of the collinearity problem observed by applying the geographically weighted regression. Subsequently, they simplified the regression model (Li and Hong 2015; Li

and Hong 2016). Cui and Caracoglia (2019) considered the use of the geographical-dependent Brownian motion models for hurricane track simulation. However, the obtained statistics of simulated tracks deviate noticeably from the statistics of those obtained from the historical best-track datasets.

Rather than using TC translation direction and velocity as the independent variables, James and Mason (2005) established an autoregressive model using the TC latitude and longitude increments directly. In this study, the rates of change of latitude, longitude, and pressure from the previous step are used. Additionally, the inversed latitude is added in the latitude prediction equation, and the central pressure difference and maximum potential intensity are incorporated in the pressure prediction equation. The examinations of model residuals using autocorrelation functions and empirical distribution functions of simulated and historical cyclone parameters were used to examine the goodness-of-fit of the simulated results. Similarly, Hall and Jewson (2007) presented a statistical track model using latitudinal and longitudinal increments as the dependent variables.

As a variate of autoregressive approaches, the random sampling technique has also been developed. Casson and Coles (2000) generated the tracks by randomly perturbing historical tracks, and the corresponding intensity is randomly drawn from the historical observations. Instead of directly using the historical TC track data, Powell et al. (2005) obtained the temporal and geographical varying probability density functions (PDFs) for TC parameters, including genesis, movement, and intensity change from the historical records; then sampled the values from the pre-calculated PDFs to predict the hurricane movement and intensity during simulation. A similar approach was used in Shen and Wei (2021). Also, by considering the inhomogeneity and clusters of the historical TC data in the whole basin, Cui et al. (2021) used the QuadTree technique to separate the Northwestern Pacific Ocean into a series of segmentation, depending on the historical data availability. The Bayesian optimization is used for model parameter tuning. Basically, these studies discussed the effect of various parameter estimation techniques on the simulated TC tracks, considering the spatial-temporal characteristics of historical data and its availability.

Two somewhat different TC track modelling approaches are presented in Emanuel et al. (2006) by considering relevant physical features. The first approach is using the Markov chain. The TC genesis is generated using a three-dimensional kernel density distribution, including the latitude, longitude, and date extracted from the historical datasets. The track propagation is predicted using the Markov process, which constructed the translation probability using the nonparametric kernel smoothing functions conditioned on the prior translation speed and direction and current location and time. The second approach was the so-called beta-advection model (BAM) originally proposed by Marks (1992). The model is physical-based and requires the use of global environmental wind fields at different pressure levels. The general formulation of BAM is presented as:

$$\mathbf{V}_{TC} = \mathbf{V}_{steer} + \mathbf{V}_{\beta} \tag{1.2}$$

where $\mathbf{V}_{TC}$ is TC translation velocity vector; $\mathbf{V}_{steer}$ represents the steering velocity, and the correction term $\mathbf{V}_{\beta}$ is called beta drift. This model was considered by several studies, including Lee et al. (2018), Chen and Duan (2018), Hong and Li (2021), for the TC track simulation.

However, it is noted that there exist various historical best-track datasets maintained by different agents or organizations. None of the mentioned studies used different sets in developing the track models and compared their studies. The effect of using the different historical best-track databases to develop stochastic track models and their effect on the assessed TC hazard is unknown.

1.2 Review of TC wind field models

Besides using TC tracks, a TC wind field model needs to be adopted for assessing the TC wind hazard. In early studies, the gradient wind field model governed by the following equation (Holton 2004) is considered:

$$\frac{1}{\rho}\frac{\partial p(r)}{\partial r} = \frac{V_g^2(r)}{r} + fV_g(r) \tag{1.3}$$

where $V_g(r)$ is the gradient wind velocity in the tangential direction at a distance r from the TC center; ρ is the air density; f is the Coriolis parameter equal to $2\Omega\sin\psi$ at latitude ψ in which Ω represents the rotation of the earth, and the horizontal pressure profile $p(r)$ can be determined based on (Holland 1980),

$$\frac{p(r)-p_c}{\Delta p}=\exp\left[-\left(\frac{R_{\max}}{r}\right)^B\right] \tag{1.4}$$

in which $R_{\max}$ is the radius at which the maximum wind speed $V_{\max}$ occurs; $\Delta p = p_a - p_c$, p_c is the minimum pressure in the storm's low centre (i.e., central pressure) and p_a is the ambient pressure far from the storm, and B is commonly referred to as the Holland B parameter. The solution of Eq. (1.3) based on the pressure profile given in Eq. (1.4) leads to,

$$V_g(r)=\left\{\frac{B\Delta p}{\rho}\left(\frac{R_{\max}}{r}\right)^B\exp\left[-\left(\frac{R_{\max}}{r}\right)^B\right]+\left(\frac{rf}{2}\right)^2\right\}^{1/2}-\frac{rf}{2} \tag{1.5}$$

Note that if the translation velocity of the TC is considered, the wind field becomes (Georgiou 1986),

$$V_g(r)=\left\{\frac{B\Delta p}{\rho}\left(\frac{R_{\max}}{r}\right)^B\exp\left[-\left(\frac{R_{\max}}{r}\right)^B\right]+\left(\frac{V_T\sin\alpha-rf}{2}\right)^2\right\}^{1/2}+\frac{V_T\sin\alpha-rf}{2} \tag{1.6}$$

where V_T is the storm translation velocity. An extensive discussion of the adequacy of Eq. (1.6) and its use to estimate the surface wind speed was given in Holland et al. (2010) and Gu et al. (2020). It was shown in Gu et al. (2020) that this wind field model could provide a reasonable approximation to the surface TC wind speed (i.e., wind speed at 10 m height above the ground surface). The gradient wind field is still employed in the TC wind hazard and risk assessment (Zeng et al. 2021; Li and Kumar 2021; Wu et al. 2021).

Another popular TC wind field model is the vertically averaged boundary layer slab model (Chow 1971; Shapiro 1983; Thompson and Cardone 1996; Vickery et al. 2000). The solution of this wind field requires the consideration of the horizontal eddy viscosity

coefficient profile K_H and drag coefficient C_D, and the height of the assumed planetary boundary layer height h. The solution of this model was presented in Vickery et al. (2000) and Li and Hong (2015) as compared with those from H*Wind datasets (Powell et al. 1998).

Other models used for the TC wind field modelling, include those presented in Meng et al. (1995, 1997), Kepert (2001), Kepert and Wang (2001), Hong et al. (2019). However, the calibration of the model parameters for these wind field models by using observed wind speed is missing. Since the model parameters for the slab model were well established, this slab model will be considered in the present study.

1.3 Review of TC generated wave modelling

For offshore structures in TC hazard-prone regions, it is important to consider both the TC wind and wave hazards. The analysis of the hurricane wave states is a challenging problem. The physics of TC wind-wave generation is primarily composed of three aspects (Group 1988; Young 2017): 1) the energy input from the TC wind; 2) the dissipation due to the wave breaking; and 3) the nonlinear interactions between the waves in the spectrum. Many studies have been carried out to enhance our understanding of the physics of the TC-generated wave field (Donelan et al. 1985; Young 1988; Ochi 1993; Thompson and Cardone 1996; Young and Vinoth 2013). With the advancement of satellite techniques, more high-quality datasets for the wave states could be used for validating and updating the TC wave model parameters. Young (1988) and Young and Vinoth (2013) gave a popular and well-developed parameterized TC wave model. The model considers a critical ‘extended fetch’. The TC-generated wave condition is not only governed by the surface wind speed (e.g., Ochi 1993) but also by the storm translation velocity. Several steps are involved in applying this model to predict the spatially distributed wave field (Young 2017), as follows:

Step 1: calculate the maximum significant wave height within the TC, $H_{s,\max}$, using the JONSWAP growth formula (Hasselmann et al. 1975),

$$\frac{gH_{s,\max}}{V_{s,\max}^2} = 0.0016\left(\frac{gF_E}{V_{s,\max}^2}\right)^{1/2} \tag{1.7}$$

where $V_{s,\max}$ is the surface (i.e., 10-m height) maximum wind speed that can be approximately estimated using the gradient wind field (Holland 1980) and a scaling factor; g is the gravitational acceleration; f_E is the 'equivalent' fetch distance and defined in terms of TC parameters using $V_{s,\max}$ and translation velocity, V_T, which is calculated using,

$$\frac{f_E}{R'} = \psi\left(\begin{array}{l} -2.175\times10^{-3}V_{s,\max}^2 + 1.506\times10^{-2}V_{s,\max}V_T - \\ 1.223\times10^{-1}V_T^2 + 8.76\times10^{-2}V_{s,\max} + 1.516V_T + 1.756 \end{array}\right) \tag{1.8}$$

and,

$$R' = 22.5\times10^3\log\left(R_{\max}\right) - 70.8\times10^3 \tag{1.9}$$

in which the coefficients to define ψ and calculate scaling factor R' have been proposed and updated in Young and Vinoth (2013).

Step 2: estimate the spatially distributed significant wave height, H_s, using a series of normalized $H_s / H_{s,\max}$ diagrams scaled by R'.

This set of diagrams is generated from the numerical modelling (Young 1988) and can provide the spatial distribution of H_s with three input parameters, $V_{s,\max}$, V_T, and $R_{\max}$, for a range of values of $V_{s,\max} \in [20,60]$(m/s) and $V_T \in [0,12.5]$(m/s). This set of equations and diagrams is simple to use and time-efficient while maintaining the primary physics of TC-induced waves.

It must be emphasized that the application of this TC wave field model, together with the TC track model and wind field model, for assessing the joint TC wind and wave hazard was unavailable in the literature. Such an assessment is essential for evaluating the reliability and risk of offshore structures such as wind turbines.

1.4 Review of structural reliability assessment for wind turbine subjected to TC

Reliability-based design code calibration is not new and has been employed to calibrate design factors implemented in structural design codes (Madsen et al. 2006). The reliability analysis and design code calibration for wind turbines were presented in several studies, including Tarp-Johansen et al. (2002), Tarp-Johansen (2003), Sørensen and Tarp-Johansen (2005), Tarp-Johansen (2005). The design philosophy of the WT implemented in International Electrotechnical Commission (IEC) codes was based on the load and resistance factor design (LRFD) approach; the load and resistance factors were calibrated based on selected target reliability indices. Earlier versions of IEC did not cover the tropical cyclone condition. This is overcome by IEC 61400-3-1 (2019) and IEC 61400-1 (2019), stating that the design wind speed at the hub height for the TC scenario is equal to 57 m/s (based on 10-min mean wind speed) should be considered. However, calibration leading to such a wind speed is unclear. Most importantly, it is unknown whether such a design wind speed is validated for the coastal regions near the coastline of mainland China.

It is well-known that TC climatology varies from geographical region to region. The statistical characteristics of TC wind and wave hazard play an important role in selecting the design wind speed and the corresponding selected target reliability indices (Tarp-Johansen and Clausen 2006). A review of the structural reliability analysis for WTs, especially focused on the structural components, was given in Jiang et al. (2017). The reliability analysis of mechanical components in terms of downtime and time-dependent failure rate assessment was given in Tavner et al. (2007).

Tarp-Johansen and Clausen (2006) investigated the feasibility of the design of wind turbines in the Philippines, which is known to be a TC-prone region. The reliability model and a simple cost-benefit model were presented to calibrate the safety factors to achieve the same target reliability level as that implied in IEC. The study indicated that the uncertainty in the extreme TC wind speed is greater than that in the extreme synoptical wind. It was recommended to use a load safety factor of 1.7 if a typical

coefficient of variation (COV) of 0.3 for the annual maximum TC wind speed is considered. The design criteria considering the offshore wind and wave combinations were discussed in Nessim et al. (1995), Tarp-Johansen (2005). Studies in Jah et al. (2010), Yu et al. (2012) investigated the implied reliability levels in the IEC and American Petroleum Institute (API) and discussed the design load cases (DLCs) that are applicable to U.S. waters regarding the TC conditions. Their results indicated that the region-specific TC characteristics could influence the structural safety level.

The turbine classes and DLCs for WT subjected to typhoon winds in China were specified in the codes (GB/T 18451.1 2012; GB/T 31519 2015), recommending the use of the 50-year return period value of the annual maximum wind speed for onshore wind turbines. However, it seems that these codes are silent on the load factors for offshore WTs subjected to TC wind and wave loads. It is inferred from industry practice that, in such a case, the use of the IEC 61400-3 (2019) could be considered. A simple feasibility study of offshore WTs by considering sites near the coastline of mainland China was given in Yan et al. (2009). The failure probability assessment for a semi-submersible offshore WT placed in the coastal region of mainland China was presented in Liu et al. (2018) but considering the historical TC tracks. The estimated failure probability is relatively high but consistent with those obtained by Rose et al. (2012) for monopole WTs installed at the sites in the coastal region of the U.S.

Other studies focused on the risk assessment of WTs subjected to TC hazard include those given by Hong and Möller (2012), Buchana and McSharry (2019), Wilkie and Galasso (2020), Jaimes et al. (2020). However, none of these studies considered both the TC induced wind and wave. Moreover, it seems that a reliability-based TC wind and wave load calibration for WTs to be designed, constructed, and installed at the sites near the coastline of mainland China is unavailable.

1.5 Objectives of this study

The main objectives of this study are:

1) To assess the differences in two commonly used best-track datasets (i.e., the China Meteorological Administration (CMA) and the Joint Typhoon Warning Center (JTWC)) for TCs affecting mainland China, to use these two best-track datasets to develop the beta-advection track model (BAM), and to estimate TC wind hazard by using the developed track models.
2) To establish a procedure to assess the joint TC wind and wave hazards, to assess their correlation, and the joint probabilistic model.
3) To develop a database-driven simulation-based (DDSB) framework to estimate the reliability of offshore WTs, to illustrate its application for a semi-submersible offshore WT.
4) To calibrate design TC wind and wave loads and companion load factors for designing monopile onshore and offshore monopole WTs for selected target reliability indices, and recommend site-dependent and information-sensitive design TC wind and wave loads for such WTs.

1.6 Chapter organization

The remaining chapters of this study are organized as follows:

Chapter 2 explored the differences in the assessed TC wind hazard caused by using different historical best TC track datasets and track modeling approaches. For the assessment, a comparison of the statistics of the TC track parameters along the coastline of mainland China using the best track datasets from the China Meteorological Administration (CMA) and the Joint Typhoon Warning Center (JTWC) is presented. A physical-based beta-advection model (BAM) is developed using these historical track datasets. The comparison is extended by considering an existing autoregressive type of track model. Finally, a comparison of the estimated T-year return period value of the annual maximum TC wind speed is presented by considering the three different track models.

Chapter 3 proposed a simulation-based framework to estimate TC-induced wind and wave hazards by considering the TC tracks, wind field, and significant wave field

models. The proposed approach is applied to several offshore sites located near the coastline of mainland China. Both the block maximum based analysis and event-based analysis of the extremes are carried out. The marginal distribution of the annual maximum wind speed and of annual maximum significant wave height is modelled using the generalized extreme value distribution. Plots of paired samples in terms of the probability of the annual maximum wind speed (significant wave height) and of its companion significant wave height (wind speed) are established using Copula. The implication of the results in assigning the load combination factors for combined TC wind and wave load effect is discussed. Finally, the hazard deaggregation results are presented to identify the most likely events causing the *p*-quantile of the annual maximum wind speed and the annual maximum significant wave height.

Chapter 4 presented an overall database-driven simulation-based (DDSB) procedure to assess the fragility and reliability of offshore WTs subjected to TC hazards. The procedure relies on establishing the synthetic databases of TC track, wind and wave fields, and structural response. The construction of the databases and their use for reliability analysis are described. The proposed analysis procedure can take into account the dependent TC induced wind and wave loads to estimate failure probability by considering multiple performance limits of various components. The evaluation of the reliability of an offshore semi-submersible WT placed at four potential locations near the coastline of mainland China is carried out. The site-varying 50-year return period values of the wind speed and wave height vary spatially are discussed. The system failure probability of the considered WT is identified, which is greater than the optimal value suggested in the literature. The dominant failure probability is identified. The sensitivity analysis by scaling the environmental variables is finally performed.

Chapter 5 calibrated the site-specific TC wind and wave loads for designing offshore and onshore WTs located in the coastline region of China, considering the information-sensitive target reliability levels. The calibration applied the developed DDSB framework that can take the correlated TC wind speed and significant wave height into account. The TC wind and wave hazard mapping for the considered region was presented for 50- and 500- year return periods. Then, the companion load factors by

considering wind load and inertial wave load effects are calibrated for the shallow water sites. Finally, the statistics of responses of the NREL onshore and offshore 5MW wind turbine are used in the reliability-based verification analysis by considering the calibrated design TC wind load and wave load requirements.

Conclusions and recommendations drawn from this thesis are summarized in Chapter 6. Also, a few potential future research topics are suggested.

1.7 Reference

Batts, M. E., Simiu, E., & Russell, L. R. (1980). Hurricane wind speeds in the United States. Journal of the Structural Division, 106(10), 2001-2016.

Bowyer, P. J., & MacAfee, A. W. (2005). The theory of trapped-fetch waves with tropical cyclones—An operational perspective. Weather and forecasting, 20(3), 229-244.

Bretschneider, C. L. (1959). Hurricane design-wave practices. Transactions of the American Society of Civil Engineers, 124(1), 39-62.

Buchana, P., & McSharry, P. E. (2019). Windstorm risk assessment for offshore wind farms in the North Sea. Wind Energy, 22(9), 1219-1229.

Casson, E., & Coles, S. (2000). Simulation and extremal analysis of hurricane events. Journal of the Royal Statistical Society: Series C (Applied Statistics), 49(3), 227-245.

Chen, X., & Xu, J. Z. (2016). Structural failure analysis of wind turbines impacted by super typhoon Usagi. Engineering failure analysis, 60, 391-404.

Chen, Y., & Duan, Z. (2018). A statistical dynamics track model of tropical cyclones for assessing typhoon wind hazard in the coast of southeast China. Journal of Wind Engineering and Industrial Aerodynamics, 172, 325-340.

Chow, S. (1971). “A study of the wind field in the planetary boundary layer of a moving tropical cyclone.” M.Sc. thesis, New York University, New York.

Cui, W., & Caracoglia, L. (2019). A new stochastic formulation for synthetic hurricane simulation over the North Atlantic Ocean. Engineering Structures, 199, 109597.

Cui, W., Zhao, L., Cao, S., & Ge, Y. (2021). Bayesian optimization of typhoon full-track simulation on the Northwestern Pacific segmented by QuadTree decomposition. Journal of Wind Engineering and Industrial Aerodynamics, 208, 104428.

Darling, R. W. R. (1991). Estimating probabilities of hurricane wind speeds using a large-scale empirical model. Journal of Climate, 4(10), 1035-1046.

Donelan, M. A., Hamilton, J., & Hui, W. (1985). Directional spectra of wind-generated ocean waves. Philosophical Transactions of the Royal Society of London. Series A, Mathematical and Physical Sciences, 315(1534), 509-562.

Emanuel, K., Ravela, S., Vivant, E., & Risi, C. (2006). A statistical deterministic approach to hurricane risk assessment. Bulletin of the American Meteorological Society, 87(3), 299-314.

GB/T 18451.1. (2012). Wind turbine generator systems - Design requirements, Standards Press of China, Beijing, China. (in Chinese)

GB/T 31519-2015. (2015). Wind turbine generator system under typhoon condition, Standards Press of China, Beijing, China. (in Chinese)

Georgiou, P.N. (1986), “Design wind speed in tropical cyclone-prone regions”, Ph.D. Dissertation, Department of Civil Engineering, University of Western Ontario, Canada.

Group, T. W. (1988). The WAM model—A third generation ocean wave prediction model. Journal of Physical Oceanography, 18(12), 1775-1810.

Gu, J. Y., Sheng, C., & Hong, H. P. (2020). Comparison of tropical cyclone wind field models and their influence on estimated wind hazard. Wind and Structures, 31(4), 321-334.

Hall, T. M., & Jewson, S. (2007). Statistical modelling of North Atlantic tropical cyclone tracks. Tellus A: Dynamic Meteorology and Oceanography, 59(4), 486-498.

Hallowell, S.T., Myers, A.T., Arwade, S. R., Pang, W., Rawal, P., Hines, E.M., ... & Carswell, W. (2018). Hurricane risk assessment of offshore wind turbines. Renewable Energy, 125, 234-249.

Hasselmann, K. F., Barnett, T. P., Bouws, E., Carlson, H., Cartwright, D. E., Eake, K., ... & Walden, H. (1973). Measurements of wind-wave growth and swell decay during the Joint North Sea Wave Project (JONSWAP). Ergaenzungsheft zur Deutschen Hydrographischen Zeitschrift, Reihe A.

Holland, G. J. (1980), "An analytic model of the wind and pressure profiles in hurricanes", Monthly weather review, 108(8), 1212-1218.

Holland, G. J., Belanger, J. I., & Fritz, A. (2010). A revised model for radial profiles of hurricane winds. Monthly weather review, 138(12), 4393-4401.

Holton, J. (2004). An introduction to dynamic meteorology, 4th Ed.

Hong L, & Möller B. (2012). An economic assessment of tropical cyclone risk on offshore wind farms. Renewable Energy, 44:180-192.

Hong, H. P., Li, S. H., & Duan, Z. D. (2016). Typhoon wind hazard estimation and mapping for coastal region in mainland China. Natural Hazards Review, 17(2), 04016001.

Hong, X., & Li, J. (2021). A beta-advection typhoon track model and its application for typhoon hazard assessment. Journal of Wind Engineering and Industrial Aerodynamics, 208, 104439.

Hong, X., Hong, H. P., & Li, J. (2019), "Solution and validation of a three dimensional tropical cyclone boundary layer wind field model". Journal of Wind Engineering and Industrial Aerodynamics, 193, 103973.

Hwang, P. A. (2016). Fetch-and duration-limited nature of surface wave growth inside tropical cyclones: With applications to air–sea exchange and remote sensing. Journal of Physical Oceanography, 46(1), 41-56.

IEC International Electrotechnical Commission (2019). IEC 61400-3-1: Wind energy generation systems –Part 3-1: Design requirements for fixed offshore wind turbines.

IEC International Electrotechnical Commission. (2019). IEC 61400-1: Wind turbines part 1: Design requirements. International Electrotechnical Commission.

Ishihara, T., Yamaguchi, A., Takahara, K., Mekaru, T., & Matsuura, S. (2005, September). An analysis of damaged wind turbines by typhoon Maemi in 2003. In Proceedings of the sixth asia-pacific conference on wind engineering (pp. 1413-1428).

Jaimes, M. A., García‐Soto, A. D., Martín del Campo, J. O., & Pozos‐Estrada, A. (2020). Probabilistic risk assessment on wind turbine towers subjected to cyclone‐induced wind loads. Wind Energy, 23(3), 528-546.

James, M. K., & Mason, L. B. (2005). Synthetic tropical cyclone database. Journal of waterway, port, coastal, and ocean engineering, 131(4), 181-192.

Jha, A., Dolan, D., Musial, W., & Smith, C. (2010). On hurricane risk to offshore wind turbines in US Waters. Proceedings from the 2010 Offshore Technology Conference. Houston, TX.

Jiang, Z., Hu, W., Dong, W., Gao, Z., & Ren, Z. (2017). Structural reliability analysis of wind turbines: A review. Energies, 10(12), 2099.

Kepert, J. (2001). The dynamics of boundary layer jets within the tropical cyclone core. Part I: Linear theory. Journal of the Atmospheric Sciences, 58(17), 2469-2484.

Kepert, J., & Wang, Y. (2001). The dynamics of boundary layer jets within the tropical cyclone core. Part II: Nonlinear enhancement. Journal of the atmospheric sciences, 58(17), 2485-2501.

King, D. B., & Shemdin, O. H. (1978). Radar observation of hurricane wave directions. In Coastal Engineering 1978 (pp. 209-226).

Lee, C. Y., Tippett, M. K., Sobel, A. H., & Camargo, S. J. (2018). An environmentally forced tropical cyclone hazard model. Journal of Advances in Modeling Earth Systems, 10(1), 223-241.

Li, S. H., & Hong, H. P. (2015). Observations on a hurricane wind hazard model used to map extreme hurricane wind speed. Journal of Structural Engineering, 141(10), 04014238.

Li, S. H., & Hong, H. P. (2016). Typhoon wind hazard estimation for China using an empirical track model. Natural Hazards, 82(2), 1009-1029.

Li, S. H., & Kumar, K. S. (2021). Cyclone wind hazard assessments for eastern coastal cities in India using a fast-predictive model. Journal of Wind Engineering and Industrial Aerodynamics, 218, 104760.

Li, Z. Q., Chen, S. J., Ma, H., & Feng, T. (2013). Design defect of wind turbine operating in typhoon activity zone. Engineering Failure Analysis, 27, 165-172.

Madsen, H. O., Krenk, S., & Lind, N. C. (2006). Methods of structural safety. Courier Corporation.

Marks, D. G., (1992). The beta and advection model for hurricane track forecasting. NOAA Tech. Memo. NWS NMC 70, 89 pp.

Meng, Y., Matsui, M. & Hibi, K. (1995). An analytical model for simulation of the wind field in a typhoon boundary layer, Journal of Wind Engineering and Industrial Aerodynamics, 56(2-3), 291-310.

Meng, Y., Matsui, M. & Hibi, K. (1997). A numerical study of the wind field in a typhoon boundary layer, Journal of Wind Engineering and Industrial Aerodynamics, 67, 437-448.

Nessim, M. A., Hong, H. P., Swail, V. R., & Henderson, C. A., (1995). Design Criteria for Offshore Structures Under Combined Wind and Wave Loading, ASME Journal of Offshore Mechanics and Arctic Engineering, Vol. 117.

Ochi, M. K. (1993). On hurricane-generated seas. In Ocean wave measurement and analysis (pp. 374-387). ASCE.

Ou, J. P., Duan, Z. D., & Chang, L. (2002). Typhoon risk analysis for key coastal cities in southeast China. J. Nat. Disaster, 11(4), 9–17 (in Chinese).

Powell, M. D., Houston, S. H., Amat, L. R., & Morisseau-Leroy, N. (1998). The HRD real-time hurricane wind analysis system. Journal of Wind Engineering and Industrial Aerodynamics, 77, 53-64.

Powell, M., Soukup, G., Cocke, S., Gulati, S., Morisseau-Leroy, N., Hamid, S., ... & Axe, L. (2005). State of Florida hurricane loss projection model: Atmospheric science component. Journal of wind engineering and industrial aerodynamics, 93(8), 651-674.

Rose, S., Jaramillo, P., Small, M. J., Grossmann, I., & Apt, J. (2012). Quantifying the hurricane risk to offshore wind turbines. Proceedings of the National Academy of Sciences, 109(9), 3247-3252.

Ross, D. (1976). A simplified model for forecasting hurricane generated waves. In Bulletin of the American Meteorological Society (Vol. 57, No. 1, pp. 113-113).

Russell, L. R. (1971). Probability distributions for hurricane effects. Journal of the Waterways, Harbors and Coastal Engineering Division, 97(1), 139-154.

Shapiro, L. J. (1983). The asymmetric boundary layer flow under a translating hurricane. Journal of Atmospheric Sciences, 40(8), 1984-1998.

Shen, Z., & Wei, K. (2021). Stochastic model of tropical cyclones along China coast including the effects of spatial heterogeneity and ocean feedback. Reliability Engineering & System Safety, 216, 108000.

Sørensen, J.D., & Tarp-Johansen, N.J. (2005). Reliability-based optimization and optimal reliability level of offshore wind turbines. International Journal of Offshore and Polar Engineering, 15(02).

Tarp-Johansen, N. J. (2003). Examples of fatigue lifetime and reliability evaluation of larger wind turbine components. Risø National Laboratory, Roskilde, March 2003.

Tarp-Johansen, N. J. (2005). Partial safety factors and characteristic values for combined extreme wind and wave load effects. J. Sol. Energy Eng., 127(2), 242-252.

Tarp-Johansen, N.J., & Clausen, N-E. (2006). Design of Wind Turbines in Typhoon area: A first study of Structural Safety of Wind Turbines in Typhoon prone areas. EC-ASEAN Energy Facility.

Tarp-Johansen, N.J., Sørensen, J.D., & Madsen, P.H. (2002). Experience with acceptance criteria for offshore wind turbines in extreme loading. In Workshop on reliability based code calibration.

Tavner, P. J., Xiang, J., & Spinato, F. (2007). Reliability analysis for wind turbines. Wind Energy: An International Journal for Progress and Applications in Wind Power Conversion Technology, 10(1), 1-18.

Thompson, E. F., & Cardone, V. J. (1996). Practical modeling of hurricane surface wind fields. Journal of Waterway, Port, Coastal, and Ocean Engineering, 122(4), 195-205.

Vickery, P. J. (2005). Simple empirical models for estimating the increase in the central pressure of tropical cyclones after landfall along the coastline of the United States. Journal of applied meteorology, 44(12), 1807-1826.

Vickery, P. J., & Twisdale, L. A. (1995). Prediction of hurricane wind speeds in the United States. Journal of Structural Engineering, 121(11), 1691-1699.

Vickery, P. J., Skerlj, P. F., & Twisdale, L. A. (2000). Simulation of hurricane risk in the US using empirical track model. Journal of structural engineering, 126(10), 1222-1237.

Vickery, P. J., Wadhera, D., Twisdale Jr, L. A., & Lavelle, F. M. (2009). US hurricane wind speed risk and uncertainty. Journal of structural engineering, 135(3), 301-320.

Wilkie, D., & Galasso, C. (2020). A probabilistic framework for offshore wind turbine loss assessment. Renewable Energy, 147, 1772-1783.

World Meteorological Organization. (2020). World's deadliest tropical cyclone was 50 years ago. Published: 12 November 2020. https://public.wmo.int/en/media/news/world%E2%80%99s-deadliest-tropical-cyclone-was-50-years-ago

Wu, F., Huang, G., & Zhou, X. (2021). Enhanced Circular Subregion Method in Typhoon Hazard Analysis. Journal of Structural Engineering, 147(6), 06021003.

Xiao, Y. F., Duan, Z. D., Xiao, Y. Q., Ou, J. P., Chang, L., & Li, Q. S. (2011). Typhoon wind hazard analysis for southeast China coastal regions. Structural Safety, 33(4-5), 286-295.

Yan et al. (2009). Feasibility study of the impact of typhoon on offshore wind farm operation in China, report no. EEP-PMU/CN/12607/RE003, 2009. See also: http://frankhaugwitz.com/doks/wind/2009_11_China_Wind_Offshore_Typhoon_EN.pdf.

Young, I. R. (1998). Observations of the spectra of hurricane generated waves. Ocean Engineering, 25(4-5), 261-276.

Young, I. R. (2017). A review of parametric descriptions of tropical cyclone wind-wave generation. Atmosphere, 8(10), 194.

Young, I. R., & Vinoth, J. (2013). An “extended fetch” model for the spatial distribution of tropical cyclone wind–waves as observed by altimeter. Ocean Engineering, 70, 14-24.

Yu, Q., Kim, K., & Lo, T. W. (2012). Design load cases required for offshore wind turbines in hurricane-prone regions. In Offshore Technology Conference. OnePetro.

Zeng, D., Zhang, H., Li, Q., & Ellingwood, B. R. (2021). Tropical cyclone damage assessment of distributed infrastructure systems under spatially correlated wind speeds. Structural Safety, 91, 102080.

Chapter 2

2 Sensitivity of typhoon wind hazard in coastal region to the track modelling and the considered historical best track database

2.1 Introduction

Tropical cyclones cause strong winds, heavy rainfalls, and large storm surges. Severe tropical cyclones (TCs) (i.e., typhoons) cause extreme natural disasters, claiming thousands of lives and economic losses in China (Liu et al. 2009; Chen et al. 2010; Peng et al. 2018). One of the earlier TC wind hazard assessments for sites in mainland China was carried out by Ou et al. (2002). They focused their study on several major cities in the coastal region of China. They adopted a simple TC wind field model and used the circular subregion method (Georgiou et al. 1983) for estimating the TC wind hazard, where only the statistics from historical tracks near the considered sites were employed. The simple TC wind field model that was used in Ou et al. (2002) was subsequently replaced in Xiao et al. (2011) by the vertically averaged boundary layer slab model that was originally developed by Chow (1971) and modified by Thompson and Cardone (1996). The use of the circular subregion method was also considered in Li and Hong (2015b) and Hong et al. (2016) to assess the TC winds affecting China but using the slab model with calibrated model parameters given by Vickery and Wadhera (2008) and Vickery et al. (2009) (see also Li and Hong 2015a). Other studies focused on the TC wind hazard assessment for the coastal regions in mainland China by using the circular subregion method include Liu et al. (2018), Fang et al. (2021), and Wu et al. (2021).

The use of the circular subregion method could be adequate for a site of interest if a sufficient number of TC track segments near the site are available. However, this may not always be the case. Also, the use of the subregion method could not provide a clear picture of the TC hazard caused by the passage of a landfilling TC for the coastal region. This problem could be overcome by using the synthetic tracks simulated using stochastic

track models that are developed based on the historical best track datasets. In fact, this approach was taken by Li and Hong (2016) for mapping the TC wind hazard for the coastal regions in mainland China, where the track model was developed based on regression analysis and the best historical track dataset available from the China Meteorological Administration (CMA) (http://tcdata.typhoon.org.cn/tcsize.html) (Ying et al. 2014). The use of the full track approach for assessing the TC wind hazard for sites in the region was also considered in Liu et al. (2019), Chen and Duan (2018), Sheng and Hong (2020), Chen et al. (2021), and Huang et al. (2021). While Liu et al. (2019) used the historical tracks directly, Chen et al. (2021) incorporated climate change effect in assessing TC wind hazard. In Chen et al. (2021), the track model was developed based on the beta-advection modelling approach (Marks, 1992; Emanuel et al. 2006) and considering the best track dataset from the Joint Typhoon Warning Center (JTWC) (https://www.metoc.navy.mil/jtwc/jtwc.html). The development of the beta-advection model was also considered in X. Hong and Li (2021). In this case, the model was developed based on the best track dataset from CMA. However, at present, a comparison of the performance of the tracks based on the autoregressive type of model and beta-advection type of model is unavailable. Most importantly, whether their use could lead to consistent TC wind hazard maps is unknown. In addition to the best track datasets given by CMA and JTWC, there are at least two other best track datasets, one given by Japan Meteorological Agency and the other given by Hong Kong Observatory. However, these two are less used as compared to those given by CMA and JTWC for the TC winds affecting the coastal region of mainland China.

Besides considering the historical or synthetic tracks for mapping the TC wind hazard, another important component for the TC wind hazard assessment is the adopted wind field model. A comparison of a few simple TC wind field models was given in Gu et al. (2020). It was indicated that some of the simple TC wind fields are deficient in producing horizontal surface wind field that mimics the one obtained based on the slab model with well-calibrated model parameters (Vickery and Wadhera 2008; Vickery et al. 2009; Li and Hong 2015a). Also, the along height wind profile predicted by some of the simple models does not follow that derived from the observational data. It is noted that a 3D nonlinear model was presented in Kepert and Wang (2001). This model was

implemented in Hong et al. (2019), showing that the model could result in the along height horizontal wind profile consistent with that obtained based on the observational data. However, a systematic calibration of the model parameters for this wind field model that can be used for the TC wind hazard assessment is currently unavailable. The use of the Weather Research Forecast model (https://www.mmm.ucar.edu/weather-research-and-forecasting-model) for the TC hazard modeling for offshore locations near the coastline in mainland China was presented in Liu et al. (2019). Because of the required computational effort and boundary conditions, only the historical tracks were considered in their analysis. The above review of the TC wind field models indicates that the simple and calibrated model for the TC wind hazard modeling is the slab model (Vickery and Wadhera 2008; Vickery et al. 2009).

The present study has two main objectives. The first one is to develop the stochastic beta-advection models for TC tracks based on the same procedure but using the best track datasets from CMA and JWTC. The use of the same procedure avoids the differences that could be caused by the differences introduced by the methods used in evaluating the model coefficients. The performance of these models is compared in terms of the TC occurrence rate, translation velocity, heading, and central pressure difference of the TCs affecting the southeast coastline in mainland China. The second objective is to compare the mapped TC wind hazard for the coastal region obtained using different stochastic track models. The remainder of this paper is organized as follows: The differences in the TC track datasets from CMA and JWTC are described; the use of the datasets to develop the beta-advection models is presented; a comparison of the statistics of the tracks simulated using the stochastic track models to those of the historical best track datasets is given for sites along the coastline; this is followed by the presentation of the estimated TC wind hazard by considering different stochastic track models, and finally the conclusions and recommendations are presented.

2.2 Description of best track datasets and comparison

2.2.1 Data description

The historical best track dataset covering years from 1949 to the present is available from CMA. The description of this database is given by Ying et al. (2014). Such a dataset can also be obtained from JTWC. While the dataset from CMA is focused on the Western North Pacific (WNP) basin, the dataset from JWTC covers different basins. The dataset from JWTC contains the TC events from 1945 to the present for WNP. The description of this dataset was given by Chu et al. (2002) (https://www.metoc.navy.mil/jtwc/products/best-tracks/tc-bt-report.html), indicating that the data before 1960 may not have a fidelity as high as after the 1960s. It is noted that the supporting documentation used to perform the data corrections was missing for dates before 1950 for WNP (Chu et al. 2002). The datasets covering the TC activities from 1949 to 2018 from CMA and JWTC are used in the following to develop the beta-advection models using the same procedure.

Some of the characteristics of the historical tracks are summarized in Table 2.1. The TC activities from the two considered datasets are shown in Figure 2.1, illustrating that the TC activities from both datasets are similar. However, there are differences. For example, the number and the length of tracks from CMA within 160^{o} to 180^{o}E and 36^{o} to 55^{o}N are less than those from JTWC. An inspection of the track data per year also indicates that there are differences. On occasion, a track that appears in the dataset from CMA is missing in JWTC and vice versa. The agreement between these two datasets improves for more recent TC activities since the number of TCs recorded in these two datasets from 2000 to the present is more consistent.

Table 2.1. Summary of characteristics of TC activities for WNP basin given in the datasets.

Data catalogue	Maximum Sustained Wind Speed	Minimum Central Pressure	Spatial resolution	Temporal resolution	Data span
CMA	2-min (m/s)	Available after 1949	0.1° (Lat. & Lon.)	6-h	1949 - present
JTWC	1-min (knots)	Available after 2000	0.1° (Lat. & Lon.)	6-h	1945 - present

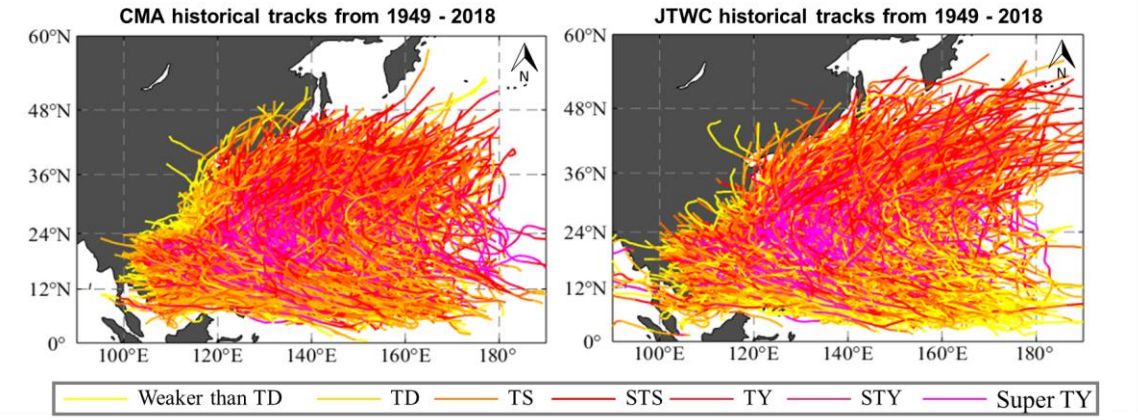

Figure 2.1. Historical TC track activities from 1949 to 2018: a) based on the dataset from CMA, b) based on the dataset from JTWC. For the plot, the intensity categories TD, TS, STS, TY, STY, Super TY represent the tropical depression, tropical storm, severe tropical storm, typhoon, severe typhoon, and super typhoon (GB/T19201 2006). These intensity categories are associated with the near-surface maximum 2-min wind speed equal to (10.8, 17.1), (17.2, 24.4), (24.5, 32.6), (32.7, 41.4), (41.5, 50.9), and greater than 51.0 m/s, respectively. The 1-min maximum sustained wind speed from JTWC is converted to the 2-min maximum by multiplying a factor of 0.97 (Vickery and Skerlj 2005), and the intensity category is then applied.

2.2.2 Comparison of statistics of the best track datasets

2.2.2.1 Genesis, occurrence rate, and translation velocity

The coordinates of the genesis of TCs are extracted from the two considered datasets, one from CMA and the other from JTWC. The geneses are plotted in Figure 2.2a, showing that the geneses from the two datasets do not always coincide. A year-to-year comparison of the TC occurrence is shown in Figure 2.2b by the considered two datasets. This plot indicates differences in the number of TC events reported in each year by the two datasets. The difference decreases as the time approaches the present. The empirical distribution of the annual occurrence rate of the TCs is presented in Figure 2.2c. The figure shows that, on average, the number of TCs in each year, X, based on the dataset from CMA is about 7% greater than that from JTWC. The coefficient of variation (COV) of X for the dataset from CMA is smaller than that for the dataset from JTWC. The figure also shows that, in both cases, X can be modelled using the negative binomial distribution, $p(x)$, is,

$$p_X(x) = \binom{x+r-1}{x}(1-p)^x\, p^r \tag{2.1}$$

where x is the value of X, and $(r, p) = (75.70, 0.70)$ for the dataset from CMA, and $(r, p) = (35.02, 0.54)$ for the dataset from JTWC. The mean of X equals 32.2 and 30.1 for data from CMA and data from JTWC, respectively. The values for the dataset from CMA differ slightly from those given in Li and Hong (2016), which were obtained using the track data up to 2012.

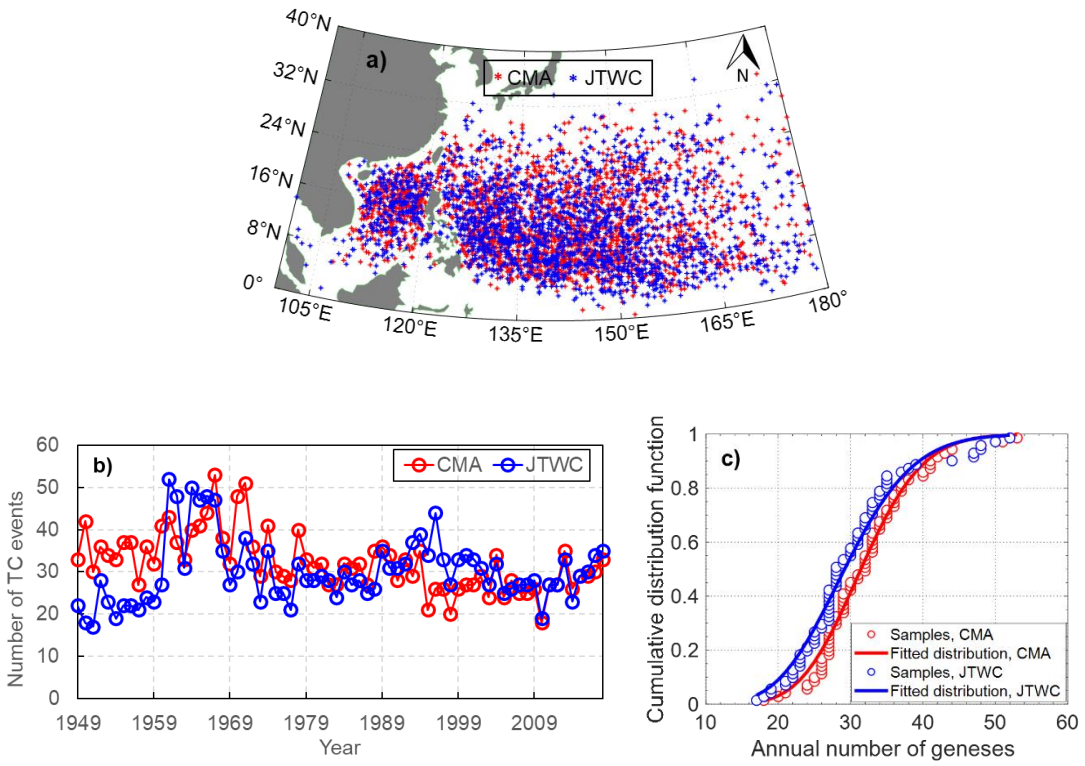

Figure 2.2. Spatial distribution of the genesis and empirical distribution of the number of TCs per year based on the datasets from CMA and JTWC (from 1949 to 2018): a) spatial distribution of TC genesis; b) comparison of occurrence per year; c) probability distribution of the number of TCs per year.

The displacement per six hours (i.e., velocity) of the TC center is calculated using two subsequent positions on each TC track that are reported every six hours. The obtained samples of the displacement are presented in Figure 2.4 in terms of histograms. The plots shown in the figure indicate that there are differences in the probability mass function of the displacements per six hours. The difference is most noticeable for the zonal displacement and the meridional displacement equal to about -0.5° .

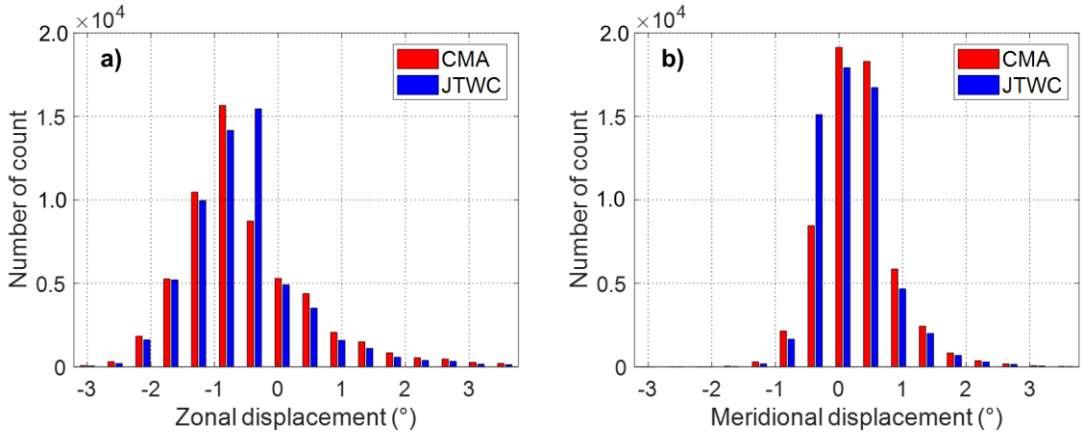

Figure 2.3. Historgram of the displacement of TC centre per six yours for all tracks within the region defined by 5º to 40ºN and 110º to 170ºE: a) zonal displacement per six hours and b) meridional displacement per six hours.

2.2.2.2 Statistics of track parameters along the coastline

The kilometer posts (KPs) along the coastline shown in Figure 2.4a are considered to aid the presentation of the statistics of the track parameters. For a circle with a radius of 250 km and the center that is located on the KPs of coastline, the statistics of the number of TCs per year, the heading of each track, and the translation velocity for each track are calculated using each of the two best track datasets. The obtained mean and standard deviation of these TC track parameters are shown in Figures 2.4b to 2.4c. Figure 4b shows that the estimated average of the annual occurrence rate using the dataset from CMA is consistently greater than that from JTWC, agreeing with the observations made earlier on the number of geneses. The largest difference is about 30%. Figures 2.4c and 2.4d do not provide clear spatial trends of the differences between the statistics of the heading or translation velocity by considering the two best track datasets. The mean of the heading and the mean of translation velocity obtained by considering one or the other best track dataset are more consistent for KPs less than 2500 km than for KPs greater than 2500 km. Note that no comparison of the central pressure difference by considering the two datasets is presented since the central pressure difference in JTWC is only available after 2001.

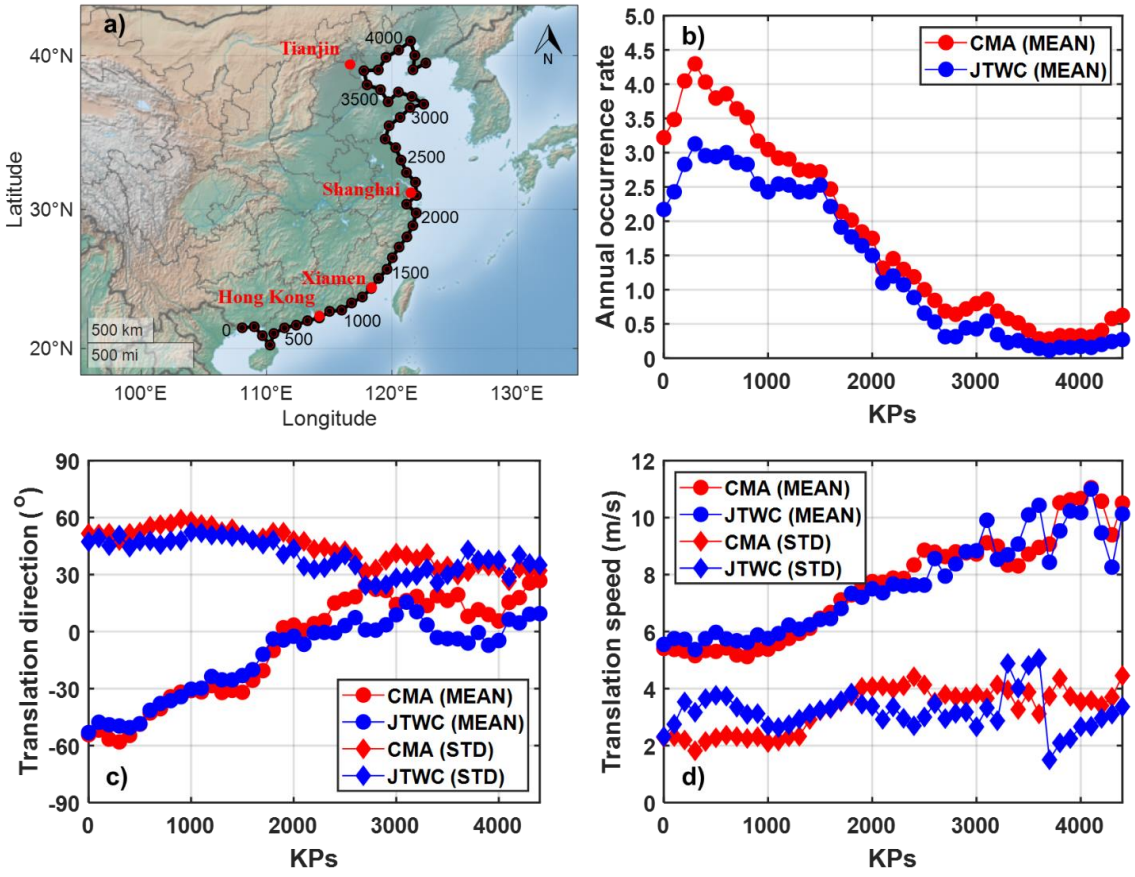

Figure 2.4 Assigned kilometer posts (KPs) and the statistics of the TC track parameters along the coastline: a) assigned KPs, b) mean of occurrence rate, c) mean and standard deviation of heading, and d) mean and standard deviation of translation velocity of TC center.

To further illustrate the differences between the two best track datasets, we consider the site representing Zhanjiang with a latitude of 21.22^{o} and a longitude of 110.35^{o}. The tracks that pass within a circle with a radius of 250 km that is centered at Zhanjiang are shown in Figure 2.5. The average annual TC occurrence rate based on the considered circle equals 3.94 by considering the best track dataset from CMA and 2.9 by considering the dataset from JTWC. Such a difference could affect the developed track models and the estimated wind hazard, which will be discussed in the following sections.

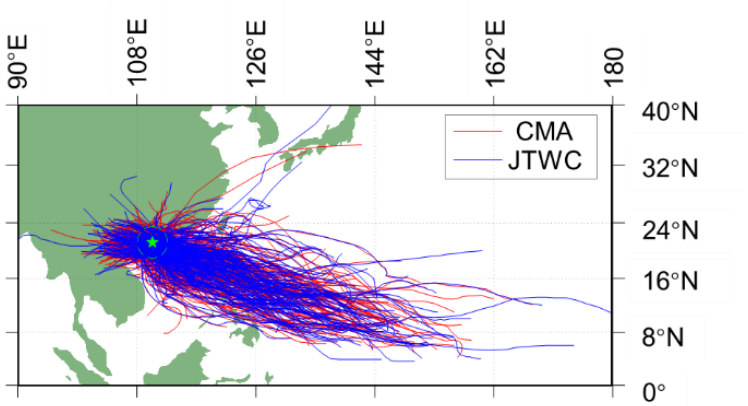

Figure 2.5. Historical TC tracks that affect a circle centered at Zhanjiang with a radius of 250 km.

2.3 Beta and advection model development and their characteristics

2.3.1 Statistics of the beta-advection model

The beta-advection model was proposed in Marks (1992). It was used in Emanuel et al. (2006) for the hurricane hazard assessment for the U.S. The development of the beta-advection model that is applicable for TCs in the WNP basin was presented in Zhao et al. (2009), Chen and Duan (2018), and X. Hong and Li (2021), although only the mean of the beta drift was given. The beta-advection model is a physical-based model. The model considers that the TC translation velocity vector, $\mathbf{V}_{TC}$, can be expressed as,

$$\mathbf{V}_{TC} = \mathbf{V}_{steer} + \mathbf{V}_{\beta} \tag{2.2}$$

where $\mathbf{V}_{steer}$ represents the steering velocity, and the correction term $\mathbf{V}_{\beta}$ is called beta drift. $\mathbf{V}_{\beta}$ is predominantly affected by the advection of the TC vortex with the large-scale environmental flows (Marks 1992; Chan 2005). A schematic illustration of the velocities terms in Eq. (2.2) and the global wind field is given in Figure 2.6.

$\mathbf{V}_{steer}$ is often calculated using the pressure-weighted mean wind speed within a particular

radius band centered at the vortex center (see Figure 2.6). According to Carr and Elsberry (1990), $\mathbf{V}_{steer}$ can be evaluated using,

$$\mathbf{V}_{steer} = \frac{1}{p_u - p_l}\int_{p_l}^{p_u} \boldsymbol{v}_{GW}\, dp \tag{2.3}$$

where $\boldsymbol{v}_{GW}$ is the global wind field, and P_u and P_l are the considered upper and lower pressure levels. For the numerical analysis to be carried out in the present study, P_u and P_l could be taken equal to 850 and 300 hPa, respectively. $\boldsymbol{v}_{GW}$ at various pressure levels could be obtained from the re-analysis data available from the National Centers for Environmental Prediction (NCEP)-National Center for Atmospheric Research (NCAR) with a resolution of 2.5°×2.5° (https://psl.noaa.gov/data/gridded/data.ncep.reanalysis.derived.pressure.html) (Kalnay et al. 1996)

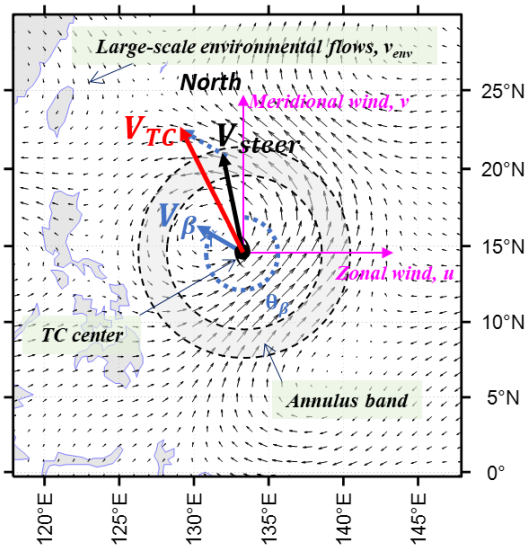

Figure 2.6. A schematic illustration of the TC track translation, steering flow, beta drift, and global wind field.

For example, consider a TC event that occurred in 2006 with the track information given from CMA shown in Figure 2.7a. We extract the re-analysis data that corresponds to the position of the TC track data on 1200UTC/15/08/2006 that is associated with the

identified position on the track denoted as *O*. The extracted $\boldsymbol{v}_{GW}$ is illustrated in Figure 2.7b for P_l equal to 300 hPa and in Figure 2.7c for P_u equal to 850 hPa. $\boldsymbol{v}_{GW}$ for pressure levels equal to 400, 500, 600, and 700 are also extracted. We then considered a circle with its center located at *O* as shown in Figure 2.7a. By considering the radius equal to 5°, we evaluate $\mathbf{V}_{steer}$ for the identified track center by applying Eq. (2.3) with its discrete form represented by,

$$\mathbf{V}_{steer} = (1/6)\left[\boldsymbol{v}_{GW,300} + \boldsymbol{v}_{GW,400} + \boldsymbol{v}_{GW,500} + \boldsymbol{v}_{GW,600} + 1.25\boldsymbol{v}_{GW,700} + 0.75\boldsymbol{v}_{GW,850}\right] \tag{2.4}$$

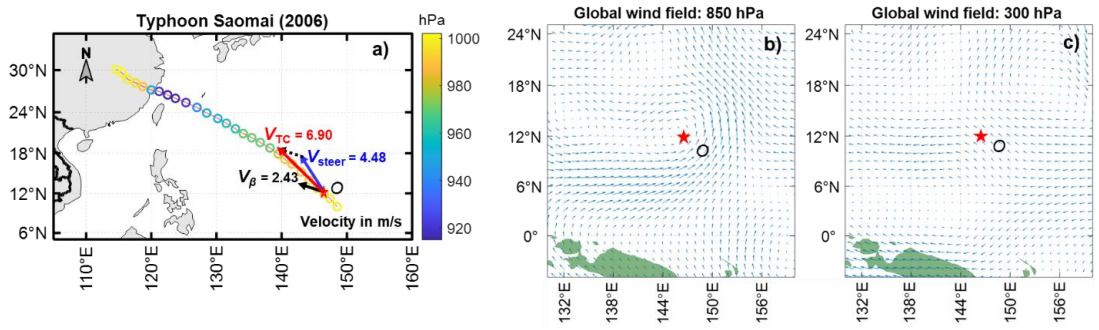

Figure 2.7. Illustration of evaluated V_{steer} and $\mathbf{V}_\beta$ (i.e., $(|\mathbf{V}_\beta|, \theta_\beta)$) for a single TC track at an instance: a) track of typhoon Saomai in 2006 and the calculated $\mathbf{V}_{steer}$ and $\mathbf{V}_\beta$ for the TC center at *O*; b) global wind field P_u equal to 850 hPa, c) global wind field P_l equal to 300 hPa.

where $\boldsymbol{v}_{GW}$ with additional subscript represents the pressure level, and the considered weights and radius are consistent with that used by Chen and Duan (2018). For the calculation, a linearly interpolated value of $\boldsymbol{v}_{GW}$ on the circle of radius of 5° is employed when necessary since the NCEP/NCAR data is given with a resolution of 2.5°×2.5°. The calculated $\mathbf{V}_{steer}$ is shown in Figure 2.7a. Using the identified $\mathbf{V}_{steer}$ and Eq. (2.2), the calculated $\mathbf{V}_\beta$ is also shown in the plot. The use of a sufficiently large radius, such as 5°, is aimed at avoiding the effect of the vortex-like flow around the TC center on the calculated $\mathbf{V}_{steer}$. Note that $\mathbf{V}_\beta$ can be represented by its magnitude and direction, denoted as $(|\mathbf{V}_\beta|, \theta_\beta)$, where the definition of the direction is shown in Figure 2.6 and $|\mathbf{V}_\beta|$ represents the magnitude of $\mathbf{V}_\beta$.

Now, to develop the spatially varying statistical model for $\mathbf{V}_\beta$ hence $\mathbf{V}_{TC}$, we consider a squared grid system with a separation of 5^o as shown in Figure 2.8. For a considered squared cell, we identify tracks from the best track dataset that traverse the cell. We separate the identified tracks into two groups: easterly and westerly tracks. Following the procedure used for the results presented in Figure 2.7, we evaluate $(|\mathbf{V}_\beta|, \theta_\beta)$ for each identified track within the cell. We then estimate the mean and standard deviation of $(|\mathbf{V}_\beta|, \theta_\beta)$ for easterly and westerly TCs for the considered cell. The obtained mean of $(|\mathbf{V}_\beta|, \theta_\beta)$ representing the "mean" of $\mathbf{V}_\beta$ is shown in Figure 8, and the obtained standard deviation of $(|\mathbf{V}_\beta|, \theta_\beta)$ is presented in Figure 2.9. The values for a cell are calculated if there are at least 30 track samples for a considered group within the cell. The consideration of a sample size of 30 is aimed at reducing the statistical uncertainty.

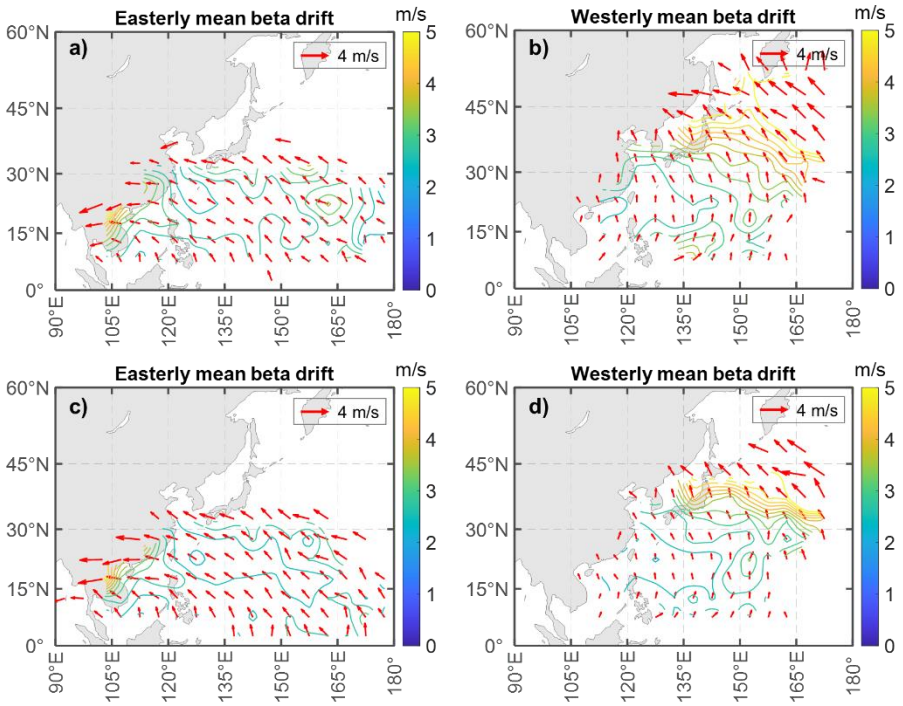

Figure 2.8. Spatial variation of $\mathbf{V}_\beta$ based on the mean of $(|\mathbf{V}_\beta|, \theta_\beta)$ for easterly and westerly tracks: a) and b) for the dataset from CMA, c and d) for the dataset from JTWC.

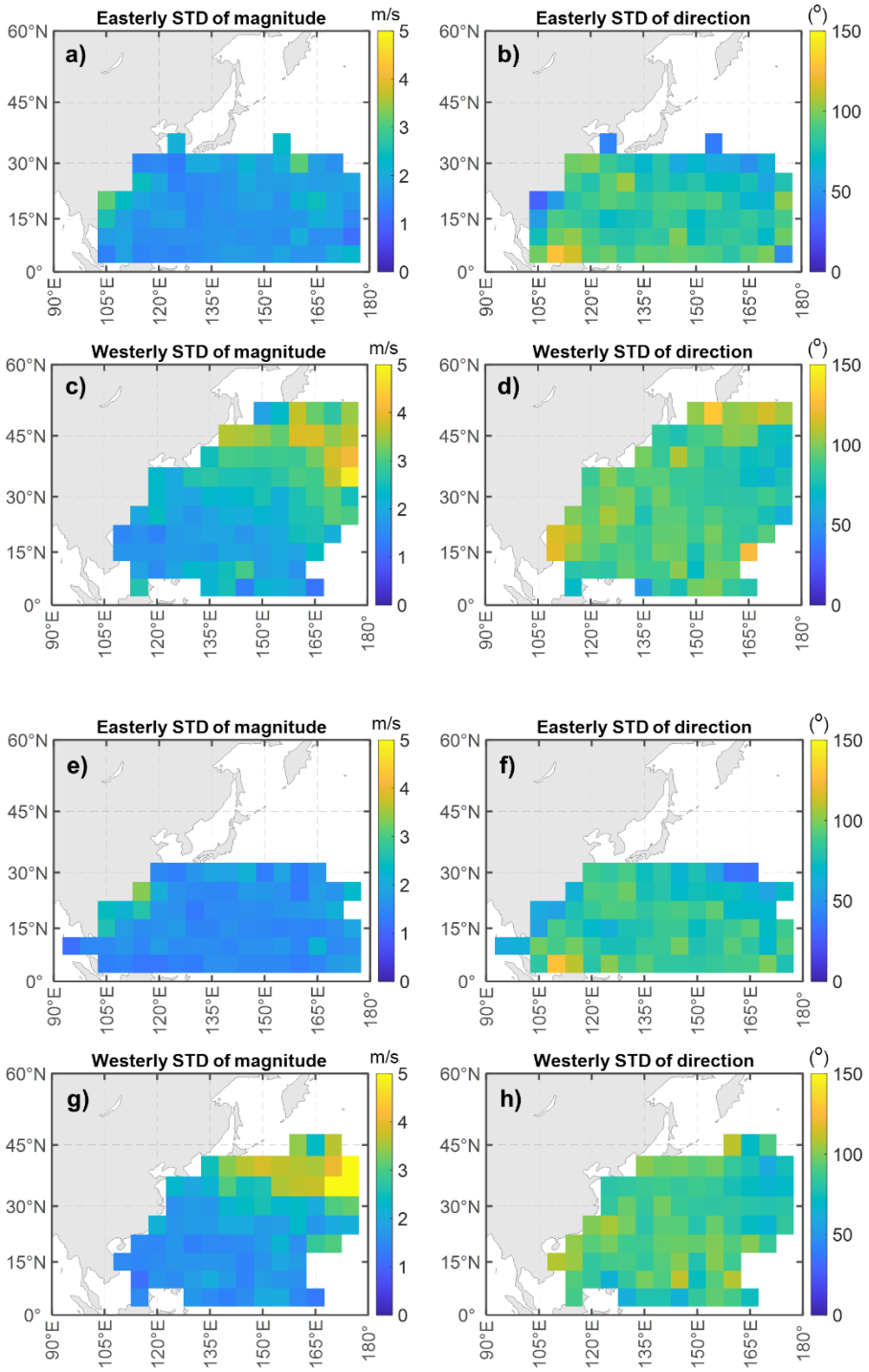

Figure 2.9. Spatial variation of the standard deviation of $(|\mathbf{V}_\beta|, \theta_\beta)$ for easterly and westerly tracks: a) to d) for the dataset from CMA, e) to h) for the dataset from JTWC.

Figure 2.8 shows that the calculated "mean" of $\mathbf{V}_\beta$ is consistent by considering the datasets from CMA and JTWC. For the vast majority of cases shown in the figure, $|\mathbf{V}_\beta|$ is within 1 to 3 m/s. A few cells located at the high latitudes have a mean $|\mathbf{V}_\beta|$ greater than 3 m/s. This is partly due to the Coriolis effect. The direction for the majority of $\mathbf{V}_\beta$ is northwestward. The overall average values of $(|\mathbf{V}_\beta|, \theta_\beta)$ are 2.99 m/s and 317.4° if the best track dataset from CMA is considered. These values become 2.71 m/s and 317° if the best track dataset from JTWC is considered. This again shows that the identified $\mathbf{V}_\beta$ by considering the datasets from CMA and JTWC is similar, but there are differences. The trends of the results obtained by considering the dataset from JTWC are consistent with those given by Zhao et al. (2009) and Chen and Duan (2018).

Figures 2.9a to 2.9d show that the standard deviation of $|\mathbf{V}_\beta|$ ranges from about 1 to 3 m/s, and the standard deviation of θ_β varies within about 50° to 90°. In general, the standard deviations of $|\mathbf{V}_\beta|$ and θ_β for the westerly tracks are around 20% higher than those for the easterly tracks. This may be partly attributed to the small sample size effect as the number of easterly tracks are more than two times of the westerly tracks. The same observations could be made for the results presented in Figures 2.9e to 2.9h, which are obtained using the dataset from JTWC. In general, the standard deviations estimated by using the dataset from JTWC are about 5% less than those estimated by using the dataset from CMA. This suggests that the tracks reported in CMA have a greater variation than those reported in JTWC.

The analysis results presented in Figures 2.8 and 2.9 for $\mathbf{V}_\beta$ are obtained by removing $\mathbf{V}_{steer}$ from $\mathbf{V}_{TC}$, where the values on a circle with a radius of 5^o are used to evaluate $\mathbf{V}_{steer}$. The effect of using a different radius on $\mathbf{V}_\beta$ is unclear. To investigate the sensitivity of $\mathbf{V}_{steer}$ to this radius, the analysis that is carried out for the results presented in Figures 2.8 and 2.9 is repeated by considering the radius equal to 4^o, 6^o, and 7^o. The obtained results are presented in Figures 2.10 and 2.11 if the best track dataset from CMA is employed. The comparison of the results presented in Figures 2.8 and 2.9 to those shown in Figures 2.10 and 2.11 indicates that the statistics of $\mathbf{V}_\beta$ are not very sensitive to the variation of

the radius within the considered values. Moreover, rather than considering the values of $\boldsymbol{v}_{GW}$ on the circle, we also estimated $\mathbf{V}_\beta$ by using $\boldsymbol{v}_{GW}$ values within an annulus band with inner and outer radius equal to 5° and 7°, respectively. The obtained mean of $(|\mathbf{V}_\beta|, \theta_\beta)$ are similar to those shown in Figure 2.8, so they are not plotted.

The analysis that is carried out for the results presented in Figures 2.10 and 2.11 for the best tracks from CMA is also performed for the best tracks from JTWC. Since the observed trends are similar to those presented in Figures 2.10 and 2.11, they are not plotted. Based on the observations from the sensitivity analysis, only the obtained statistics of $(|\mathbf{V}_\beta|, \theta_\beta)$ based on the radius equal to 5° are considered in the following.

2.3.2 Probability distribution models

As indicated in the previous section, $\mathbf{V}_\beta$, which can be represented by $(|\mathbf{V}_\beta|, \theta_\beta)$, is uncertainty for each considered cell and for easterly or westerly tracks. To assess and assign the probability distributions of $(|\mathbf{V}_\beta|, \theta_\beta)$ by considering a radius of 5^o in developing the models, we represent them as the sum of their mean and residuals

$$(|\mathbf{V}_\beta|, \theta_\beta) = \left(m_{|\mathbf{V}|} + \varepsilon_{|\mathbf{V}|}, m_\theta + \varepsilon_\theta\right) \tag{2.5}$$

where $m_{|\mathbf{V}|}$ and $\varepsilon_{|\mathbf{V}|}$ are the mean and zero-mean residual of $|\mathbf{V}_\beta|$, and m_θ and ε_θ are the mean and zero-mean residual of θ_β. The means $m_{|\mathbf{V}|}$ and m_θ are already discussed in the previous section (see Figure 2.8).

We extract the residuals $(\varepsilon_{|\mathbf{V}|}, \varepsilon_\theta)$ for easterly or westerly tracks for each set and use the samples to assign their distribution. We fit the residuals using several commonly employed distribution types. It is found that the Johnson S_B distribution (Johnson 1949),

$$f(x;\eta,\gamma,\delta,\zeta) = \frac{\eta\delta}{\sqrt{2\pi}\left(x-\zeta+0.5\delta\right)\left(-x+\zeta+0.5\delta\right)} \exp\left(-0.5\left(\gamma+\eta\ln\left(\frac{x-\zeta+0.5\delta}{-x+\zeta+0.5\delta}\right)\right)^2\right) \tag{2.6}$$

could be used to fit $\varepsilon_{|\mathbf{V}|}$, where x denotes the value of $\varepsilon_{|\mathbf{V}|}$, $x \in [\zeta - 0.5\delta, \zeta + 0.5\delta]$, and η, γ, δ and ζ are model parameters. Also, the distribution fitting exercise indicates that the binormal distribution,

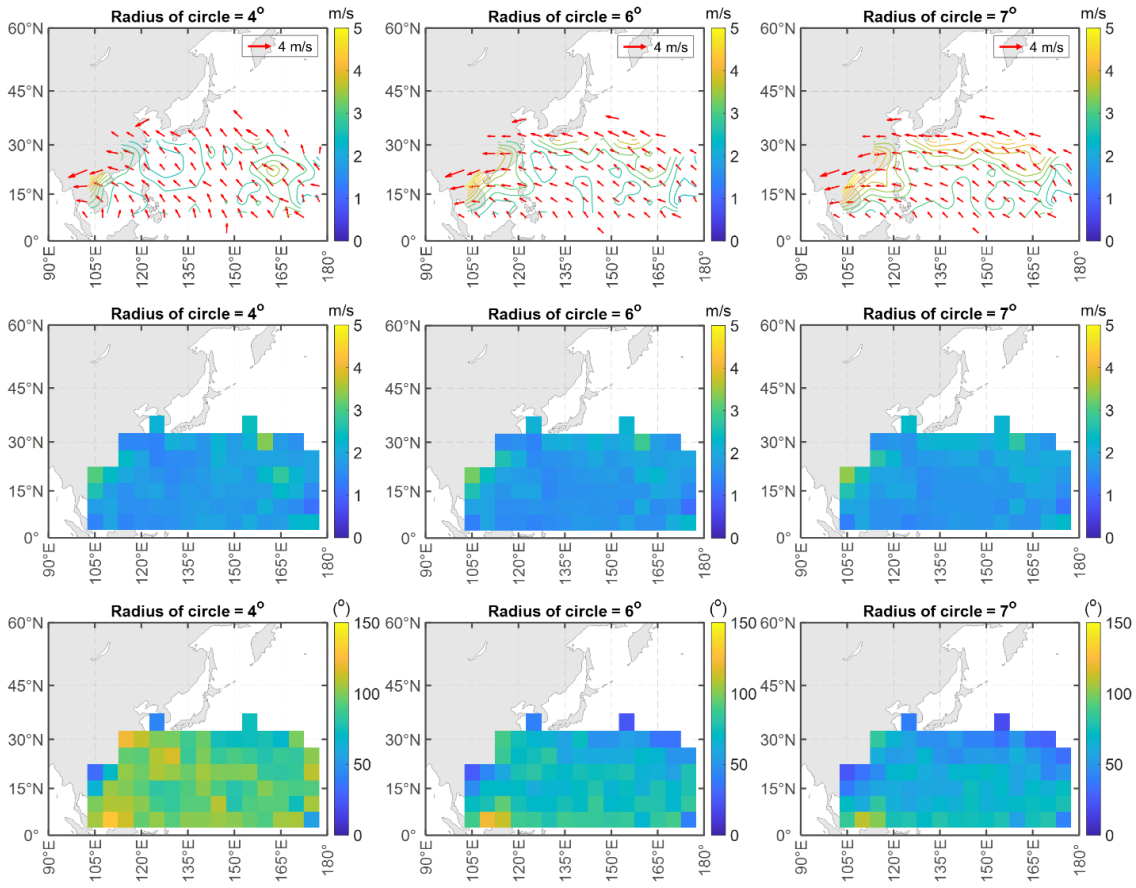

Figure 2.10. Sensitivity of the spatial variation of the mean and standard deviation of V_β to the radius of the circle for easterly tracks extracted from the best track dataset from CMA. The first row is the mean of V_β; the second row is the standard deviation of $|\mathbf{V}_\beta|$; the third row is the standard deviation of θ_β.

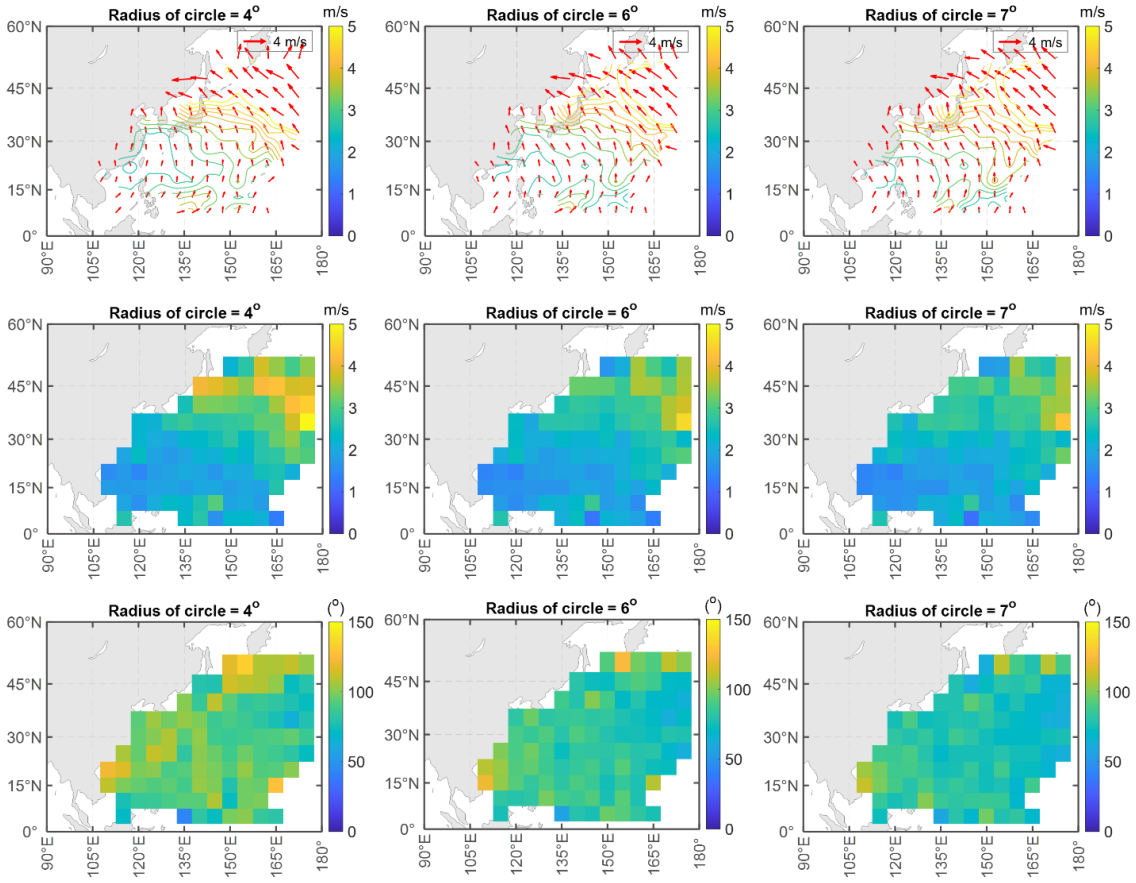

Figure 2.11. Sensitivity of the spatial variation of the mean and standard deviation of V_β to the radius of the circle for westerly tracks extracted from the best track dataset from CMA. The first row is the mean of V_β; the second row is the standard deviation of $|V_\beta|$; the third row is the standard deviation of θ_β.

$$f(x;\alpha,\mu_1,\mu_2,\sigma_1,\sigma_2) = \alpha\frac{1}{\sqrt{2\pi}\sigma_1}\exp\left(-\frac{1}{2}\left(\frac{x-\mu_1}{\sigma_1}\right)^2\right)+(1-\alpha)\frac{1}{\sqrt{2\pi}\sigma_2}\exp\left(-\frac{1}{2}\left(\frac{x-\mu_2}{\sigma_2}\right)^2\right) \quad (2.7)$$

is adequate for fitting ε_θ, where x represents the value of ε_θ and α, μ_1, σ_1, μ_2, and σ_2 are model parameters. The fitted distributions for three selected cells are shown in Figure 2.12. In all cases, the fitting is carried out using the maximum likelihood method.

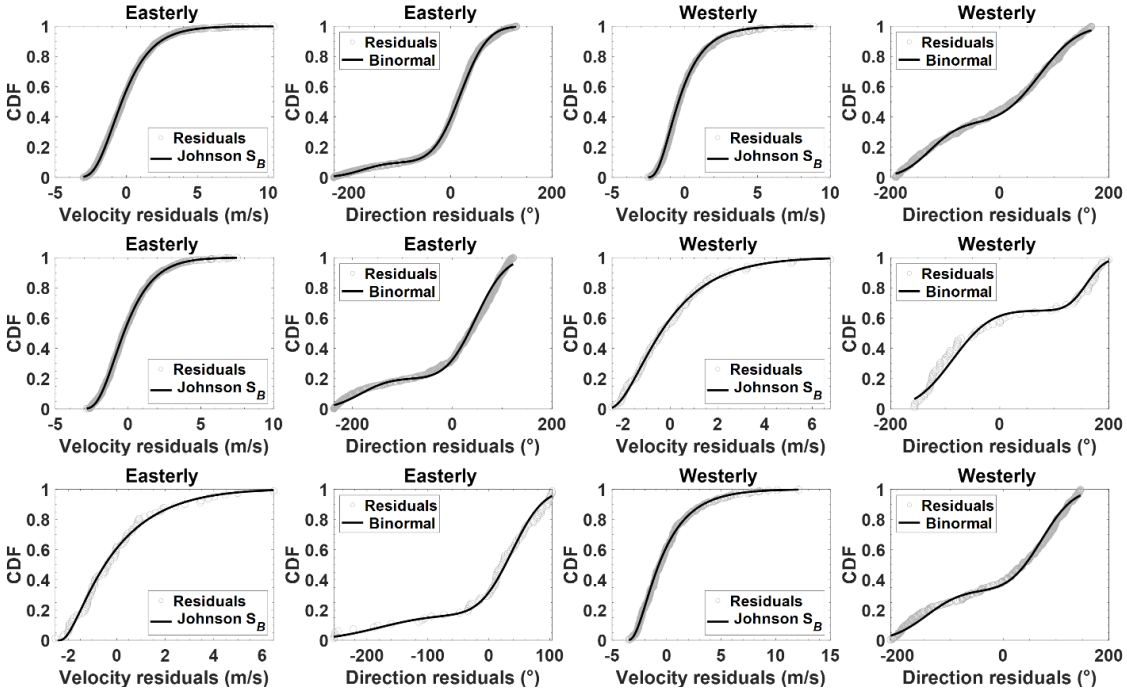

Figure 2.12. Fitted probability distribution for $\varepsilon_{|V|}$ and ε_{θ} for three selected cells by considering easterly or westerly TC tracks from CMA. The first, second, and third rows are for the cells located at [17.5 ° N, 117.5 ° E], [12.5 ° N, 147.5 ° E], and [32.5 ° N, 147.5 ° E], respectively. Each cell is a 5º×5º squared cell.

Note that, by considering each of the two datasets, the fitting exercise is carried out for each squared cell considering easterly or westerly TC tracks. The developed stochastic beta-advection models with the means of $(|\mathbf{V}_{\beta}|, \theta_{\beta})$ and the parameters for the probability distribution of $(\varepsilon_{|\mathbf{V}|}, \varepsilon_{\theta})$ for each cell are stored and used to simulate synthetic tracks. For the simulation, the cells without statistics of $(|\mathbf{V}_{\beta}|, \theta_{\beta})$ and the distribution parameters of the residuals are extrapolated using those of the values of its nearest neighbouring cells. The simulation procedure is explained in the following sections.

2.4 Comparison of performance of the simulated tracks

2.4.1 Environmental wind field and relative intensity of TC

Before using a beta-advection model with the re-analysis data to generate synthetic TC

tracks, the wind velocity field obtained from the re-analysis data from NCEP/NCAR needs to be filtered. The objective of this filtering is to remove the vortex-like component of the wind field caused by the TC events. This can be done according to the procedure described in Kurihara et al. (1993, 1995). In the procedure, a smoothing technique is applied to decompose the original global wind velocity field (covering the region of interest) into the basic wind field, h_B, and the disturbance wind field, h_D. Since the disturbance wind field contains the climatological features imposed by the TC vortex, a filter is applied to remove the vortex-like field. The removed component is refilled by spatial interpolation using h_D but without the vortex-like field. This reconstructed disturbance field that is without the vortex-like field, $h_{\text{non-TC}}$, is superimposed to the basic wind field h_B to form the environmental wind field (i.e., $h_B + h_{non\text{-}TC}$). For the computational details, the reader is referred to Kurihara et al. (1993, 1995).

An illustration of the evaluated environmental wind field by following this procedure is shown in Figure 2.13, where the NCEP/NCAR re-analysis data corresponding to typhoon Saomai at 1200UTC/15/08/2006 is considered. The original wind velocity field is presented in Figure 2.13a. The obtained basic wind field and the disturbance wind field by a filtering operator given by Kurihara et al. (1993, 1995) are shown in Figures 2.13b and 2.13c. By removing the vortex-like field through a filtering process, the obtained $h_{\text{non-TC}}$, including the effect of refill, is presented in Figure 2.13d. Finally, the obtained environmental wind field is shown in Figure 2.13e.

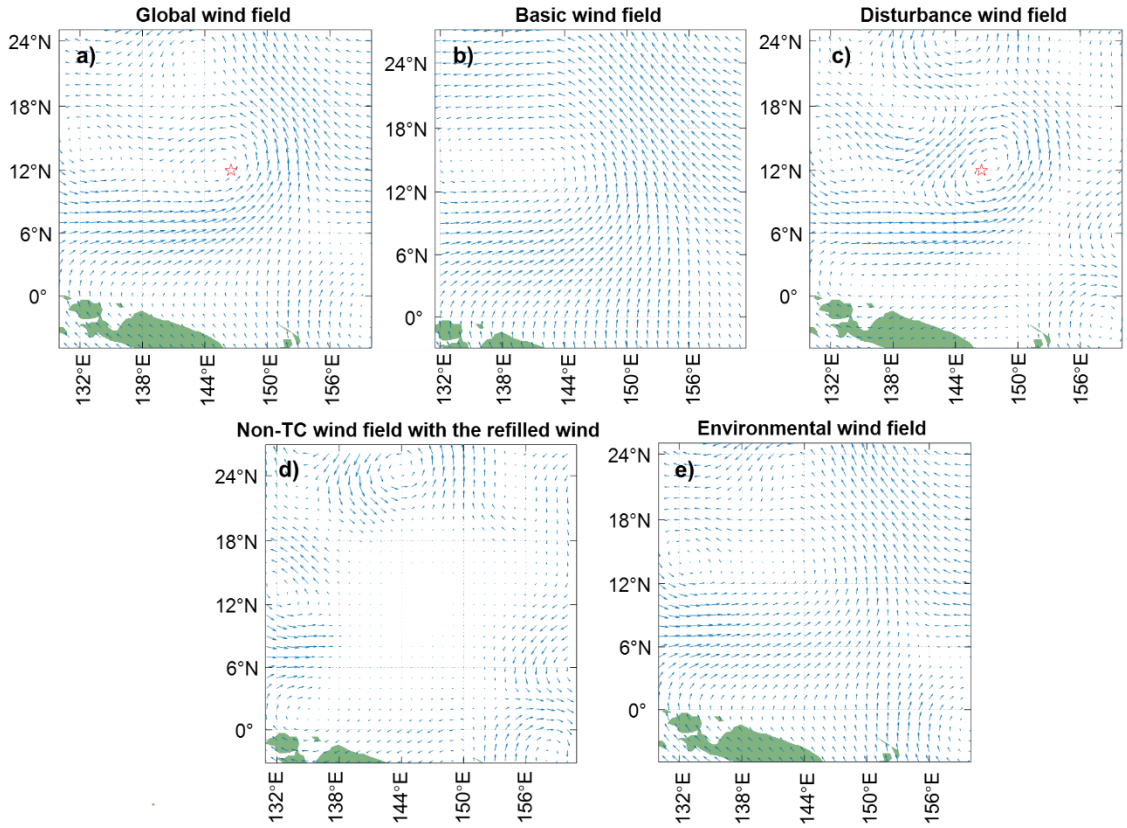

Figure 2.13. Analysis for an instance of the wind field for the pressure level of 850 hPa that is influenced by the TC Saomai 1200UTC/05/08/2006: a) original global wind field, b) basic wind field, c) disturbance wind field, d) non-hurricane wind component, e) environmental wind field (i.e., wind field in b) plus wind field in d)).

The above-illustrated procedure is applied to the spatial-temporal instance of the data in NCEP/NCAR re-analysis dataset from 1949 to 2018 and covering the WNP basin. The NCEP/NCAR data with the vortex-like component removed are then stored and referred to as the environmental wind field (EWF) database. This database is used in simulating the synthetic tracks, as will be explained in the next section.

Note that an additional component for the TC track that is not discussed so far is the TC intensity. The intensity could be represented by the relative intensity, I, which is defined as $I = (p_{da}\text{-}p_c + e_s)/(p_{da}\text{-}p_{dc})$, where p_{da} hPa is the ambient pressure, p_c hPa is the central pressure, $e_s = 6.112 \times \exp\left[17.67 \times (T_s - 273)/(T_s - 29.5)\right]$ is the saturation vapour pressure, T_s °K is the sea surface temperature (SST), and p_{dc} hPa is the minimum

sustainable surface value of central pressure (of dry air) (Darling 1991). A regression equation for the relative intensity at the (i+1)-th position of the track that is developed in Li and Hong (2016) can be written as,

$$\ln(I_{i+1}) = d_1 + d_2 \ln(I_i) + d_3 T_{s_i} + d_4 \left(T_{s_{i+1}} - T_{s_i} \right) + \varepsilon_I \tag{2.8}$$

where d_i are spatially varying model coefficients, ε_I is zero-mean normally distributed residual with standard deviation varying spatially, the subscripts i or i +1 to a symbol denotes the value of the symbol at the i-th or (i+1)-th position of the track. The time between the i-th and (i+1)-th position is six hours. For the evaluation, if T_{s_i} is unavailable, the monthly averaged SST derived from the HadISST dataset from 1870 to 2011 (Rayner et al. 2003), which has a 1°×1° resolution (http://www.metoffice.gov.uk/hadobs/hadisst/data/download.html, accessed, 2012) is employed. Note that once the value of I_{i+1}, is evaluated, the corresponding p_c can be calculated based on the definition of the relative intensity, and the central pressure difference then given by,

$$\Delta p = p_{da} - p_c \tag{2.9}$$

can be evaluated. Note that Eqs. (2.8) only applies if the TC center is located over water. After the landfalling, a filling-rate model applicable to the considered region should be used to evaluate Δp for the landfalling segment of the track. The filling-rate model developed in Hong et al. (2016) is employed in the present study.

2.4.2 Comparison of statistics of simulated tracks using the beta-advection models

Using the prepared EWF database and the developed beta-advection model based on the best track dataset from CMA, the synthetic tracks can be simulated according to the following steps:

1. Sample the number of TCs for a year according to the negative binomial distribution (see Eq. (2.1) with the distribution parameters corresponding to those obtained for the

dataset from CMA);

2. Randomly select the genesis of each TC from the historical best track dataset from CMA;

3. For each genesis, applying Eqs. (2.2) and (2.3), including the use of the EWF database and the distribution parameters for $(|\mathbf{V}_\beta|, \theta_\beta)$, which depends on the spatial position of the track, to generate $\mathbf{V}_{TC}$ and to calculate the position of the track every six hours until the lysis. When using Eq. (2.3) to evaluate, V_{steer}, for simulation, the global wind field $\boldsymbol{v}_{GW}$ in Eq. (2.3) is replaced by the environmental wind field from the EWF database.

4. Repeat Steps 1) to 3) N_T times to generate the synthetic TC tracks, where N_T denotes the number of TCs for T_T years of TC activities.

These simulation steps are also applicable if the model developed based on the dataset from JTWC is considered. In such a case, the reference to CMA in the steps is replaced by JTWC.

For T_T =10,000 years of TC activities, synthetic tracks are simulated by using the beta-advection model derived based on the dataset from CMA. Based on the simulated tracks, the statistics of the parameters of the landfalling TCs along the KPs are shown in Figure 2.14. Similar to the calculation of the results presented in Figure 2.4, the results presented in Figure 2.14 for a given KP are calculated. These statistics are compared with those obtained based on the best track dataset from CMA in the same figure, showing that, in general, the statistics of the simulated tracks agree with those from the considered best track datasets. However, there are observable differences.

By repeating the analysis but considering the model that is developed based on the best track dataset from JTWC, the obtained statistics along the KPs are also shown in Figure 2.14 and compared with those estimated based on the best-tracks dataset from JTWC. The standard deviation of the translation speed for the model developed from the database from JTWC is deficient in matching that of the original data for KPs less than

1000 or KPs greater than 2000. In general, the statistics from the models are in better agreement if the site is located in the region with KPs less than about 2500.

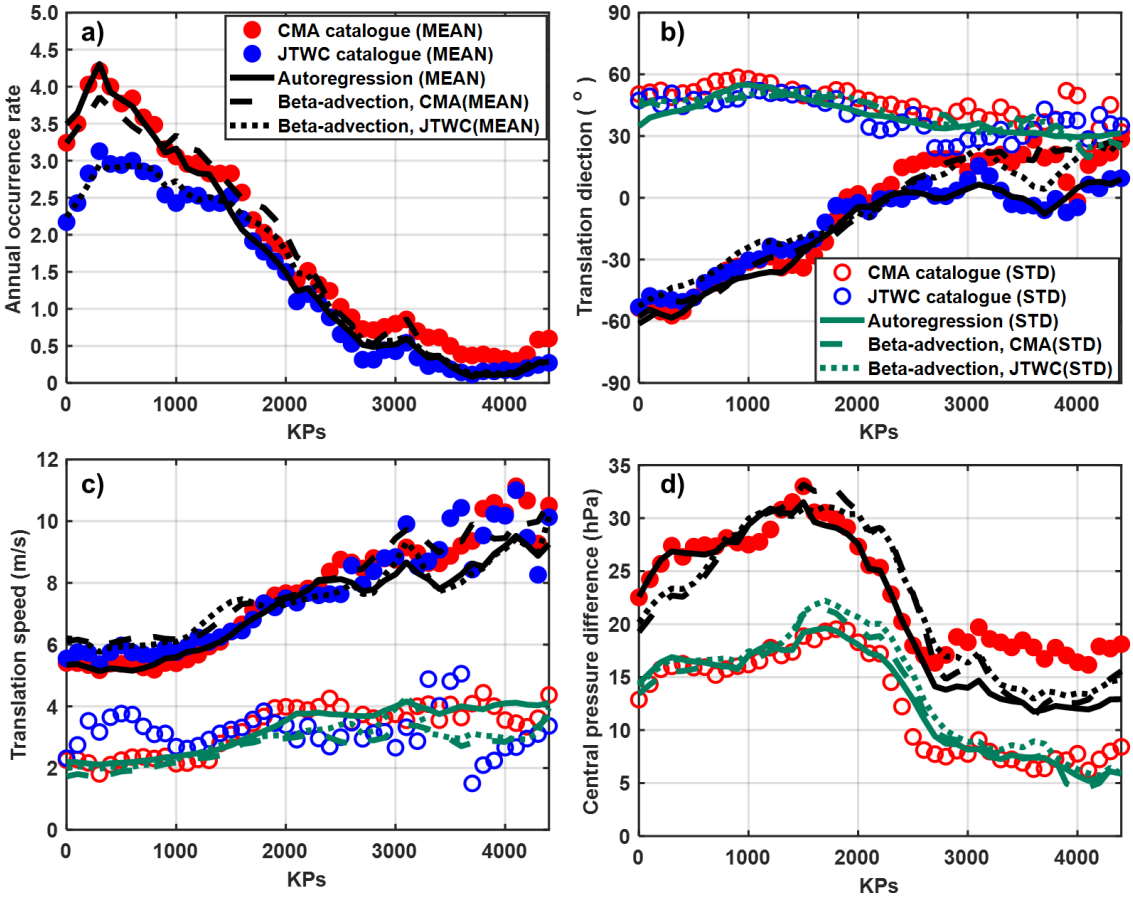

Figure 2.14. Comparison of the statistics of the annual occurrence rate, heading, translation velocity, and central pressure difference of the landfalling TCs along the coastline in mainland China: a) occurrence rate, b) heading, c) translation velocity, and c) central pressure difference. The autoregressive model referred to that shown in Eqs. (2.8) - (2.11) (developed in Li and Hong (2016).

2.4.3 Comparison of statistics of the simulated tracks based on two different types of models

As mentioned in the introduction, one of the popular approaches to developed stochastic models to simulate the TC tracks is based on the autoregressive type of modeling. One

such model was developed by Li and Hong (2016), where the increment of the logarithm of the translation velocity, $\Delta \ln c$, and the increment of heading $\Delta\theta$ per six hours are given by

$$\Delta \ln c = a_1 + a_2 \ln c_i + a_3 \theta_i + \varepsilon_c \tag{2.10}$$

and

$$\Delta\theta = b_1 + b_2 c_i + b_3 \theta_i + \varepsilon_\theta \tag{2.11}$$

where a_i, and b_i are the geographically varying model parameters; c m/s and θ (°) with subscripts are the translation velocity and heading. Using their model (i.e., Eqs. (2.8), (2.10), and (2.11), which will be referred to as LH model), 10,000 years of activities of the TC tracks are simulated. The statistics of the simulated tracks along the KPs are also included in Figure 2.14 as well. The comparison shown in the figure indicates that the statistics of the track from the model agree well with those obtained from the database. However, the model underestimates the mean of the central pressure difference for KPs greater than 2500. Such a deficiency was noted in Li and Hong (2016) and was attributed to the lack of sufficient statistics. The deficiency in predicting the central pressure difference remains if the trajectories of the tracks from the beta-advection models are employed.

Two additional aspects of the track models deserve comments. As can be observed, the autoregressive type of model is simple to use and does not require the EWF database. However, it can not be used directly with the changes in the environmental wind field caused by climate change. In other words, it could not be used with the output from the simulated global wind field by considering a representative concentration pathway (RCP) (https://www.ipcc.ch). This problem is overcome by using the beta-advection model. However, the beta-advection model requires the use of the EWF database, making the model more challenging to implement and use as compared to the autoregressive type of model. Moreover, the beta-advection model only deals with the stochastic modeling of the position or trajectory of the TC track, and the intensity of TC needs to be evaluated using an alternative approach such as Eq. (2.8).

2.5 Comparison of the assessed wind hazard maps considering different stochastic track models

As mentioned in the introduction, the slab model (Vickery et al. 2009) is adopted to evaluate the TC wind field for the TC wind hazard assessment in the present study because the parameters used for this wind field model are well-calibrated based on observed wind records and re-analysis data. The implemented version of this model in Li and Hong (2015a) is used for the numerical analysis in the following. This wind field is defined by Δp, translation velocity v_T (representing $|\mathbf{V}_{TC}|$ if Eq. (2.2) is used and c if Eq. (2.10) is used), radius to maximum wind speed $R_{\max}$, and Holland's B parameter. The values of B and $R_{\max}$ for a given Δp can be evaluated using (Vickery and Wadhera 2008; Vickery et al. 2009),

$$\ln\left(R_{\max}/1000\right) = 3.015 - 6.291\times10^{-9}\Delta p^2 + 0.0337\psi + \varepsilon_{lnR\max} \tag{2.12}$$

and,

$$B = 1.833 - 0.326\sqrt{fR_{\max}} + \varepsilon_B \tag{2.13}$$

where ε_{lnRmax} is a zero-mean normally distributed random variable with the standard deviation $\sigma_{\ln R_{\max}}$ that equals 0.448 for $\Delta p \le 8700$ (Pa), $1.137 - 7.92\times10^{-5}\Delta p$ for 8700 Pa $< \Delta p \le 12000$ (Pa), and 0.186 for $\Delta p > 12000$ (Pa), and ε_B is a zero-mean normally distributed random variable with standard deviation $\sigma_{\ln B}$ equal to 0.221.

The evaluation of the TC wind at a site of interest is carried out following the same procedure as the one used in Li and Hong (2016). It involves converting the TC track defined every six hours into a TC track defined every 15 minutes through linear interpolation. At each point on the TC track that is defined every 15 minutes, Δp is calculated using the relative intensity value (see Eq. (2.9)) before the TC makes landfall, and is evaluated using the filling-rate model after landfalling. The obtained Δp is then used in Eqs. (2.12) and (2.13) to evaluate B and $R_{\max}$. Note that, unlike in Li and Hong

(2016), in the present study, it is considered that only a single randomly generated probability level for each track is used to evaluate $\varepsilon_{ln\mathrm{Rmax}}$ by using its probability distribution. The same is done for ε_B as well. Using the obtained (v_T, Δp, $R_{\max}$, B) at each point on the TC track, the TC wind field is evaluated, and the wind velocity at the site of interest (see Li and Hong 2016). Also, the annual maximum TC wind velocity, V_A, experienced at the site of interest is extracted and used to evaluate the T-year return period value of V_A, $v_{A\text{-}T}$,

For nine selected major cities identified in Figure 2.15a and Table 2.2, the obtained samples of V_A are plotted in Figure 2.15b to 2.15j by considered two developed beta-advection models and LH model. The mean and COV of V_A are shown in Table 2.2, and the estimated $v_{A\text{-}50}$ and $v_{A\text{-}100}$ are summarized in Table 2.3. Note that the values reported in the tables based on LH model differ slightly from those reported in Li and Hong (2016) since the parameters of the TC occurrence model used in the present study, which is estimated using a longer TC catalogue, differs from that employed in Li and Hong (2016).

In general, as the site of interest moved towards the northeast, the mean of V_A is decreased and the COV of V_A is increased. Considering that the COV value ranges from 0.49 to 0.82, the COV of V_A obtained by using different track models is consistent. The mean of V_A varies from 10.5 to 18 m/s. The maximum absolute value of the relative difference is 15%. The use of the beta-advection model developed based on the database from JTWC leads to a reduced mean value as compared to that based on the database from CMA. The difference is up to 10%.

The differences observed from Table 2.3 are similar to those reported in Li and Hong (2016). Let $R_{CMA/LH\text{-}T}$ denote the ratio of $v_{A\text{-}T}$ obtained by using the beta-advection model derived based on the database from CMA to that obtained by using LH model. The value of $R_{CMA/LH\text{-}T}$ calculated from the results shown in Table 2.3 ranges from 0.97 to 1.11 for T = 50 years, and from 0.99 to 0.11 for T = 100 years. The mean of $R_{CMA/LH\text{-}T}$ approximately equals 1.05 for both T = 50 and 100 years.

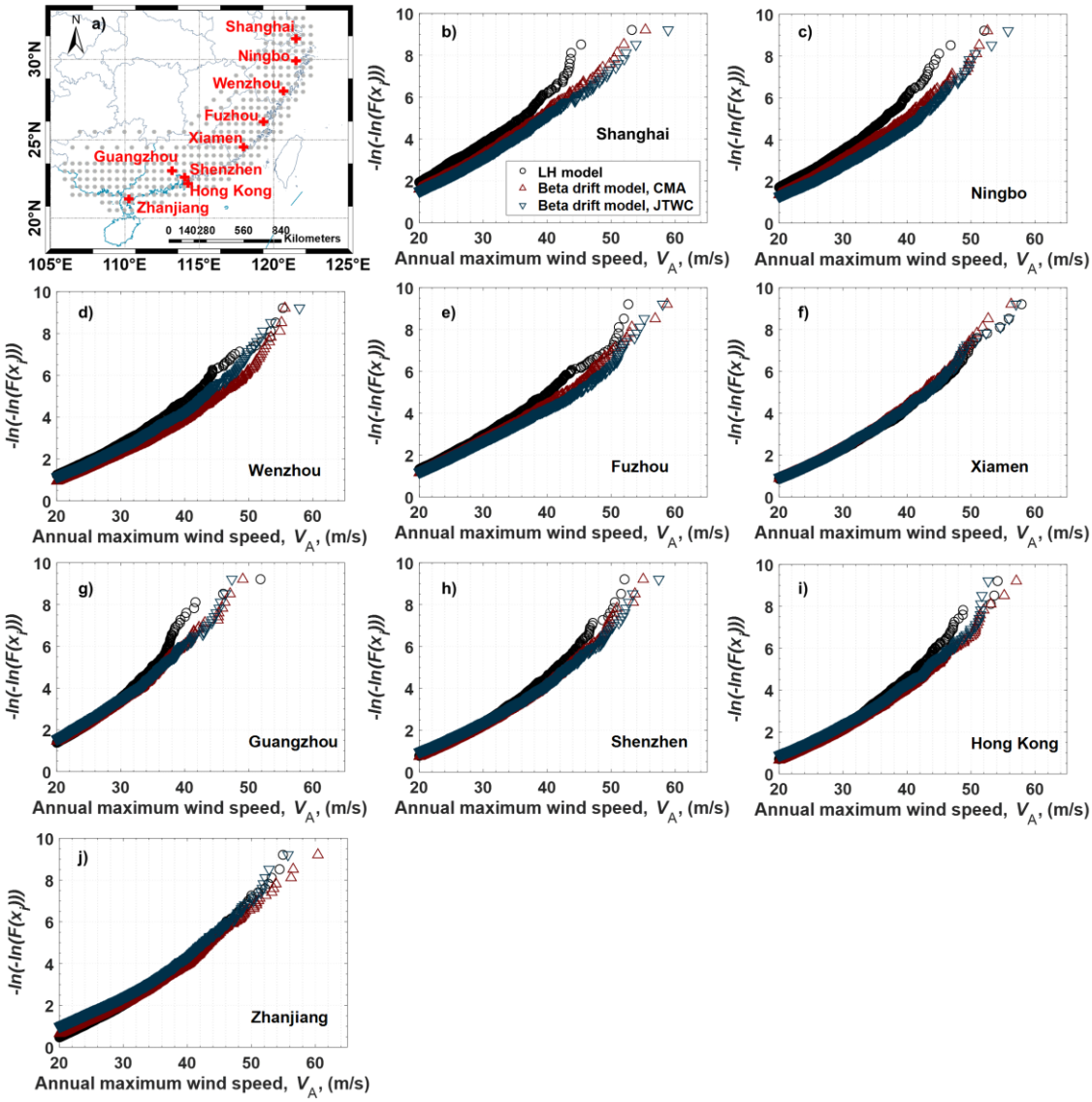

Figure 2.15. Comparison of estimated $V_{A\text{-}50}$ and $V_{A\text{-}100}$ considering different stochastic track models for nine identified sites: a) identified sites, b) to j) empirical distribution of V_A based on simulation results by considering three stochastic track models.

Let $R_{JTWC/CMA\text{-}T}$ denote the ratio of $v_{A\text{-}T}$ obtained by using the beta-advection model derived based on the database from JTWC to that based on the database from CMA. The calculated $R_{JTWC/CMA\text{-}T}$ by using the results shown in Table 2.3 ranges from 0.95 to 1.05 for T = 50 or 100 years. The mean of $R_{JTWC/CMA\text{-}T}$ equals about 1.0. In general, using the best track database from JTWC results in the estimated $v_{A\text{-}T}$ that is lower in the south and higher in the north as compared to that by using the best track database from CMA.

Table 2.2. The statistics of the annual maximum wind speed (m/s) for the considered 9 major cities along the southeast coastline of China using three stochastic track models.

Cities	LH model		Using the beta-advection model developed based on CMA catalogue		Using the beta-advection model developed based on JTWC catalogue	
	Mean	CoV	Mean	CoV	Mean	CoV
Shanghai	10.5	0.82	11.7	0.80	11.7	0.85
Ningbo	12.0	0.72	13.8	0.66	13.4	0.74
Wenzhou	14.6	0.64	16.4	0.61	15.0	0.66
Fuzhou	14.6	0.59	15.5	0.58	15.0	0.64
Xiamen	17.2	0.54	17.0	0.54	16.2	0.60
Guangzhou	14.7	0.50	14.5	0.52	13.2	0.62
Shenzhen	17.8	0.49	18.0	0.50	16.4	0.58
Hong Kong	18.2	0.47	18.5	0.49	16.9	0.56
Zhanjiang	19.9	0.43	18.5	0.49	16.2	0.58

Table 2.3. Comparison of estimated $v_{A\text{-}50}$ and $v_{A\text{-}100}$ considering different stochastic track models. The wind speed represents 10-minute mean wind speed at 10 m height for z_0 = 0.05 m (z_0 is terrain roughness coefficient).

City	$v_{A\text{-}50}$ (m/s)				$v_{A\text{-}100}$ (m/s)			
	Code	LH-model	Beta-advection model		Code	LH-model	Beta-advection model	
			Using dataset from CMA	Using dataset from JTWC			Using dataset from CMA	Using dataset from JTWC
Shanghai	29.7	30.4	33.2	34.4	31	34.2	36.5	37.9
Ningbo	28.3	32.0	34.3	36.5	31	34.9	37.8	40.1
Wenzhou	31	36.1	40.1	37.9	33.5	39.0	43.3	41.7
Fuzhou	33.5	35.1	37.1	38.1	36.9	38.0	41.1	42.9
Xiamen	35.8	38.9	37.8	38.3	39	41.3	40.8	41.2
Guangzhou	28.3	31.4	32.5	32.3	31	33.7	35.1	35.1
Shenzhen	34.6	37.2	38.8	38.7	37.9	40.1	41.5	41.9
Hong Kong	37.9	37.2	39.1	38.3	39	40.1	42.2	41.6
Zhanjiang	35.8	38.6	39.7	38.2	39	41.2	42.2	41.1

To better appreciate the spatial trends of $v_{A\text{-}T}$, $R_{CMA/LH\text{-}T}$, and $R_{JTWC/CMA\text{-}T}$, the analysis that is carried out for the nine cities shown in Table 2.2 is repeated for the grid system shown in Figure 2.15a. The obtained map of $v_{A\text{-}T}$ based on LH model is shown in Figures 2.16a and 2.16b. The values of $R_{CMA/LH\text{-}T}$ and $R_{JTWC/CMA\text{-}T}$ are presented in Figures 2.16c and 16d for T = 50 years and in Figures 2.16e and 2.16f for T = 100 years. In general, the observations made for from Table 2.3 is applicable to the results presented in Figure 2.16.

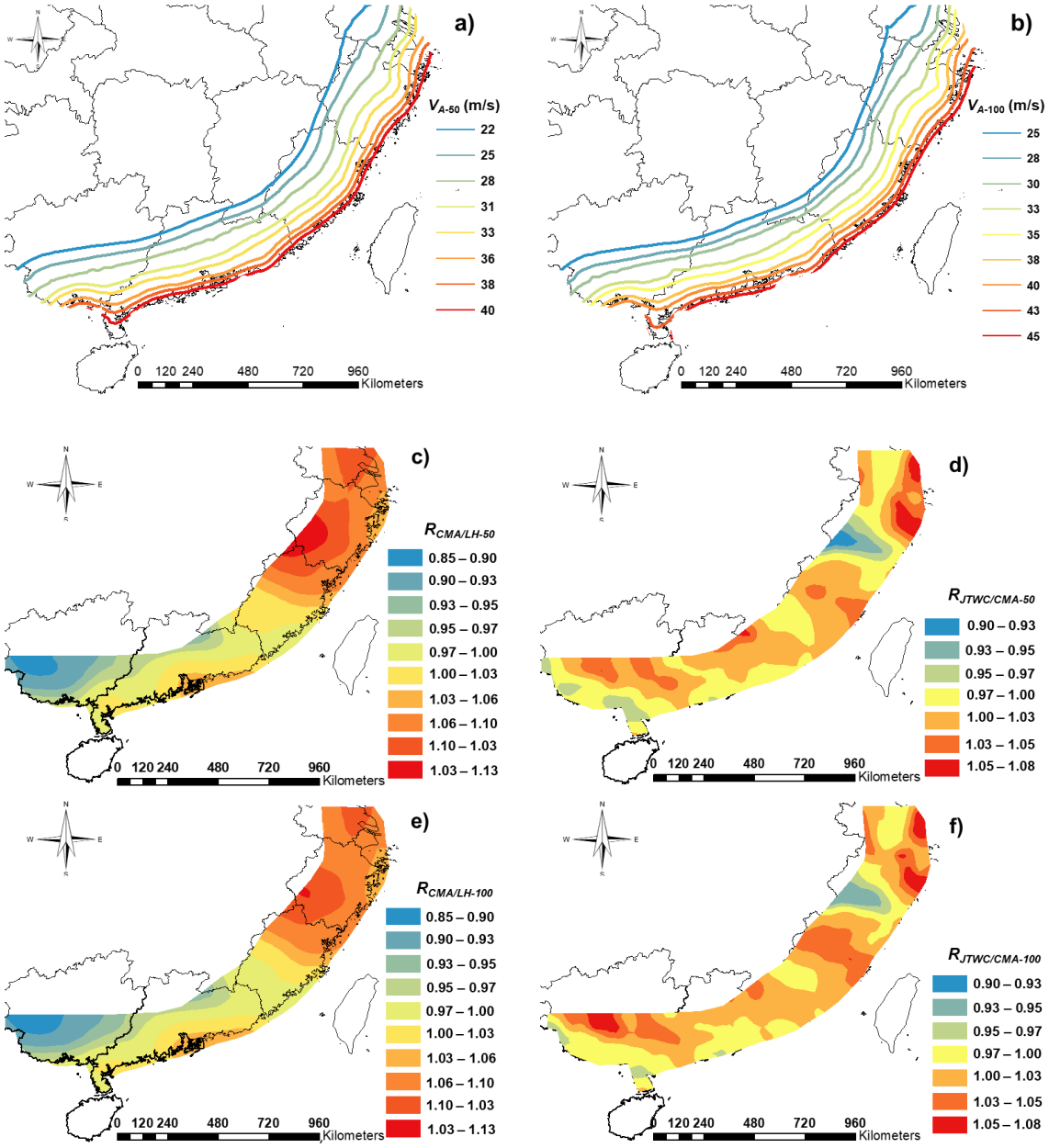

Figure 2.16. Mapped $v_{A\text{-}50}$ and $v_{A\text{-}100}$ and evaluated ratios of $v_{A\text{-}T}$ by considering different stochastic track models: a) & b) mapped $V_{A\text{-}50}$ and $V_{A\text{-}100}$ using LH-model with mentioned modification, c) $R_{CMA/LH\text{-}T}$ for T = 50 years, d) $R_{JTWC/CMA\text{-}T}$ for T = 50 years, e) $R_{CMA/LH\text{-}T}$ for T = 50 years, f) $R_{JTWC/CMA\text{-}T}$ for T = 100 years.

2.6 Conclusions

We compare the statistics of two best tropical cyclone (TC) track datasets, one from

CMA and the other from JTWC. We use these two datasets to develop two different beta-advection models by using the same procedure. The development is focused on the TCs originating in the Western North Pacific basin and affecting China. We then carry out the TC wind hazard assessment using these two stochastic models and one additional autoregressive type of track model from literature that is developed based on the dataset from CMA. The main conclusions that can be drawn from the results are:

A comparison of statistics of TC track parameters along the coastline of mainland China using tracks simulated by applying developed models is presented. The comparison is extended by considering an existing autoregressive type of track model. Moreover, a comparison of the estimated TC wind hazard by using these track models is presented. The results show that the number of genesis per year based on the dataset in CMA is about 7% greater than that in JTWC. The statistics of the TC tracks from the two datasets differ, especially in terms of landfalling TC for southwest China and of the TC heading and translation velocity for northeast China. In general, the mapped *T*-year return period value of the annual maximum TC wind speed, $v_{A\text{-}T}$, based on the beta-advection model developed using the dataset from CMA is greater than that developed using the dataset from JTWC. For a few selected major cities, the former is greater than the latter by up to 7% and 9% for *T* equal to 50 and 100, respectively. The corresponding average differences are 3% and 6%.

The comparison of $v_{A\text{-}T}$ estimated using the autoregressive type of model and the beta-advection model that are developed using the dataset from CMA indicates that their differences are up to 10% and 12% for *T* equals 50 and 100 years.

2.7 Reference

Carr III, L. E., & Elsberry, R. L. (1990). Observational evidence for predictions of tropical cyclone propagation relative to environmental steering. Journal of Atmospheric Sciences, 47(4), 542-546.

Chan, J. C. (2005). The physics of tropical cyclone motion. Annu. Rev. Fluid Mech., 37, 99-128.

Chen, Y., & Duan, Z. (2018). A statistical dynamics track model of tropical cyclones for assessing typhoon wind hazard in the coast of southeast China. Journal of Wind Engineering and Industrial Aerodynamics, 172, 325-340.

Chen, Y., Duan, Z., Yang, J., Deng, Y., Wu, T., & Ou, J. (2021). Typhoons of western North Pacific basin under warming climate and implications for future wind hazard of East Asia. Journal of Wind Engineering and Industrial Aerodynamics, 208, 104415.

Chow, S. (1971). A study of the wind field in the planetary boundary layer of a moving tropical cyclone. M.Sc. Thesis, New York University, New York, NY.

Chu et al. (2002). The Joint Typhoon Warning Center Tropical Cyclone Best-Tracks, 1945-2000. Naval Research Laboratory, Reference Number: NRL/MR/7540-02-16. https://www.metoc.navy.mil/jtwc/products/best-tracks/tc-bt-report.html

Darling, R. W. R. (1991). Estimating probabilities of hurricane wind speeds using a large-scale empirical model. Journal of Climate, 4(10), 1035-1046.

Emanuel, K., Ravela, S., Vivant, E., & Risi, C. (2006). A statistical deterministic approach to hurricane risk assessment. Bulletin of the American Meteorological Society, 87(3), 299-314.

Fang, G., Pang, W., Zhao, L., Cui, W., Zhu, L., Cao, S., & Ge, Y. (2021). Extreme Typhoon Wind Speed Mapping for Coastal Region of China: Geographically Weighted Regression–Based Circular Subregion Algorithm. Journal of Structural Engineering, 147(10), 04021146.

GB/T19201 (2006) China meteorology administration, grade of tropical cyclones (GB/T19201-2006), Beijing: China Standards Press. (in Chinese)

Georgiou, P. N., Davenport, A. G., & Vickery, B. J. (1983). Design wind speeds in regions dominated by tropical cyclones. Journal of Wind Engineering and Industrial Aerodynamics, 13(1-3), 139-152.

Gu, J. Y., Sheng, C., & Hong, H. P. (2020). Comparison of tropical cyclone wind field models and their influence on estimated wind hazard. Wind and Structures, 31(4), 321-334.

Hong, H. P., Li, S. H., & Duan, Z. D. (2016). Typhoon wind hazard estimation and mapping for coastal region in mainland China. Natural Hazards Review, 17(2), 04016001.

Hong, X., & Li, J. (2021). A beta-advection typhoon track model and its application for typhoon hazard assessment. Journal of Wind Engineering and Industrial Aerodynamics, 208, 104439.

Hong, X., Hong, H. P., & Li, J. (2019). Solution and validation of a three dimensional tropical cyclone boundary layer wind field model. Journal of Wind Engineering and Industrial Aerodynamics, 193, 103973.

Huang, M., Wang, Q., Li, Q., Jing, R., Lin, N., & Wang, L. (2021). Typhoon wind hazard estimation by full-track simulation with various wind intensity models. Journal of Wind Engineering and Industrial Aerodynamics, 218, 104792.

Johnson, N. L. (1949). Systems of frequency curves generated by methods of translation. Biometrika, 36(1/2), 149-176.

Kalnay, E., Kanamitsu, M., Kistler, R., Collins, W., Deaven, D., Gandin, L., ... & Joseph, D. (1996). The NCEP/NCAR 40-year reanalysis project. Bulletin of the American meteorological Society, 77(3), 437-472.

Kepert, J., & Wang, Y. (2001). The dynamics of boundary layer jets within the tropical cyclone core. Part II: Nonlinear enhancement. Journal of the atmospheric sciences, 58(17), 2485-2501.

Kurihara, Y., Bender, M. A., & Ross, R. J. (1993). An initialization scheme of hurricane models by vortex specification. Monthly weather review, 121(7), 2030-2045.

Kurihara, Y., Bender, M. A., Tuleya, R. E., & Ross, R. J. (1995). Improvements in the GFDL hurricane prediction system. Monthly Weather Review, 123(9), 2791-2801.

Li, S. H., & Hong, H. P. (2015a). Observations on a hurricane wind hazard model used to map extreme hurricane wind speed. Journal of Structural Engineering, 141(10), 04014238.

Li, S. H., & Hong, H. P. (2015b). Use of historical best track data to estimate typhoon wind hazard at selected sites in China. Natural Hazards, 76(2), 1395-1414.

Li, S.H., & Hong, H.P., 2016. Typhoon wind hazard estimation for China using an empirical track model. Natural Hazards, 82 (2), 1009–1029. https://doi.org/10.1007/s11069-016- 2231-2.

Liu, D., Pang, L., & Xie, B. (2009). Typhoon disaster in China: prediction, prevention, and mitigation. Natural Hazards, 49(3), 421-436.

Liu, Y. C., Chen, D. Y., Li, S. W., & Chan, P. W. (2018). Revised power-law model to estimate the vertical variations of extreme wind speeds in China coastal regions. Journal of Wind Engineering and Industrial Aerodynamics, 173, 227-240.

Liu, Y., Chen, D., Li, S., Chan, P. W., & Zhang, Q. (2019). A three-dimensional numerical simulation approach to assess typhoon hazards in China coastal regions. Natural Hazards, 96(2), 809-835.

Marks, D. G., 1992: The beta and advection model for hurricane track forecasting. NOAA Tech. Memo. NWS NMC 70, 89 pp.

Ou, J. P., Duan, Z. D., & Chang, L. (2002). “Typhoon risk analysis for key coastal cities in southeast China.” J. Nat. Disaster, 11(4), 9–17 (in Chinese).

Peng, Y., Wang, Z., & Ai, X. (2018). Wind-induced fragility assessment of urban trees with structural uncertainties. Wind & structures, 26(1), 45-56.

Rayner, N. A. A., Parker, D. E., Horton, E. B., Folland, C. K., Alexander, L. V., Rowell, D. P., ... & Kaplan, A. (2003). Global analyses of sea surface temperature, sea ice, and night marine air temperature since the late nineteenth century. Journal of Geophysical Research: Atmospheres, 108(D14).

Sheng, C., & Hong, H. P. (2020). On the joint tropical cyclone wind and wave hazard. Structural Safety, 84, 101917.

Thompson, E. F., & Cardone, V. J. (1996). Practical modeling of hurricane surface wind fields. Journal of Waterway, Port, Coastal, and Ocean Engineering, 122(4), 195-205.

Vickery, P. J., & Skerlj, P. F. (2005). Hurricane gust factors revisited. Journal of Structural Engineering, 131(5), 825-832.

Vickery, P. J., & Wadhera, D. (2008). Statistical models of Holland pressure profile parameter and radius to maximum winds of hurricanes from flight-level pressure and H* Wind data. Journal of Applied Meteorology and climatology, 47(10), 2497-2517.

Vickery, P. J., Wadhera, D., Powell, M. D., & Chen, Y. (2009). A hurricane boundary layer and wind field model for use in engineering applications. Journal of Applied Meteorology and Climatology, 48(2), 381-405.

Wu, F., Huang, G., & Zhou, X. (2021). Enhanced Circular Subregion Method in Typhoon Hazard Analysis. Journal of Structural Engineering, 147(6), 06021003.

Xiao, Y. F., Duan, Z. D., Xiao, Y. Q., Ou, J. P., Chang, L., & Li, Q. S. (2011). Typhoon wind hazard analysis for southeast China coastal regions. Structural Safety, 33(4-5), 286-295.

Ying M, Zhang W, Yu H, Lu X, Feng J, Fan Y, Zhu Y, & Chen D (2014) An overview of the China Meteorological Administration tropical cyclone database. J Atmos Oceanic Technol 31:287–301.

Zhao, H., Wu, L., & Zhou, W. (2009). Observational relationship of climatologic beta drift with large-scale environmental flows. Geophysical research letters, 36(18).

Chapter 3

3 On the joint tropical cyclone wind and wave hazard

3.1 Introduction

Offshore structures such as oil and gas platforms and wind turbines are subjected to the wind load and wave load. These loads can be caused by the passing of the tropical cyclone (TC) events. The consideration of the TC wind and wave actions for wind turbines located onshore and offshore near the coastline of mainland China is given in GB/T 31519. It indicates that Class I wind turbine can be installed at locations where the 50-year return period value of the annual maximum 10-min mean wind speed at hub height is less than 55 m/s. The corresponding extreme wind speed at 10 m height equals 43.8 m/s if the hub height is 90 m since the code also recommends the use of a power-law with an exponent equal to 0.11 for the vertical wind profile. This value is exceeded in several sites near the coastline of mainland China (Hong et al. 2016; Liu et al. 2019).

The international standards for the design of offshore wind turbines (IEC 61400-3 2009) did not consider the TC wind hazard for design, although the wind turbines can be vulnerable to the TC wind hazard (Jha et al. 2010; Hallowell et al. 2018). In the newly released IEC 61400-3-1, an informative appendix provides the guideline to predict the extreme TC wind speed by using Monte Carlo technique. Many studies have been carried out to estimate the TC wind hazard through the application of Monte Carlo technique. These include Batts et al. (1980), Georgiou et al. (1983), Vickery et al. (2000, 2009a, b, 2010), Powell et al. (2005), James and Mason (2005), Emanuel et al. (2006), Hall and Jewson (2007), Xiao et al. (2011) Hong et al. (2016), and Li and Hong (2016), among others. The TC wind hazard analysis involves in using three models: the TC spatial occurrence model, track model, and wind field model. For most engineering applications, the spatial occurrence could be obtained by randomly sampling the historical TC genesis or by using a parametric/nonparametric stochastic model. The results of the track model can be used to define the position, storm center motion, relative intensity of TC, and variables that are used to solve the TC wind field. Both the gradient

balance equation and momentum equation (Holton 2004) are used to define the TC wind field, and a vertical wind profile could be considered to describe the height varying horizontal wind speed and to estimate the surface wind speed. In fact, the wind load for structural design in ASCE 7 was partly based on the TC wind hazard model given in Vickery et al (2009a, b, 2010), which includes extensive model validation using observation data.

The offshore platforms and wind turbines are subjected to the combined wind and wave actions. Recommendations and validation analysis of the combined wind and wave load format in design codes are presented in Nessim et al. (1995) and Tarp-Johansen (2005). However, these studies are not focused on TC wind and wave hazard assessment.

Studies on TC generated sea states include those given in Young (1988), Ochi (1993), Thompson and Cardone (1996), Young and Vinoth (2013) and Liu et al. (2017). A comparison of the performance of several sophisticated TC wave models implemented in software packages indicated that none of the models can be identified as the most accurate model (Liu et al. 2017). Reviews of simple to use TC wave models are given in Young (2003, 2017). It is noted that the wave field model developed by Young (1988) and subsequently updated in Young and Burchell (1996) and Young and Vinoth (2013) based on the equivalent fetch concept is extensively calibrated using observation data. The model can be used to evaluate the TC induced maximum significant wave height as well as the significant wave height field. A procedure to carry out probabilistic offshore hurricane hazard analysis is given in Valamanesh et al. (2016). As in many other types of natural hazard assessment, the essential idea is to apply the probabilistic analysis to estimate the TC wind (or wave) hazard using the probability distribution of the TC wind (or wave) conditioned on a set of TC parameters that characterize the TC events. The study in Valamanesh et al. (2016) provided a forward step towards the assessment of joint wind and wave hazards due to the TC event. It adopted the gradient wind field model used by Georgiou et al. (1983) and applied a scaling factor of 0.71 to the gradient wind to obtain 10 m height surface wind speed, although it is well-known that the wind field obtained from slab-resolving or height-resolving model differs from the gradient wind field. The wave model proposed in Young (1988) was considered in Valamanesh et

al. (2016) to estimate the maximum significant wave height but neglected the updated model parameters validated using additional observation data (Young and Burchell 1996; Young and Vinoth 2013). It was noted that Young's model was developed for deep water conditions in the open ocean and suggested a water depth-dependent correction factor so it can be applied to sites located in shallow water. Also, it is worth mentioning that the use of the TC induced maximum significant wave height within the considered wave field rather than the significant wave height caused at a site of interest may be too conservative. In general, the assessment of the joint probability distribution of extreme TC wind speed and significant wave height is missing in the literature.

The main objectives of the present study are to 1) provide a framework to estimate simultaneous TC wind and wave hazard; 2) assess the marginal and joint probability distribution of extreme TC wind speed and significant wave height at offshore sites that can be directly used to assess the TC risk of offshore structures, including wind turbines; 3) compare block maximum and event-based probabilistic models for the joint probabilistic wind and wave hazard models, 4) assess the companion load factor considering simultaneous TC wind and wave actions, and 5) carry out deaggregation analysis.

The framework, and the TC wind hazard model and wave hazard model used to assess the joint probability distribution of extreme TC wind speed and wave height are described in the following sections. This is followed by the assessment of marginal as well as the joint probabilistic models for the wind and wave hazards, by the evaluation of the companion load combination factors considering simultaneous TC wind and wave actions, and by the deaggregation results used to identify the most likely events leading to the specified return period values of the annual maximum wind or significant wave height.

3.2 TC wind speed and wave height hazard modelling

3.2.1 Wind field model

A schematic illustration of the tropical cyclone (TC) wind field, the track orientation and site of interest is presented in Figure 3.1. In the figure, θ denotes the orientation of the track, α denotes the orientation of the site and $D_{\min}$ is the minimum distance to the track. The commonly used wind pressure profile to evaluate the TC wind speed is the one proposed by Holland (1980),

$$\frac{p(r)-p_c}{\Delta p}=\exp\left[-\left(\frac{R_{\max}}{r}\right)^B\right] \tag{3.1}$$

where $p(r)$ (Pa) is the pressure at a distance r (m) from the TC center, B is commonly referred to as Holland B parameter, $R_{\max}$ (m) is the radius at which maximum wind speed occurs, $\Delta p = p_a - p_c$, p_c (Pa) is the central pressure and p_a (Pa) is the ambient pressure far away from the storm center.

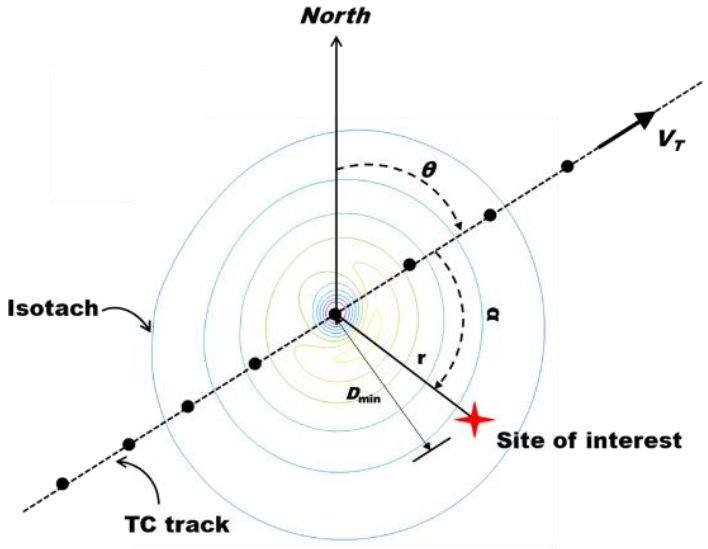

Figure 3.1. Illustration of TC track orientation and wind field contours in relation to a site of interest.

By considering Eq. (3.1), the gradient balance equation (Holton 2004) and the curvature effect for the wind flow, the obtained (tangential) gradient wind speed $V_g(r,\alpha)$ is given by (Georgiou et al. 1983),

$$V_g(r,\alpha)=\left\{\frac{B\Delta p}{\rho}\left(\frac{R_{\max}}{r}\right)^B \exp\left[-\left(\frac{R_{\max}}{r}\right)^B\right]+\left(\frac{V_T-rf}{2}\right)^2\right\}^{1/2}+\frac{V_T-rf}{2} \tag{3.2}$$

where ρ is the air density that is considered to be equal to 1.15 kg/m^3; f (rad/s) is Coriolis parameter equal to $2\Omega\sin\psi$ at latitude ψ (in degrees) in which Ω (rad/s) represents the rotation of the Earth with magnitude 2π/day, and V_T (m/s) is the storm translation speed.

By using the ratio between the gradient wind to surface 10-min mean wind speed, the maximum surface 10-min mean wind speed at $r = R_{\max}$, $V_{s,\max}$, could be estimated from Eq. (3.2). Young (2003) and Young (2017) considered that $V_{s,\max}$ for estimating the significant wave height can be approximated by,

$$V_{s,\max}\approx 0.8\left\{\frac{B_0\Delta p}{\rho e}\right\}^{1/2}+\frac{V_T}{2} \tag{3.3}$$

where B_0 is to be estimated using,

$$B_0=1.5+(980-p_a+\Delta p)/120 \tag{3.4}$$

As will be seen in the next section, V_T, $V_{s,\max}$, and $R_{\max}$ are all needed to estimate the significant wave height in a TC event.

Rather than using the simple gradient balance equation the use of the fluid momentum equation to model the planetary boundary layer slab wind field was presented by Chow (1971). This model was subsequently considered by others (Shapiro 1983; Cardone et al. 1992; Thompson and Cardone 1996; Vickery et al. 2009a, b, 2010; Li and Hong 2014, 2016) by making use of different solution schemes and surface drag coefficient models. The estimated extreme TC wind speed presented by Vickery et al. (2000; 2009a, b; 2010) formed the basis for the recommended design wind speed in ASCE 7 for sites affected by

TC wind hazard. The TC wind hazard mapping for the coastal region of mainland China by using the same slab-resolving wind field model was presented in Hong et al. (2016) and Li and Hong (2016).

In the present study, the TC wind hazard model used in Li and Hong (2016) (see also Vickery et al. 2009a, b) is adopted. Given the occurrence of a TC event, the analysis procedure of their model essentially consists of four steps. In the first step, the TC genesis is randomly selected from historical TC genesis. In the second step, their TC track model is used to simulate the storm intensity, and the position and motion of the storm center. In the third step, the central pressure difference Δp is evaluated based on the storm intensity or using the filling-rate model for the landfalling segment of the track. For each point on the track, the TC characteristics defined by $R_{\max}$ and B are calculated using (Vickery and Wadhera 2008),

$$\ln\left(R_{\max}/1000\right) = 3.015 - 6.291\times10^{-9}\Delta p^2 + 0.0337\psi + \varepsilon_{lnR\max} \tag{3.5}$$

and,

$$B = 1.833 - 0.326\sqrt{fR_{\max}} + \varepsilon_B \tag{3.6}$$

where the standard deviation of $\varepsilon_{lnR\max}$, $\sigma_{\ln R_{\max}}$ equals 0.448 for $\Delta p \le 8700$ (Pa), $1.137 - 7.92\times10^{-5}\Delta p$ for 8700 Pa $< \Delta p \le 12000$ (Pa), and 0.186 for $\Delta p > 12000$ (Pa), and the standard deviation of ε_B, $\sigma_{\ln B}$, equals 0.221.

In the final step, the TC wind field for each considered storm center on the track is obtained by solving the slab-resolving model (Chow 1971),

$$\begin{aligned}&\frac{\partial \vec{u}_s}{\partial t} + \vec{u}_c \bullet \nabla\vec{u}_s + \vec{u}_s \bullet \nabla\vec{u}_s = \\ &-f\hat{k}\times\left[\vec{u}_s + \vec{u}_c - \vec{u}_g\right] - \frac{1}{\rho}\nabla p_s + \nabla\bullet\left[K_H\nabla\vec{u}_s\right] - \frac{C_D}{h}\left|\vec{u}_s + \vec{u}_c\right|\left[\vec{u}_s + \vec{u}_c\right]\end{aligned} \tag{3.7}$$

where $\vec{u}_s$ (m/s) is the wind velocity relative to the moving centre of the vortex; $\vec{u}_c$ (m/s) is the TC translation velocity; $\vec{u}_g$ (m/s) is the wind velocity resulting from the large-scale pressure field; $\hat{k}$ is the unit vector in the vertical direction; ρ (kg/m^3) is the density of air, p_s (Pa) is considered equal to $p(r)$ shown in Eq. (3.1); h (m) is the depth of the planetary boundary layer for the slab model that is usually taken equal to 1000 m; C_D is the surface drag coefficient; and K_H is the horizontal eddy viscosity coefficient. For the details to solve this equation and the adopted eddy viscosity coefficient and C_D, the reader is referred to Li and Hong (2014, 2016).

The hourly mean wind speed at 10 m height $V(10)$ is then estimated by considering that the vertical wind profile can be modelled using Vickery et al. (2009b),

$$V(z) = \frac{u^*}{\kappa}\left[\ln\left(\frac{z}{z_0}\right) - a\left(\frac{z}{H^*}\right)^n\right] \tag{3.8}$$

where $V(z)$ is the surface mean wind speed at a height z (m) above the ground surface, κ is the von Karman coefficient having a value of 0.4, u^* is the friction velocity, and z_0 is the surface roughness, the parameters a and n equal to 0.4 and 2.0, respectively; and the boundary layer height parameter H^* is estimated using the initial stability. A typical value of H^* ranges from 400 to 1000 m. u^* can be calculated by equating solution from the TC wind field (i.e., Eq. (3.7)) to $V(H^*)$ shown in Eq. (3.8). $V(10)$ obtained by solving Eq. (3.7) and using Eq. (3.8) is treated as the hourly-mean wind speed, a ratio of the 10-min to the hourly-mean wind speed that equals 1.06 is used in (Li and Hong 2016) to calculate the 10-min surface mean wind speed, V_s. Additional discussion and recommendations on the estimation of the time-averaged mean wind speed can be found in Harper et al. (2010). It must be emphasized that the use of this approach to calculate V_s is preferable than the use of scaled gradient wind speed since the slab model and model parameters are validated extensively in (Vickery et al. 2009a, b, 2010) using observation data.

Besides the 10-min surface mean wind speed hazard characterization, the turbulent wind needs to be characterized. Although the investigation of turbulent wind characteristics is

beyond the scope of the present study, it is noted that the Kaimal spectrum is well accepted for synoptic wind (Simiu and Scanlan 1996). However, studies in Zhang (2010) and Li et al. (2012) found that the shape of the spectrum for turbulent TC winds resembles the shape of the Kaimal spectrum but could be shifted to higher or lower normalized frequencies. At present, it seems that there is no consensus on the parameters of the power spectrum of TC wind.

3.2.2 Significant wave height model

A simple equation to predict the maximum significant wave height within a storm, $H_s^{\max}$ (m), is given by Young (1988),

$$\frac{gH_s^{\max}}{V_{s,\max}^2} = 0.0016\left(\frac{gf_E}{V_{s,\max}^2}\right)^{1/2} \tag{3.9}$$

where this relation is known as JONSWAP growth relation (Hasselmann et al. 1973); $V_{s,\max}$ is calculated by using Eqs. (3.3) and (3.4); and the equivalent fetch, f_E (m), is calculated using (Young and Vinoth 2013; Young 2017),

$$\frac{f_E}{R'} = \psi\left(-2.175\times10^{-3}V_{s,\max}^2 + 1.506\times10^{-2}V_{s,\max}V_T - 1.223\times10^{-1}V_T^2 + 8.76\times10^{-2}V_{s,\max} + 1.516V_T + 1.756\right) \tag{3.10}$$

in which $\psi = 1$ and the scaling factor R' (m) is given by,

$$R' = 22.5\times10^3 \log\left(R_{\max}\right) - 70.8\times10^3 \tag{3.11}$$

Young (1988) further indicated that not only f_E but also the spatial distribution of $H_s / H_s^{\max}$ can be scaled based on R'. This is advantageous since only a few diagrams are needed to interpolate H_s (i.e., $H_s / H_s^{\max}$) for a given set of $V_{s,\max}$, $R_{\max}$, and V_T values. The sets of diagrams for the combinations of $V_{s,\max}$, $R_{\max}$ and V_T given in Young (1988) are used in the present study to interpolate $H_s / H_s^{\max}$ and estimate H_s. Figure 3.2 illustrates two typical spatial distribution of H_s by using those normalized significant

wave height diagrams, where it is considered that the TC center is located at the origin of the coordinate system and the TC translates vertically in the horizontal plane. Note that as only sites located in deep water conditions are considered in the present study, the water depth-dependent correction factor suggested in Valamanesh et al. (2016) for sites located in shallow water is not considered.

It is worth mentioning that given the wind speed and H_s at a site for a TC event, especially within 8R' of the center of TC, sets of equations to evaluate the wave spectrum, can be found in Donelan et al. (1985) and Young (2003, 2017).

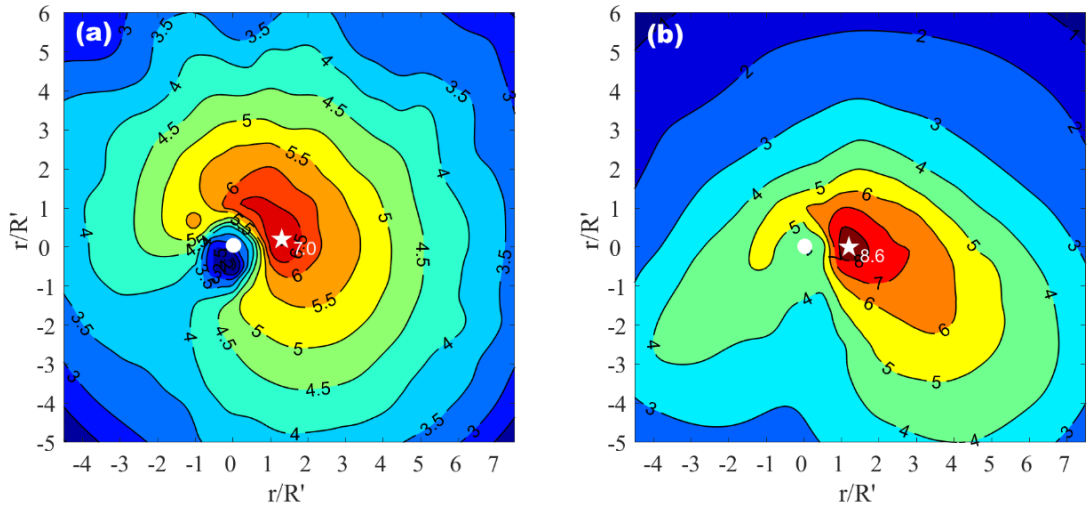

Figure 3.2 Spatial distribution of H_s for TC events that translate upwards: (a) V_T = 2.5 (m/s) and $V_{s,max}$ = 30 (m/s) and (b) V_T = 7.5 (m/s) and $V_{s,max}$ = 30 (m/s), where the circle at the origin of the coordinate system represents the TC centre. (The plots are based on H_s / H_s^{max} from Professor I. Young, personal communication; see also Young (1988)).

3.3.3 Overall procedure to assess wind and wave hazards at a site

In this section, an overall procedure to assess the joint TC wind and wave hazard is described. Although the described procedure is focused on offshore sites near the coastline of mainland China, it can be adopted to assess the joint TC wind and wave hazard for other offshore locations. The occurrence of the TC events is considered to be

a stochastic process and the occurrence of the number of TC events per year can be modelled using the negative binomial distribution with the model parameters given in Li and Hong (2016). By adopting the TC wind hazard model and wave hazard model given in the previous sections, samples of the TC wind speed and significant wave height can be obtained according to the steps shown in Figure 3.3 and described in the following:

I) Sample the number of TC events per year according to its probabilistic model.

II) For each TC event, carry out the following,

II.1) Randomly select a TC genesis from the best track dataset (e.g., from China Meteorological Administration (CMA) (Ying et al. 2014; Li and Hong 2016).

II.2) Sample the TC track using the model developed in Li and Hong (2016) (see their equations (2) and (3)). The sampling is carried out at 6 hours increment and provides the relative intensity, orientation, and V_T of the TC event. Interpolate the position and parameters of the TC event for the considered six-hour interval using a time increment of 15 minutes.

II.3) For each storm center on the TC track if the distance from the considered position on the track to the site of interest is less than 250 km (see illustration in Figure 3.3), carry out the following:

II.3.1) Calculate Δp, $R_{\max}$ and B according to Eqs. (3.5) to (3.6)), calculate $V_{s,\max}$ using Eqs. (3.3) and (3.4);

II.3.2) Based on the obtained wind field, evaluate V_s at the site of interest using Eq. (3.8).

II.3.3) Based on $R_{\max}$, $V_{s,\max}$, and V_T calculated $H_s^{\max}$ using Eqs. (3.9) to (3.11), and find H_s at the site by interpolating the normalized wave height diagrams such as the ones shown in Figure 3.2 (Young 1988).

II.4) For the simulated TC event affecting the site, extract:

II.4.1) The maximum V_s due to the passage of the TC event, denoted as $V_{s\text{-max}}$, and its companion values for [H_s, Δp, R_{max}, B, $d_{c\text{-}s}$] for the same instance of the TC activity, where $d_{c\text{-}s}$ denote the distance from the storm center to the site these companion values are denoted using the same symbols but with an additional subscript W. The symbol H_s is used to replace H_s^{max} to simply the notation.

II.4.2) The maximum H_s, denoted as $H_{s\text{-max}}$, and the values of its companion variables such as [V_s, H_s, Δp, R_{max}, B, $d_{c\text{-}s}$] at the same instance of the TC activity that are denoted, again, using the same symbols but with an additional subscript H.

III) Repeat Steps I and II to obtain sufficient samples of the mentioned variables in Step II).

The use of the extracted samples to develop the probabilistic model for the joint TC wind and wave hazard and the deaggregation of TC hazard for offshore sites are presented in the following sections.

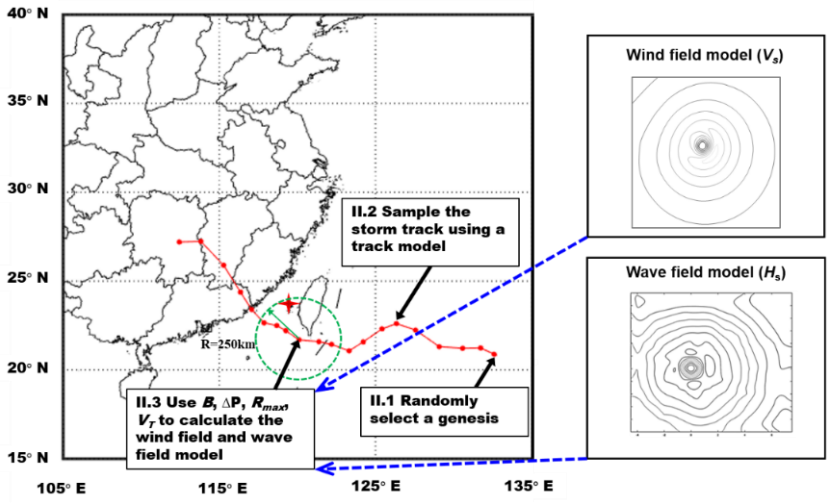

Figure 3.3. Overall procedure to simulate TC wind speed and significant wave height at a site.

3.3 Simulation results and vector-valued TC wind and wave hazards

3.3.1 Annual maximum analysis for vector-valued hazard evaluation

Consider the selected offshore sites shown in Figure 3.4. For each site, simulation of TC activities for 100,000 years is carried out by using the procedure presented in the previous section; samples of the parameters identified in Step II) for each TC event are obtained. From the extracted samples, the annual maximum of $V_{s\text{-max}}$ and its companion value H_{sW}, denoted as $V_{s\text{-maxA}}$ and H_{sWA}, as well as the annual maximum of $H_{s\text{-max}}$, and its companion value V_{sH}, denoted as $H_{s\text{-maxA}}$ and V_{sHA} are identified. The mean and the coefficient of variation (cov) of samples of these variables for the five sites identified in Figure 3.4 are calculated and presented in Table 3.1. The sites are located along the coastline of mainland China, with latitude range from about 21° to 31°.

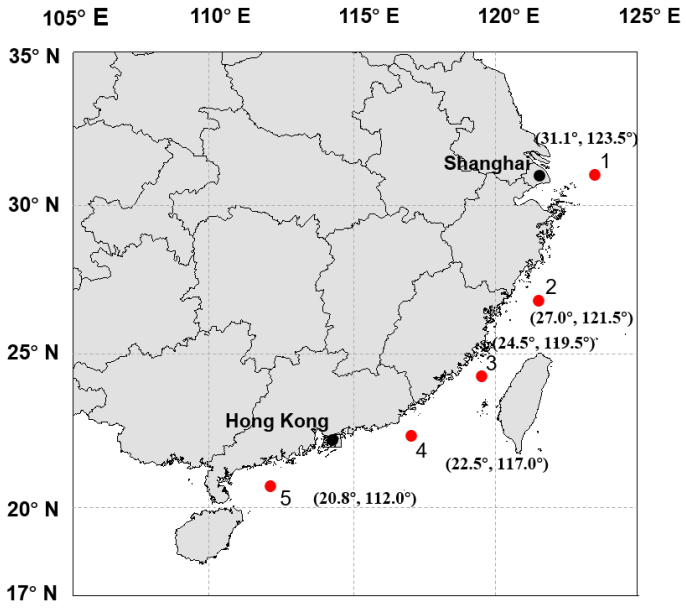

Figure 3.4. Five selected sites near the coastline of mainland China.

The results shown in Table 3.1 indicate that:

1) The mean of $V_{s\text{-maxA}}$, in general, increases from north to south. Its value is greater than 22 m. The TC events affecting Site 3 located in Taiwan Strait are influenced by the

orography of Taiwan, leading to a decreased mean for Site 3 as compared to that for Sites 2 and 4.

2) The cov of $V_{s\text{-maxA}}$ is greater than 0.3 and decreases slightly from north to south. This cov is greater than that of annual maximum wind speed reported for onshore sites in (Mo et al. 2015, Hong et al. 2016).

3) The mean of H_{sWA} (i.e., the companion variable of $V_{s\text{-maxA}}$) is relatively consistent for the considered sites. The cov of H_{sWA} is greater than that of $V_{s\text{-maxA}}$ by about 0.05.

4) The mean of $V_{s\text{-maxA}}$ is about 4 m/s (or 20%) greater than that of V_{sHA} (i.e., companion mean of $H_{s\text{-maxA,}}$). The mean of H_{sWA} is about 1 m (or 15%) less than that of $H_{s\text{-maxA}}$. These imply that the use of $V_{s\text{-maxA}}$ and $H_{s\text{-maxA}}$ to describe the simultaneous occurring TC wind and wave hazard can be very conservative.

Table 3.1. Mean, cov, and quantiles of the principal as well as its companion variables for the annual exceedance probability of 2% (All the mean wind speed values are in m/s and the significant wave heights are in m. λ is the average annual occurrence rate of typhoon with the minimum distance of storm center to the site of interest that is less than 250 km).

		Annual maximum analysis		Event-based analysis		
Site	Variable	$V_{s\text{-maxA}}$, H_{sWA}	V_{sHA}, $H_{s\text{-maxA}}$	$V_{s\text{-max}}$, H_{sW}	V_{sH}, $H_{s\text{-max}}$	Rate λ
1	Mean,	22.11, 6.47	18.12, 7.41	19.13, 5.69	16.12, 6.34	1.3
	cov	0.38, 0.44	0.37, 0.41	0.41, 0.47	0.40, 0.46	
	x_{50}	42.05, 13.44	33.93, 14.60	40.46, 13.08	32.49, 14.06	
2	Mean,	26.35, 7.74	21.84, 8.94	20.65, 6.29	17.93, 7.03	2.3
	cov	0.36, 0.40	0.35, 0.36	0.43, 0.47	0.41, 0.45	
	x_{50}	48.02, 14.58	39.63, 15.67	47.55, 14.62	39.34, 15.50	
3	Mean,	25.38, 7.51	21.43, 8.63	18.78, 5.81	16.81, 6.36	3.1
	cov	0.33, 0.38	0.32, 0.33	0.43,0.47	0.40, 0.45	
	x_{50}	44.63, 13.91	37.69, 14.90	44.47, 14.03	37.91, 14.80	
4	Mean,	26.10, 7.41	21.63, 8.57	18.79, 5.78	16.78, 6.33	3.3
	cov	0.33, 0.38	0.33, 0.33	0.45, 0.45	0.41, 0.44	

	x_{50}	46.18, 13.69	39.02, 14.68	46.09, 13.93	39.37, 14.62	
5	Mean,	27.71, 7.25	22.41, 8.62	18.66, 5.59	16.52, 6.13	4.2
	cov	0.31, 0.35	0.31, 0.28	0.46, 0.42	0.42, 0.41	
	x_{50}	46.24, 12.59	38.43, 13.48	46.22, 12.86	38.77, 12.45	

Note: x_{50} is calculated based on 0.98-quantile estimated from the empirical marginal distributions for the case of annual maximum analysis. If the event-based analysis is considered, x_{50} is calculated with an annual exceedance probability of 2% and by taking λ into account.

5) In all cases, the cov values of $V_{s\text{-maxA}}$ and H_{sWA} for a considered site are comparable to those of V_{sHA} and $H_{s\text{-maxA}}$. The cov of extreme wind in most cases are smaller than or comparable to that of extreme significant wave height.

6) The 50-year return period value of the annual maximum wind speed for Sites 2 to 5 is greater than 43.8 m/s which is the allowed design value for the installation of Class I wind turbine (see Introduction section).

The empirical marginal distributions of four variables are plotted on the Gumbel probability paper as shown in Figure 3.5. The estimated quantile based on the empirical distributions for the annual exceedance probability of 2% is also shown in Table 3.1. It can be observed that the estimated quantiles for the four random variables following the same trends as those for their mean values discussed earlier. This again indicates that the use of quantiles of $V_{s\text{-maxA}}$ and $H_{s\text{-maxA}}$ to represent the simultaneous occurring TC wind and wave hazard can be very conservative. A quantitative assessment of such a conservatism will be discussed shortly.

The plots shown in Figure 3.5 indicate that at least the annual maximum winds may not all fitted adequately by the commonly adopted Gumbel distribution (GD) and that the use of the generalized extreme value distribution (GEVD) may be suitable for the extreme TC induced wind and significant wave height. Note that in some cases as the radius of TC is limited to 250 km, the TC wind speed at the site for a year will be equal to zero. This can be eliminated by extending the radius of TC. The GEVD, $F_{GE}(x)$, is given by (Coles, 2001),

$$F_{GE}(x) = \exp\left(-\left(1-k(x-u_0)/a_0\right)^{1/k}\right), \text{ for } k \neq 0 \quad (3.12)$$

where u_0, a_0, and k are the model parameters. If $k > 0$, $-\infty < x \leq u_0 + a_0/k$ and X has an upper bound that equals $u_0 + a_0/k$; if $k < 0$, $u_0 + a_0/k \leq x < \infty$ and X has a lower bound. The GD, $F_G(x)$, is given by,

$$F_G(x) = \exp(-\exp(-\alpha_{10}(x-u_{10}))) \quad (3.13)$$

where u_{10} and α_{10} are location and scale parameters.

Distribution fitting using these two models is carried out by applying the maximum likelihood method. The application of the Akaike information criterion (AIC) indicates that in almost all cases GEVD is preferable than GD. However, a comparison of the fitted distribution to the empirical distribution indicates that the fitting in many cases is inadequate, at least in the upper tail region. To overcome this, distribution fitting by using the least-squares method is carried out by considering the samples in the upper tail region (i.e., with empirical cumulative distribution value greater than 0.5) considering GEVD and GD. The fitted distributions are shown in Figure 3.5 as well. It can be observed that in all cases, GEVD fits the data adequately in the upper tail portion of the data. Therefore, it is recommended that the GEVD is to be used for the considered four random variables.

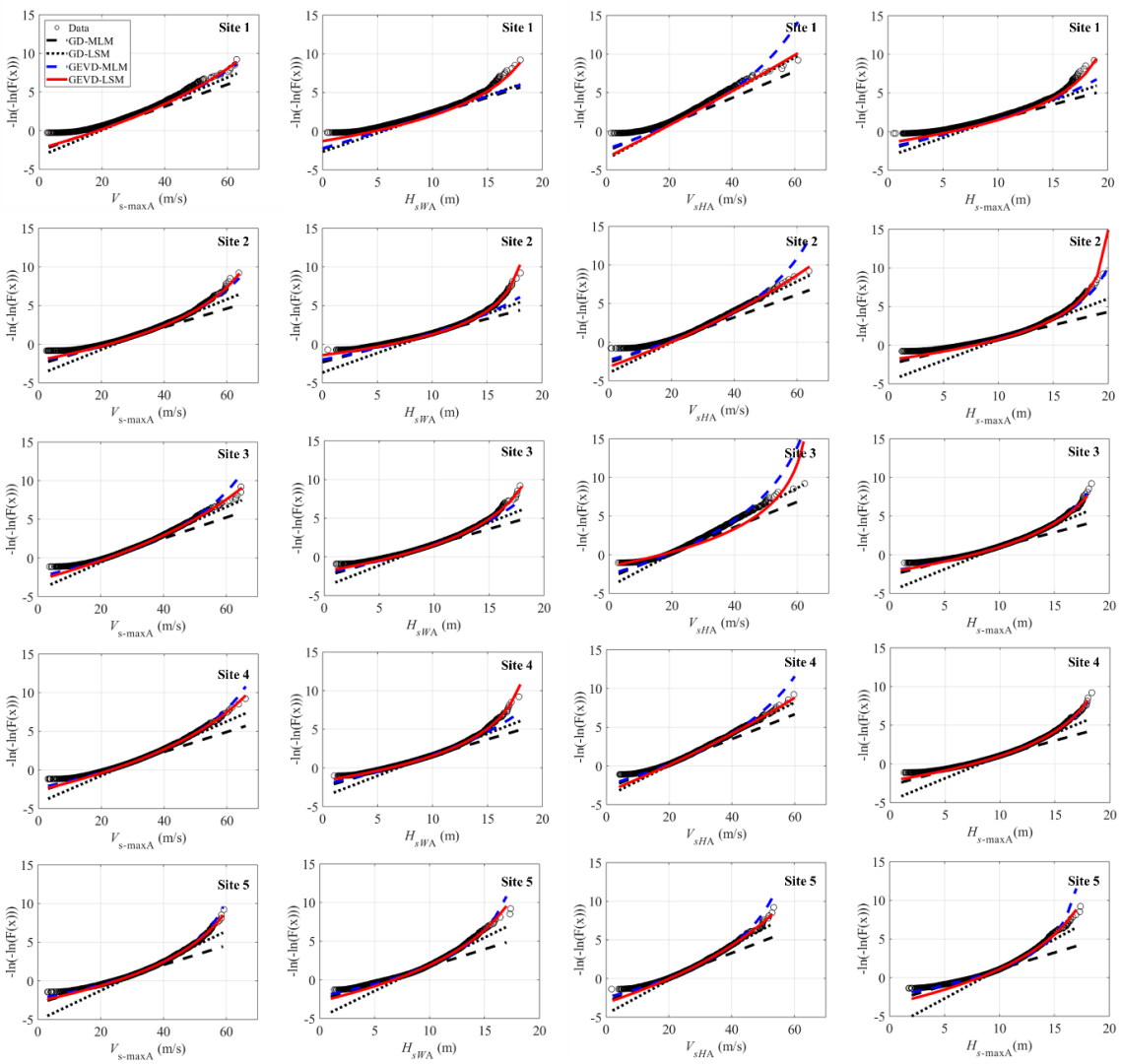

Figure 3.5. Empirical and fitted marginal distributions of $V_{s\text{-maxA}}$, H_{sWA}, V_{sHA} and $H_{s\text{-maxA}}$ (in the legend, GD and GEVD denote the Gumbel distribution and generalized extreme value distribution, respectively; MLM and LSM denote the maximum likelihood method and least-squares method, respectively).

To assess the correlation between $V_{s\text{-maxA}}$ and its companion variable H_{sWA} and the correlation between $H_{s\text{-maxA}}$ and its companion variable V_{sHA}, the paired samples ($V_{s\text{-maxA}}$, H_{sWA}) and ($H_{s\text{-maxA}}$, V_{sHA}) are used to obtain the probability of nonexceedance and shown in Figure 3.6. Also, the Kendall's τ representing the ranked correlation is calculated and shown in the figure. The calculated value ranges from about 0.40 to 0.67 for different cases. The correlation coefficient with such a magnitude may not be neglected since it

could impact the assessment of probabilistically combined wind and wave loading. The comparison of the plots shown in Figure 3.6 to the samples from the Gaussian, Gumbel and Clayton copula plots (Hong et al. 2014), such as those illustrated in Figure 3.7 based on an assigned τ value, indicates that the Gumbel copula could be adopted to model the paired random variables considered in Figure 3.6.

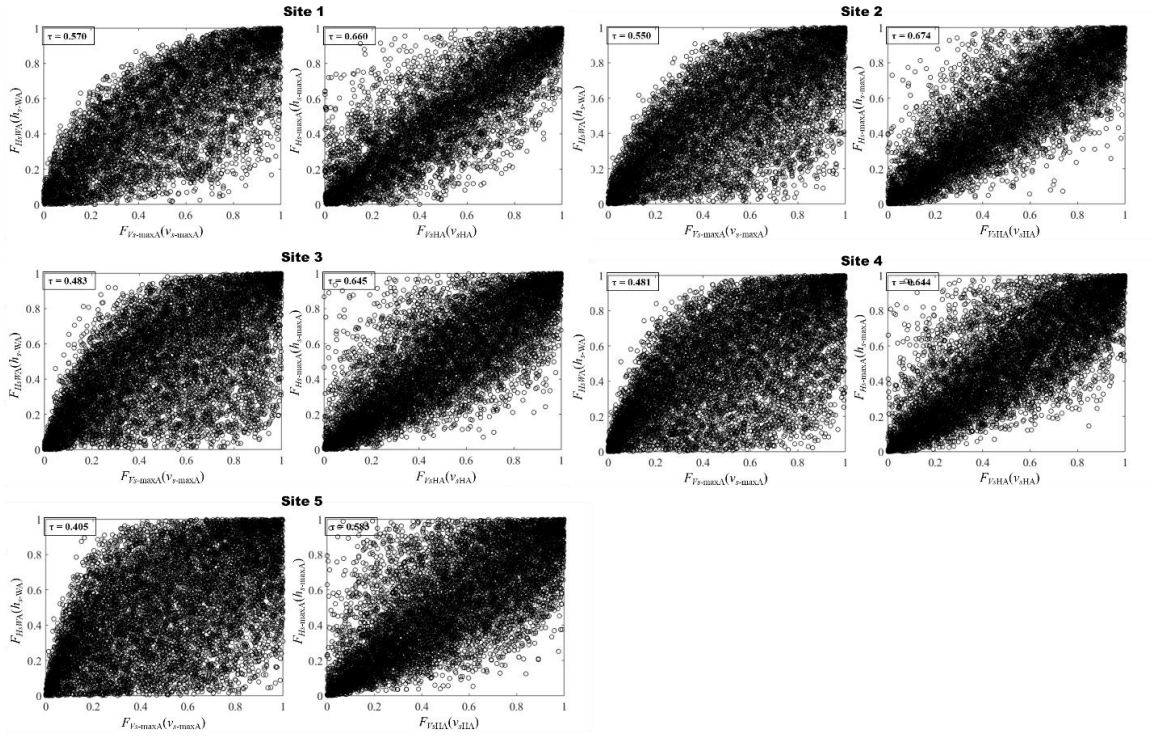

Figure 3.6. Plots of $F(V_{S\text{-maxA}})$ versus $F(H_{SWA})$, and $F(V_{SHA})$ versus $F(H_{S\text{-maxA}})$, where $F(\,)$ denotes the marginal distribution of a random variable and the Kendall's τ is included in the plot.

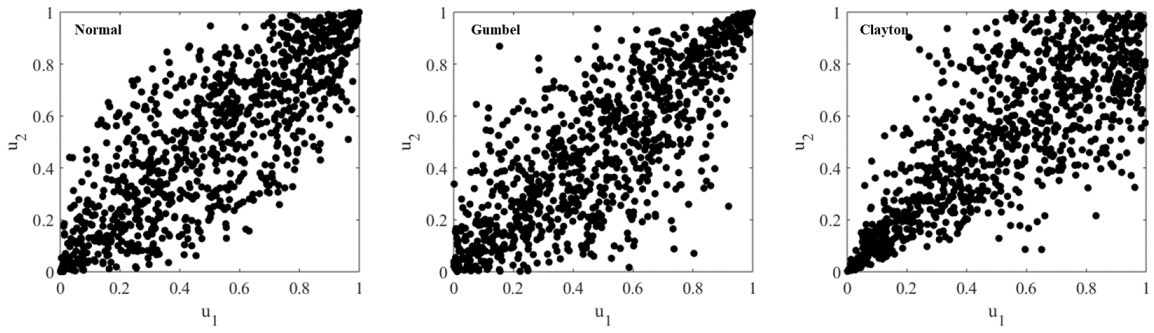

Figure 3.7. Plots of typical samples from normal, Gumbel and Clayton copula for τ = 0.6.

For a paired random variables, X_1 and X_2 with its corresponding marginal probability distribution denoted as $F_{X1}(x_1)$ and $F_{X2}(x_2)$, if the Gumbel copula is considered, $F(x_1, x_2)$ is given by (Nelsen 2006),

$$F(x_1, x_2) = \exp\left(-\left(u_1^{\alpha_G} + u_2^{\alpha_G}\right)^{1/\alpha_G}\right) = \exp\left(-\left(\left(-\ln(F_{X1}(x_1))\right)^{\alpha_G} + \left(-\ln(F_{X2}(x_2))\right)^{\alpha_G}\right)^{1/\alpha_G}\right) \quad (3.14)$$

where u_1 and u_2 are standard uniformly distributed random variables. The model parameters for Eq. (3.14) can be calculated by noting that Kendall's τ correlation coefficient equals $1-\alpha_G^{-1}$ for the Gumbel copula.

As an illustration, consider Site 2. Since Kendall's τ equals 0.55 by considering $V_{s\text{-maxA}}$ and H_{sWA}, the obtained α_G = 2.22. The contours for the nonexceedance probability $p = F(v_{s-\text{maxA}}, h_{sHA})$ equal to 0.9, 0.98, and 0.998 are shown in Figure 3.8a. Based on this probability plot, by using the fitted marginal distributions of $V_{s\text{-maxA}}$ and of H_{sWA} shown in Figure 3.5, the calculated $V_{s\text{-maxA}}$ and H_{sWA} values are shown in Figure 3.8b. The results indicate that there are combinations of values of $V_{s\text{-maxA}}$ and of H_{sWA} that can lead to the same specified probability of nonexceedance p. For example, for p = 0.98, H_{sWA} tends to 14.58 m as $V_{s\text{-maxA}}$ tends to its upper limit, and $V_{s\text{-maxA}}$ tends to 48.02 m/s as H_{sWA} tends to its upper limit. These values are in agreement with those shown in Table 3.1 for Site 2. A similar analysis is carried out by considering V_{sHA} and $H_{s\text{-maxA}}$ for the same site. The obtained values of V_{sHA} and $H_{s\text{-maxA}}$ are presented in Figures 3.8c and 3.8d. In this case,

for p = 0.98, as V_{sHA} or $H_{s\text{-maxA}}$ tends to their upper limits, $H_{s\text{-maxA}}$ or V_{sHA} tends 15.67 m and 39.63 m/s, respectively. A comparison of the results shown in Figure 3.8 for a given p value shows that the contour lines for the combinations of $V_{s\text{-maxA}}$ and H_{sWA} and for V_{sHA} and $H_{s\text{-maxA}}$ differ, illustrating the differences in the joint probability distributions.

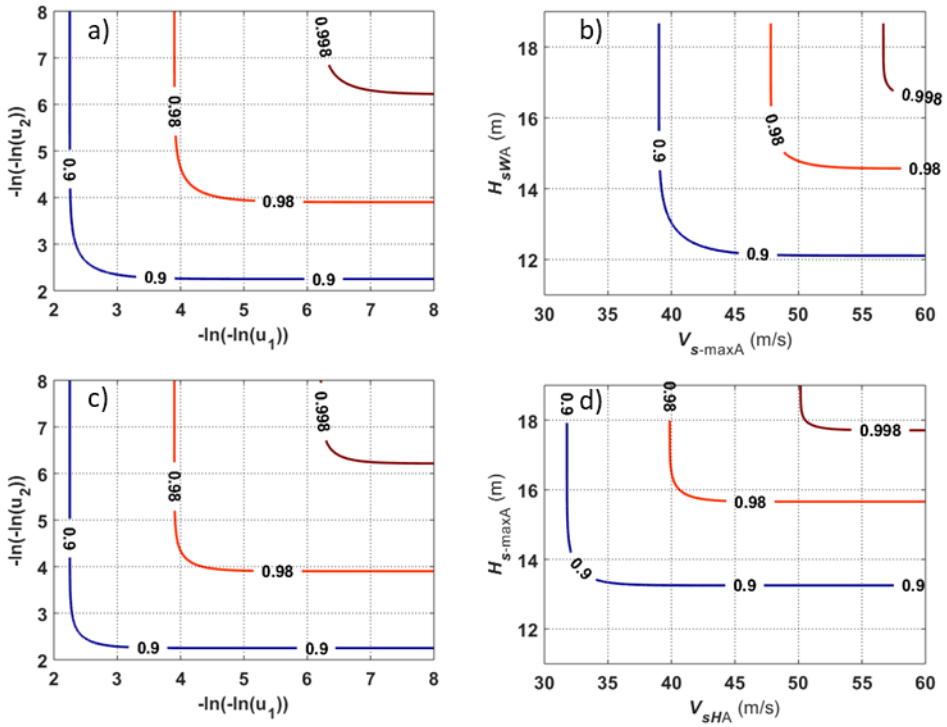

Figure 3.8. Contours for $p = F(v_{s-\max A}, h_{sHA})$ by considering Gumbel copula with α_G = 2.22 (plots a and b), and contours for $p = F(v_{sHA}, h_{s-\max A})$ by considering Gumbel copula with α_G = 3.06 (plots c and d). α_G values are for Site 2.

3.3.2 Assessment of the companion load combination factor

It is noteworthy that for structural reliability analysis and design code calibration, the combined load effect due to $(V_{s\text{-maxA}})^2$ and H_{sWA} (i.e., $c_1 V_{s-\max A}^2 + c_2 H_{sWA}$), and due to $(V_{sHA})^2$ and $H_{s\text{-maxA}}$ (i.e., $c_1 V_{sHA}^2 + c_2 H_{s-\max A}$) need to be considered, where c_1 and c_2 include the structural analysis coefficients and the transformation from environmental parameters to load effects. Similar to the analysis of environmental load combination for

the offshore platform (Nessim et al (1995) and Tarp-Johansen (2005)), let $Z(t)$ denote the simultaneous TC wind and wave load actions expressed as,

$$Z(t) = c_1 V^2(t) + c_2 H(t) \tag{3.15}$$

where $V(t)$ and $H(t)$ denotes the wind speed and wave height that vary with time t. Based on the observations made previously, the use of (1-p)-quantiles of $V_{s\text{-maxA}}$ and of $H_{s\text{-maxA}}$ for $V(t)$ and $H(t)$ to evaluate the (1-p)-quantile of the load effect $Z(t)$ is likely to be very conservative. To simplify the calculation of combined load effect with the same exceedance probability for ranges of c_1 and c_2 values and aimed at structural design code development, consider the following normalized load effect (Nessim et al. 1995),

$$Z^*(t) = \frac{Z(t)}{c_1 v_p^2 + c_2 h_p} \tag{3.16}$$

where v_p and h_p represent the wind speed and significant wave height with an annual exceedance probability of p, respectively. This equation can be re-written as,

$$Z^*(t) = (1-r)\left(\frac{V(t)}{v_p}\right)^2 + r\left(\frac{H(t)}{h_p}\right) \tag{3.17}$$

where $r = c_2 h_p / \left(c_1 v_p^2 + c_2 h_p\right)$ takes the value from 0 to 1. The combined load action with an annual probability of exceedance p, z_p, can then be calculated using the value of $Z^*(t)$ with annual probability of exceedance p, z_p^*, resulting in,

$$z_p = z_p^* \left(c_1 v_p^2 + c_2 h_p\right) \tag{3.18}$$

The calculation of v_p and h_p is already presented in the previous sections with the results for the five selected sites shown in Table 3.1 for p = 1/50. The calculation of z_p^* can be carried out using the simulated TC wind speed and significant wave height for a site of interest. More specifically, for example, one can form the samples of the annual maximum $Z^*(t)$ using samples of ($V_{s\text{-maxA}}$, H_{sWA}) and (V_{sHA}, $H_{s\text{-maxA}}$), develop the

empirical distribution of annual maximum $Z^*(t)$, and find z_p^* from the empirical distribution.

The obtained z_p^* for r ranging from 0 to 1 in such a manner is shown in Figure 3.9a for the five considered sites shown in Figure 3.4 for p = 1/50. As expected, z_p^* = 1 for r = 0 (i.e., c_2 = 0), representing the case where there is wind load effect only, and z_p is simply equal to $z_p = c_1 v_p^2$. Also, z_p^* = 1 for r = 1 (i.e., c_1 = 0), representing the case where there is wave load effect only, and z_p is simply equal to $z_p = c_2 h_p$. For r within 0 and 1, approximate combination rules can be developed based on the load combination diagram shown in Figure 9a.

Rather than using the actual curves, if the (conservative) bilinear approximation shown in the figure is deemed acceptable,

$$z_p^* = \max\left[(1-r) + r\eta_2, (1-r)\eta_1 + r\right] \tag{3.19}$$

and consequently,

$$z_p = \max\left(c_1 v_p^2 + \eta_2 c_2 h_p, \eta_1 c_1 v_p^2 + c_2 h_p\right) \tag{3.20}$$

where the values of η_1 = 0.75 and η_2 = 0.85 are shown in Figure 3.9a. For completeness, the calculation for p = 1/500 is also carried out and the results are shown in Figure 3.9b. A comparison of the results shown in Figure 3.9 indicates that the combination rule is not very sensitive to whether p = 1/50 or 1/500 is considered. However, the coefficients slightly lower coefficients η_1 and η_2 could be considered as the exceedance probability decreases. The plots shown in Figure 3.9 represent a version of implementing Turkstra's rule for the companion action factor method (Turkstra and Madsen, 1980). It implicitly assumes that the load combination problem is governed by the extreme of one action in combination with its companion action; it is desirable such an assumption to be validated for offshore wind turbines subjected to TC wind and wave hazard. To the author's acknowledge, the assessment of the load combination factor for the simultaneous TC

wind and wave actions has not been addressed in the literature. Note that the analysis carried out in this section did not consider the uncertainty in the coefficients c_1 and c_2, and different p values. These issues should be taken into account for a rigorous design code calibration analysis.

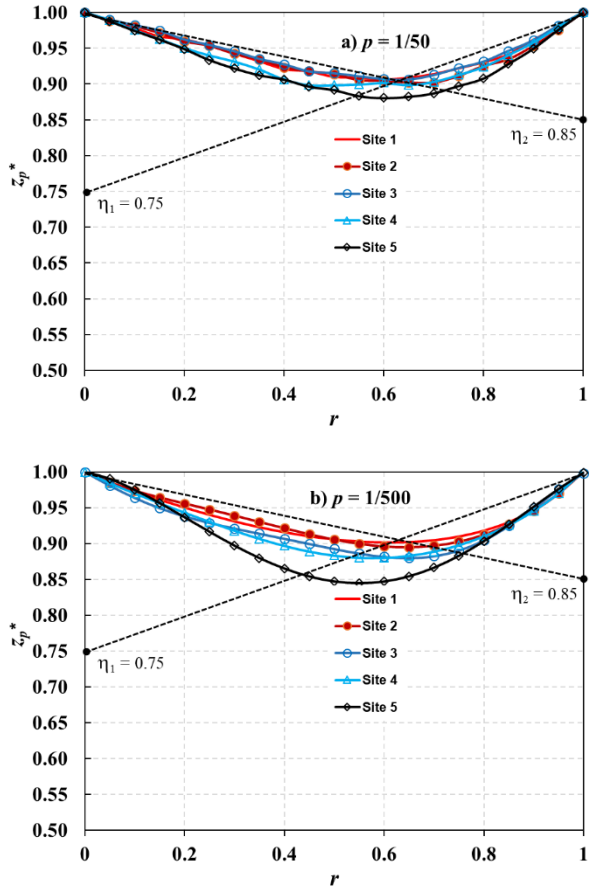

Figure 3.9. Load combination diagram for simultaneous TC wind and wave actions: a) for p = 1/50 and b) for p = 1/500.

3.3.3 Event-based analysis for vector-valued hazard evaluation

Rather than carrying out the TC hazard assessment based on the block maximum analysis, an alternative is to carry out an event-based analysis. From the simulated samples for 100,000 years, it was observed that the average number of TC events affecting the considered offshore differs and the annual occurrence rate, λ, for each site is shown in Table 3.1 for p = 1/50. Values of ($V_{s\text{-max}}$, H_{sW}) and (V_{sH}, $H_{s\text{-max}}$) for each event

are used to establish their empirical marginal probability distributions as shown in Figure 3.10. For the considered random variables, the mean and standard deviation are calculated and the quantiles corresponding to the annual probability of exceedance of 2% are estimated from the empirical distributions. For the estimation of the quantiles, it is assumed that a site experiencing TC events follows a Poisson process with the rate λ shown in Table 3.1. The calculated statistics and quantiles are shown in Table 3.1.

A comparison of the results shown in Table 3.1 indicates that the values of x_{50} based on the annual maximum analysis and the event-based analysis are in good agreement. Table 3.1 also indicates that the mean of the event-based extreme values is slightly less than that of the annual maximum extreme value and the cov of the event-based extreme values is greater than that of the annual maximum extreme values. This is expected and is in agreement with extreme value theory (Coles, 2001).

To assess the correlation between $V_{s\text{-max}}$ and H_{sW} and the correlation between $H_{s\text{-max}}$ and V_{sHA}, the paired samples ($V_{s\text{-max}}$, H_{sW}) and ($H_{s\text{-max}}$, V_{sH}) are mapped in terms of probability and shown in Figure 3.11, where the calculated values of the Kendall's τ are included. The calculated values range from about 0.57 to 0.72 for different cases. These values are similar to but slightly greater than those obtained based on annual maximum analysis shown in Figure 3.6. Again, the comparison of these plots to the samples from the Gaussian, Gumbel and Clayton copula plots indicates that the normal or Gumbel copula could be used to model the paired random variables shown in Figure 3.11.

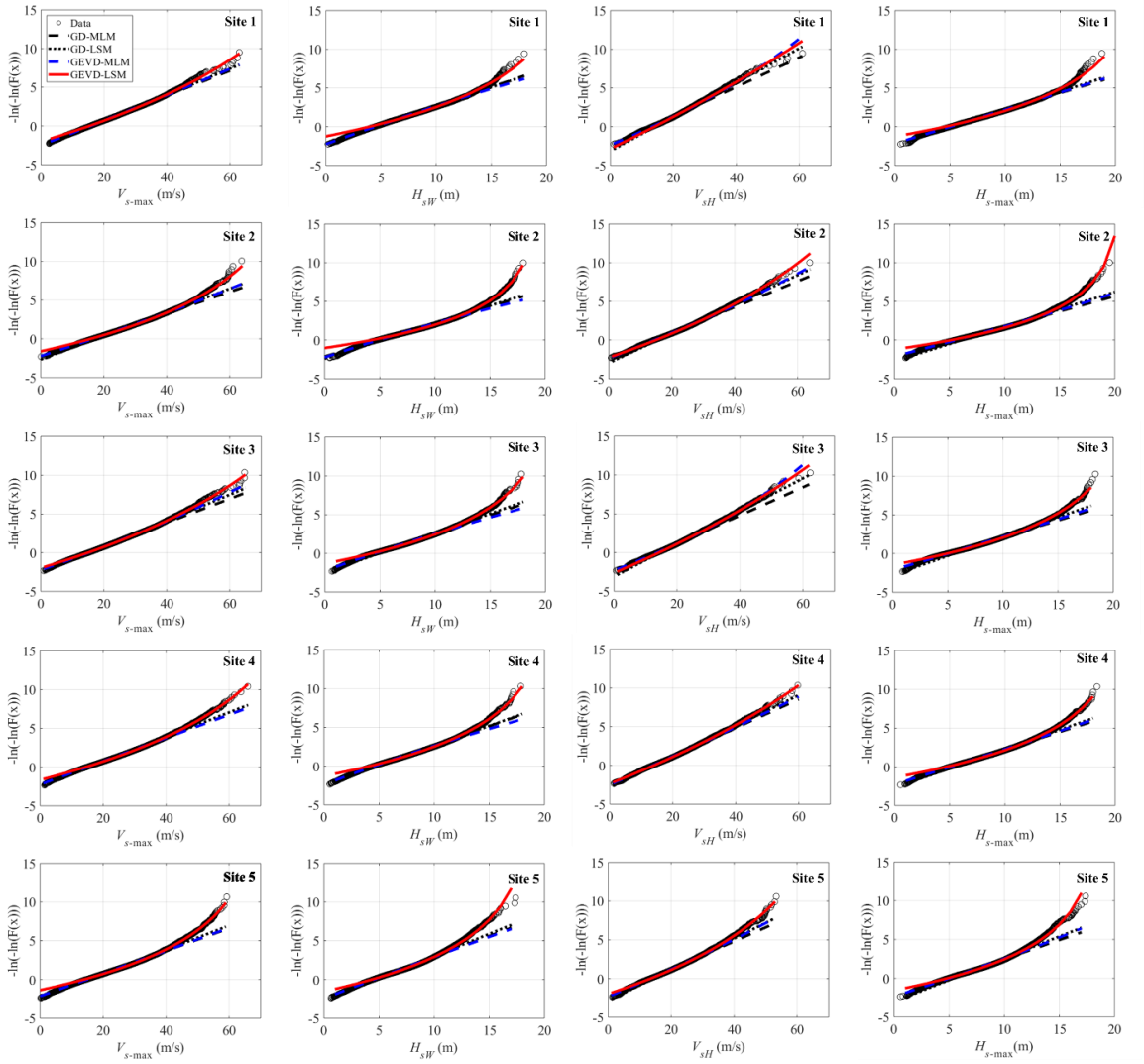

Figure 3.10. Marginal probability distributions of $V_{s\text{-max}}$, H_{sW}, V_{sH}, and $H_{s\text{-max}}$ (in the legend, GD and GEVD denote the Gumbel distribution and generalized extreme value distribution, respectively; MLM and LSM denote the maximum likelihood method and least-squares method, respectively).

Based on the above observations, the probabilistic models based on the annual maximum analysis or based on event-based analysis lead to consistent TC induced wind and wave hazard characterizations. Therefore, either one of them can be used to analyze TC induced hazard and risk for offshore structures, including offshore wind turbines. The consideration of the frequency of TC events and their corresponding wind and wave hazard can be important for the operation and emergency planning of these structures.

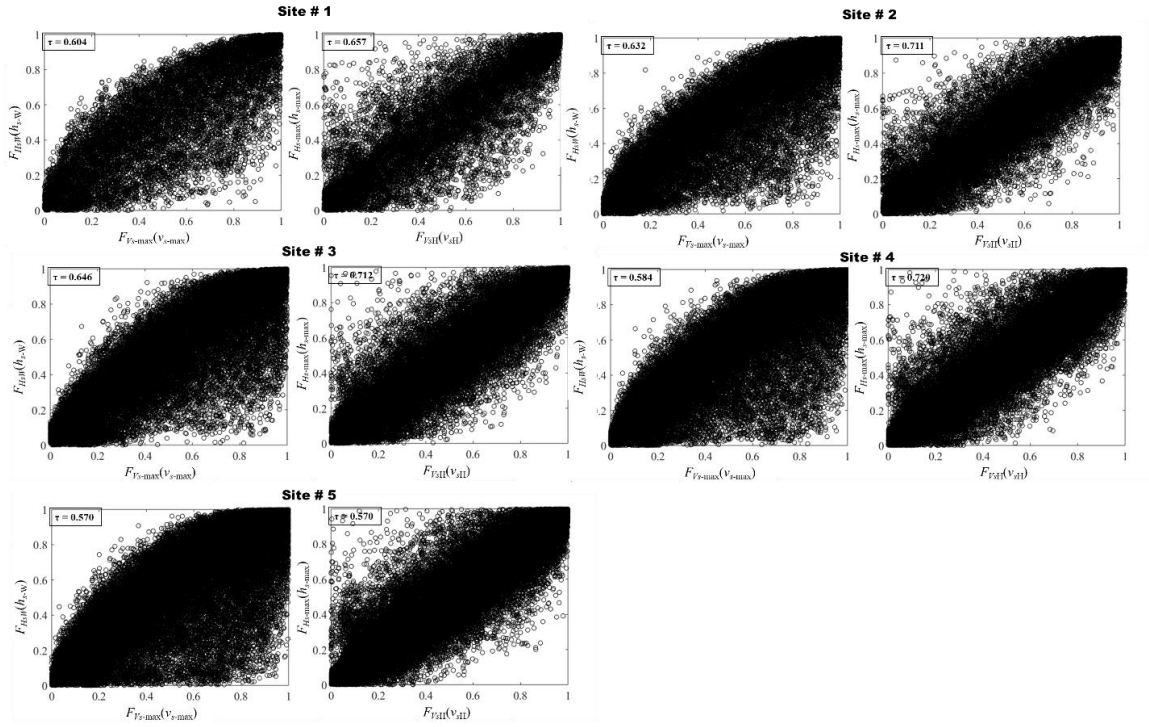

Figure 3.11. Plots of $F(V_{s\text{-max}})$ versus $F(H_{sW})$, and $F(V_{sH})$ versus $F(H_{s\text{-max}})$, where $F(\,)$ denotes the marginal distribution of a random variable and the Kendall's τ is included in the plot.

3.3.4 Deaggregation of TC wind and wave hazards

In hazard and risk assessment, risk communication and emergency planning, it is often instructive to identify possible scenario events associated with specified return period value or quantile of a natural hazard. In the context of TC wind hazard and TC wave hazard, it is valuable to identify the TC events leading to the p-quantile of $V_{s\text{-maxA}}$. For p = 0.98 and 0.998, the identified values of the variables $(\Delta p, R_{max}, B, d_{c\text{-}s})_W$ defining the TC events for or corresponding to $V_{s\text{-maxA}}$ within 95% to 105% of p-quantile of $V_{s\text{-maxA}}$ are shown in Table 3.2 for the five sites and illustrated in Figures 3.12 and 3.13 for Sites 1, 3, and 5. Similarly, the deaggregation results based on quantiles of $H_{s\text{-maxA}}$ are shown in Table 3.2 and illustrated in Figures 3.14 and 3.15. The observations that can be made from the table and figures are:

1. The most likely events identified by the deaggregation differ from site to site.

2. The central pressure difference Δp increases as p increases.

3. The values of B for the deaggregation results based on quantiles of $V_{s\text{-maxA}}$ are greater than those based on the quantiles of $H_{s\text{-maxA}}$. This indicates that the identified TC events for the former are associated with a rapid horizontally changing pressure profile as compared to those for the latter.

4. The values of R_{max} and $d_{c\text{-}s}$ for the deaggregation results based on quantiles of $V_{s\text{-maxA}}$ are smaller than those based on the quantiles of $H_{s\text{-maxA}}$. In general, values of R_{max} and $d_{c\text{-}s}$ decreases as p increases.

Table 3.2. Most likely values of the TC parameters identified from deaggregation results based on p-quantile of $V_{s\text{-maxA}}$ and of $H_{s\text{-maxA}}$.

Site	p	$V_{s\text{-maxA}}$				$H_{s\text{-maxA}}$			
		Δp (hPa)	R_{max} (km)	B	$d_{c\text{-}s}$ (km)	p (hPa)	R_{max} (km)	B	$d_{c\text{-}s}$ (km)
1	0.98	46.6	100	1.5	21.7	44.9	100	1.1	81.3
	0.998	59.3	47.1	1.5	20.4	64	100	1.2	29.5
2	0.98	75.7	35.2	1.4	23.4	60.2	100	1.3	43.1
	0.998	67.3	48.4	1.7	19.5	76.5	38.8	1.5	31.1
3	0.98	53.3	100	1.5	25	45.5	100	1.3	34.3
	0.998	57.7	20.8	1.4	4.7	76.9	27.3	1.3	58.5
4	0.98	35	26.7	1.6	25.1	58.4	100	1.4	49.6
	0.998	58.1	9.4	1.6	7.7	58.7	40.9	1.4	29.4
5	0.98	46.7	24	1.6	35.2	45.7	100	1.4	58.5
	0.998	47.8	25.4	1.8	15.4	56.8	39.5	1.5	37.1

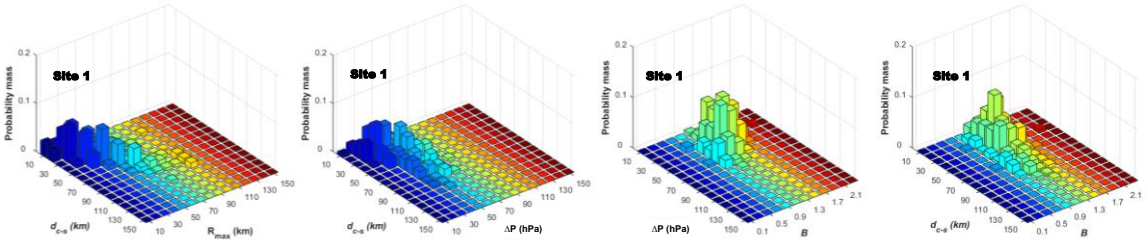

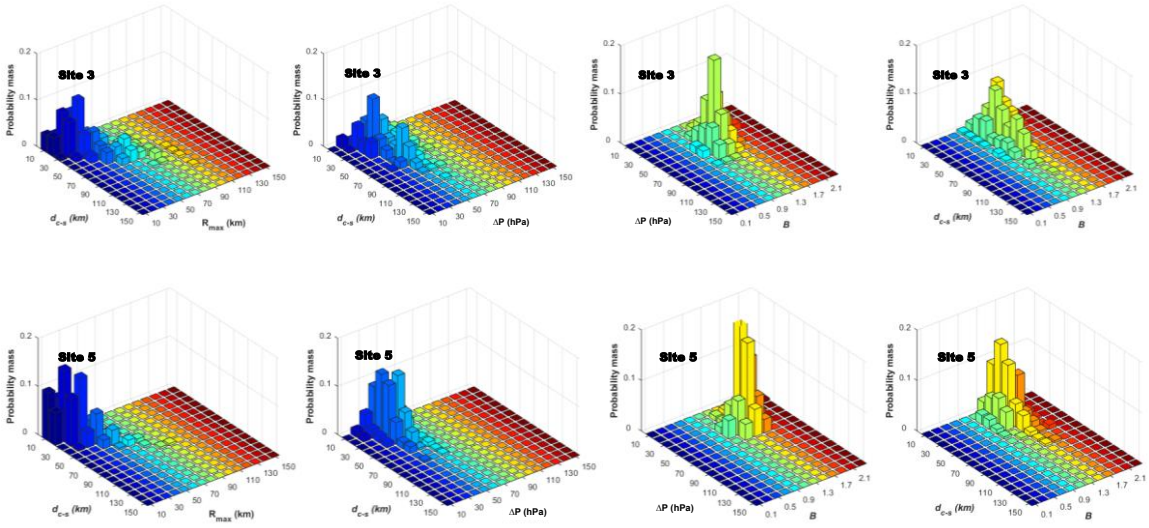

Figure 3.12. Deaggregation results based on 0.98-quantile of $V_{s\text{-}maxA}$ for Site 1, 3 and 5.

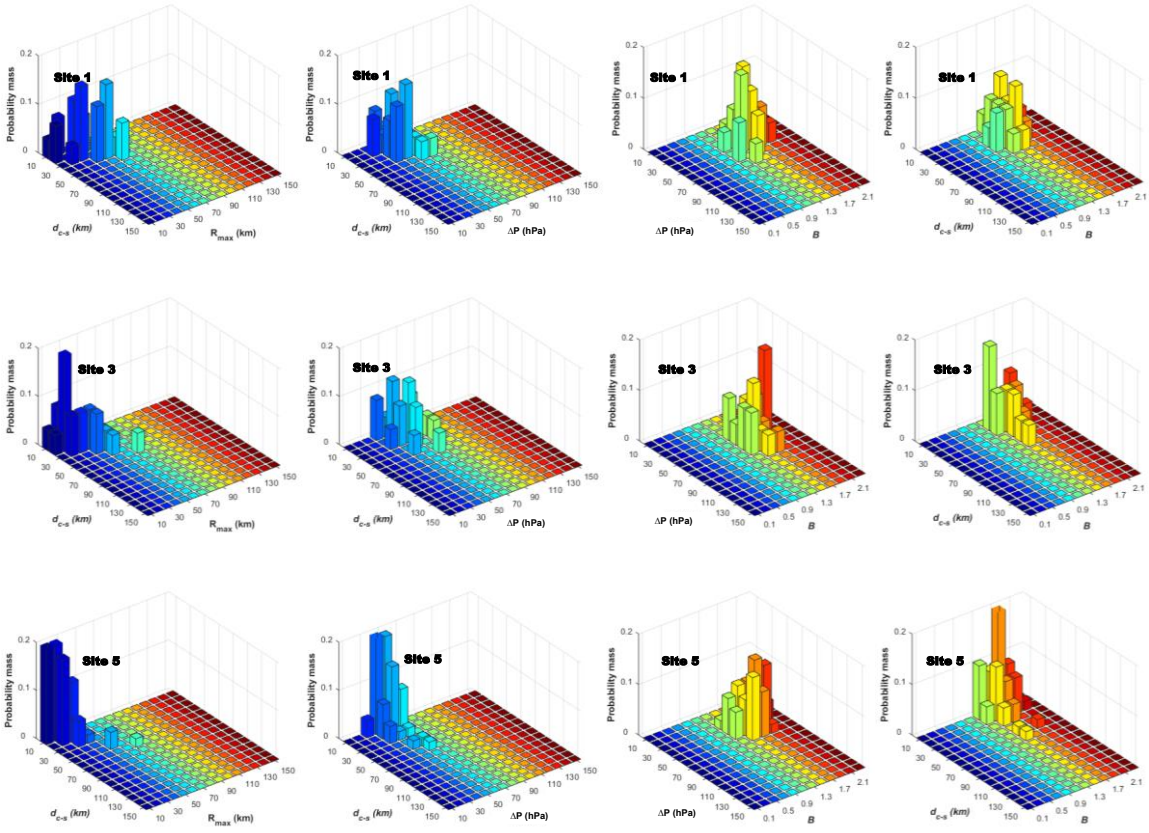

Figure 3.13. Deaggregation results based on 0.998-quantile of $V_{s\text{-}maxA}$ for Site 1, 3, and 5.

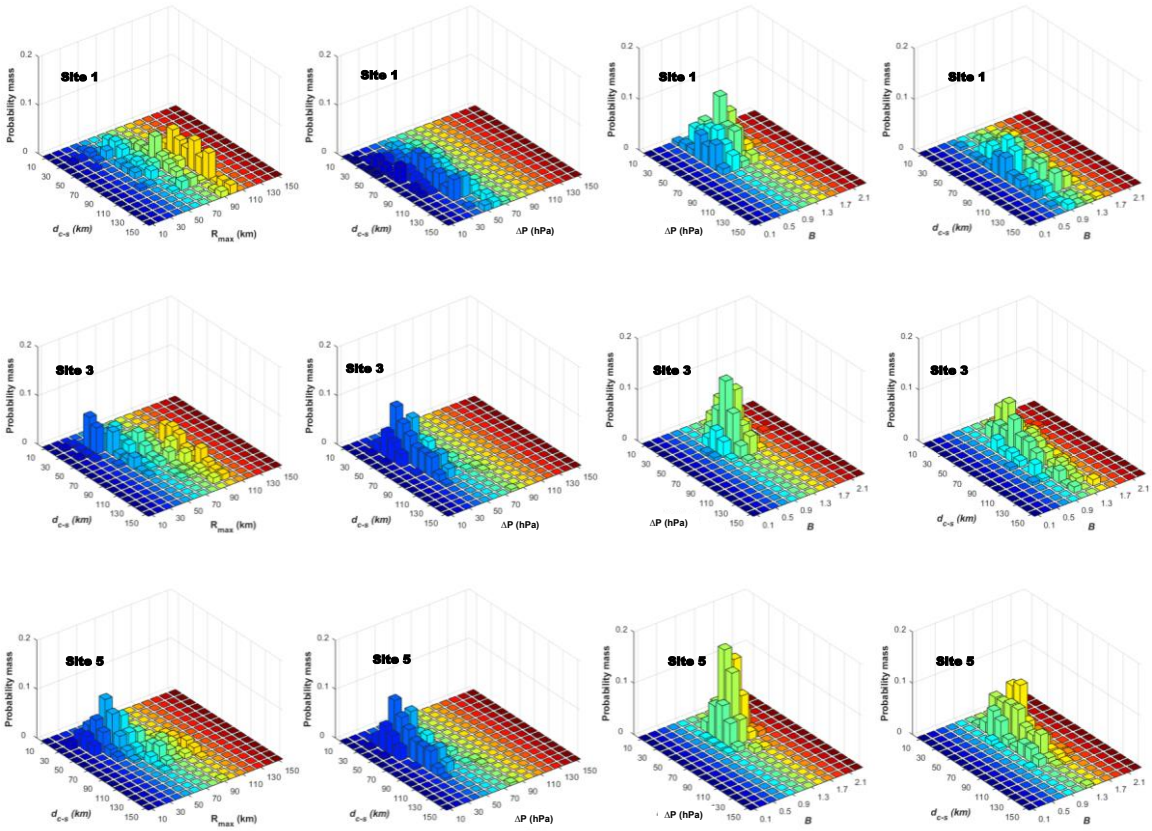

Figure 3.14. Deaggregation results based on 0.98-quantile of $H_{s\text{-maxA}}$ for Site 1, 3 and 5.

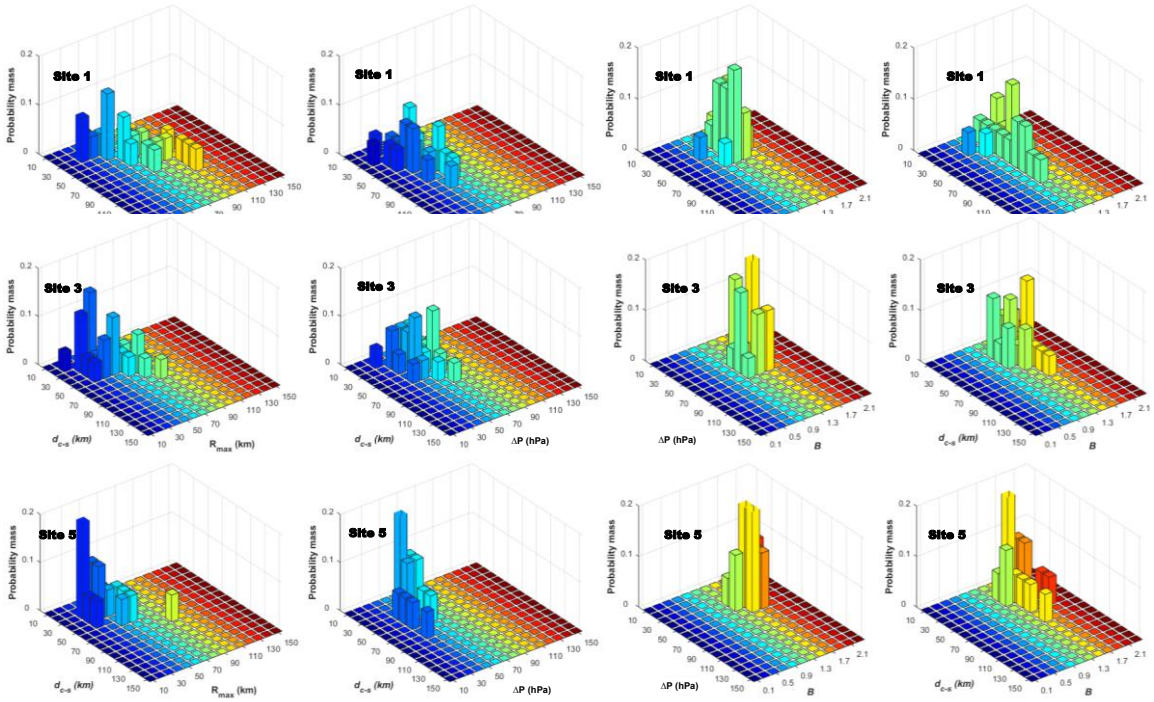

Figure 3.15. Deaggregation results based on 0.998-quantile of $H_{s\text{-}maxA}$ for Site 1, 3 and 5.

3.4 Conclusions

A simulation-based framework to estimate TC induced wind and wave hazards is presented. The framework and adopted TC wind field and significant wave height model are successfully used to assess the marginal and joint probability distributions of extreme TC wind speed and significant wave height. The simulation results are used for the deaggregation analysis of wind and wave hazards for a few selected offshore sites near the coastline of mainland China.

The results indicate that the use of the generalized extreme value distribution for the annual maximum wind speed and the annual maximum significant wave height at a site is preferred. Also, the ranked correlation coefficient (i.e., Kendall's τ) of the annual maximum wind speed and its companion significant wave height ranges from about 0.4 to 0.7. Similar ranked correlation coefficient is obtained for the annual maximum significant wave height and its companion wind speed. Plots of paired samples in terms

of probability indicate that the Gumbel copula could be adopted to model the joint probability distribution of the annual maximum wind (significant wave height) and its companion significant wave height (wind speed). The results also indicate that the statistics of the TC induced wind and wave hazards vary for sites along the coastline of mainland China.

The use of the simulation results in assessing the companion load combination factor by considering the simultaneous TC wind and wave actions is presented. The results indicate that: a) a load companion factor of 0.85 for wave action could be considered if the wind action is the principal load action and b) a companion load combination factor of 0.75 for the wind action could be considered if the wave action is the principal load action. The suggested companion load combination factors are based on an annual exceedance probability of 2% and for the considered offshore sites. The sensitivity analysis results also indicates that these suggested values are not very sensitive to p = 1/50 or 1/500.

The deaggregation results indicate that the identified TC events contributing to a specified quantile of the annual maximum wind speed differ from those identified for the quantile of the annual maximum significant wave height. In general, the identified events based on the former are associated with a rapid horizontally changing pressure profile as compared to those based on the latter. Therefore, the reliability and risk assessment of offshore structures located near the coastline of mainland China should consider the identified scenario events from the quantile of wind speed as well as those from the significant wave height.

3.5 References

Batts, M. E., Cordes, M. R., Russell, C. R., Shaver, J. R., and Simiu. E. Hurricane windspeeds in the United States. Nat. Bureau of Standards Rep. No. BSS·I24, U.S. Dept. of Commerce, Washington, D.C. 1980.

Cardone, V.J., Jensen, R.E., Resio, D.T., Swail, V.R., and Cox, A.T. Evaluation of contemporary ocean wave models in rare extreme events: the “halloween storm” of

October 1991 and the “Storm of the Century” of March 1993. J. Atmos. Oceanic Technol. 1996; 13 (1), 198–230.

Chow, S. A study of the wind field in the planetary boundary layer of a moving tropical cyclone. M.Sc. Thesis, New York University, New York, NY. 1997.

Coles, S. An introduction to statistical modeling of extreme values, (Vol. 208, p. 208). London: Springer. 2001.

Donelan, M.A., Hamilton, J., and Hui, W.H. Directional spectra of wind-generated waves. Philos. Trans. R. Soc. B Ser. A. 1985; 315, 509–562.

Emanuel, K.A., Ravela, S., Vivant, E., and Risi, C. A statistical-deterministic approach to hurricane risk assessment. Bull. Am. Meteorol. Soc. 2006; 19, 299-314.

GB/T 31519-2015. Wind turbine generator system under typhoon condition, Standards Press of China; Beijing, China. 2015.

Georgiou, P.N., Davenport, A.G., and Vickery, B.J. Design wind speeds in regions dominated by tropical cyclones. J. Wind Eng. Ind. Aerodyn. 1983; 13, 139–152.

Hall, T. and Jewson, S. Statistical modelling of North Atlantic tropical cyclone tracks, Tellus.2007; 59A, 486–498.

Hallowell, S. T., Myers, A. T., Arwade, S. R., Pang, W., Rawal, P., Hines, E. M.,and Carswell, W.. Hurricane risk assessment of offshore wind turbines. Renew. Energ. 2018;125, 234-249.

Harper, B. A., Kepert, J. D., and Ginger, J. D. (2010). Guidelines for converting between various wind averaging periods in tropical cyclone conditions. Geneva, Switzerland: WMO.

Hasselmann K, et al. Measurem ents of wind-wave growth and swell decay during the Joint North Sea Wave Project (JONSWAP). Dtsch Hydrogr Z, Suppl. A. 1973; 8(12): 95.

Holland, G. J. An analytic model of the wind and pressure profiles in hurricanes. Mon. Weather Rev.. 1980 108(8), 1212-1218.

Holton, J. R. An Introduction to Dynamic Meteorology, Int. Geophys. 2004; Ser, 88, 313-369.

Hong, H. P., Li, S. H., and Duan, Z. D. Typhoon wind hazard estimation and mapping for coastal region in mainland China. Nat. Hazards Rev. 2016; 17(2), 04016001.

Hong, H. P., Zhou, W.Z., Zhang, S.W., and Ye, W. Optimal condition-based maintenance decisions for systems with dependent stochastic degradation of components. Reliab. Eng. Syst. Safety. 2014; 121(1), 276-288.

IEC International Electrotechnical Commission. IEC 61400-3 Wind Turbines - Part 1: Design Requirements for Offshore Wind Turbines, Edition 1. 2009.

IEC International Electrotechnical Commission. IEC 61400-3-1:2019 Wind energy generation systems –Part 3-1: Design requirements for fixed offshore wind turbines. 2019.

James, M.K. and Mason, L.B. Synthetic tropical cyclone database. J. Waterw. Port Coastal Ocean Eng. 2005; 131, 181–192.

Jha, A., Dolan, D., Musial, W., and Smith, C. On hurricane risk to offshore wind turbines in US Waters. Proceedings from the 2010 Offshore Technology Conference. 2010; Houston, TX.

Li, L., Xiao, Y., Kareem, A., Song, L., and Qin, P. Modeling typhoon wind power spectra near sea surface based on measurements in the South China sea. J. Wind Eng. Ind. Aerodyn. 2012; 104, 565-576.

Li, S. H., and Hong, H. P. Observations on a hurricane wind hazard model used to map extreme hurricane wind speed. J. Struct. Eng. 2014; 141(10), 04014238.

Li, S. H., and Hong, H. P. Typhoon wind hazard estimation for China using an empirical track model. Nat. Hazards. 2016; 82(2), 1009-1029.

Liu, Q., Babanin, A., Fan, Y., Zieger, S., Guan, C., and Moon, I. J. Numerical simulations of ocean surface waves under hurricane conditions: Assessment of existing model performance. Ocean Modelling. 2017; 118, 73-93.

Liu, Y., Chen, D., Li, S., Chan, P. W., and Zhang, Q. A three-dimensional numerical simulation approach to assess typhoon hazards in China coastal regions. Nat. Hazards. 2019; 1-27.

Mo, H. M., Hong, H. P., and Fan, F. Estimating the extreme wind speed for regions in China using surface wind observations and reanalysis data. J. Wind Eng. Ind. Aerodyn.. 2015; 143, 19-33.

Nelsen R. B. An introduction to copulas. 2nd edition. NewYork,USA:Springer. 2006

Nessim, M. A., Hong, H. P., and Swail, V. R., and Henderson, C. A. Design criteria for offshore structures under combined wind and wave loading. Transactions American Society of Mechanical Engineers, J. Offshore Mech. Arct. Eng. 1995; 117, 1-1.

Ochi, M. K.. On hurricane-generated seas. In Ocean wave measurement and analysis (pp. 374-387). 1993; ASCE.

Powell, M.D., Soukup, G., Cocke, S., Gulati, S., Morisseau-Leroy, N., Hamid, S., Dorst, N., and Axe, L. State of Florida hurricane loss projection model: atmospheric science component. J. Wind Eng. Ind. Aerodyn. 2005; 93, 651–674.

Shapiro, L.J. The asymmetric boundary layer flow under a translating hurricane. J. Atmos. Sci.. 1983; 40(8), 1984-1998.

Simiu, E., and Scanlan, R. H. Wind effects on structures: fundamentals and applications to design. Wiley New York. 1996.

Tarp-Johansen, N. J. Extreme wind and wave loads site-specific combination of design rules. In Copenhagen Offshore Wind 2005. Copenhagen Offshore Wind. 2005.

Thompson, E. F., and Cardone, V. J. Practical modeling of hurricane surface wind fields. J. Waterway, Port, Coastal, Ocean Eng. 1996; 122(4), 195-205.

Turkstra, C. J., and Madsen, H. O. Load combinations in codified structural design. J. of the Struct. Division.1980; 106(12), 2527-2543.

Valamanesh, V., Myers, A. T., Arwade, S. R., Hajjar, J. F., Hines, E., and Pang, W. Wind-wave prediction equations for probabilistic offshore hurricane hazard analysis. Nat. Hazards. 2016; 83(1), 541-562.

Vickery, P. J., Wadhera, D., Galsworthy, J., Peterka, J. A., Irwin, P. A., and Griffis, L. A. Ultimate wind load design gust wind speeds in the United States for use in ASCE-7. J. Struct. Eng. 2010 136(5), 613-625. .

Vickery, P.J. and Wadhera, D. Powell, M.D., and Chen, Y. A hurricane boundary layer and wind field model for use in engineering applications. J. Appl. Meteor. 2009b; 48, 381–405.

Vickery, P.J., and Wadhera, D. Statistical models of Holland pressure profile parameter and radius to maximum winds of hurricanes from flight level pressure and H*Wind data. J. Appl. Meteorol. Climatol. 2008; 46:2497–2517.

Vickery, P.J., Skerjl, P., and Twisdale, L. Hurricane wind field model for use in hurricane simulations. J. Struct. Eng. 2000; 126(10), 1203-1221.

Vickery, P.J., Wadhera, D. Twisdale, L.A., and Lavelle, F. M. U.S. hurricane wind speed risk and uncertainty. J. Struct. Eng. 2009a 135(3), 301-320.

Xiao YF, Duan ZD, Xiao YQ, Ou JP, Chang L, Li QS. Typhoon wind hazard analysis for southeast China coastal regions. Struct Saf 2011; 33(4–5):286–295.

Ying M, Zhang W, Yu H, Lu X, Feng J, Fan Y, Zhu Y, Chen D. An overview of the China Meteorological Administration tropical cyclone database. J Atmos Oceanic Technol 2014; 31:287–301.

Young, I. A review of parametric descriptions of tropical cyclone wind-wave generation. Atmosphere. 2017; 8(10), 194.

Young, I. R. A review of the sea state generated by hurricanes. Mar. struct. 2003; 16(3), 201-218.

Young, I. R. Parametric hurricane wave prediction model. J. Waterway, Port, Coastal, Ocean Eng. 1988; 114(5), 637-652.

Young, I. R., and G. P. Burchell. Hurricane generated waves as observed by satellite. Ocean Eng. 1996; 23(8), 761-776.

Young, I.R. and Vinoth, J. An ‘extended fetch’ model for the spatial distribution of tropical cyclone wind-waves as observed by altimeter. Ocean Eng. 2013; 70, 14–24.

Zhang, J. A. Spectral characteristics of turbulence in the hurricane boundary layer over the ocean between the outer rain bands. Q. J. Royal Meteorol. Soc. 2010; 136(649), 918-926.

Chapter 4

4 Reliability and fragility assessment of offshore floating wind turbine subjected to tropical cyclone hazard

4.1 Introduction

Offshore wind energy is abundant, renewable, and clean. The installation of offshore wind power production capacity is increasing. Offshore wind turbines (WTs) are likely to experience less turbulent winds than their onshore counterparts; floating platforms could be used to support large WTs for deep-water sites. However, the offshore wind farms in some regions are subjected to tropical cyclone (TC) induced wind and wave hazards. An economic assessment of potential offshore wind farms near the coastal region of mainland China subjected to TC hazard was presented in Hong and Moller (2012) by using very simplistic TC hazard and structural fragility models. They pointed out that there is no specific design standard worldwide, at the time, for offshore wind farms subjected to TC hazard. In fact, guidelines to predict the extreme TC wind speed were given in an appendix of the recently released IEC 61400-1 (2019) and the Chinese code for the design of the wind turbine generator system under typhoon conditions (GB/T 31519 2015). Also, the influence due to a large coefficient of variation of TC wind in a TC hazard-prone area was discussed (IEC 61400-1 2019).

Tarp-Johansen and Clausen (2006) investigated the structural safety of the WTs in the Philippines that is known to experience severe TC events. Their study is focused on the selection of the design wind speed and associated safety factors for the design of the onshore WTs subjected to TC hazard. Their results indicate that the different wind load specifications for regions with and without TC hazards need to be considered to design structures to achieve the same target reliability index. This is because the reliability of designed structures subjected to the wind loading is sensitive to the coefficient of variation (COV) of extreme winds that differs for regions with and without TC hazard (Tarp-Johansen and Clausen 2006; IEC 61400-1 2019). The COV for the TC annual

maximum wind speed for the coastal region that is greater than that for the synoptic wind has been incorporated in the design code making (Vickery et al. 2010). Rose et al. (2012) indicated that the buckling of the turbine tower subjected to TC hazard was observed. They estimated the percentage of turbines that would buckle by TC winds in offshore wind farms at four representative sites in the Atlantic and Gulf Coastal waters of the U.S. It was suggested that in the most vulnerable area, about half the turbines in a wind farm are likely to be destroyed in a 20-year period. Jha et al. (2010) focused on the comparison of implied reliability by using two different design standards and on the estimation of reliability of monopile-foundation offshore WTs subjected to operational and extreme loads. It was concluded that the reliability of designed offshore WTs for different sites in the U.S. varies with spatially varying TC hazards. Hallowell et al. (2018) evaluated the reliability of offshore monopole WTs subjected to TC hazard, where the offshore monopile WTs are by considering locations along the U.S. Atlantic coast. The range of the estimated failure probability for an average service life of 20 years ranges widely from about 7×10^{-10} to 3×10^{-4} for the functional yaw control system and from about 2×10^{-7} to 2×10^{-3} for a non-functional yaw control system. They indicated that the use of very sophisticated models based on the physical laws governing the atmosphere and ocean to assess TC wind and wave hazards, such as ADCIRC/SWAN or MIKE 21 (Dietrich et al. 2012; DHI 2017), could be difficult considering the extend of simulation cycles. Consequently, for their TC wind hazard assessment, they adopted a gradient wind field model (Georgiou 1985). This is very efficient, although the weakness of using the gradient wind field as a proxy to the TC wind field is well-known. An improved TC wind hazard modeling could be carried out using the slab-resolving model with a calibrated vertical wind profile given by Vickery et al. (2009, 2010). It should be noted that none of the above-mentioned reliability studies were focused on the semi-submersible offshore WTs, and the considered locations were away from the coastal region of mainland China.

An assessed the failure probability of a semi-submersible offshore WT model was presented in Liu et al. (2018) by considering locations near the coastal region of mainland China subjected to the TC wind and wave hazard. The adopted WT model is the OC4-DeepCwind semi-submersible developed for the DeepCwind project (Robertson et al.

2014) and will be referred to as OC4 henceforth. The model was implemented as part of a test case in a very popular WT structural analysis software package, FAST (Fatigue, Aerodynamics, Structures, and Turbulence) (Jonkman and Buhl 2005). For the TC wind hazard assessment, Liu et al. (2018) carried out the three-dimensional simulations by using the Weather Research and Forecast (WRF) model (Grell et al. 2005). They used WRF by considering terrain-following layers to simulate 1510 artificial TC wind fields for a wide region. Such an assessment is very valuable, especially if the initial and boundary conditions for the TC events could be well established. Moreover, the 1510 simulated TC events amount to, at most, approximately only 50 years of TC activities since the average number of TC events affecting the considered region is about 32. The consideration of such a short simulation period of TC activities may not be sufficient for reliability evaluation. This is because the statistics of characteristics of the track such as translation speed, heading, intensity varies spatially, the parameters (e.g., central pressure difference) controlling the TC wind field are uncertainty varies along the TC track as well. Therefore, the number of historical TC tracks and wind fields affecting a given site is very small for structural reliability analysis. For the TC wave hazard modelling, Liu et al. (2018) adopted the model developed based on the long-term wind and wave data from buoy stations in the Pacific Ocean (Teng and Liu 2000). The validity of using such a wave model for TC induced significant wave height is unknown. The above noted possible drawbacks could be overcome by using the TC wind hazard based on stochastically simulated TC tracks and wind fields and by using a wave model that is developed based on TC induced wave height. Both of these issues are addressed in the present study.

The main objectives of the present study are to 1) develop and implement a database-driven simulation-based procedure to estimate fragility curve and reliability of offshore structures subjected to TC wind and wave hazard, 2) evaluate the effect of spatially varying TC wind and wave hazard on the reliability of offshore WT, and 3) analyze the sensitivity of failure probability to design wind and wave loads for the coastal region of mainland China. The overall proposed framework consists of three major components: TC wind and wave hazard modelling, structural response and fragility evaluation, and reliability assessment. The procedure that relies on the use of synthetic databases

established for the TC tracks, TC wind and wave fields, and structural responses is described in the following section. The proposed framework overcomes the mentioned weaknesses in the existing literature and takes into account the dependent TC induced wind and wave loads. Numerical analysis is carried out based on the proposed procedure for OC4, and the results are presented and discussed in the context of reliability-based design for WTs subjected to TC wind and wave loads.

4.2 Proposed analysis framework and procedures

The proposed overall procedure to estimate the reliability of offshore floating WT in the present study is based on the simulation techniques. It consists of essentially three major components. The first component is focused on the TC wind and wave hazard assessment, the second component is to evaluate the structural responses and develop fragility curves, and the third component is focused on the reliability analysis. The diagram for the components is shown in Figure 4.1. The description and discussion of each component are given in the following sections.

4.2.1 TC wind and wave hazard assessment

The component to assess the TC wind and wave hazard uses the TC track model, wind field, and significant wave height model. The overall steps to develop and use the TC wind and wave hazard models include:

1) Gathering historical TC activity, wind and wave related data such as TC track data (e.g., from China Meteorological Administration (Ying et al. 2014)), surface wind and wave records from meteorological agencies, dropesonde data, in situ buoy data, and data from satellite and aircraft-based remote sensing systems;

2) Developing the track model and wind field model:

2.1) Developing the TC track based on the autoregressive type of model (Vickery et al. 2000; Li and Hong 2016) or other stochastic models that can be found in the literature (James and Mason 2005; Emanuel et al. 2006, Hall and Jewson 2007). The model usually predicts the TC center, heading, central pressure difference Δp, and

radius to maximum wind speed R_{max}. The models described in Li and Hong (2016) for the track and wind field are adopted for the numerical analysis presented in this study. The track model is an autoregressive model with spatially varying coefficients and residuals that are developed based on historical TC tracks.

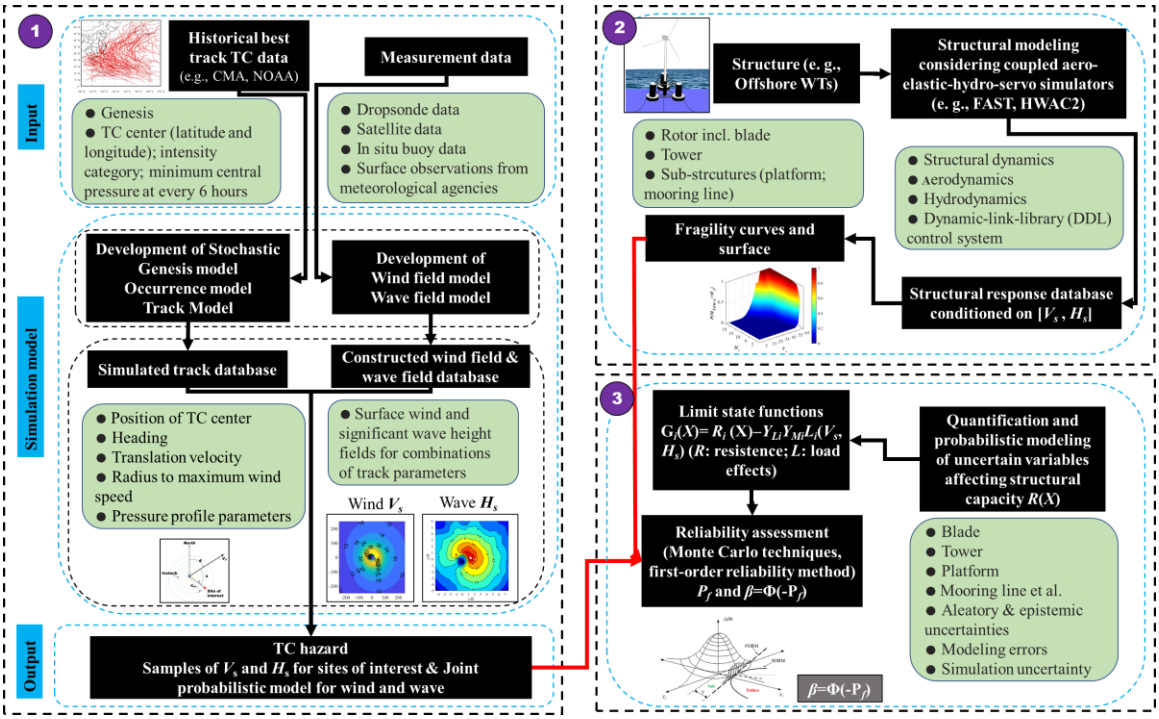

Figure 4.1. Diagram for assessing fragility and reliability of offshore WT subjected to TC wind and wave hazard.

2.2) Establishing a TC wind field model using the momentum equation (Holton 2004) or its simplified version. Popular TC wind field models include the gradient wind field model (Holland 1980, Georgiou et al. 1983), slab-resolving model (Thompson and Cardone 1996; Vickery et al. 2000, 2009, Li and Hong 2016), or linear and nonlinear height-resolving model (Meng at al. 1997; Kepert 2001, 2012; Kepert and Wang 2001, Hong et al. 2019). The slab-resolving model and the vertical wind profile model developed by Vickery and associates are well-calibrated using observation data and used to develop design wind speed in the U.S. Its use for China was also validated but using very limited data, and it was adopted to map the TC wind hazard onshore and along the coastal region in mainland China (Hong et al. 2016; Li and

Hong 2016). The use of this wind field model to assess the TC wind hazard at offshore locations near the coastal region of mainland China is considered in the present study.

3) Developing the significant wave height model. A very practical TC wave model based on the concept of an equivalent fetch was developed and validated using observational data in Young (1988, 2003, 2017). Other available models include those given and discussed in Ochi (1993), Cardone et al. (1996), and Liu et al. (2017). The model given by Young (1988, 2003, 2017) is adopted in the present study.

4) Simulating the TC tracks and their corresponding TC parameters (e.g., location, Δp, R_{max}), pressure profile parameter, translation velocity) by using the track model for a sufficiently long period (e.g., 100,000 years) and store the simulated tracks in a database that is referred to as TC-database.

5) Computing wind fields and wave fields for combinations of the TC parameters, and store the precomputed fields in a database that is referred to as the wind and wave database (WW-database).

The precomputing and storing of the simulated tracks and wind and wave fields in databases are for computational efficiency. As will be explained, they can be accessed and used directly to carry out TC wind and wave hazard assessment and reliability analysis. This facilitates the reliability analysis since it avoids the need to assume joint probability distribution models for the TC wind and wave and to carry out sophisticated distribution fitting (Sheng and Hong 2020). Note that the analysis does not include the directionality of wind and wave. Such a consideration can be valuable, but it is left out since it significantly complicates the analysis of hazard and structural response of an offshore structure.

As an illustration, consider a site of interest shown in Figure 4.2. A TC track is extracted from TC-database and shown on the map. A segment of the track that is within a circle of 250 km radius of the site of interest is identified in the figure, where the intersecting

points with the circle are denoted as Points 1 and *n*. The TC parameters for the intermediate points on the track from Point 1 to Point *n* with a time step of one hour (other time steps can also be used) will be calculated. For the TC parameters corresponding to each listed point, the wind and wave fields are extracted from WW-database, and the hourly surface mean wind speed, V_s (m/s), and the significant wave height, H_s (m), at the site are calculated. The time histories of the calculated V_s and H_s are also shown in the same figure. The results indicate that the maximum wind speed may occur when the TC center is close but slightly ahead of the location of the interest, and the maximum significant wave height and maximum wind speed may not occur simultaneously. The extracted wind field and wave field corresponding to the occurrence of their maximum values for the site are also presented in Figure 4.2. In these cases, the crescents of the wind field are located at the right side of the translation direction, and the contours of the wave field are more irregular than those of the wind field.

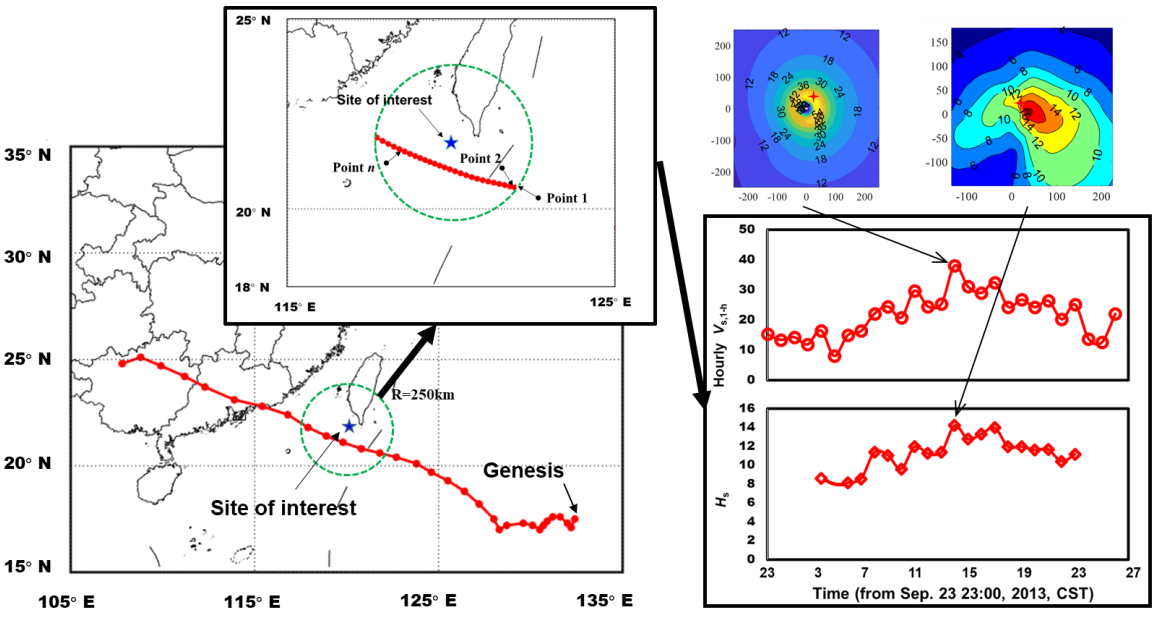

Figure 4.2. The time history of TC wind and wave affecting a site of interest for a considered track.

4.2.2 Probabilistic responses of offshore WT

The second component shown in Figure 4.1 describes the structural analysis and development of the fragility curves. The structural analysis of an offshore WT is complicated because of the aerodynamics and structural interaction and the hydrodynamic structural interaction. There are several well-accepted WT structural analysis software packages, including FAST (Jonkman and Buhl 2005), GH Bladed (Bossanyi 2003), and HAWC2 (Larsen and Hansen 2007). Each software includes several modules, such as structural dynamics, aerodynamics, hydrodynamics and mooring modelling, and WT operation control modules.

FAST that is developed by the National Renewable Energy Laboratory (NREL) is a very popular WT analysis tool. The modules in FAST are described in Jonkman and Buhl (2005). For a given value of the mean wind speed, the wind (field) time histories acted on a WT are modelled and simulated by considering the wind profile, wind spectrum, and coherency function. The wind field is used to determine the wind loads for the rotor using the blade element momentum theory or generalized dynamic wake model. The wave loads acted on the floating system are calculated based on the trip theory derived from Morison's equation or potential flow theory. By setting the turbine configuration, structural parameters, and the number of the degree of freedom, and by assigning control strategies for power generation or parked condition, FAST provides the time history of the structural responses.

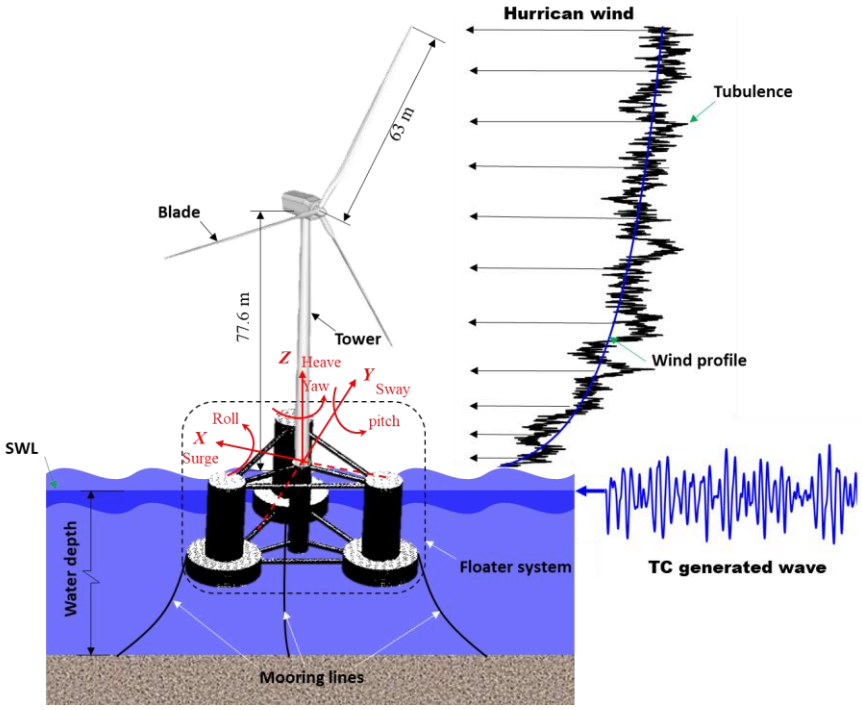

Figure 4.3. Schematic illustration of OC4 subjected to TC wind and wave.

The OC4 mentioned in the introduction is included in the FAST test archive. The model that is designed for a water depth of 200 m is illustrated in Figure 4.3. The OC4 that is implemented in FAST is used for the numerical analysis in the following. However, it is unclear as to which wind turbine classes it was designed for, considering that the wind turbine class I, II, and III are defined in IEC 61400-1 (2019) with a reference mean wind speed (i.e., 10-min at hub height) of 50, 42.5, and 37.5 m/s, respectively.

It should be noted that given the values of V_s and H_s obtained from the TC wind and wave hazard assessment, the stochastic time-varying wind speed and wave height are characterized by their power spectral density (PSD) functions. Similar to Liu et al. (2018) and Hallowell et al. (2018), the Kaimal spectrum for fluctuating wind speed and JONSWAP spectrum for wave elevation generations, which are recommended in IEC 61400-3-1 (2019) and implemented in FAST, are used in the present study. Also, the exponential coherence model, power law wind profile with an exponent of 0.11, and turbulence intensity of 0.14 for site Class B that are recommended in IEC 61400-1 (2019) and implemented in FAST are adopted for the numerical analysis to be carried out.

Besides the uncertainties in the time histories of the wind speed and significant wave height, the wind profile, turbulence intensity, coefficients affecting the aerodynamic and hydrodynamic forces are also uncertain. Let $\boldsymbol{X}_L$ denote the random variables describing these uncertainties that are associated with load effects. Moreover, the material properties and geometric variables of the structural members of the system, $\boldsymbol{X}_{\mathrm{M}}$, are also uncertain. These uncertainties can be taken into account by repeatedly running the numerical model in FAST using the sampled values of $\boldsymbol{X}_{\mathrm{L}}$ and $\boldsymbol{X}_{\mathrm{M}}$ for each set of time histories of wind and wave loading. This can drastically increase the required computational effort.

Since the uncertainty in the responses is dominated by the uncertainty in the stochastic wind speed and wave height, an alternative is to assess the probabilistic responses based on the mean of $\boldsymbol{X} = [\boldsymbol{X}_{\mathrm{L}}, \boldsymbol{X}_{\mathrm{M}}]$ and to incorporate the uncertainty in $\boldsymbol{X}$ into the structural responses, approximately, through the application of a series of modelling correction factors or errors. This simplified approach could be adequate (e.g., Tarp-Johansen et al. 2002; Sørensen and Tarp-Johansen 2005), especially as the full-scale measurements of the spatially varying loading and the corresponding responses are not available to verify and calibrate the numerical model.

Based on the above consideration, time histories of the bending moment at the base of the tower, $M_{Tow\text{-}L}(t,\boldsymbol{X})$, flapwise bending moment at the root of the blade, $M_{flap\text{-}L}(t,\boldsymbol{X})$, tension in mooring line $T_{M\text{-}L}(t,\boldsymbol{X})$, and the absolute values of the orientation-independent overturning moment, $M_{OM\text{-}L}(t,\boldsymbol{X})$, for the system can be approximated by ,

$$\begin{aligned}&[M_{Tow-L}(t,\boldsymbol{X}), M_{flap-L}(t,\boldsymbol{X}), T_{M-L}(t,\boldsymbol{X}), M_{OM-L}(t,\boldsymbol{X})]\\ &=[Y_{L1}Y_{M1}M_{Tow-L}(t,\boldsymbol{\mu}_{\boldsymbol{X}}), Y_{L2}Y_{M2}M_{flap-L}(t,\boldsymbol{\mu}_{\boldsymbol{X}}), Y_{L3}Y_{M3}T_{M-L}(t,\boldsymbol{\mu}_{\boldsymbol{X}}), Y_{L4}Y_{M4}M_{OM-L}(t,\boldsymbol{\mu}_{\boldsymbol{X}})]\end{aligned} \tag{4.1}$$

where $[M_{Tow-L}(t,\boldsymbol{\mu}_{\boldsymbol{X}}), M_{flap-L}(t,\boldsymbol{\mu}_{\boldsymbol{X}}), T_{M-L}(t,\boldsymbol{\mu}_{\boldsymbol{X}}), M_{OM-L}(t,\boldsymbol{\mu}_{\boldsymbol{X}})]$ denote the load effects estimated by using the mean of $\boldsymbol{X}$, $\boldsymbol{\mu}$x; and Y_{Li}, i = 1,…,4, denote the modelling errors associated with the loading and Y_{Mi}, i = 1,…,4, represent the modelling errors associated with material properties and geometric variable. Possible correlation among these random variables is neglected.

To assess the uncertainty in the peak values of $[M_{Tow-L}(t,\boldsymbol{\mu}_{\boldsymbol{X}}), M_{flap-L}(t,\boldsymbol{\mu}_{\boldsymbol{X}}), T_{M-L}(t,\boldsymbol{\mu}_{\boldsymbol{X}}), M_{OM-L}(t,\boldsymbol{\mu}_{\boldsymbol{X}})]$ conditioned on the values of V_s and H_s, denoted as $[M_{Tow-L}(\boldsymbol{\mu}_{\boldsymbol{X}}), M_{flap-L}(\boldsymbol{\mu}_{\boldsymbol{X}}), T_{M-L}(\boldsymbol{\mu}_{\boldsymbol{X}}), M_{OM}(\boldsymbol{\mu}_{\boldsymbol{X}})]$, one can repeatedly run FAST for the same values of V_s and H_s. Samples of $[M_{Tow-L}(\boldsymbol{\mu}_{\boldsymbol{X}}), M_{flap-L}(\boldsymbol{\mu}_{\boldsymbol{X}}), T_{M-L}(\boldsymbol{\mu}_{\boldsymbol{X}}), M_{OM-L}(\boldsymbol{\mu}_{\boldsymbol{X}})]$ can be used to provide their probabilistic characteristics and to assess and develop their joint probability distribution conditioned on V_s and H_s. The samples can also be stored in a structural response database (SR-database) for assessing structural reliability, as will be explained shortly. The probabilistic characterizations facilitate the evaluation and assignment of the probabilistic characterizations of the peak responses of $[M_{Tow-L}(t,\boldsymbol{X}), M_{flap-L}(t,\boldsymbol{X}), T_{M-L}(t,\boldsymbol{X}), M_{OM-L}(t,\boldsymbol{X})]$,

$$\begin{aligned}&[M_{Tow-L}(\boldsymbol{X}), M_{flap-L}(\boldsymbol{X}), T_{M-L}(\boldsymbol{X}), M_{OM-L}(\boldsymbol{X})]\\&=[Y_{L1}Y_{M1}M_{Tow-L}(\boldsymbol{\mu}_{\boldsymbol{X}}), Y_{L2}Y_{M2}M_{flap-L}(\boldsymbol{\mu}_{\boldsymbol{X}}), Y_{L3}Y_{M3}T_{M-L}(\boldsymbol{\mu}_{\boldsymbol{X}}), Y_{L4}Y_{M4}M_{OM-L}(\boldsymbol{\mu}_{\boldsymbol{X}})]\end{aligned} \tag{4.2}$$

By carrying out this analysis for given combinations of V_s and H_s values, the probability distributions or samples of $[M_{Tow-L}(\boldsymbol{X}), M_{flap-L}(\boldsymbol{X}), T_{M-L}(\boldsymbol{X}), M_{OM-L}(\boldsymbol{X})]$ are then used to establish the fragility surfaces. This will be discussed further shortly.

4.2.3 Reliability evaluation for offshore WT subjected to TC wind and wave hazard

Given the limit state functions, established joint probability distribution (or fragility surfaces) of load effects, the probability distribution of the environmental parameters (i.e., V_s and H_s) and probabilistic resistance models, the failure probability can be estimated by applying efficient structural reliability analysis methods or simulation techniques (Madsen et al. 2006; Melchers and Beck 2018). The use of reliability methods such as the first-order reliability method or second-order reliability method requires the knowledge of the joint probability distribution of the random variables involved in the limit state functions. Finding a preferred joint probabilistic model for a set of random variables, in general, is no trivial task, although the use of copula (Nelsen 2006)

simplifies the assignment of the joint probability distribution. For example, V_s and H_s could be correlated, and the preferred joint probability distribution model is unknown. The problem is further complicated by noting that the maximum load effect for a limit state function of interest may not necessarily be associated with the largest V_s and its companion H_s or with the largest H_s and its companion V_s for a given TC track affecting the considered offshore WT. However, the use of simulation techniques to estimate the failure probability of an offshore WT is straightforward, and it implicitly considers the correlation between V_s and H_s, especially given that the TC-database and WW-database for a (very long) period of T_T years are already precomputed.

More specifically, for simplicity and without loss generality, consider that there are four limit state functions, g_i, $i = 1, \ldots, 4$, to be considered. These limit state functions depend on the peak load effects listed in Eq. (4.2). The i-th failure mode occurs if g_i is less than zero. Failure of the offshore WT system occurs if the minimum of g_i, $i = 1, \ldots, 4$, is less than zero. Let $P_{fi} = \text{Prob}(g_i \le 0)$ denote the failure probability for the i-th failure mode, and let $P_{fsys} = \text{Prob}\big((g_1 \le 0) \cup (g_2 \le 0) \cup (g_3 \le 0) \cup (g_4 \le 0)\big)$ denote the failure probability of the system.

A flowchart describing the procedure to estimate P_{fsys} and P_{fi}, $i = 1,\ldots, 4$, is given in Figure 4.4 and is explained below:

1) Divide the simulated TC events and tracks in 20 years of non-overlapping periods, resulting in a total of N_m periods. Let $P_{fsys} = 0$, $P_{fi} = 0$, and $m = 1$.

2) Simulate values of the random variables listed in Table 4.3 that are needed to evaluate Eq. (4.2).

3) Find the total number of such tracks, N_m, from TC-database that passes within 250 km of the site of the offshore WT for the m-th period. Let $j = 1$.

4) Find the segment of the track that is within 250 km of the site for the j-th track. Define the sequence of points on the track within the identified segment with a time

increment of one hour between the two consecutive points. Let N_j denote the total number of such points (e.g., see Figure 4.2). Let $k = 1$.

4.1) Identify the TC parameters for the k-th point on the track;

4.2) Extract the wind and wave fields from WW-database and calculate V_s and H_s for the site based on the identified TC parameters;

4.3) For the identified V_s and H_s, sample $[M_{Tow-L}(\boldsymbol{\mu}_{\boldsymbol{X}}), M_{flap-L}(\boldsymbol{\mu}_{\boldsymbol{X}}), T_{M-L}(\boldsymbol{\mu}_{\boldsymbol{X}}), M_{OM}(\boldsymbol{\mu}_{\boldsymbol{X}})]$ according to their probabilistic models or extract them from SR-database;

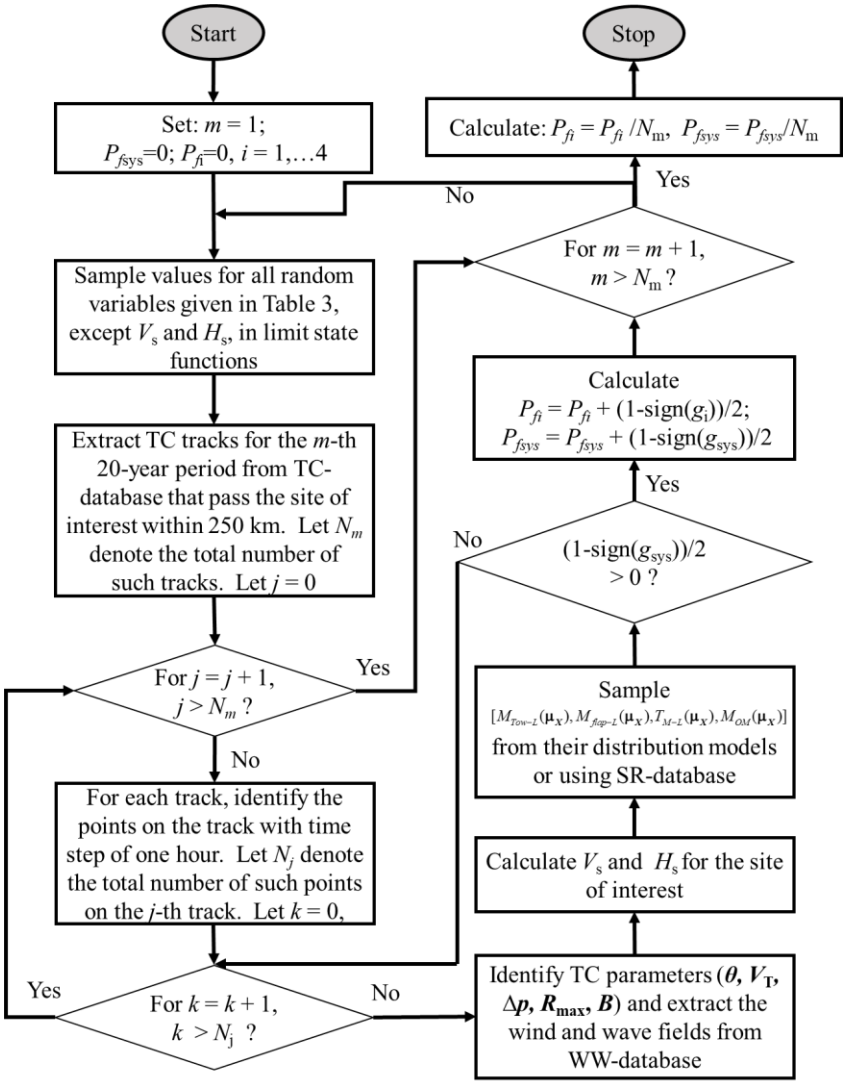

Figure 4.4. Flowchart for the reliability analysis.

4.4) Evaluate g_{sys} = min(sign(g_i)). If (1-sign(g_{sys}))/2 is greater than zero, calculate P_{fi} = P_{fi} + (1-sign(g_i))/2 for i = 1,…, 4, and P_{fsys} = P_{fsys} + (1-sign(g_{sys}))/2; set $m = m + 1$ and go to step 4.7). Otherwise set $k = k + 1$.

4.5) If k is less than or equal to N_j, go to Step 4.1). Otherwise set $j = j$+1;

4.6) If j is less than or equal to N_m, go to Step 4);

4.7) Set $m = m + 1$. if m is less than or equal to N_m, go to Step 2);

5) Calculate P_{fi} = P_{fi} /N_m. and P_{fsys} = P_{fsys} /N_m.

Note that the use of blocks of 20 years is based on the consideration that random variables needed to evaluate the capacity as well as $\boldsymbol{X}_L$ and $\boldsymbol{X}_M$, hence Y_{Li} and Y_{Mi}, are random but remain the same for a service period of 20 years.

4.3 Numerical analysis for a submersible offshore WT

4.3.1 OC4 DeepCwind semi-submersible WT

As illustrated in Figure 4.3, the tower for OC4 is supported by the platform at a location 10 m above the still-water level (SWL). OC4 has the same turbine (including the rotor-nacelle-assemble (RNA)) as the offshore Monopile-based NREL 5-MW WT (Jonkman et al. 2009) with 3 identical blades. Some of the essential properties of NERL 5-MW baseline WT are presented in Table 4.1. For additional detailed information, the reader is referred to Jonkman et al. (2009) and Robertson et al. (2014).

Table 4.1. Overall properties of the semi-submersible WT with NERL 5-MW (Jonkman et al. 2009; Robertson et al. 2014.)

Type and Configuration	Rated power (kW)	5,000
	Wind turbine type	Upwind horizontal-axis wind turbine
	Control strategy	Variable-speed pitch control
Blade	Cut-in and -out speed, rated (m/s)	3 and 25, 11.4
	Rotor diameter (m)	126
	Length (m)	61.5
	Root section stiffness ($N \cdot m^2$)	1.811×10^6
	Structural damping	0.48%
Tower	Hub height (m)	90
	Base section diameter (thickness) (m)	6.5 (0.027)
	Structural damping	1%
Platform	Center of buoyancy under SWL (m)	13.15 m
	Displaced water (m^3)	13917
	Structural damping	1%
Mooring line	Line diameter (mm)	76.6
	Unstretched length (m)	835.5
	Structural damping	2%

Table 4.2. Model comparison and validation through free-decay analysis.

DOF of Platform	Tuned FAST model (Coulling et al. 2013)	1/50 scaled tank Experiment (Coulling et al. 2013)	Fully-coupled CFD (Tran and Kim 2016)	Present study
Surge (s)	107	107	108.1	113.1
Sway (s)	113	112	114.5	114.2
Heave (s)	17.3	17.5	17.8	17.6
Roll (s)	26.7	26.9	25.3	25.6
Pitch (s)	26.8	26.8	25.2	25.7
Yaw (s)	82.7	82.3	83.3	80.2

By using the adopted parameters, a free-decay analysis is carried out, and the obtained vibration frequencies are shown in Table 4.2. These values are comparable with those given by Coulling et al. (2013) and Tran and Kim (2016). The observed slight differences are attributed to possible differences in the versions of FAST and the data used in different studies.

4.3.2 Estimation of peak load effects and fragility surface

The load effects $[M_{Tow-L}(\boldsymbol{\mu_X}), M_{flap-L}(\boldsymbol{\mu_X}), T_{M-L}(\boldsymbol{\mu_X}), M_{OM-L}(\boldsymbol{\mu_X})]$ for given values of V_s and H_s are obtained by carrying out the dynamic time history analysis using FAST for OC4 implemented in its CertTest archive. The calculation of load effects follows the practice suggested in FAST user's manual and takes into account that the WT is in the normal operation condition if the mean wind speed at hub height is less than the cut-out wind speed of 25 m/s, and it is in the parked condition if the cut-out wind speed is exceeded (Jonkman and Buhl 2005). For the peak wave period, T_p, needed for JONSWAP spectrum, the equation recommended in Young (2003, 2017) that can be written as,

$$T_p = \frac{U_{10}}{g^{0.394} \times \left((H_s / 4)^2 / 6.365 \times 10^{-6} / {U_{10}}^4 \right)^{-1/3.3}} \tag{4.3}$$

is used, where U_{10} (m/s) represents 10-minute mean wind speed at 10 m height, and g is the gravitational acceleration.

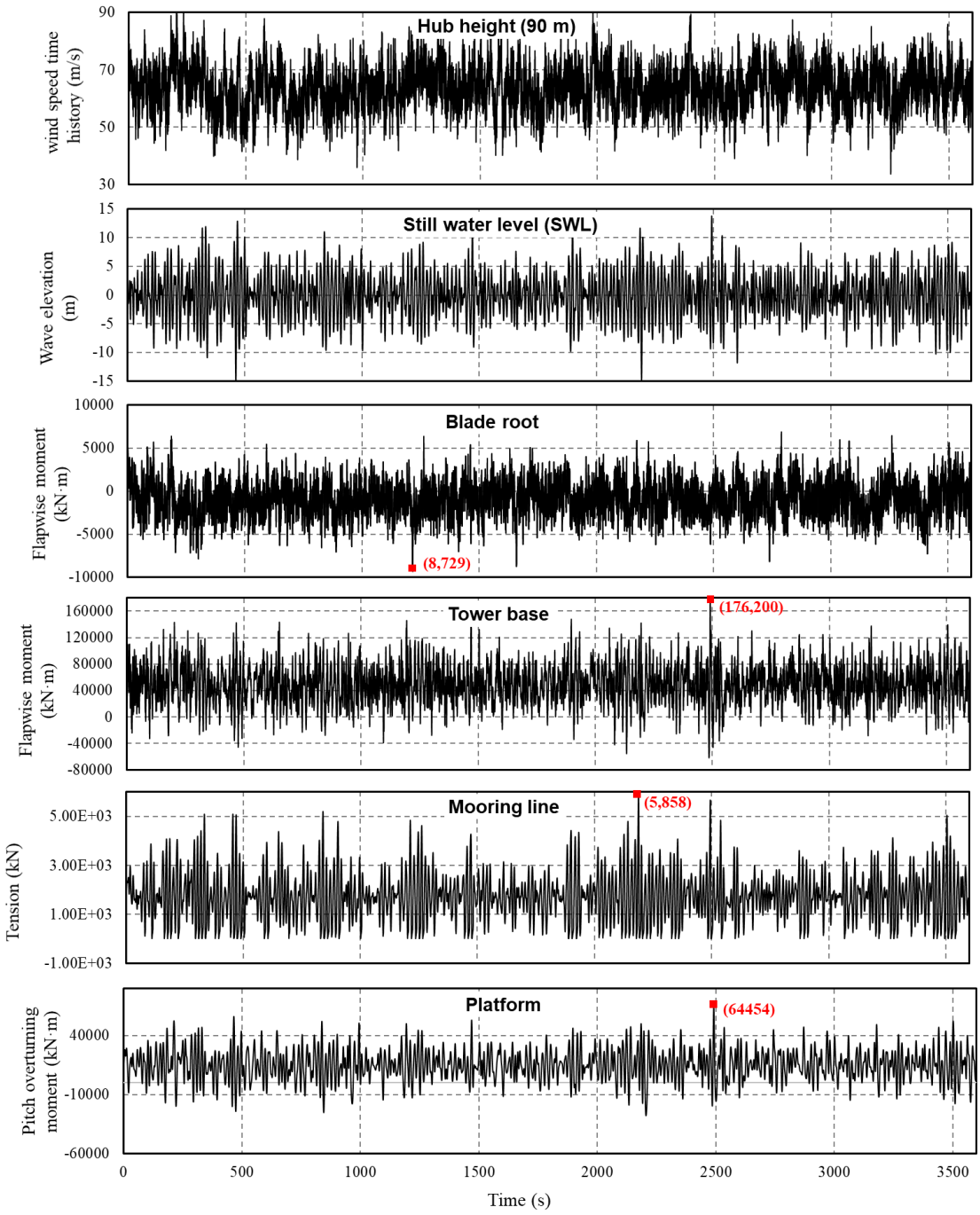

Figure 4.5. A sample of the time histories of wind speed, wave height, and absolute maximum of the load effects on OC4 obtained by using FAST for [V_s, H_s] = [49 m/s, 16 m] and T_p = 15.49 s: a) Along-direction wind speed at hub height; b) Wave elevation at the still water level; c) Blade root flapwise moment; d) Tower base flapwise moment; e) Mooring line tension force and f) Platform pitch overturning moment. These times histories correspond to the parked condition.

Given the values of V_s and H_s, the time history analysis is carried out for one hour with a time step of 0.0125 s, and a burn-in period of 30 s. An example of the simulated wind speed and wave height, as well as the calculated time histories of $[M_{Tow-L}(t,\boldsymbol{\mu}_{\boldsymbol{X}}), M_{flap-L}(t,\boldsymbol{\mu}_{\boldsymbol{X}}), T_{M-L}(t,\boldsymbol{\mu}_{\boldsymbol{X}}), M_{OM-L}(t,\boldsymbol{\mu}_{\boldsymbol{X}})]$ is illustrated in Figure 4.5. The considered environmental condition shown in Figure 4.5 corresponds to the parked condition. The peak responses are also identified in the figure. It can be observed that the responses are time-varying, and the peak load effects for different responses of interest occur at different times.

The time history analysis is repeated for the same set of values of V_s and H_s, and peak values for each run are identified and extracted, and stored in SR-database. In particular, for a simulation cycle of 100, the obtained samples are presented in Figures 4.6a to 4.6d for [V_s, H_s] = [49 m/s, 16 m]. As can be observed from the figure that the maximum load effects vary, reflecting the stochastic characteristics of wind and wave processes. By using the samples shown in Figures 4.6a to 4.6d, the empirical marginal probability distributions of the peak load effects are in Figures 4.6e to 4.6h on the Gumbel probability paper. Probability distribution fitting analysis carried out by using several commonly employed distribution types, and the Akaike information criterion (AIC) indicates that the Gumbel distribution is preferred for the peak responses. More specifically, the obtained AIC values for the Gumbel distribution, generalized extreme value distribution, and the generalized Pareto distribution are, respectively, equal to (1331, 1333, 1345) for the blade root flapwise moment, (1373, 1375, 1396) for the tower base flapwise moment, (1253, 1254, 1285) for the platform pitch moment, and (1291, 1293, 1330) for the platform pitch moment.

Furthermore, the calculated correlation coefficient matrix of $[M_{Tow-L}(t,\boldsymbol{\mu}_{\boldsymbol{X}}), M_{flap-L}(t,\boldsymbol{\mu}_{\boldsymbol{X}}), T_{M-L}(t,\boldsymbol{\mu}_{\boldsymbol{X}}), M_{OM-L}(t,\boldsymbol{\mu}_{\boldsymbol{X}})]$, C_{LE}, is,

$$C_{LE} = \begin{bmatrix} 1 & 0.041 & -0.138 & -0.052 \\ & 1 & 0.283 & 0.207 \\ & & 1 & 0.329 \\ & & & 1 \end{bmatrix} \tag{4.4}$$

The matrix indicates that the correlation coefficient is less than 0.21 except for the one between the tower base moment and platform pitch moment that equals 0.283, and the one between the platform pitch moment and mooring line tension that equals 0.329. The correlation among these load effects at best is moderate.

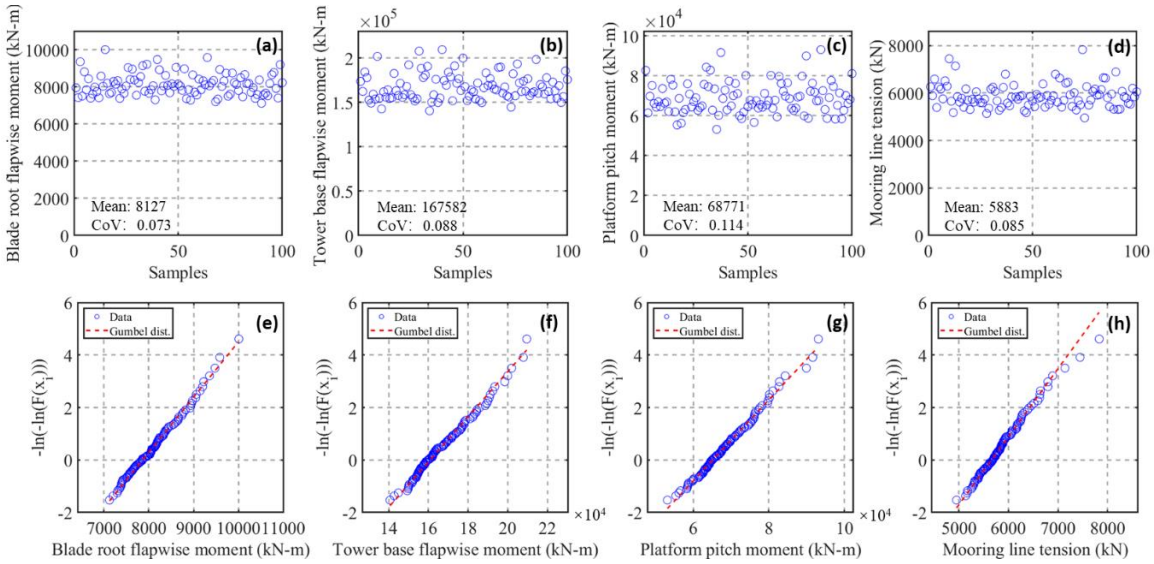

Figure 4.6. Samples of peak load effects for [V_s, H_s] = [49 m/s, 16 m]. The dash line shown in the second row of the plots represents the fitted Gumbel distribution.

By repeating such an analysis for combinations of V_s and H_s, the SR-database is established by considering V_s ranging from 5 to 65 m/s and H_s ranging from 2 to 20 m. The smoothed mean and standard deviation of the load effects $M_{Tow-L}(t,\boldsymbol{\mu}_X)$, $M_{flap-L}(t,\boldsymbol{\mu}_X)$, $T_{M-L}(t,\boldsymbol{\mu}_X)$ and $M_{OM-L}(t,\boldsymbol{\mu}_X)$ are shown in Figure 4.7. The plots shown in the figure indicate that the means of the maximum load effects vary with V_s and H_s. For V_s within the cut-in and -out wind speeds (i.e., 3 to 25 m/s, see Table 4.1), the means of the load effects peak around rated wind speed of 11.4 m/s (because of the controlled operating condition). After the cut-out wind speed, the responses increase with the increased V_s and H_s. The pattern of the standard deviations of the load effects follows approximately to those of the means, although for V_s within the cut-in and -out wind speeds, the trends of the standard deviations are less apparent.

The samples could also be used to establish the probability distribution of the peak load effects and the fragility surface. The assessment of the fragility surface can be carried out using the samples in the SR-database. For example, one can find the exceedance probability for a given value of $M_{Tow-L}(\mu_X)$ conditioned on the values of V_s and H_s. The estimated exceedance probability as a function of V_s and H_s is based on the bending moment at the base of the tower is used to form the fragility surface as depicted in Figure 4.8 for a threshold level of 181867 (kNm). It must be emphasized that the fragility curve developed is structure-dependent and should not be applied for a different design.

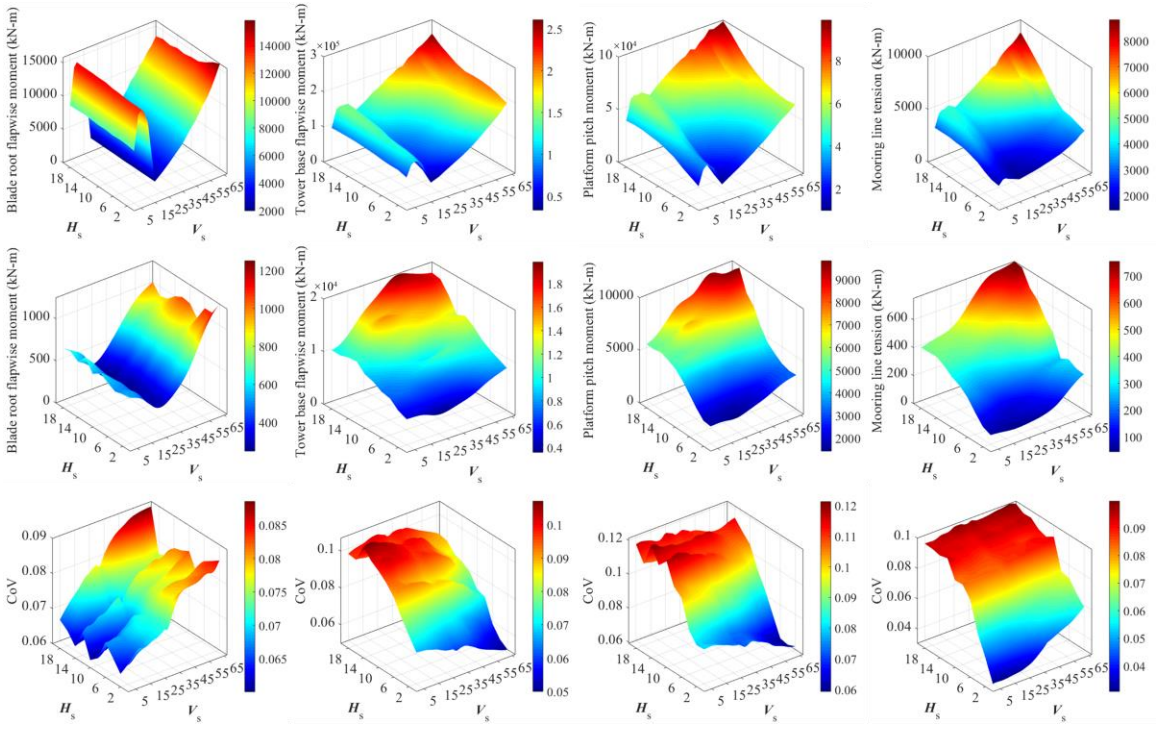

Figure 4.7. Variation of the mean, standard deviation and COV of $M_{Tow-L}(t,\mu_X)$, $M_{flap-L}(t,\mu_X)$, $T_{M-L}(t,\mu_X)$ and $M_{OM-L}(t,\mu_X)$ as functions of V_s and H_s.

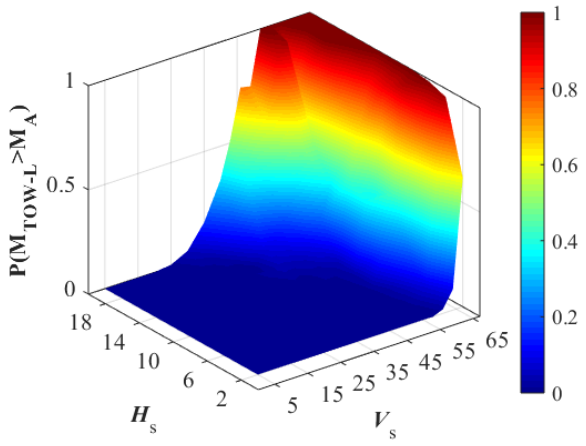

Figure 4.8. Fragility surfaces for M_A=181867 (kNm).

4.3.3 Limit state functions and considered probabilistic models

Although the electric or mechanic failure causes the failure of the WT system (Tavner et al. 2007; Tavner 2012), the four limit state functions considered in the following are for the local buckling of the tower, the blade root subjected to bending, the breaking of the mooring line, and global instability of OC4 since the present study is focused on structural performance. The subject of considering these actions to establish the limit state functions for WT is extensively discussed in several studies, including Ronold and Larsen (2000), Tarp-Johansen et al. (2002), Wayman et al. (2006), Benassai et al. (2014) and Wilkie and Galasso (2017).

Based on Tarp-Johansen et al. (2002), the limit state function for the local buckling of the tower can be written as,

$$g_1 = M_{cr} - Y_{L1} Y_{M1} M_{Tow-L}(\boldsymbol{\mu}_X) \tag{4.5}$$

where M_{cr} is the critical bending moment capacity for local buckling. The modelling errors Y_{L1} and Y_{M1} depend on the degree of sophistication of the model used to evaluate $M_{Tow-L}(\boldsymbol{\mu}_X)$. By using a relatively simple procedure to evaluate the wind load effect, Tarp-Johansen et al. (2002) suggested that the modelling error should include those arising from the evaluation of the dynamic response of the turbine from a numerical

model, exposure coefficient, lift and drag coefficients (or shape factor), model-scale test to full-scale response, and statistical variability in assessing wind speed. It is considered that some of these could be neglected if a sophisticated numerical model and analysis package such as FAST is employed. In such a case, Y_{L1} should include the effect of uncertainty in exposure and shape factor, and Y_{M1} describes the accuracy in predicting the stress at a location in the structural system. Based on the probabilistic models given in Tarp-Johansen et al. (2002), it is assumed that Y_{L1} can be models as a lognormal variate with the mean of unity and coefficient of variation of 0.22 and that Y_{M1} can be modelled as a lognormal variate with the mean of unity and coefficient of variation of 0.03. It must be emphasized that this and subsequently limit state functions are functions of V_s and H_s. However, for the simplicity of the notation, they are not shown.

According to Tarp-Johansen et al. (2002), the critical bending moment capacity can be evaluated using,

$$M_{cr} = \left(1 - 0.84 \frac{D}{t} \frac{Y_{y,ss} F_y}{Y_{E,ss} E}\right) \frac{1}{6} \left(D^3 - \left(D - 2t\right)^3\right) Y_{y,ss} X_{cr} F_y \tag{4.6}$$

where $Y_{y,ss}$ and $Y_{E,ss}$ are model uncertainties that account for scale effects resulting from the differences between test specimens and full-scale structures for yield strength F_y and the Young's Modulus E, respectively; D is the diameter of a section of the tower at the height of interest; t_{tower} is the wall thickness, and X_{cr} represents the modelling error taking into account that the use of the numerical model presented in Eq. (4.2) alone cannot predict the test results precisely. $Y_{y,ss}$, $Y_{E,ss}$ and X_{cr} are considered independent lognormally distributed with means equal to 1 and COV of 0.05, 0.02, and 0.1, respectively (Tarp-Johansen et al. 2002; Wilkie and Galasso, 2017). For easy reference, they are summarized in Table 4.3. Also, values or probabilistic models for other variables involved in all the considered limit state functions are presented in Table 4.3. Note that it is considered that the modeling errors are applicable to the structure whether the WT is in operation or in the parked condition. This is inferred from the analysis and formulation given in Tarp-Johansen et al. (2002), Tarp-Johansen and Clausen (2006), and Sørensen and Berzonskis (2017).

Table 4.3. Parameters considered for the reliability analysis (Dist., LN, N, and DET represent the lognormal, normal probability distributions, and deterministic quantity, respectively). All random variables used are assumed to be independent.

Parameter	Mean, COV	Dist.	Reference and notes
Yield strength, F_y (MPa)	240, 0.05	LN	Tarp-Johansen et al. (2002)
Scale effect for yield strength, $Y_{y,ss}$	1.0, 0.05	LN	Tarp-Johansen et al. (2002)
Scale effect for Young's Modulus, $Y_{E,ss}$	1.0, 0.02	LN	Tarp-Johansen et al. (2002)
Modelling error for the adopted numerical model, X_{cr}	1.0, 0.1	LN	Tarp-Johansen et al. (2002)
Modelling errors associated with the loading for blade and tower, Y_{L1}, Y_{L2}	1.0, 0.22	LN	Tarp-Johansen et al. (2002) (i.e., exposure & mode scale)
Modelling errors associated with material properties for blade and tower, Y_{M1}, Y_{M2}	1.0, 0.03	LN	Tarp-Johansen et al. (2002) (i.e., stress)
Young's Modulus, E (GPa)	210, 0.02	LN	Tarp-Johansen et al. (2002)
Blade tensile strength, $\sigma_{b,f}$ (MPa)	518, 0.03	N	Ronold and Larsen (2000); Mandell et al. (2016)
Radius of blade root section, $R_{b,r}$ (m)	1.77	DET	Jonkman et al. (2009)
Second moment of blade root section, $I_{b,r}$ (m^4)	0.566	DET	Jonkman et al. (2009)
Modelling error associated with the loading for platform, Y_{L3}	1.0, 0.08	N	Vazquez-Hernandez et al. (2006)
Modelling error associated with the material properties for platform, Y_{M3}	1.0, 0.10	N	Horte and Mathisen (1998)
Breaking load capacity, Q (kN)	7334, 0.05	LN	Benassai et al. (2014)
Nominal diameter of mooring lines, d (mm)	77.9	DET	Hallowell et al. (2017)
Modelling error associated with the loading for mooring line, Y_{L4}	1.0, 0.17	LN	Tarp-Johansen et al. (2002); Muskulus and Schafhirt (2015)
Modelling error associated with the material properties for mooring line, Y_{M4}	1.0, 0.03	LN	Tarp-Johansen et al. (2002)
Maximum allowable pitch rotation, ζ_a (^{o})	10°	DET	Wayman et al. 2006
Pitch rotational stiffness due to hydrostatic effect, C_h (Nm/rad)	3.776×10^8	DET	Jonkman et al. (2009)

The limit state function for the blade root subjected to bending can be written as (Ronold and Larsen 2000),

$$g_2 = I_{\boldsymbol{b,r}}\sigma_{b,f} / R_{b,r} - Y_{L2}Y_{M2}M_{flap-L}(\boldsymbol{\mu_X}) \tag{4.7}$$

where $\sigma_{b,f}$ is blade tensile strength, and $R_{b,r}$ and $I_{\boldsymbol{b,r}}$ are the radius and second moment of the area at the blade root section, respectively.

The limit state function for the break of the mooring line can be written as (Benassai et al. 2014),

$$g_3 = Q - Y_{L3}Y_{M3}T_{M-L}(\boldsymbol{\mu_X}) \tag{4.8}$$

where the breaking load capacity *Q* for the mooring cable Grade R5 with the mean and cov shown in Table 4.4. The mean of *Q* is calculated by assuming that the mean to nominal ratio equals 1.0 and the nominal value could be calculated using $0.032(44-0.08d)d^2$ (DNV OS E302 2015), and *d* is the nominal diameter of mooring lines.

For the stability of the floating WT, the limit state function by considering the overturning moment can be formulated through the restoring stiffness and allowable displacement represented as (Wayman et al. 2006),

$$g_4 = C_{st}\zeta_a - Y_{L4}Y_{M4}M_{OM-L}(\boldsymbol{\mu_X}) \tag{4.9}$$

where C_{st} is the system pitch rotational stiffness and ζ_a is the maximum allowable pitch rotation in degrees, Y_{L4} and Y_{M4} are modelling errors. C_{st} equals C_h + C_m, where C_h and C_{m} are the contributions due to the hydrostatic effect and pitch mooring line, respectively. C_{m} is negligible since its contribution to the total stiffness is trivial (Wayman et al. 2006).

Based on the established limit state functions and the analysis procedure described in the previous section, failure probabilities can be estimated.

4.3.4 Site-specific conditions and estimated failure probability

For the analysis, it is considered that OC4 is to be placed at one of the four locations shown in Figure 4.9a, where the water depth is about 200 m (https://www.gebco.net/data_and_products/gridded_bathymetry_data/). By applying the TC hazard analysis procedure described on the left panel of Figure 4.1 and described in Section 4.2.1, the obtained empirical probability distribution of the annual maximum wind speed and significant wave height are shown in Figures 4.9b and 4.9c. For the analysis, a simulation run of 100,000 years is carried out.

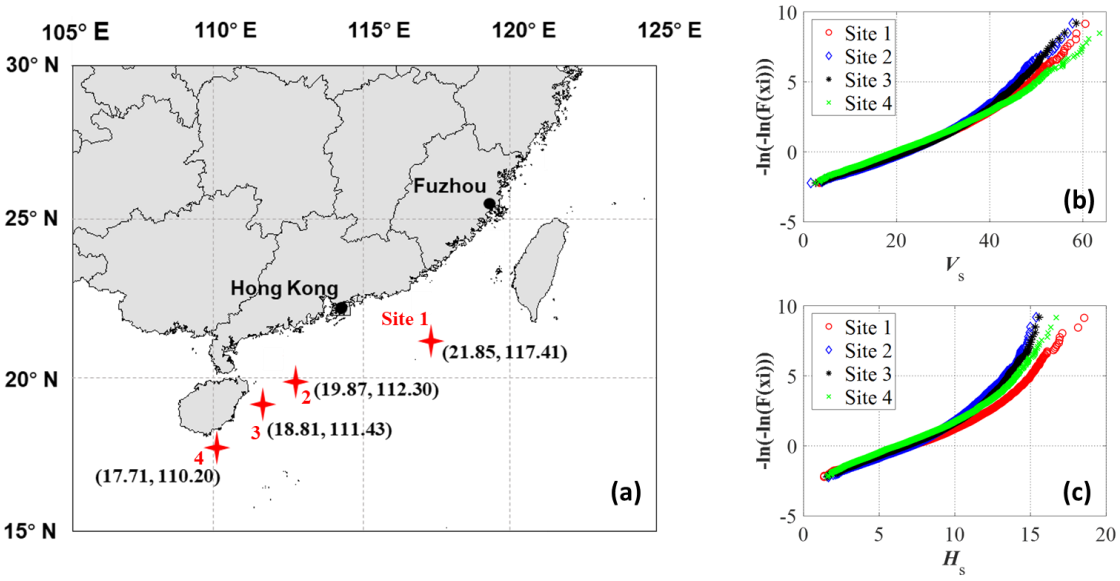

Figure 4.9. Empirical probability distribution of the annual maximum wind speed and significant wave height for four considered offshore sites: a) Identification of the sites, b) Empirical probability distribution of the annual maximum wind speed, and c) Empirical probability distribution of significant wave height.

The estimated 50-year return period values of annual maximum wind speed and significant wave height, denoted as V_{s50} and H_{s50}, from the plots shown in Figures 4.9b and 4.9c are shown in Table 4.4 for the four sites considered. The mean and COV values

shown in Table 4.4 are for the annual maximum variables. The statistics agree with those given in Sheng and Hong (2020). The COV of the annual maximum TC wind speed is also consistent with those considered by Tarp-Johansen and Clausen (2006) for WT situated in the Philippines, but greater than that for synoptic winds which is about 0.135 (Hong et al. 2014). The estimated V_{s50} for the considered sites is greater than the 10-min mean wind speed at 10 height, V_{10}, that equals 39.3 m/s (corresponding to the 10-min mean wind speed at hub height V_{hub} of 50 m/s) for the design of Class I site specified in IEC 61400-1 (2019). The value of 39.3 m/s is also the design wind speed for OC4, which is inferred from Jonkman (2007). The estimated values of V_{s50} for the considered sites are spatially varying but very close to V_{10} = 43.2 m/s (i.e., V_{hub} = 55 m/s), which is recommended for the design of Class TI system in GB/T 31519 (2015). Also, the significant wave height is approximately equal to or greater than 12.9 m that is inferred design value from Jonkman (2007) and DNVGL-ST-0119 (2018).

Based on the above considerations, reliability analysis is carried out in the following. Before estimating the reliability, it is emphasized that OC4 was not designed for the considered sites or according to IEC61400-1 (2019) or GB/T 31519 (2015). It is used to illustrate the proposed data-driven simulation procedure for reliability analysis of an offshore structure subjected to the wind and wave load time histories caused by the passage of typhoons. By carrying out the reliability analysis following the flowchart presented in Figure 4.4, the failure probability is calculated by considering that OC4 is located at each of the locations depicted in Figure 4.9a, where GB/T 31519 (2015) should be considered. The obtained annual failure probability, P_{fsys1}, and the failure probability for a service period of 20 years, P_{fsys20}, are presented in Table 4.5 and referred to as Base Case. The results shown in the table indicate that the failure probability varies from site to site, but the difference is less than about 20%. In all cases, P_{fsys1} ranges from about 3.3% to 3.9%, and P_{fsys20} ranges from 51% to 58%. These estimated failure probabilities are consistent with but can be slightly greater than those inferred from the study reported by Rose et al. (2012) but for NREL 5-MW monopile turbine that is located in the offshore regions in the U.S. In fact, Rose et al. (2012) indicated that about 50% of WTs are likely to be destroyed in a 20-year period if the wind farm is located in the most vulnerable coastal region in the U.S. and the monopile turbine rather than a submersible

system is considered. The estimated P_{fsys1} is within those inferred from Liu et al. (2018), which is for the same OC4. The inference is made by considering that in their study: a) 200 typhoons are extracted from 1510 simulated typhoons for the entire Northwestern Pacific Basin, b) the average annual typhoon activity is about 30, and they estimated failure probability ranges from 0.2 to 0.6 resulting in P_{fsys1} about 2.8% to 8.7% per year. However, the variability of P_{fsys1} shown in Table 4.5 is smaller. Part of the smaller variability is likely attributed to the fact that a large number of samples is considered in the present study (i.e., 100,000 years of simulation cycle) is considered.

If each individual limit state function is considered, the obtained annual failure probability is summarized in Table 4.6. As can be observed from the table, the dominant failure mode is contributed by the tower buckling, followed by the platform overturning of the structural system. The failure probability by considering the limit state functions for the blades and for the mooring lines is negligible (i.e., practically equal to zero).

Table 4.4. The 50-year return period value of wind speed V_{s50} and of significant wave height H_{s50}.

Site	Mean of V_s (m/s)	COV of V_s	V_{s50} (m/s)	Mean of H_s (m)	COV of H_s	H_{s50} (m)
1	23.23	0.45	44.65	7.61	0.44	13.93
2	24.23	0.36	41.85	7.51	0.34	12.23
3	24.54	0.37	42.35	7.47	0.36	12.66
4	22.66	0.45	45.39	6.94	0.43	13.07

Table 4.5. Estimated failure probability by considering the described four cases (The failure probability for one year and for 20 years (i.e., P_{fsys1}, and P_{fsys20}) are calculated based on all four limit state functions shown in Eqs. (4.5) to (4.9)).

Case	Base Case		Case 1		Case 2		Case 3		Case 4	
Site	P_{fsys1}	P_{fsys20}	P_{fsys1}	P_{fsys20}	P_{fsys1}	P_{fsys20}	P_{fsys1}	P_{fsys20}	P_{fsys1}	P_{fsys20}
1	0.037	0.570	0.023	0.410	0.029	0.468	0.030	0.484	0.031	0.496
2	0.033	0.506	0.025	0.422	0.030	0.484	0.034	0.516	0.034	0.512
3	0.038	0.558	0.027	0.444	0.032	0.508	0.038	0.558	0.038	0.559
4	0.039	0.572	0.024	0.422	0.029	0.478	0.031	0.504	0.030	0.484

Table 4.6. Annual failure probability for the considered limit state functions (Prob(g_1<0) and Prob(g_4<0) (i.e., failure of tower and failure of platform). Failure of blades and mooring lines is not shown since they are practically equal to zero

Case	Annual failure probability	Site			
		1	2	3	4
Base Case	Prob(g_1< 0), Eq. (4.5)	0.0258	0.0299	0.0322	0.0302
	Prob(g_4< 0), Eq. (4.9)	0.0120	0.0037	0.0061	0.0092
Case 1	Prob(g_1< 0), Eq. (4.5)	0.0226	0.0252	0.0265	0.0236
	Prob(g_4< 0), Eq. (4.9)	0.0007	0.0001	0.0005	0.0008
Case 2	Prob(g_1< 0), Eq. (4.5)	0.0260	0.0293	0.0304	0.0272
	Prob(g_4< 0), Eq. (4.9)	0.0031	0.0011	0.0013	0.0014
Case 3	Prob(g_1< 0), Eq. (4.5)	0.0246	0.0303	0.0322	0.0274
	Prob(g_4< 0), Eq. (4.9)	0.0056	0.0037	0.0062	0.0037
Case 4	Prob(g_1< 0), Eq. (4.5)	0.0264	0.0300	0.0323	0.0275
	Prob(g_4< 0), Eq. (4.9)	0.0050	0.0037	0.0061	0.0024

4.3.5 Sensitivity analysis

First, it must be emphasized that OC4 is not designed for the considered sites following IEC61400-1 (2019) or GB/T 31519 (2015). Therefore, the results presented in Tables 4.5 and 6 may not represent the reliability of wind turbines designed according to codes for the considered sites, rather the numerical examples are used to illustrate the proposed data-driven reliability analysis procedure. It would be ideal to carry out a series of designs of submersible WT system, to evaluate its failure probability subjected to site-specific TC hazards and to find the optimum tolerable failure probability by minimizing the expected cost or by using advanced decision theory following a similar approach that was used in Goda and Hong (2006) to identify optimal reliability index for seismic design. However, the design of a submersible WT system is not a trivial task and is beyond the scope of the present study.

Second, there is large uncertainty in the variables representing the transformation from environmental parameter to load effects (i.e., Y_{L1}, Y_{L2}, and Y_{L4}) as shown in Table 4.1. These random variables affect significantly the calculated reliability index. The uncertainty in these transformation factors could arise from the uncertainty in the exposure, gust coefficient and pressure coefficient, and overall wind load transformation

factor. In the design of buildings, such uncertainty could be taken into account by assigning a nominal value that equals its upper quantile value. For example, the pressure coefficient in building codes is often taken equal to its upper quantile value (Cook and Mayne 1979), and the mean to nominal value of the transformation from wind speed to wind load effect for a codified building design could be modelled as a lognormal distribution with a bias of 0.68 and COV of 0.22 (Bartlett et al. 2003). This bias factor is about 1.5 times of COV value below the unity.

Third, since the wind turbine is safe and operates satisfactorily for a mean wind speed at hub height that is less than the cut-out wind speed of 25 m/s (see Table 4.1), the wind turbine is proof load tested. This proof load testing aspect could be considered in evaluating the reliability of wind turbines subjected to the tropical cyclone hazard.

To approximately investigate the impact of the design wind and wave loads on the failure probability of the submersible system, a sensitivity analysis is carried out in this section by scaling the environmental parameters based on the 50-year return period value of the considered environmental parameter (i.e., V_{s50} or H_{s50}). This implies that the submersible WT for the scaled environmental parameter scenarios is designed based on factored 50-year return period value of the environmental parameters.

As part of the sensitivity analysis, the scaling factors are determined for the following four cases:

Case 1. It is considered that the load effect governing the design is directly proportional to the square of the wind speed, and the load effect is proportional to the significant wave height. A scaling factor equal to V_d/V_{s50} is to be used to scale the wind speed value and $(V_d/V_{s50})^2$ is used to scale the significant wave height value for reliability analysis, where V_d = 39.3 m/s as mentioned previously. The use of this scaling factor is aimed at treating the structure as if it is designed based on the site-specific 50-year return period value of the wind speed.

Case 2. This case is the same as Case 1 except, it is considered the load effect is proportional to the square of the significant wave height. Therefore, the same scaling factor V_d/V_{s50} is to be applied to wind speed and to wave height values.

Case 3. This case is the same as Case 1, except that the design is governed by the significant wave height. The scaling factors that equal $(H_d/H_{s50})^{1/2}$ and H_d/H_{s50} are to be used to scale wind speed value and significant wave height value for the reliability analysis, where H_d equals 12.9 m as mentioned previously

Case 4. This case is the same as Case 2, except that the design is governed by the significant wave height. The scaling factor that equals H_d/H_{s50} is to be used to scale wind speed value and significant wave height value for the reliability analysis.

By considering these cases, and the site-specific TC hazards for the four sites identified in Figure 4.9a, reliability analysis is carried out following the flowchart shown in Figure 4.4. The obtained failure probabilities are also presented in Tables 4.5 and 4.6. The results presented in Table 4.5 show that the estimated failure probability decreased except for Cases 3 and 4 when Site 2 is considered. This is expected as the H_d/H_{s50} are larger 1.0 except for these two cases when Site 2 is considered. However, the decrease in the estimated failure probability is about < 38%, even the smallest scaling factor for the loads is about 0.75. This observed modest decrease is due to the controlled operation of WT subjected to strong winds leading to the load effect patterns, as shown in Figure 4.7. Moreover, it is observed that even the "design" is adjusted to the site-specific 50-year return period values of wind speed and significant wave height, the failure probability is not identical. This is due to the site-specific statistical characteristics of TC hazard (i.e., the COV of V_s and COV of H_s vary from site to site, as shown in Table 4.4). In addition, from Table 4.6, it can be observed that the relative change in the failure probability of towers for Cases 1 to 4 as compared to that for Base Case is only slight. However, the small failure probability of overturning of the floating platform decreases in orders of magnitude. It must be emphasized that the estimated annual failure probabilities shown in Tables 4.5 and 4.6 are much larger than the suggested optimal tolerable failure probability by Sørensen and Tarp-Johansen, which is within the interval of 2×10^{-4} to 10^{-3}.

Since the suggested design wind speed at 10 m height for Class TI specified in GB/T 31519 (2015) equals 43.2 m/s as mentioned earlier. The sensitivity analysis indicates that if the tolerable annual failure probability is about 3%, the current design code would be adequate. If a lower tolerable failure probability is justified and considered, an increased environmental load would be required, although the determination of such a tolerable failure probability based on social economics investigation and reliability and risk-based design code calibration is beyond the present study.

For the parametric analysis in dealing with the uncertainty in the load parameter to transformation factor, it is assumed that the uncertainty in the transformation factor could be taken into account in design codes by specifying the nominal values such that the bias (or mean) for Y_{L1} and Y_{L2} equal to 0.65, and the mean of Y_{L4} equal to 0.75 (i.e., approximately equal to 1 minus 1.5 times of the COV value shown in Table 4.1). In this case, the obtained failure probabilities are shown in Table 4.7. These values are about only 20% of those shown in Table 4.5.

Table 4.7. Estimated failure probability for cases shown in Table 4.5 but considering the mean Y_{L1} and Y_{L2} equal to 0.65, and the mean of Y_{L4} equal to 0.75.

Case	Base Case		Case 1		Case 2		Case 3		Case 4	
Site	P_{fsys1}	P_{fsys20}	P_{fsys1}	P_{fsys20}	P_{fsys1}	P_{fsys20}	P_{fsys1}	P_{fsys20}	P_{fsys1}	P_{fsys20}
1	7.8E-03	0.146	5.5E-03	0.110	6.4E-03	0.124	6.4E-03	0.124	6.3E-03	0.120
2	7.7E-03	0.154	6.3E-03	0.124	6.8E-03	0.136	7.1E-03	0.142	6.9E-03	0.134
3	7.9E-03	0.154	6.0E-03	0.120	6.4E-03	0.126	7.1E-03	0.140	6.9E-03	0.136
4	7.9E-03	0.150	5.7E-03	0.114	6.5E-03	0.130	6.9E-03	0.136	6.9E-03	0.134

Finally, by considering that the safe operation of the wind turbine for a mean wind speed at hub height less than 25 m/s could be used as the successful proof load testing condition, the reliability analysis that is carried out for the results presented in Tables 4.5 and 4.7 is repeated. The obtained annual failure probability P_{fsys1} is shown in Table 4.8. The table shows that by considering the safe operating condition of the wind turbine, P_{fsys1} is less than about 2.2×10^{-3} if the uncertainty in the transformation factor is taken into account in design codes (i.e., the bias for Y_{L1} and Y_{L2} equal to 0.65, and for Y_{L4} equal to 0.75).

Table 4.8. Estimated failure probability with the first and second entries corresponding to those shown in Tables 4.5 and 4.7, respectively, but considering the safe operation of wind turbine for a mean wind speed at hub height less than 25 m/s.

	P_{fsys1}				
Site	Base Case	Case 1	Case 2	Case 3	Case 4
1	0.0173,0.0021	0.0016,0.0001	0.004,0.0005	0.0068,0.0007	0.0061,0.0008
2	0.0054,0.0008	0.0008,0.0001	0.0014,0.0002	0.0023,0.0003	0.0017,0.0002
3	0.0082,0.0014	0.0008,0.0001	0.0026,0.0004	0.0039,0.0006	0.0032,0.0006
4	0.0113,0.0019	0.0011,0.0001	0.0024,0.0005	0.0046,0.0009	0.0036,0.0007

Note that although systematic sensitivity analysis by considering the parameters controlling the wind characteristics (i.e., parameters for wind profile and for wind and wave spectra) could be very valuable, such parametric investigation is beyond the present study because of the amount of computing resource required.

4.4 Conclusions

An overall simulation-based database-driven framework to assess the fragility and reliability of offshore WTs is proposed. This approach avoids the need for sophisticated distribution fitting of the joint wind and wave hazard. The analysis based on the proposed framework relies on establishing the synthetic TC track database, TC wind and wave field database, and structural response database. Details on establishing such databases are elaborated extensively.

Numerical analysis carried out indicates that the TC wind and wave hazards vary from site to site for offshore locations near the coastline of mainland China. The estimated 50-year return period value of the TC wind speed indicates that they can be greater than that suggested for the design of the wind turbine under typhoon conditions in GB/T 31519 (2015). Also, the assessed statistics of the significant wave height, as well as its 50-year return period value, could be valuable for the code making.

The application of the proposed data-driven simulation-based procedure for reliability analysis is illustrated by a numerical example, where a semi-submersible WT (i.e., OC4) is adopted. The results show that if such a structure, which is not designed according to

IEC61400-1 or GB/T 31519, is placed in the coastal region of mainland China, the failure probability is spatially varying because of the spatially varying statistics of TC wind and wave hazards. It is shown that failure is dominated by the buckling of the tower, followed by the overturning of the floating platform. The failure probability by considering the limit state functions for the blades and for the mooring lines is negligible (i.e., practically equal to zero) if the normal operation control can be ensured. The significantly greater failure probability could be attributed to the large coefficient of variation of the annual maximum TC wind speed and wave height, and to the fact that the considered wind turbine is not designed for the considered sites with the applicable design codes.

Results from sensitivity analysis imply that if the design is carried out based on the 50-year return period value of TC wind or significant wave height, the uncertainty in the transformation from load parameter to load effects is considered in the codified structural design, and the safe operating condition of wind turbine for wind speed below the cut-out wind speed is considered, the annual failure probability is about less than 2×10^{-3}, which is deemed small. It must be emphasized that for an actual semi-submersible wind turbine to be designed and constructed in the considered region, the statistical models used for the illustrative reliability analysis require further scrutiny and validation.

4.5 Reference

Bartlett, F. M., Hong, H. P., & Zhou, W. (2003). Load factor calibration for the proposed 2005 edition of the National Building Code of Canada: Statistics of loads and load effects. Canadian Journal of Civil Engineering, 30(2), 429-439.

Benassai, G., Campanile, A., Piscopo, V., & Scamardella, A. (2014). Ultimate and accidental limit state design for mooring systems of floating offshore wind turbines. Ocean Engineering, 92, 64-74.

Bossanyi, E.A. (2003). GH bladed theory manual. GH & Partners Ltd, 2, 56-58.

Cardone, V.J., Jensen, R. E., Resio, D. T., Swail, V.R., & Cox, A.T. (1996). Evaluation of contemporary ocean wave models in rare extreme events: The “Halloween Storm” of October 1991 and the “Storm of the Century” of March 1993. Journal of Atmospheric and Oceanic Technology, 13(1), 198-230.

Cook, N. J., & Mayne, J. R. (1979). A novel working approach to the assessment of wind loads for equivalent static design. Journal of Wind Engineering and Industrial Aerodynamics, 4(2), 149-164.

Coulling, A.J., Goupee, A.J., Robertson, A.N., Jonkman, J.M., & Dagher, H.J. (2013). Validation of a FAST semi-submersible floating wind turbine numerical model with DeepCwind test data. Journal of Renewable and Sustainable Energy, 5(2), 023116.

DHI, MIKE 21 SW - Spectral Wave Model: Scientific Documentation, 2017 http://manuals.mikepoweredbydhi.help/2017/Coast_and_Sea/M21SW_Scientific_Doc.pdf

Dietrich, J. C., Tanaka, S., Westerink, J. J., Dawson, C. N., Luettich, R. A., Zijlema, M., ... & Westerink, H. J. (2012). Performance of the unstructured-mesh, SWAN+ ADCIRC model in computing hurricane waves and surge. Journal of Scientific Computing, 52(2), 468-497.

DNV OS E302 (2015). Offshore mooring chain - Rules and standards, DNV AS, Høvik, Norway.

DNVGL-ST-0119. (2018). Floating wind turbine structures. Det Norske Veritas Germanischer Lloyd, Høvik, Norway.

Emanuel, K., Ravela, S., Vivant, E., & Risi, C. (2006). A statistical deterministic approach to hurricane risk assessment. Bulletin of the American Meteorological Society, 87(3), 299-314.

GB/T 31519-2015. (2015). Wind turbine generator system under typhoon condition, Standards Press of China; Beijing, China.

Georgiou, P.N., Davenport, A.G., & Vickery, B.J. (1983). Design wind speeds in regions dominated by tropical cyclones. Journal of Wind Engineering and Industrial Aerodynamics, 13(1-3), 139-152.

Goda, K., & Hong, H.P. (2006). Optimal seismic design considering risk attitude, societal tolerable risk level, and life quality criterion. Journal of Structural Engineering, 132(12), 2027-2035.

Grell, G.A., Peckham, S.E., Schmitz, R., McKeen, S.A., Frost, G., Skamarock, W.C., & Eder, B. (2005). Fully coupled "online" chemistry within the WRF model. Atmospheric Environment, 39(37), 6957-6975.

Hall, T.M., & Jewson, S. (2007). Statistical modelling of North Atlantic tropical cyclone tracks. Tellus A: Dynamic Meteorology and Oceanography, 59(4), 486-498.

Hallowell, S.T., Arwade, S.R., Fontana, C.M., DeGroot, D.J., Diaz, B.D., & Landon, M.E. (2017). Reliability of mooring lines and shared anchors of floating offshore wind turbines. In The 27th International Ocean and Polar Engineering Conference. International Society of Offshore and Polar Engineers.

Hallowell, S.T., Myers, A.T., Arwade, S. R., Pang, W., Rawal, P., Hines, E. M., ... & Carswell, W. (2018). Hurricane risk assessment of offshore wind turbines. Renewable Energy, 125, 234-249.

Holland, G.J. (1980). An analytic model of the wind and pressure profiles in hurricanes. Monthly weather review, 108(8), 1212-1218.

Holton, J. R. (2004). An introduction to dynamic meteorology: Elsevier Academic Press. Burlington USA.

Hong, H.P., Li, S.H., & Duan, Z.D. (2016). Typhoon wind hazard estimation and mapping for coastal region in mainland China. Natural Hazards Review, 17(2), 04016001.

Hong, L., & Möller, B. (2012). An economic assessment of tropical cyclone risk on offshore wind farms. Renewable energy, 44, 180-192.

Hong, H. P., Mara, T. G., Morris, R., Li, S. H., & Ye, W. (2014). Basis for recommending an update of wind velocity pressures in Canadian design codes. Canadian Journal of Civil Engineering, 41(3), 206-221.

Hong, X., Hong, H.P., & Li, J. (2019). Solution and validation of a three dimensional tropical cyclone boundary layer wind field model. Journal of Wind Engineering and Industrial Aerodynamics, 193, 103973.

Horte, T., Lie, H., & Mathisen, J. (1998). Calibration of an ultimate limit state for mooring lines. In Proc. of the OMAE conference. Paper OMAE98-1457.

IEC International Electrotechnical Commission (2019). IEC 61400-3-1: Wind energy generation systems –Part 3-1: Design requirements for fixed offshore wind turbines.

IEC International Electrotechnical Commission. (2019). IEC 61400-1: Wind turbines part 1: Design requirements. International Electrotechnical Commission.

James, M.K. and Mason, L.B. (2005). Synthetic tropical cyclone database. J. Waterw. Port Coastal Ocean Eng.; 131, 181–192.

Jha, A., Dolan, D., Musial, W., and Smith, C. (2010). On hurricane risk to offshore wind turbines in US Waters. Proceedings from the 2010 Offshore Technology Conference. Houston, TX.

Jonkman, J.M., & Buhl Jr, M.L. (2005). FAST user's guide. National Renewable Energy Laboratory, Golden, CO, Technical Report No. NREL/EL-500-38230.

Jonkman, J. M. (2007). Dynamics modeling and loads analysis of an offshore floating wind turbine (No. NREL/TP-500-41958). National Renewable Energy Lab.(NREL), Golden, CO (United States).

Jonkman, J., Butterfield, S., Musial, W., & Scott, G. (2009). Definition of a 5-MW reference wind turbine for offshore system development (No. NREL/TP-500-38060). National Renewable Energy Lab.(NREL), Golden, CO (United States).

Kepert, J. (2001). The dynamics of boundary layer jets within the tropical cyclone core. Part I: Linear theory. Journal of the Atmospheric Sciences, 58(17), 2469-2484.

Kepert, J. and Wang, Y. (2001). The dynamics of boundary layer jets within the tropical cyclone core. Part II: Nonlinear enhancement. Journal of the atmospheric sciences, 58(17), 2485-2501.

Kepert, J.D. (2012). Choosing a boundary layer parameterization for tropical cyclone modelling. Mon. Weather Rev. 140, 1427–1445,

Larsen, T.J., & Hansen, A. M. (2007). How 2 HAWC2, the user's manual.

Li, S.H., & Hong, H.P. (2016). Typhoon wind hazard estimation for China using an empirical track model. Natural Hazards, 82(2), 1009-1029.

Liu, Q., Babanin, A., Fan, Y., Zieger, S., Guan, C., & Moon, I.J. (2017). Numerical simulations of ocean surface waves under hurricane conditions: Assessment of existing model performance. Ocean Modelling, 118, 73-93.

Liu, Y., Li, S., Chan, P.W., & Chen, D. (2018). On the failure probability of offshore wind turbines in the China coastal waters due to typhoons: A case study using the OC4-DeepCwind semisubmersible. IEEE Transactions on Sustainable Energy.

Madsen, H.O., Krenk, S., & Lind, N.C. (2006). Methods of structural safety. Courier Corporation.

Mandell, J.F., Samborsky, D.D., Miller, D.A., Agastra, P., & Sears, A.T. (2016). Analysis of SNL/MSU/DOE Fatigue Database Trends for Wind Turbine Blade Materials 2010-2015 (No. SAND-2016-1441). Sandia National Lab.(SNL-NM), Albuquerque, NM (United States).

Melchers, R.E., & Beck, A.T. (2018). Structural reliability analysis and prediction. John Wiley & Sons.

Meng, Y., Matsui, M. and Hibi, K. (1997). A numerical study of the wind field in a typhoon boundary layer. Journal of Wind Engineering and Industrial Aerodynamics, 67, 437-448.

Muskulus, M., & Schafhirt, S. (2015). Reliability-based design of wind turbine support structures. In Proceedings of the Symposium on Reliability of Engineering System, Hangzhou, China (Vol. 1517).

Nelsen R.B. (2006). An introduction to copulas. 2nd edition. New York, USA: Springer.

Ochi, M.K. (1993). On hurricane-generated seas. In Ocean wave measurement and analysis (pp. 374-387). ASCE.

Robertson, A., Jonkman, J., Vorpahl, F., Popko, W., Qvist, J., Froyd, L., ... & Luan, C. (2014). Offshore code comparison collaboration, continuation within IEA Wind task 30: phase II results regarding a floating semisubmersible wind system (No. NREL/CP-5000-61154). National Renewable Energy Lab.(NREL), Golden, CO (United States).

Ronold, K.O., & Larsen, G.C. (2000). Reliability-based design of wind-turbine rotor blades against failure in ultimate loading. Engineering Structures, 22(6), 565-574.

Rose, S., Jaramillo, P., Small, M. J., Grossmann, I., & Apt, J. (2012). Quantifying the hurricane risk to offshore wind turbines. Proceedings of the National Academy of Sciences, 109(9), 3247-3252.

Sheng, C. & Hong, H.P. (2020) On the joint tropical cyclone wind and wave hazard, Structural Safety, 84, 101917.

Sørensen, J.D., & Berzonskis, A. (2017). Probabilistic design and estimation of life of wind turbine components. In 12th International Conference on Structural Safety & Reliability: ICOSSAR 2017 (pp. 2889-2898). TU Verlag.

Sørensen, J.D., & Tarp-Johansen, N.J. (2005). Reliability-based optimization and optimal reliability level of offshore wind turbines. International Journal of Offshore and Polar Engineering, 15(02).

Tarp-Johansen, N. J., & Clausen, N-E. (2006). Design of Wind Turbines in Typhoon area: A first study of Structural Safety of Wind Turbines in Typhoon prone areas. EC-ASEAN Energy Facility.

Tarp-Johansen, N. J., Sørensen, J. D., & Madsen, P. H. (2002). Experience with acceptance criteria for offshore wind turbines in extreme loading. In Workshop on reliability based code calibration.

Tavner, P. (2012). Offshore wind turbines: reliability, availability and maintenance. The Institution of Engineering and Technology.

Tavner, P. J., Xiang, J., & Spinato, F. (2007). Reliability analysis for wind turbines. Wind Energy: An International Journal for Progress and Applications in Wind Power Conversion Technology, 10(1), 1-18.

Teng, C., & Liu, P. C. (2000). Estimating wave height distributions from wind speed distributions. Coastal Engineering(2000), 310-319.

Thompson, E. F., & Cardone, V. J. (1996). Practical modeling of hurricane surface wind fields. Journal of Waterway, Port, Coastal, and Ocean Engineering, 122(4), 195-205.

Tran, T. T., & Kim, D. H. (2016). Fully coupled aero-hydrodynamic analysis of a semi-submersible FOWT using a dynamic fluid body interaction approach. Renewable energy, 92, 244-261.

Vazquez-Hernandez, A. O., Ellwanger, G. B., & Sagrilo, L. V. S. (2006). Reliability-based comparative study for mooring lines design criteria. Applied Ocean Research, 28(6), 398-406.

Vickery, P. J., Wadhera, D., Galsworthy, J., Peterka, J. A., Irwin, P. A., & Griffis, L. A. (2010). Ultimate wind load design gust wind speeds in the United States for use in ASCE-7. Journal of structural engineering, 136(5), 613-625.

Vickery, P. J., Wadhera, D., Powell, M. D., & Chen, Y. (2009). A hurricane boundary layer and wind field model for use in engineering applications. Journal of Applied Meteorology and Climatology, 48(2), 381-405.

Vickery, P. J., Skerlj, P. F., Steckley, A. C., & Twisdale, L. A. (2000). Hurricane wind field model for use in hurricane simulations. Journal of Structural Engineering, 126(10), 1203-1221.

Wayman, E. N., Sclavounos, P. D., Butterfield, S., Jonkman, J., & Musial, W. (2006). Coupled dynamic modeling of floating wind turbine systems (No. NREL/CP-500-39481). National Renewable Energy Lab.(NREL), Golden, CO (United States).

Wilkie, D., & Galasso, C. (2017). Ultimate Limit State Fragility of Offshore Wind Turbines on Monopile Foundations. ICOSSAR.

Ying, M., Zhang, W., Yu, H., Lu, X., Feng, J., Fan, Y., ... & Chen, D. (2014). An overview of the China Meteorological Administration tropical cyclone database. Journal of Atmospheric and Oceanic Technology, 31(2), 287-301.

Young, I. R. (2017). A review of parametric descriptions of tropical cyclone wind-wave generation. Atmosphere, 8(10), 194.

Young, I. R. (2003). A review of the sea state generated by hurricanes. Marine structures, 16(3), 201-218.

Young, I. R. (1988). Parametric hurricane wave prediction model. Journal of Waterway, Port, Coastal, and Ocean Engineering, 114(5), 637-652.

Chapter 5

5 Reliability-based calibration of site-specific design typhoon wind and wave loads for wind turbine

5.1 Introduction

China has a long coastline with wind energy potentials. The characteristics of wind energy near the coastline of mainland China were investigated by several studies, including Jiang et al. (2013), Nie and Li (2018), Li et al. (2020), and Feng et al. (2020). According to the best tropical cyclone (TC) track dataset available from the China Meteorological Administration (CMA) (Ying et al. 2014), the coastal region is affected by about eight landfalling TC each year. The wind turbines (WTs) that are designed, constructed, and installed near the coastline of mainland China are faced with TC wind and wave hazards. Failure of WTs during the passage of TC events in the region has been reported in Chen and Xu (2016). The tropical cyclones, known as typhoons in the region, are classified according to their near-surface maximum 2-min mean wind speed (GB/T19201 2006). The assessment of the TC wind hazard for the considered coastal region has been reported in several studies. For example, Xiao et al. (2011), Li and Hong (2015b), Hong et al. (2016), Fang et al. (2021), and Wu et al. (2021) assessed TC wind hazard for onshore sites based on the statistics of the local TC track activities (i.e., circular subregion method (Georgiou et al. 1983)) but using different wind field models. Li and Hong (2016) developed a stochastic model for the TC track from genesis to lysis and mapped TC wind hazard for the region. They showed that the TC track characteristics of the landfalling TCs, such as the annual occurrence rate, central pressure difference, heading, and translation velocity, vary along the coastline that extends more than 4000 km. The evaluation of the concurrent TC wind and wave hazards was given in Sheng and Hong (2020) for the region. One of the salient features of the assessed TC hazards is that the mean and coefficient of variation (COV) of the annual maximum TC wind speed and significant wave height are geographically varying. Since the structural reliability is sensitive to the COV of random variables involved in the limit state function

(Madsen et al. 2006), the calibrated design load and resistance factors are sensitive to the considered COV of the random variables (Nessim et al. 1995a,b). This implies that the WTs designed using a single fixed set of the wind and wave load factors stipulated in a structural design code and at different locations are unlikely to achieve a very consistent safety level if the COV values of the annual maximum wind speed and significant wave height are geographically varying.

The design wind speed for the WT generator system under typhoon conditions in China is recommended in GB/T 31519 (2015), and the design wind load factor for onshore wind turbines is given in GB/T 18451.1 (2012). However, these codes are silent on the load factors for offshore WTs subjected to TC wind and wave loads. It is inferred from the industry practice (CCS 2012) that, in such a case, the use of the International Electrotechnical Committee (IEC) (IEC 61400-3 2019) could be considered.

The reliability-based calibration of the load factors for designing WT structures was extensively presented by Ronold and Larsen (2000), Tarp-Johansen et al. (2002), and Sorensen and Tarp-Johansen (2005), Tarp-Johansen and Clausen (2006). A range of the optimum target reliability indices (or tolerable annual failure probability ranging from 2×10^{-4} to 10^{-3}) was suggested in Sorensen and Tarp-Johansen (2005) for calibrating the design loads. They also recommended the limit state functions and the probability distributions of the random variables involved in the limit state functions. Wilkie and Galasso (2020) indicated that the current design procedures do not sufficiently consider extreme TC conditions, and the safety factors for offshore wind turbines are often adapted from the offshore oil and gas industry or design guidelines for onshore wind turbines. We note that the design wind load for WT subjected to typhoon winds in China is specified in the codes (GB/T 18451.1 2012; GB/T 31519 2015). However, it seems that a reliability-based structural design code calibration for WT subjected to typhoon wind and wave hazards affecting mainland China has not been reported in the literature.

Besides the above-mentioned studies focused on calibrating the design loads for WTs, the reliability evaluation and risk modeling were reported in several studies for the onshore and offshore WTs subjected to TC wind and wave hazards. A review of works on the

structural reliability analysis of WTs was presented in Jiang et al. (2017). Tarp-Johansen and Clausen (2006) investigated the structural safety of WTs in the Philippines that is known to experience severe TC events. Jha et al. (2010) compared the reliability levels achieved for a generic offshore wind turbine structure by considering two design guidelines (IEC and American Petroleum Institute). Wei et al. (2014) proposed an incremental wind-wave analysis procedure to evaluate the responses and capacity of WT subjected to extreme TC wind and wave hazards. Since this approach is based on a nonlinear inelastic pushover analysis considering the load configuration defined based on the return period values of wind and wave, it considers the nonlinear inelastic structural behaviour. The capacity, in this case, is defined based on the critical load effects or critical load scaling factor for the load profile defined based on return period values of wind speed and significant wave height. An approximate procedure to evaluate failure probability was presented based on the minimum value of the return period. Hallowell et al. (2018) evaluated the reliability of offshore monopile WTs that are located along the U.S. Atlantic coast and subjected to the TC hazard. Wilkie and Galasso (2020) developed fragility curves based on the time-history analysis of WT by considering the fluctuating wind and wave loads. Their developed fragility curves are conditioned on the time-averaged mean wind speed and significant wave height. Similar to several other studies (e.g., Pokhrel and Seo 2019) Wilkie and Galasso (2020) used the National Renewable Energy Laboratory (NREL) 5 MW wind turbine (Jonkman et al. 2009), and carried out the time history analysis for the considered WT by using the software package FAST (Fatigue, Aerodynamics, Structures, and Turbulence) (Jonkman and Buhl 2005; Vorpahl et al. 2013). Procedures for assessing the structural reliability of a semi-submersible offshore WT placed near or in the coastal region of mainland China were presented in Liu et al. (2018) and Sheng and Hong (2021). A database-driven simulation-based framework for estimating the structural reliability of WT subjected to TC wind and wave hazards was proposed in Sheng and Hong (2021). Their approach considered the time-varying time-averaged mean wind speed and significant wave height during the passages of the TC events and used FAST to estimate the structural responses by considering fluctuating wind and wave height. This framework will be described in the next section since it is used in the present study for the structural reliability analysis.

Note that a review of the use of mechanical devices such as the tunned damper to reduce the vibration and to evaluate the fragility curves (Zhang et al. 2019; Martin del Campo et al. 2021) as well as the consideration of the foundation design of WT (Myer et al. 2015) are outside the scope of the present study, although these subjects can be important.

The main objective of the present study is to calibrate the site-specific design wind and wave loads for designing offshore and onshore WTs located near the southeast coastline of mainland China and subjected to typhoon wind and wave loads. The calibration of the site-specific or information-sensitive design TC wind and wave loads is to be carried out for selected reliability indices. The calibration considers the correlated TC wind speed and significant wave height during the passage of TC events. To carry out the calibration, first, the steps to generate the synthetic TC tracks and to estimate TC wind and wave hazards for the coastal region of mainland China are described. This is followed by establishing the database for the structural responses conditioned on the time-averaged wind and wave condition. The reliability-based calibration is then carried out, and site-specific (factored) design wind and wave loads are suggested.

5.2 TC hazard and statistics of responses of monopile wind turbine

5.2.1 TC wind and wave hazards and hazard mapping

In this section, we briefly summarize the simulation-based procedures described in Li and Hong (2016) and Sheng and Hong (2020) to generate synthetic tracks and estimate the TC wind and wave hazards for sites near the coastline of mainland China. We use these procedures to establish the TC track database (TC-database) and wind and wave database (WW-database) that are to be used to calibrate the site-specific design TC wind and wave loads. Essentially, the simulation-based procedure consists of three components:

a) Generate TC tracks for T_T years of the TC activities. For generating a synthetic track, a genesis within the Western North Pacific (WNP) basin is randomly sampled from the historical geneses, and its corresponding track is sampled using the stochastic track

model given in Li and Hong (2016). Each sampled track is defined, every 6 hours, by its position (i.e., latitude and longitude denoted as (L_a, L_o)), translation velocity u_c, heading direction θ, central pressure difference Δp, radius to the maximum wind speed R_{max}, and Holland's B parameters. For the simulation, it is considered that the residual for predicting R_{max} based on Δp can be calculated based on the same randomly generated probability level for each track. The same consideration is made for B. The generated synthetic tracks are stored in the TC-database.

b) The wind and wave fields are computed for ranges of ((L_a, L_o), u_c, θ, Δp, R_{max}, B) values. The calculated fields are stored in the WW-database. This is efficient since we can simply extract the precomputed wind and wave fields from the database for a considered point on a track when needed.

   For evaluating TC wind field conditioned on ((L_a, L_o), u_c, θ, Δp, R_{max}, B), the vertically averaged boundary layer slab model (Vickery et al. 2009a, b; Li and Hong 2015a) is adopted. The calculated wind speed, denoted as V_s, represents the 10-min mean wind speed at 10 m height. Evaluate the significant wave height, H_s, from the TC wave field using the parametric model advanced by Young (1988, 2003, 2017).

For estimating the TC wind and wave hazards at a site, we use the TC-database and extract the segment of each track that is within a radius of 250 km of the site of interest. For the values of ((L_a, L_o), u_c, θ, Δp, R_{max}, B) associated with each defined point on a segment of an identified track, we extract the precalculated wind and wave fields from the WW-database to evaluate V_s and H_s at the site of interest. This is done for all identified points on the segments of the tracks mentioned earlier. For a segment of a track, samples of the time history of V_s and H_s are obtained. This procedure is schematically illustrated in Figure 5.1, showing a simulated track, the calculated TC wind and wave fields at two instances, and time-varying V_s and H_s for the segment of track that is within a site of interest. The plot shows that there is a time lag between the maximum V_s, $V_{s\text{-}max}$, and maximum H_s, $H_{s\text{-}max}$, at a site of interest for a considered TC event. The concurrent wave to $V_{s\text{-}max}$, H_{sW}, and the concurrent wind to $H_{s\text{-}max}$, V_{sH}, are also identified in the figure. This non-simultaneous occurrence of the maximum wind speed and wave

height is typically observed from simulation analysis; it also occurs if the simulation is carried out for the track defined every one hour.

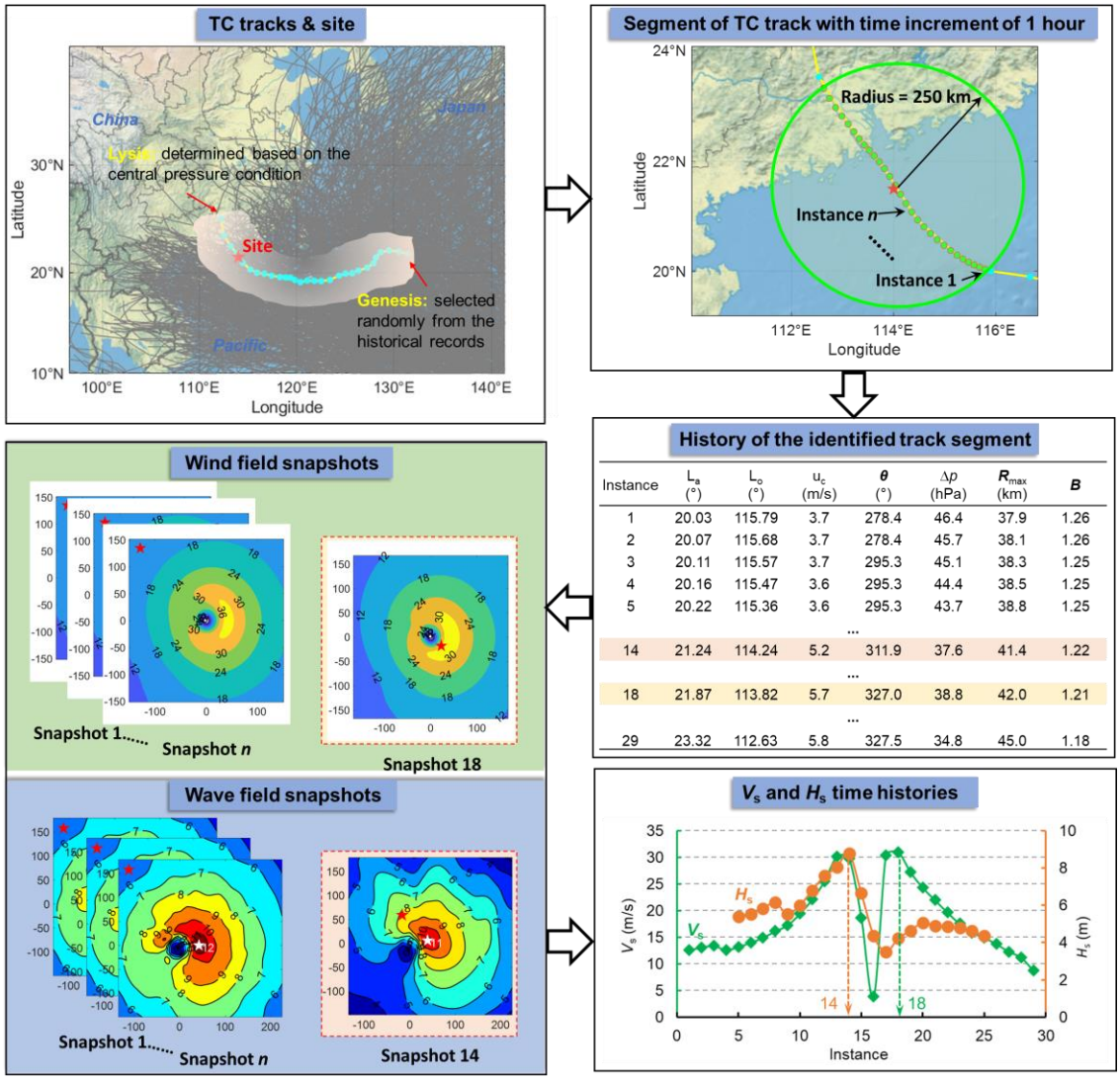

Figure 5.1. Illustration of a simulated track, evaluated wind and wave fields, calculated time-varying V_s and H_s, and the identified maximum values of V_s and H_s at the site of interest during the passage of TC.

The maximum values of V_s and H_s per year can be extracted to form samples of annual maximum values of V_s and H_s and used to assess the wind and wave hazards. Note that the consideration of a radius of 250 km is justified. This is because the calculation of V_s and H_s for a distance greater than 250 km are too small to affect the structural reliability

or TC hazard values (Li and Hong 2016; Sheng and Hong 2021).

To map the TC wind and wave hazards for the coastal region, in the present study, we use a squared grid system with a spatial increment of 0.5^o (see Figure 5.2a), and consider simulated TC tracks representing T_T = 100000 years of TC activities. For each grid point, following the above-described procedure, the TC event-based (($V_{s\text{-}max}$, H_{sW}), ($H_{s\text{-}max}$, V_{sH})) values are obtained. Using these values, samples of the annual maximum value of V_s, $V_{s\text{-}maxA}$, and the annual maximum value of the significant wave height H_s, $H_{s\text{-}maxA}$, are obtained for 100000 years of TC activities. Also, samples of the concurrent value of H_s for $V_{s\text{-}maxA}$, H_{sWA}, and the concurrent value of V_s for $H_{s\text{-}maxA}$, V_{sHA}, are obtained for the same considered TC activities.

The statistics and the probability distributions of $V_{s\text{-}maxA}$ and $H_{s\text{-}maxA}$ are shown in Figure 5.2 for ten selected sites. As can be observed, the mean and COV values vary from site to site, indicating the geographically varying characteristics of $V_{s\text{-}maxA}$ and $H_{s\text{-}maxA}$. The results indicate that the mean of $V_{s\text{-}maxA}$ decreases, and the COV of $V_{s\text{-}maxA}$ increases as latitude increases. The same trends are observed for $H_{s\text{-}maxA}$. The empirical probability distribution plots show that they may not be adequately fitted using the Gumbel distribution since they do not follow straight lines in the Gumbel probability paper. The symbol p_0 shown in the plots denotes the probability that there is no TC event affecting the considered site in a year. This probability increases as the latitude of the site increases, which agrees with the observation that the TC activities decrease as the latitude increases. Also, the (1-p)-quantiles (i.e., (1/p)-year return period values) of $V_{s\text{-}maxA}$ and $H_{s\text{-}maxA}$, denoted as $v_{s\text{-}maxA\text{-}p}$ and $h_{s\text{-}maxA\text{-}p}$ are calculated from the empirical distributions and shown in the figure for p = 0.02 and 0.002. The calculated quantiles indicate that $v_{s\text{-}maxA\text{-}p}$ for S1 to S5 offshore sites is about 20% to 40% greater than that for L1 to L5 onshore sites, respectively.

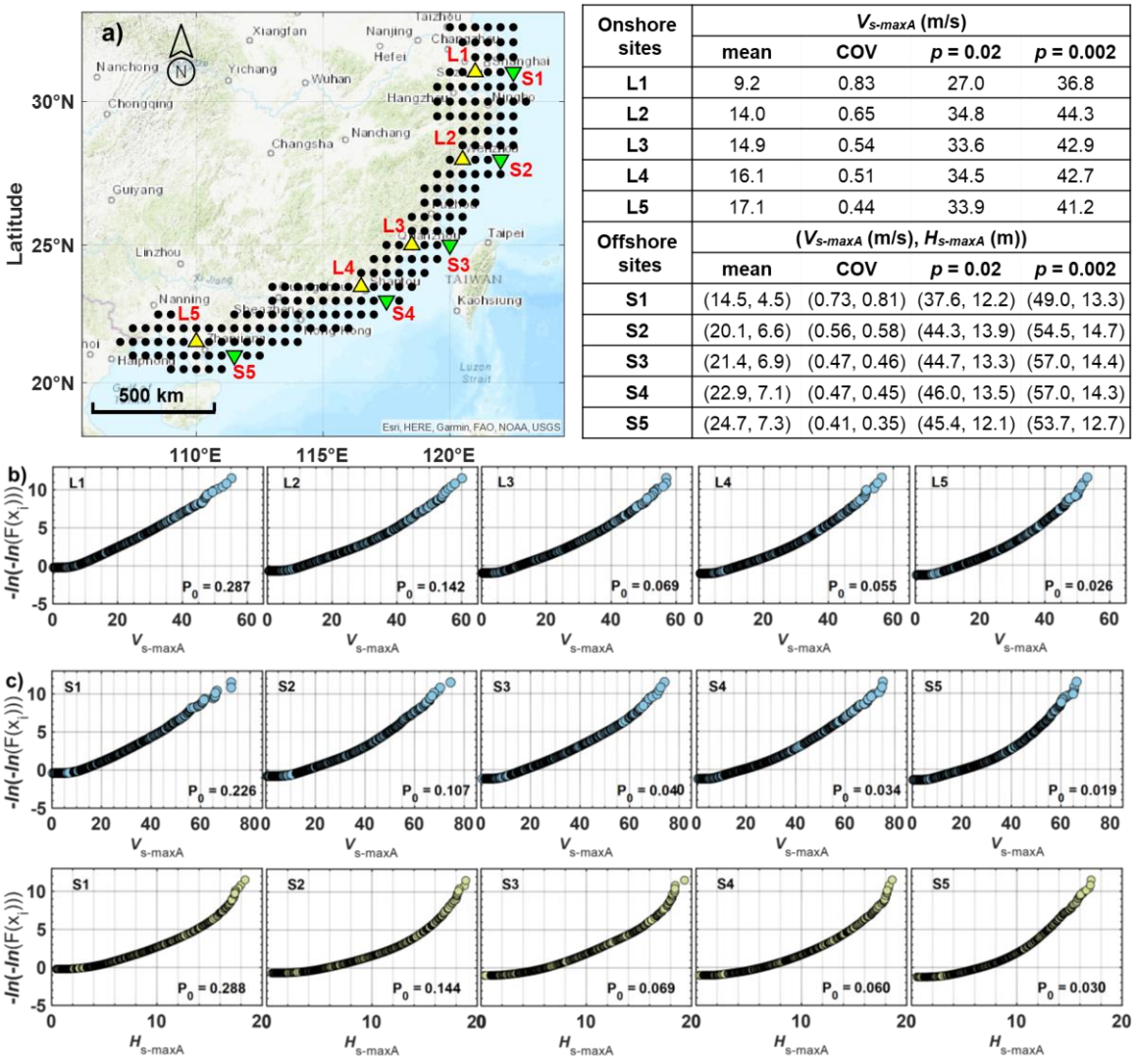

Onshore sites	$V_{s\text{-}maxA}$ (m/s)			
	mean	COV	p = 0.02	p = 0.002
L1	9.2	0.83	27.0	36.8
L2	14.0	0.65	34.8	44.3
L3	14.9	0.54	33.6	42.9
L4	16.1	0.51	34.5	42.7
L5	17.1	0.44	33.9	41.2
Offshore sites	($V_{s\text{-}maxA}$ (m/s), $H_{s\text{-}maxA}$ (m))			
	mean	COV	p = 0.02	p = 0.002
S1	(14.5, 4.5)	(0.73, 0.81)	(37.6, 12.2)	(49.0, 13.3)
S2	(20.1, 6.6)	(0.56, 0.58)	(44.3, 13.9)	(54.5, 14.7)
S3	(21.4, 6.9)	(0.47, 0.46)	(44.7, 13.3)	(57.0, 14.4)
S4	(22.9, 7.1)	(0.47, 0.45)	(46.0, 13.5)	(57.0, 14.3)
S5	(24.7, 7.3)	(0.41, 0.35)	(45.4, 12.1)	(53.7, 12.7)

Figure 5.2. Grid system and selected ten sites, and empirical probability distributions of $V_{s\text{-}maxA}$ and of $H_{s\text{-}maxA}$ for ten sites based on simulation results: a) selected sites and grid system for mapping TC hazard; b) empirical distributions of $V_{s\text{-}maxA}$ for five onshore sites; c) empirical distributions of $V_{s\text{-}maxA}$ and $H_{s\text{-}maxA}$ for five offshore sites.

Note that the codes (GB/T 18451.1 2012; GB/T 31519 2015) suggest that the nominal design (10-min) wind speed of 55 m/s and 50 m/s at hub height for Classes TI and TII WTs, with a wind load factor of 1.35 for onshore sites. This implies a (factored) design wind speed at 10 m height equal to 50.2 and 45.7 m/s for Classes TI and TII WTs,

respectively, if the hub height equals 90 m. A comparison of these values to those shown in the figure indicates that the factored design wind speed is greater than 0.998-quantiles (or 500-year return period value) of the annual maximum TC wind speed if the onshore sites are considered. Since the codes suggested the design wind loads for the onshore sites may be used as references for the offshore sites, the comparison indicates that the factored design wind speed, in this case, is between 50-year and 500-year return period value of the annual maximum TC wind speed.

By using the calculated mean and COV of $V_{s\text{-}maxA}$ and $H_{s\text{-}maxA}$ and the (1-p)-quantiles of $V_{s\text{-}maxA}$ and $H_{s\text{-}maxA}$ for all grid points depicted in Figure 5.2a, we map the mean and COV values in Figure 5.3, and $v_{s\text{-}maxA\text{-}p}$ and $h_{s\text{-}maxA\text{-}p}$ in Figure 5.4 for p = 0.02 and 0.002. The results presented in Figure 5.3 emphasized that the mean and COV of $V_{s\text{-}maxA}$ and $H_{s\text{-}maxA}$ are geographically varying. The means of the $V_{s\text{-}maxA}$ and $H_{s\text{-}maxA}$ decrease as the latitude increases, while the COV of $V_{s\text{-}maxA}$ and $H_{s\text{-}maxA}$ increases as the latitude increases. This increase in mean and decrease in COV correspond to the decreased landfalling TC rate as latitude increases. The estimated quantiles shown in Figure 5.4 are also spatially varying. In general, $v_{s\text{-}maxA\text{-}p}$ and $h_{s\text{-}maxA\text{-}p}$ decreases as latitude increases. This is consistent with that detailed in Figure 5.2. Moreover, the calculated ratio of the 0.998-quantile to 0.98-quantile of $V_{s\text{-}maxA}$ and of $H_{s\text{-}maxA}$ is shown in Figure 5.5. The ratio ranges from 1.16 to 1.4 for $V_{s\text{-}maxA}$ and from 1.13 to 1.35 for $H_{s\text{-}maxA}$. This implies that the application of a single load factor to the nominal wind load or wave load that is specified using p = 0.02 does not result in the factored design load having the same probability of exceedance for the considered sites. Therefore, according to such a design load format, the reliability of a designed structure for the considered geographic region may not have a very consistent reliability index.

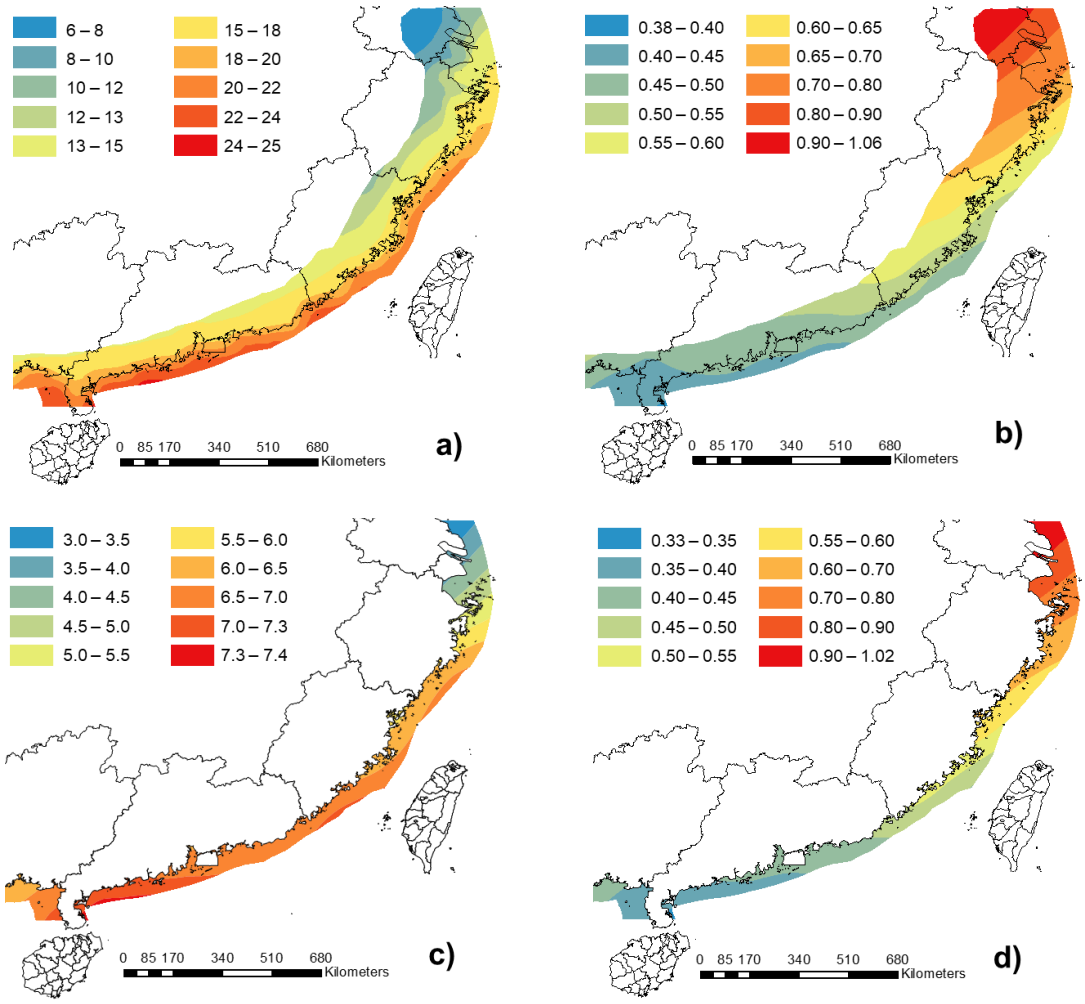

Figure 5.3. Mean and COV of $V_{s\text{-}maxA}$ and $H_{s\text{-}maxA}$. a) the mean of $V_{s\text{-}maxA}$ (m/s), b) COV of $V_{s\text{-}maxA}$; c) the mean of $H_{s\text{-}maxA}$ (m); d) COV of $H_{s\text{-}maxA}$.

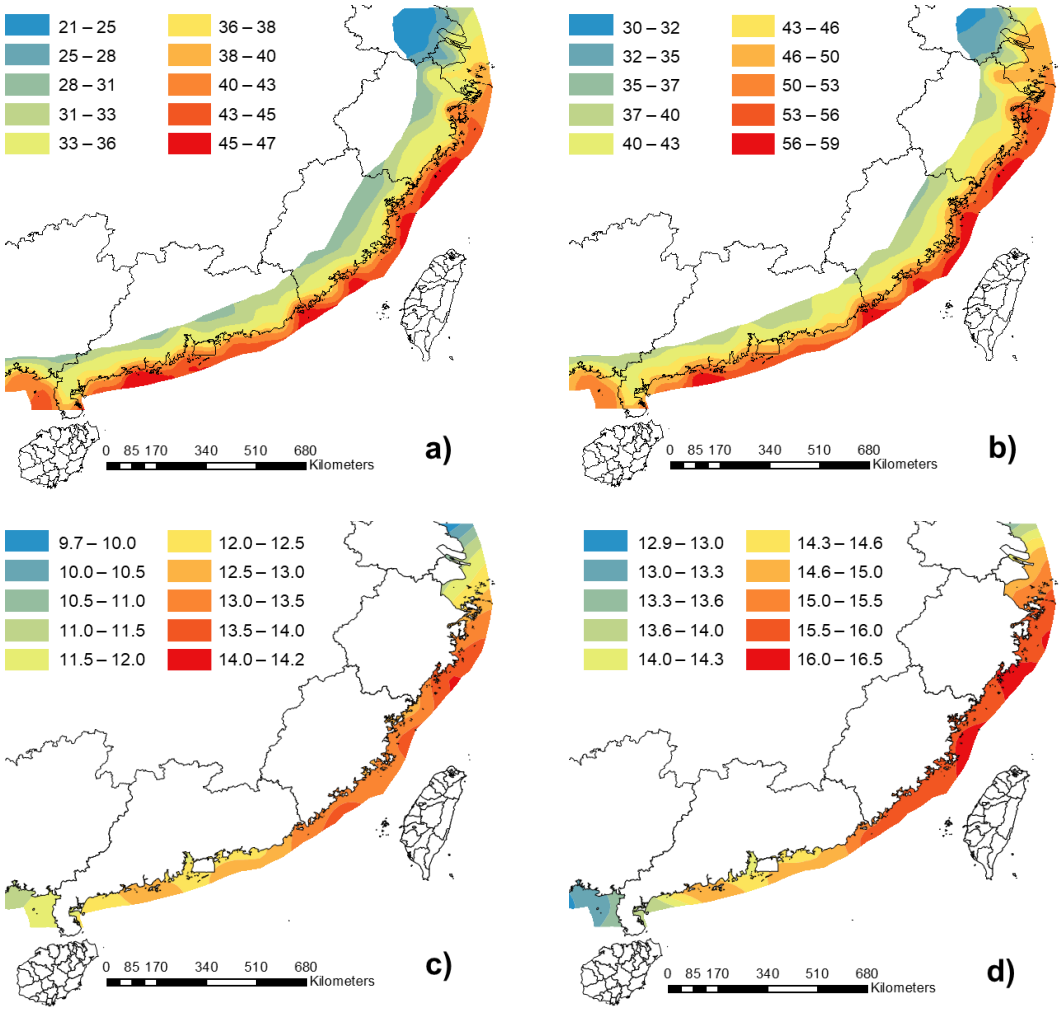

Figure 5.4. Estimated $v_{s\text{-}maxA\text{-}p}$ and $h_{s\text{-}maxA\text{-}p}$ for p = 0.02 and 0.002: a) $v_{s\text{-}maxA\text{-}p}$ (m/s) for p = 0.02; b) $v_{s\text{-}maxA\text{-}p}$ (m/s) for p = 0.002 ; c) $h_{s\text{-}maxA\text{-}p}$ (m) for p = 0.02; d) $h_{s\text{-}maxA\text{-}p}$ (m) for p = 0.002.

Since the database-driven simulation-based (DDSB) framework (Sheng and Hong 2021) is to be used to estimate the structural reliability, no distribution fitting to samples of $V_{s\text{-}maxA}$ and $H_{s\text{-}maxA}$ is required. It is noted that Kendall's τ correlation for the paired random variables ($V_{s\text{-}maxA}$, H_{sWA}) and (V_{sHA}, $H_{s\text{-}maxA}$) is relatively consistent and ranges from 0.40 to 0.67 for the considered sites. This range is consistent with that indicated in Sheng and Hong (2021) but for sites in the deepwater and far away from the coastline. The correlation coefficient between extreme wind and wave is important to estimate the quantile of the combined wind and wave load (Nessim et al. 1995b; Tarp-Johansen 2005). This aspect will be considered in subsequent sections to develop the load

combination rule and carry out reliability-based calibration of design wind and wave loads.

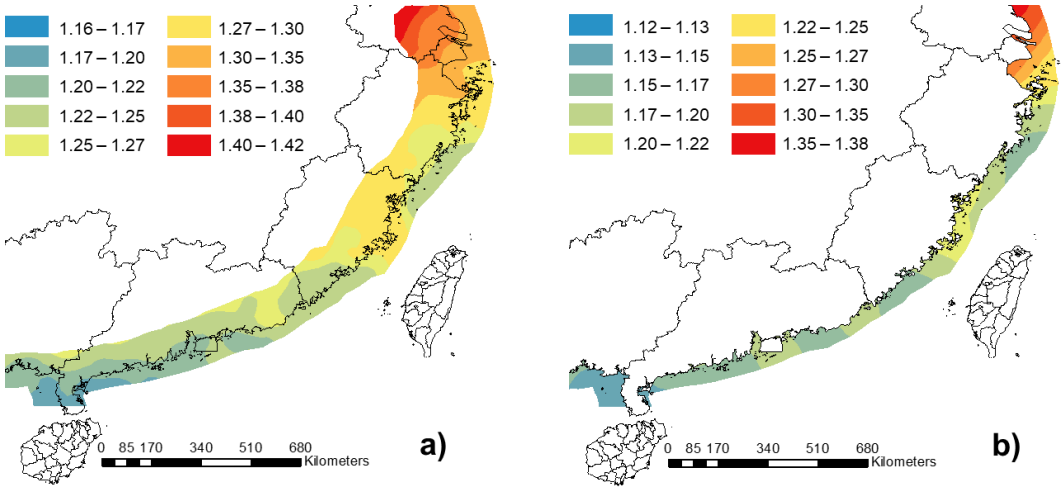

Figure 5.5. Ratio of the quantiles: a) ratio of $v_{s\text{-}maxA\text{-}0.002}$ to $v_{s\text{-}maxA\text{-}0.02}$, b) ratio of $h_{s\text{-}maxA\text{-}0.002}$ to $h_{s\text{-}maxA\text{-}0.02}$.

5.2.2 Statistics of the responses for onshore and offshore monopile wind turbine

Similar to other studies (e.g., Hallowell et al. 2018; Wilkie and Galasso 2020), we consider the offshore monopile NREL 5 MW wind turbine (Jonkman et al. 2009) shown in Figure 5.6. It is inferred that the WT is designed for a wind speed at 10 m height of 39.3 m/s (i.e., the wind speed at the hub height equal to 50 m/s that corresponds to Class I in IEC 61400-1 (2019) for non-TC condition). Also, it is inferred that the WT is designed for a significant wave height of about 12.9 m (Jonkman 2007). However, the statistics of the wind speed and wave height that were considered for the design are unknown to the present study. For completeness, we also consider the onshore version of NREL 5MW WT that is archived in the FAST package (https://www.nrel.gov/wind/nwtc/fast.html).

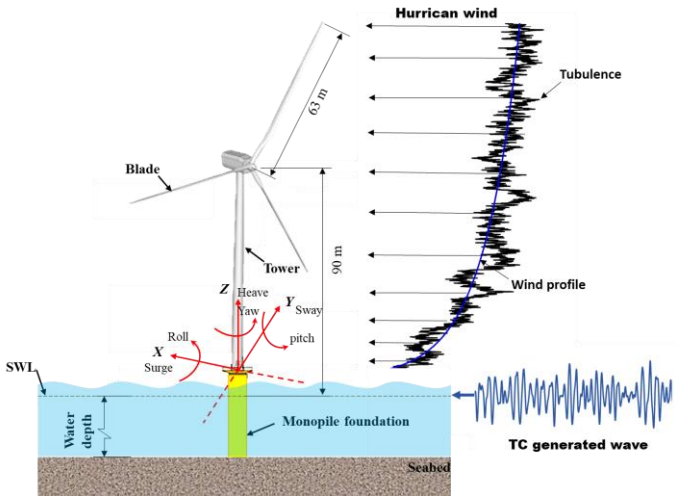

Figure 5.6. Illustration of offshore NREL 5 MW wind turbine placed at an offshore location.

The computation of the responses of the onshore or offshore version of WT subjected to fluctuating wind and waves for given time-average mean wind speed and significant wave height can be carried out using FAST (Jonkman and Buhl 2005; Vorpahl et al. 2013), as mentioned earlier. For the numerical analysis, the Kaimal spectrum for fluctuating wind and JONSWAP spectrum for wave elevation generations are used. Furthermore, the exponential coherence model and the power-law wind profile with an exponent of 0.11 and turbulence intensity of 0.14 for site Class B are used. These spectra, coherence model, and the wind profile are recommended in IEC 61400-1 (2019) and implemented in FAST.

Besides the stochastic wind speed and significant wave height, the wind profile, turbulence intensity, coefficients for evaluating the aerodynamic and hydrodynamic forces are also uncertain. This set of random variables is denoted as $\boldsymbol{X}_L$. Furthermore, the material properties and geometric variables of the structural members of the system, $\boldsymbol{X}_M$, are uncertain as well. One could sample $\boldsymbol{X} = [\boldsymbol{X}_\mathrm{L}, \boldsymbol{X}_\mathrm{M}]$, and use the sampled values of $\boldsymbol{X}$ in FAST to evaluate the responses. This may not be efficient considering the stochastic wind and wave loads. To gain efficiency, we carry out the structural analysis using FAST based on the mean values of $\boldsymbol{X}$, $\boldsymbol{\mu}_\mathrm{X}$, and the specified values of V_s and H_s. The effect of the uncertainty in $\boldsymbol{X}$ is to be incorporated in the limit state function for fragility and reliability analysis - an approach that is consistent with that used in Tarp-Johansen et

al. (2002) and Sørensen and Tarp-Johansen (2005).

Based on these considerations, the time-varying bending moment (due to stochastic fluctuating wind and wave) at the base of the tower, $M_{Tow}(t; \boldsymbol{X}, V_s, H_s)$ and the flapwise bending moment at the root of the blade, $M_{Flap}(t; \boldsymbol{X}, V_s, H_s)$ are calculated using FAST for $\boldsymbol{X} = \boldsymbol{\mu}_{\mathbf{X}}$, $V_s = v_s$, and $H_s = h_s$. Note that, for an offshore site with shallow water conditions, h_s represents the adjusted value for the shallow water (Valamanesh et al. 2016). Let the peak values of $M_{Tow}(t; \boldsymbol{X}, V_s, H_s)$ and $M_{Flap}(t; \boldsymbol{X}, V_s, H_s)$ due to the fluctuating stochastic wind and wave be denoted as $M_{Tow}(v_s, h_s)$ and $M_{Flap}(v_s, h_s)$. The obtained mean and standard deviation of $M_{Tow}(v_s, h_s)$ and $M_{Flap}(v_s, h_s)$ are shown in Figure 5.7 if the onshore version of NREL 5 MW WT (placed at an onshore site) is considered and in Figure 5.8 if the offshore version of NREL 5 MW WT (placed at an offshore site) is considered. For the onshore case, although h_s in $M_{Tow}(v_s, h_s)$ and $M_{flap}(v_s, h_s)$ should be removed, for consistency in writing the limit state functions in the next section, we have retained it. The values of the mean and standard deviation shown in Figure 5.7 are obtained by 500 runs in FAST for each specified wind condition. Each run is carried out for a time history of wind with a duration of 10 minutes. If the offshore version of WT is considered, 100 runs are carried out for each combined wind and wave condition, and each run is carried out for a set of the time histories of wind and wave with a duration of one hour as stipulated in IEC 61400-3 (2019). The obtained samples of $M_{Tow}(v_s, h_s)$ and $M_{flap}(v_s, h_s)$ are stored in the structural response database (SR-database) and are used in the reliability analysis to be discussed in the following sections.

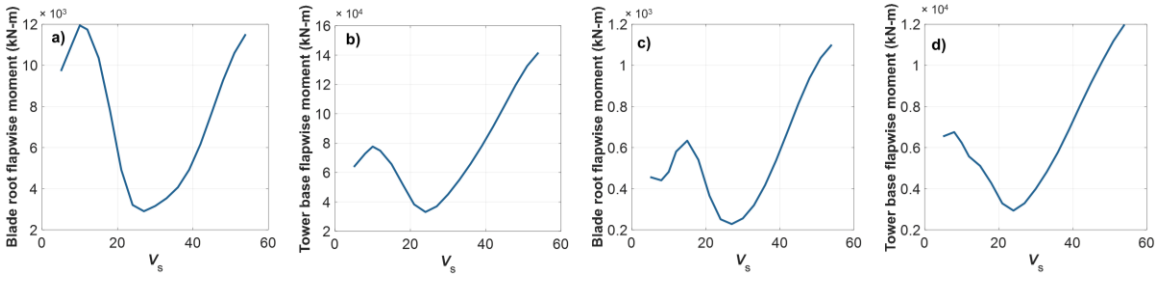

Figure 5.7. Response by considering NREL 5 MW WT is placed at an onshore site: a) mean of blade root flapwise moment, b) mean of tower base flapwise moment, c) standard deviation of blade root flapwise moment, d) standard deviation of tower base flapwise moment. V_s (m/s) in this plot represents 10-min mean wind speed.

The results shown in Figure 5.7 indicate that the responses decrease for V_s greater than about 10 m/s and then increase. This is caused by the change of the blade pitch angle to gain energy production and the cut-out condition under high wind speed. Similar decreasing and increasing behaviour can be observed from Figure 5.8, where the WT is placed at an offshore site. The results for $M_{Tow}(v_s, h_s)$ alone suggest that the WT may experience damage or failure during the energy production stage under moderate wind speed (i.e., V_s less than about 20 m/s) or for extreme wind condition (i.e., V_s in excess of 35 m/s). The reliability-based calibration of wind turbine design in the following section is focused on the latter and it is implicitly considered that the blade pitch angle during the energy production can be programmed such that the former can be avoided.

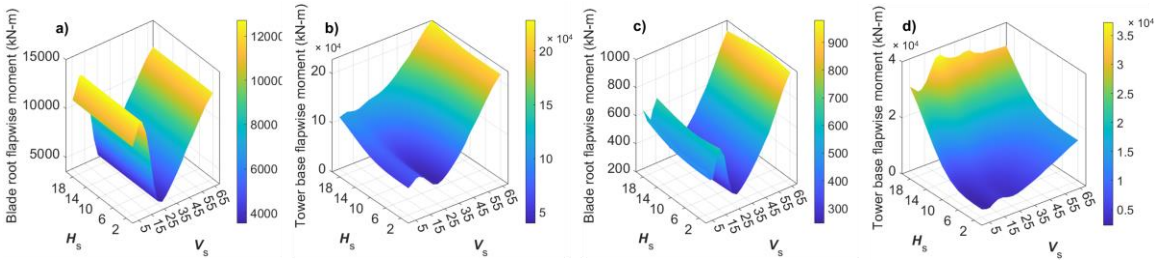

Figure 5.8. Response by considering NREL 5 MW WT is placed at an offshore site: a) mean of blade root flapwise moment, b) mean of tower base flapwise moment, c) standard deviation of blade root flapwise moment, d) standard deviation of tower base flapwise moment. V_s (m/s) in this plot represents hourly mean wind speed.

5.3 Calibration of site-specific design wind and wave loads for monopile wind turbine

5.3.1 Limit state functions and reliability evaluation procedure

It is instructive to consider the problem of evaluating the required design wind load or design wave load for a structure in a region that experiences significant TC hazard. This could allow one to gain some insight into the reliability of an onshore or offshore wind turbine subjected to typhoon wind hazards. Following the standard design code calibration practice for buildings (Ellingwood et al. 1980; Madsen et al. 2006; Bartlett et

al. 2003a, b), the limit state function by considering the resistance and wind load only, g_{01}, can be written as,

$$g_{01} = \frac{1}{\gamma} X_R - \frac{Z_{WI-L}}{b_{WI}} \frac{c_1 V_{s-maxA}^2}{c_1 v_{s-maxA-p}^2} = \frac{1}{\gamma} X_R - \frac{Z_{WI-L}}{b_{WI}} \left(\frac{V_{s-maxA}}{v_{s-maxA-p}} \right)^2, \tag{5.1}$$

where γ is the resistance factor, X_R is the resistance normalized with its nominal value, $Z_{WI\text{-}L}$ is an uncertain factor transforming the wind speed to wind load effect, c_1 is a structural analysis coefficient, and b_{WI} is a constant that takes into account that the structural design codes usually specify an exposure coefficient, pressure coefficient, and an overall wind load transformation factor that are greater than their corresponding mean value. A review of b_{WI} is given in Bartlett et al. (2003a, b), concluding that b_{WI} equal to 1.45 (i.e., approximately equal to 1/0.64, where 0.64 is known as the bias factor) is appropriate for calibrating Canadian structural design code. Since the discussion of the bias factor for the WT is unavailable, this value of b_{WI} is considered in this study. However, if the actual structural design code implementation for WT differs from this considered b_{WI} value, the results presented in the following sections are still applicable, provided that an additional overall load factor that equals the ratio of the actual to the adopted b_{WI} value is to be considered. Note also that, the often considered wind load factor is included in selecting the (1-p)-quantile of $V_{s\text{-}maxA}$ in Eq. (5.1). This facilitates the structural design code making to achieve a consistent target reliability index for geographically varying COV of wind speed (Hong et al. 2021). Similarly, the limit state function by considering the resistance and wave load only, g_{02}, can be written as,

$$g_{02} = \frac{1}{\gamma} X_R - \frac{Z_{WA-L}}{b_{WA}} \frac{c_2 H_{s-maxA}^2}{c_2 h_{s-maxA-p}^2} = \frac{1}{\gamma} X_R - \frac{Z_{WA-L}}{b_{WA}} \left(\frac{H_{s-maxA}}{h_{s-maxA-p}} \right)^n, \tag{5.2}$$

where $Z_{WA\text{-}L}$ is an uncertain factor transforming the wave height to wave load effect, and c_2 is a structural analysis coefficient, b_{WA} is a constant that considers the differences in the code assigned coefficients such as the inertial coefficient and drag coefficient are greater than their average values, and n takes 1 or 2 if the force is dominated by inertial force or drag force, respectively.

By considering the combined wind and wave load, the limit state function can be written as,

$$g_{012} = \frac{1}{\gamma} X_R - \frac{Z_{WW-L}}{b_{WW}} \frac{c_1 V_{s-maxA}^2 + c_2 H_{s-maxA}^n}{\max\left(c_1 v_{s-\max A-p}^2 + \eta_2 c_2 h_{s-maxA-p}^n, \eta_1 c_1 v_{s-\max A-p}^2 + c_2 h_{s-maxA-p}^n\right)}, \quad (5.3a)$$

where

$$\max\left(c_1 v_{s-\max A-p}^2 + \eta_2 c_2 h_{s-maxA-p}^n, \eta_1 c_1 v_{s-\max A-p}^2 + c_2 h_{s-maxA-p}^n\right), \quad (5.3b)$$

represents *p*-quantile of the combined wind and wave actions according to Turkstra's rule (Madsen et al. 2006; Nessim et al. 1995b), Z_{WW-L} denotes the factor transforming the wind and wave height to the loads, η_1 and η_2 are known as the companion load combination factors, and b_{WW} serves in a similar manner as b_{WI} and b_{WA} mentioned earlier. Values of η_1 and η_2 are calibrated in Sheng and Hong (2020) for the case when $n = 1$, resulting in $(\eta_1, \eta_2) = (0.75, 0.85)$ for p ranging from 0.002 to 0.02. They further pointed out that these load combination factors are relatively insensitive to p. The evaluation of (η_1, η_2) for $n = 2$ will be carried out in the following sections.

To simplify the parametric investigation of the reliability analysis by considering both wind and wave actions, by letting $r = c_2 h_{s-\max A-p}^2 / \left(c_1 v_{s-\max A-p}^2 + c_2 h_{s-\max A-p}^n\right)$, Eq. (5.3a) can be re-written as,

$$g_{012} = \frac{1}{\gamma} X_R - \frac{Z_{WW-L}}{b_{WW}} \frac{(1-r)(V_{s-maxA} / v_{s-maxA-p})^2 + r(H_{s-maxA} / h_{s-maxA-p})^n}{\max\left((1-r) + \eta_2 r, (1-r)\eta_1 + r\right)}, \quad (5.4)$$

which allows the analysis to be carried out based on the percentage of the contribution of the wave load to the total load. Note that by setting $r = 0$ and 1 in Eq. (5.4), we obtain Eq. (5.1) and Eq. (5.3), respectively, if Z_{WI-L}, Z_{WA-L}, and Z_{WW-L} are considered to be the same.

The use of Eqs. (5.1), (5.2), and (5.4) are advantageous since their use facilitates structural design code making as it can be used for a generic structure. However, they do

not include the specific properties of a particular structure. To take into account the specifics of the prototype NREL 5 MW WT in reliability analysis, we consider two ultimate limit state functions. The first one considers the bending moment at the base of the tower and the second one deals with the flapwise bending moment at the root of the blade. Based on Tarp-Johansen et al. (2002) and Tarp-Johansen and Clausen (2006), the limit state function for the local buckling of the tower can be written as,

$$g_1 = M_{cr} - Y_{L1} Y_{M1} M_{Tow}(V_s, H_s), \tag{5.5}$$

where M_{cr} is the critical bending moment capacity for local buckling. The modelling errors Y_{L1} and Y_{M1} depend on the degree of sophistication of the model used to evaluate $M_{Tow}(V_s, H_s)$. For simple analysis, Tarp-Johansen et al. (2002) suggested that Y_{L1} and Y_{M1} should include those arising from the evaluation of the dynamic response of the turbine from a numerical model, exposure coefficient, lift and drag coefficients (or shape factor), model-scale test to full-scale response, and statistical variability in assessing wind speed. Since FAST is used in evaluating $M_{Tow}(V_s, H_s)$ in the present study, Y_{L1} should include the effect of uncertainty in exposure and shape factor, and Y_{M1} describes the accuracy in predicting the stress at a location in the structural system. Based on this consideration and the models given in Tarp-Johansen et al. (2002), the adopted distributions of Y_{L1} and Y_{M1} are listed in Table 5.1. It is noteworthy that since Y_{L1} and Y_{M1} are independent lognormally distributed, based on the statistics shown in Table 5.1, $Y_{L1} \times Y_{M1}$ is also lognormally distributed with a mean of 1 and COV of 0.222. The COV practically equal to that used for building in Bartlett et al. (2003a). However, a bias of 0.64 (i.e., approximately equal to 1/1.45) was considered in their study because the specified values of a series of coefficients in design code are much greater than their corresponding mean values. If a similar practice is considered in the design of WT, such a b_{TOW} value should be incorporated in the limit state function when considering the design requirement. Moreover, the critical bending moment capacity in Eq. (5.5) or (5.6) can be evaluated using (Tarp-Johansen et al. 2002),

$$M_{cr} = \left(1 - 0.84 \frac{D}{t} \frac{Y_{y,ss} F_y}{Y_{E,ss} E}\right) \frac{1}{6} \left(D^3 - \left(D - 2t\right)^3\right) Y_{y,ss} X_{cr} F_y, \tag{5.6}$$

where $Y_{y,ss}$ and $Y_{E,ss}$ are model uncertainties, F_y is the yield strength, E is the Young's Modulus, D is the diameter of a section of the tower at the height of interest; t is the wall thickness, and X_{cr} represents the structural analysis modeling error. The probability distributions of these random variables are also listed in Table 5.1. It is considered that the probabilistic models shown in Table 5.1 are applicable whether the WT is placed at an onshore or offshore location, and in operation or parked condition (Tarp-Johansen et al. 2002; Tarp-Johansen and Clausen 2006; Sørensen and Berzonskis 2017). Eq. (5.6) does not include an overall resistance reduction factor due to the uncertainty in $Y_{y,ss}$ and X_{cr}, denoted as γ_M which is considered to be equal to 1.15, that is potentially implemented in the codified structural design for WT. By including these factors, and considering that at the limit the factored design resistance equal to the factored load effect (i.e., $\gamma_M M_{crD} = b_{Tow} M_{Tow}(v_{s-\max A-p}, h_{s-\max A-p})$), Eq. (5.5) becomes,

$$g_1 = \frac{M_{cr}}{\gamma_M M_{crD}} - \frac{1}{b_{Tow} M_{Tow}(v_{s-\max A-p}, h_{s-\max A-p})} Y_{L1} Y_{M1} M_{Tow}(V_s, H_s), \tag{5.7}$$

where M_{crD} is evaluated by using Eq. (5.6) with the values of the random variables equal to their mean value, except that F_y is taken equal to 0.9 times its nominal value where 0.9 represents the resistance factor for the yield strength F_y. The values of $v_{s-\max A-p}$ and $h_{s-\max A-p}$ are the design values of the wind speed and wave height (to be calibrated and discussed).

Similarly, the limit state function for the flapwise bending moment at the root of the blade is given by (Ronold and Larsen 2000),

$$g_2 = \frac{M_{FlapR}}{M_{FlapD}} - \frac{1}{b_{Flap} M_{Flap}(v_{s-\max A-p}, h_{s-\max A-p})} Y_{L2} Y_{M2} M_{Flap}(V_s, H_s), \tag{5.8}$$

Table 5.1. Probability distributions considered for the reliability analysis. The model for $\sigma_{b,f}$ is from Ronold and Larsen (2000) and Mandell et al. (2016). The values of D, t, $R_{b,r}$, and $I_{b,r}$ are from Jonkman et al. (2009). The remaining ones are from Tarp-Johansen et al. (2002).

Parameter	Mean, COV	Dist.
Yield strength, F_y (MPa)	240, 0.05	Lognormal
Scale effect for yield strength, $Y_{y,ss}$	1.0, 0.05	Lognormal
Scale effect for Young's Modulus, $Y_{E,ss}$	1.0, 0.02	Lognormal
Modelling error for the adopted numerical model, X_{cr}	1.0, 0.1	Lognormal
Modelling errors associated with the loading for blade and tower, Y_{L1}, Y_{L2}	1.0, 0.22	Lognormal
Modelling errors associated with material properties for blade and tower, Y_{M1}, Y_{M2}	1.0, 0.03	Lognormal
Young's Modulus, E (GPa)	210, 0.02	Lognormal
Blade tensile strength, $\sigma_{b,f}$ (MPa)	518, 0.03	Normal
Base section diameter for offshore (onshore) WT, D (m)	6 (6.5)	Deterministic
Base section thickness for offshore (onshore) WT, t (m)	0.027 (0.027)	Deterministic
Radius of blade root section, $R_{b,r}$ (m)	1.77	Deterministic
Second moment of blade root section, $I_{b,r}$ (m^4)	0.566	Deterministic
Normalized resistance, X_R	1.17, 0.108	Lognormal
Resistance factor, γ	0.9	Deterministic
Uncertain transformation factor for load effects, $Z_{WI\text{-}L}$, $Z_{WA\text{-}L}$, and $Z_{WW\text{-}L}$	1, 0.222	Lognormal
Variable related to bias factor, b_{WI}, b_{WA}, and b_{WW}	1.45	Deterministic

where $M_{FlapR} = I_{b,r}\sigma_{b,f} / R_{b,r}$, $I_{b,r}$ and $R_{b,r}$ are the second moment of the area and radius at the blade root section respectively; $\sigma_{b,f}$ is blade tensile strength; M_{FlapD} is evaluated by using M_{FlapR} with the values of the random variables involved equal to their mean value, except that $\sigma_{b,f}$ is taken equal to 0.9 times its nominal value, where 0.9 represents the resistance reduction factor of blade tensile strength; Y_{L2} and Y_{M2} are the modeling errors similar to those in Y_{L1} and Y_{M1}; and b_{Flap} serves in a similar manner as b_{Tow}, accounting conservatism in assigning a series of coefficients in structural design. In writing Eq. (5.8), it is considered that the factored design resistance is equal to the factored load effect, that is, $M_{FlapD} = b_{Flap} M_{Flap}(v_{s-\max A-p}, h_{s-\max A-p})$. The probability distributions of the random variables involved in Eq. (5.8) are listed in Table 5.1.

In general, the reliability analysis could be carried out by applying the efficient first-order reliability method or simulation techniques (Madsen et al. 2006; Melchers and Beck 2018). The application of the first-order reliability method to limit state functions shown in Eqs. (5.4), (5.7) and (5.8) required the parametric joint probability distribution of (($V_{s\text{-}max}$, H_{sW}), ($H_{s\text{-}max}$, V_{sH})) or (($V_{s\text{-}maxA}$, H_{sWA}), ($H_{s\text{-}maxA}$, V_{sHA})), which are not available or difficult to assign. To avoid potential subjectivity and epistemic uncertainty in fitting the joint probability distributions to these random variables, where the preferred joint probability distribution is unknown, the DDSB approach, as described in Sheng and Hong (2020), is used in the following to evaluate the reliability and to calibrate the design wind load and wave load for a selected target reliability index and the considered limit state functions (i.e., Eqs. (5.1), (5.2), (5.4), (5.7) and (5.8)). The use of this approach is straightforward since the required TC tracks and (V_s, H_s) are already available and stored in the TC-database and WW-database, respectively, for a period of T_T years. Also, the peak structural responses due to stochastic fluctuating wind and wave that are conditioned on (V_s, H_s) are already calculated and stored in SR-database.

The DDSB approach is shown in the flowchart in Figure 5.9 for estimating the failure probability for the i-th failure mode $P_{fi} = \text{Prob}(g_i \le 0)$ for i = 1 and 2, the failure probability of the system, $P_{fsys} = \text{Prob}\big((g_1 \le 0) \cup (g_2 \le 0)\big)$ and the failure probability by considering the limit state functions shown in Eq. (5.1), Eq. (5.2) or Eq. (5.4). The failure probability is calculated for a service period of 20 years as this is the commonly considered design working life for a WT. Based on the DDSB framework, the steps to evaluate the failure probabilities are:

1) Divide the TC activities during T_T year in N_B blocks of 20 years. Let P_f = 0 for a considered limit state function or union of several limit state function, and j_B = 1;
2) For a given block, simulate values of all random variables in Eqs. (5.6), (5.7), and (5.8) (also refer to Table 5.1), except for V_s and H_s. From TC-database, find the segment of each track that is within a radius of 250 km from the WT site. Let N_S denote the total number of such segments;
3) Form a sequence of points on the identified segment of each track with a time increment Δt and ((L_a, L_o), u_c, θ, Δp, $R_{\max}$, B). Loop through each point: extract the

wind and wave fields from WW-database and find V_s and H_s at the WT site, extract randomly $M_{Tow}(V_s, H_s)$ and $M_{Flap}(V_s, H_s)$ (conditioned on V_s and H_s) from SR-database, and evaluate the limit state functions.

4) If no failure is observed, repeat Step 3) for the next track. Otherwise, repeat for the next block until all the blocks are considered

5) Count the number of blocks that failure occurs for a considered condition. Estimate the failure probability based on the ratio of the number of failed blocks for a considered condition to the total number of blocks considered.

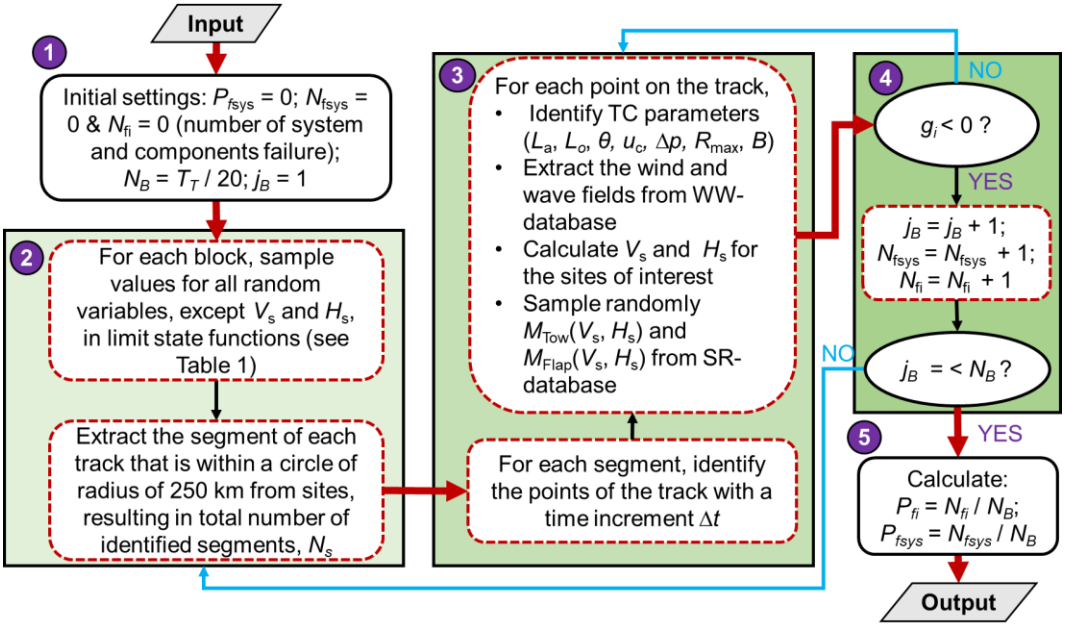

Figure 5.9. Flowchart for the reliability analysis.

5.3.2 Target reliability and calibration of site-specific design wind and wave loads for selected target reliability indices

A range of the optimum target reliability indices (or tolerable annual failure probability ranging from 2×10^{-4} to 10^{-3}) was suggested in Sorensen and Tarp-Johansen (2005) by minimizing life-cycle cost. This means that the failure probability for 20-year service life is about 4×10^{-3} to 2×10^{-2}, and the corresponding target reliability index for 20-year service life, β_{T20}, is about 2.65 to 2.05.

By considering the target reliability indices of 2.65 and 2.05 and that $Z_{WI\text{-}L}$ and $Z_{WA\text{-}L}$ are

lognormally distributed with a mean of 1 and COV of 0.22 (which is practically equal to the distribution model for $Y_{L1}Y_{M1}$), and b_{WI} = 1.45 and b_{WA} = 1.45, the reliability analysis is carried out. For the analysis, the procedure described in the previous section is employed by considering Eq. (5.1) and the statistics of wind speed for the grided points shown in Figure 5.2a. The obtained exceedance probability p (i.e., the return period T = 1/p) that leads to the estimated reliability index for a 20-year service life equals β_{T20} = 2.05 is shown in Figure 5.10a, and spatially variation of the estimated T for β_{T20} = 2.05 and β_{T20} = 2.65 are presented in Figure 5.10b and 5.10c. This analysis is repeated for β_{T20} = 2.65 with the results shown in the same plot. Figure 5.10a indicates that the return T varies even for the same COV value of $V_{s\text{-}maxA}$, $v_{Vs\text{-maxA}}$. This can be explained by noting that p_0 is geographically varying, and the non-zero $V_{s\text{-}maxA}$ cannot be characterized by its mean and COV alone since it could not be characterized by a two-parameter probability distribution (e.g., Gumbel distribution) (see Figure 5.2). Figure 5.10a also indicates that the required return period T increases almost linearly as $v_{Vs\text{-maxA}}$ increases. A simple regression equation indicates that

$$T = 12.5 + (-974.7 + 524.1 \times \beta_{T20}) \times v_{Vs-\max A}, \text{ for } \beta_{T20} = 2.65 \text{ or } 2.05. \quad (5.9)$$

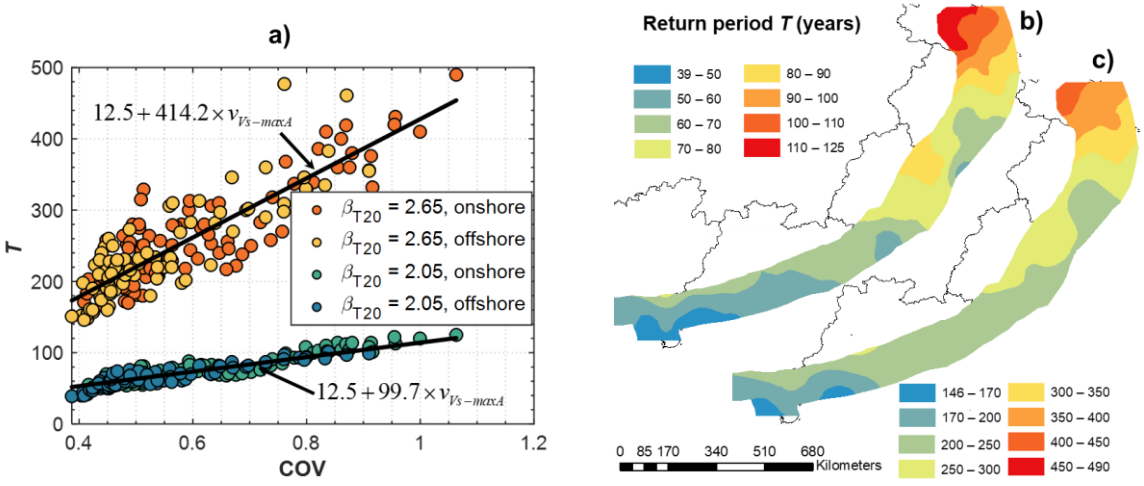

Figure 5.10. Calculated return period T for WT subjected to wind load alone (onshore) by considering β_{T20} = 2.05 and β_{T20} = 2.65. a) relation between T and COV, b) spatial variation of the estimated T for β_{T20} = 2.05, c) spatial variation of the estimated T for β_{T20} = 2.65.

By considering the limit state function shown in Eq. (5.2) and the wave effects, the obtained T values are presented in Figure 5.11 for and considering n = 1 or 2. In this case, the required T to achieve a specified target reliability index is an increasing function of COV of $H_{\text{s-maxA}}$, $v_{Hs\text{-maxA}}$. A comparison of the results presented in Figures 4.10 and 5.11, indicates that the requires T for the design subjected wind load alone is greater than that for the wave load. This can be explained by noting that the probability distribution of $H_{\text{s-maxA}}$ in the upper tail has a much steeper slope than that of $V_{\text{s-maxA}}$ (i.e., the distribution tail for $H_{\text{s-maxA}}$ is shorter than that for $V_{\text{s-maxA}}$). The estimated T shown in Figure 5.11 depends on whether the load is dominated by the inertial force or drag force (i.e., n = 1 or 2). For a WT with monopole foundation, the wave force on a slender cylinder is dominated by the drag force (Chakrabarti 1987), the required return period T shown in Figure 5.11 could be approximated by,

$$T = 14.6 + (-567.0 + 305.9 \times \beta_{T20}) \times v_{Hs-\max A}, \text{ for } \beta_{T20} = 2.65 \text{ or } 2.05. \quad (5.10)$$

The calculated T using this equation is conservative for the case where the wave force on an offshore WT is dominated by the inertial force

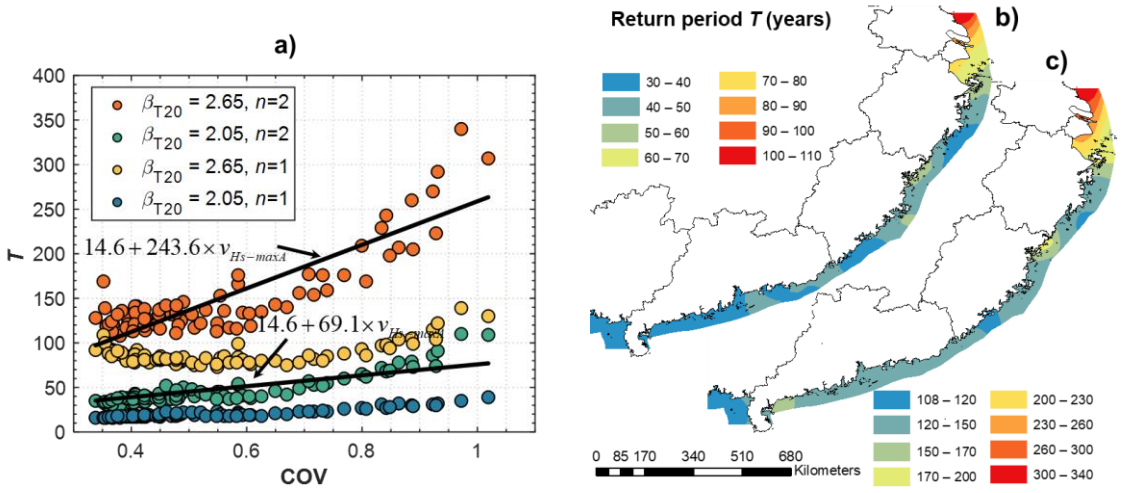

Figure 5.11. Calculated return period T for WT subjected to wave load alone by considering β_{T20} = 2.05 and β_{T20} = 2.65. a) relation between T and COV, b) spatial variation of the estimated T for β_{T20} = 2.05, c) spatial variation of the estimated T for β_{T20} = 2.65.

Before carrying out the calibration for the limit state function shown in Eq. (5.4), we note that the companion load factors η_1 and η_2 by considering the typhoon hazard for the considered coastal region are only available when the wave load is dominated by the inertial force (i.e., n =1), as mentioned earlier. To obtain η_1 and η_2 for n = 2, we carry out the same analysis as was done in Sheng and Hong (2021) but considering n = 2 and the statistics of wind and wave at five selected sites identified as S1 to S5 in Figure 5.2a. The obtained load combination diagram is shown in Figure 5.12. From the figure, it is concluded that, as a conservative measure, the companion load factors (η_1, η_2) = (0.85, 0.90) for p equal to 0.002 or 0.02 can be adopted to evaluate the combined wind and wave loads. Since the suggested value is not very sensitive to the value of p, it is considered that they can also be used for the case when the p values used for the wind load and wave load are different, as shown in Figures 5.10 and 5.11.

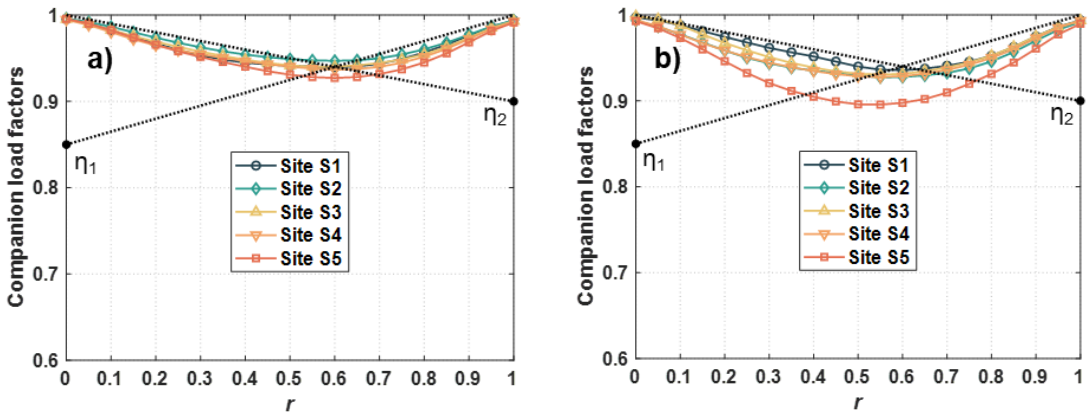

Figure 5.12. Estimated companion load factors for wind and wave actions. a) companion load factors for T = 50 (i.e., p = 0.02); b) companion load factors for T = 500 (i.e., p = 0.002).

By using these adopted (η_1, η_2), reliability analysis is carried out by considering the limit state function shown in Eq. (5.4) and considering β_{T20} = 2.05 and 2.65. The obtained reliability indices are shown in Figure 5.13 for three selected values of r, representing the ratio of the design wave load effect to the combined wind and wave loads (see Eq. (5.4)). The results shown in Figure 5.13 indicate that the estimated reliability indices in all cases are consistent with the target reliability indices used to calibrate the design loads by

considering the wind load alone or wave load alone. This implies that the calibrated design TC wind and wave loads and the load combination factors are adequate.

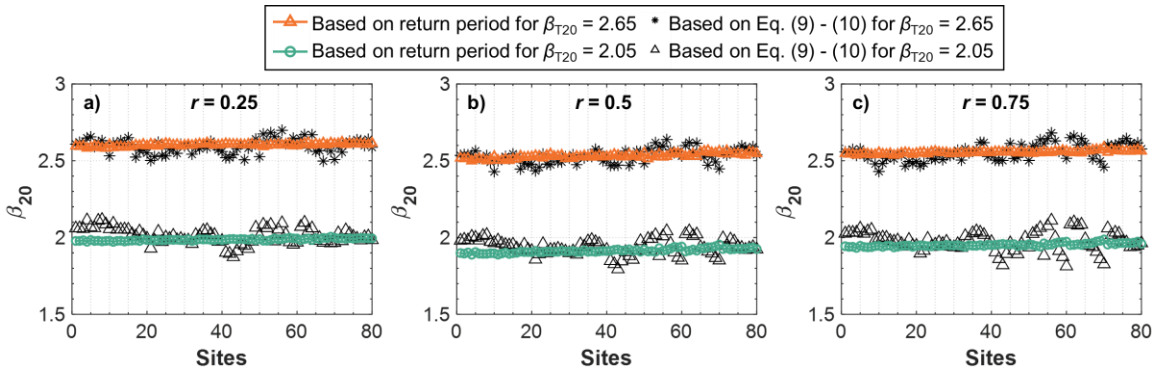

Figure 5.13. Estimated reliability indices by considering n = 2 and β_{T20} = 2.05 and β_{T20} = 2.65: a) for r = 0.25, b) for r = 0.5, c) for r = 0.75.

In summary, the results in this section indicate that the return periods for evaluating the TC wind load and wave load are functions of the site-dependent COV of $V_{s\text{-}maxA}$ and $H_{s\text{-}maxA}$. The maps for these return period values are shown in Figures 5.10 and 5.11, while the developed empirical equations are given in Eqs. (5.9) and (5.10). The recommended companion load factors for the TC wind and wave load combination are given by Eq. (5.3b) with (η_1, η_2) = (0.85, 0.90) for monopole WT.

It must be emphasized that the calibration results presented in this section are carried out based on commonly used reliability-based design code calibration procedures (Madsen et al. 2006). For the calibration, it is assumed that the bias factors are assumed to be equal, resulting in b_{WI}, b_{WA}, and b_{WW} equal to 1.45. This value may not be adequate for specific code implementation. In such a case, if a_{WI}, a_{WA}, and a_{WW} represent the actual bias factors, the results obtained in this section is still applicable, except that the scaling factors a_{WI}/1.45, a_{WA}/1.45, and a_{WW}/1.45 should be applied to the design wind load alone, wave load alone or combined wind and wave load, respectively.

5.3.3 Validation considering system behaviour

To validate the calibrated design wind and wave load for WT located at an onshore or

offshore site, in this section, we consider the onshore and offshore versions of NREL 5 MW WT mentioned in the previous sections. Two limit state functions shown in Eqs. (5.7) and (5.8) are considered for evaluating the reliability of the WT. For the evaluation, we consider that the nominal values of the yield or tensile strengths equal their corresponding 0.05-quantiles, and that the values of the remaining random variables equal 1.0. Based on these considerations, the evaluated M_{crD} and M_{FlapD} equal to 177 mN-m and 142 mN-m for the onshore version of the NREL 5 MW WT, and 154 mN-m and 142 mN-m for the offshore version of the NREL 5 MW WT.

For a considered onshore or offshore site shown in Figure 5.2a, we calculated $v_{s-\max A-p}$ and $h_{s-\max A-p}$ based on the obtained statistics of $V_{s-\max A}$ and $H_{s-\max A}$ for the calculated value of p shown in Figures 5.10 and 5.11. Since the offshore WT is located at a shallow water site, the calculated significant wave height from TC hazard, $h_{s-\max A-p}$ (or samples of $H_{s-\max A}$), is to be adjusted using the suggested equation given by Valamanesh et al. (2016). The adjusted significant wave height for the shallow water, H_{SS}, is given by,

$$\ln(H_{SS}) = -\exp(-0.06d) + \ln(H_s), \tag{5.11}$$

where d is the water depth, Hs represents the significant wave height (without considering the shallow water effect), and H_{SS}, H_S, and d are in meters. Unless otherwise indicated, for simplicity, the significant wave height mentioned below (e.g., $h_{s-\max A-p}$ and $H_{s-\max A}$) refers to that for the shallow water condition.

Given values $v_{s-\max A-p}$ and $h_{s-\max A-p}$, we then read the load effects from Figure 5.7 or Figure 5.8 (i.e., extract the mean values of $M_{Tow}(v_{s-MaxA-p}, h_{s-MaxA-p})$ and $M_{Flap}(v_{s-MaxA-p}, h_{s-MaxA-p})$ from SR-database). Since the considered WTs are not designed according to the calibrated design wind and wave loads, the ratio of the factored resistance to the factored load effect, R_0,

$$R_0 = \min((\gamma_M M_{crD}) / (b_{Tow} M_{Tow}(v_{s-MaxA-p}, h_{s-MaxA-p})), M_{FlapD} / (b_{Flap} M_{Flap}(v_{s-MaxA-p}, h_{s-MaxA-p})))$$

, (5.12)

can be calculated. Rather than revising the design of these WTs, which is beyond the means of this study, because of the resources that are required to assess the new aerodynamic pressure coefficient for the blads, new hydrodynamic pressure coefficient for the tower, programing the blade pitch angle for the energy production, we adjust the design resistance (hence the resistance) by dividing the calculated ratio R_0. In other words, the limit state functions shown in Eqs. (5.7) and (5.8) become,

$$g_1 = \left(M_{cr} / R_0\right) - Y_{L1} Y_{M1} M_{Tow}(V_s, H_s)\,, \tag{5.13}$$

and

$$g_2 = \left(M_{FlapR} / R_0\right) - Y_{L2} Y_{M2} M_{Flap}(V_s, H_s)\,, \tag{5.14}$$

This described approach is efficient and often used in the parametric investigation in reliability assessment (Ellingwood et al. 1980; Zhou and Hong 2001; Madsen et al. 2006) without carrying out the redesign of the structure.

For β_{T20} = 2.05 and β_{T20} = 2.65, the value of R_0 is calculated by using Eq. (5.12) and for the T value (i.e., p = 1/T) shown in Figures 5.10b - 5.10c and Figures 5.11b - 5.11c, respectively. Using the calculated R_0 in Eqs. (5.13) and (5.14), and carrying out reliability analysis based on the DDSB approach (see Figure 5.9), the calculated reliability indices are shown in Figure 5.14. It must be emphasized that, for the calculation, it is assumed that the blade pitch angle during the energy production can be reprogrammed such that the failure during the energy production stage can be neglected, as mentioned earlier. The results shown in Figure 5.14 indicate that the obtained reliability indices are close to the target β_{T20} = 2.05 and for β_{T20} = 2.65. This indicates that the calibrated information-sensitive return periods for the geographically varying TC hazards are adequate.

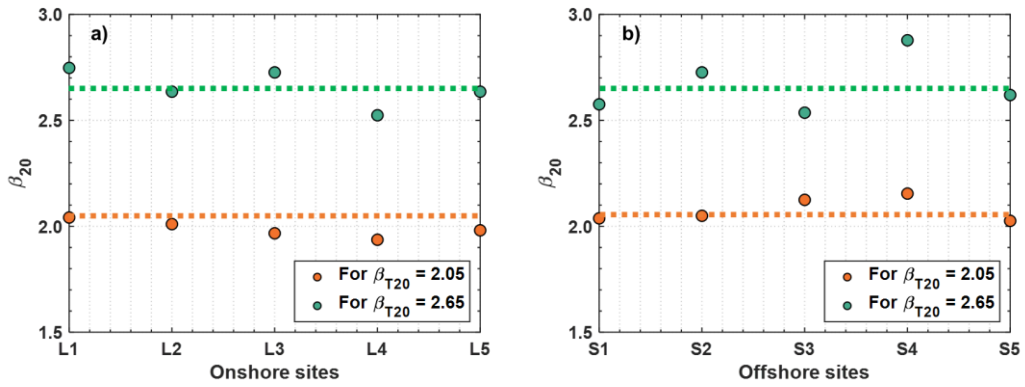

Figure 5.14. Estimated reliability indices by considering NREL 5 MW WT for the considered onshore a) and offshore b) site conditions.

5.4 Conclusions

In the present study, we carried out reliability-based calibration of the site-specific typhoon wind load and wave load for the design of the monopole onshore and offshore wind turbine. The calibration considers the correlated TC wind speed and significant wave height during the passage of TC events. The calibration results show that, for specified target reliability index, the return period or the annual exceedance probability that is required for evaluating the design wind speed and wave height is geographically varying since the statistical characteristics of the annual maximum TC wind speed and significant wave height vary spatially. Maps of the required return period for the design TC wind speed and for significant wave height are presented. Also, simple to use empirical equations (see Eqs. (5.10) and (5.11)) are developed to evaluate such required return periods. These equations depend on the COV values of the annual maximum TC wind speed and significant wave height as well as on the selected target reliability index. In addition, the companion load combination factors for TC wind and wave loads are calibrated. It is suggested that if the TC wind load is taken as the principal load, the companion load factor of 0.9 is to be considered for the wave load. Alternatively, the companion load factor of 0.85 is to be considered for the wind load if the TC wave load is taken as the principal load.

A verification analysis of the adequacy of using the calibrated design loads for the

selected target reliability indices is carried out by considering the onshore and offshore versions of NREL 5MW wind turbine. The analysis results indicate that the use of the suggested design TC wind and wave loads can be adequate for the considered region.

5.5 Reference

Bartlett, F.M., Hong, H.P., & Zhou, W. (2003a). Load factor calibration for the proposed 2005 edition of the National Building Code of Canada: Statistics of loads and load effects. Canadian Journal of Civil Engineering, 30(2), 429-439.

Bartlett, F. M., Hong, H. P., & Zhou, W. (2003b). Load factor calibration for the proposed 2005 edition of the National Building Code of Canada: Companion-action load combinations. Canadian Journal of Civil Engineering, 30(2), 440-448.

Chakrabarti, S. K. (1987). Hydrodynamics of offshore structures. Computational Mechanics Publications and Springer-Verlag, London, U.K.

Chen, X., & Xu, J. Z. (2016). Structural failure analysis of wind turbines impacted by super typhoon Usagi. Engineering failure analysis, 60, 391-404.

Ellingwood, B. et al. (1980). Development of a probability based load criterion for American National Standard A58: Building code requirements for minimum design loads in buildings and other structures (Vol. 13). US Department of Commerce, National Bureau of Standards.

Fang, G., Pang, W., Zhao, L., Rawal, P., Cao, S., & Ge, Y. (2021). Toward a refined estimation of typhoon wind hazards: Parametric modeling and upstream terrain effects. Journal of Wind Engineering and Industrial Aerodynamics, 209, 104460.

Feng, J., Feng, L., Wang, J., & King, C. W. (2020). Evaluation of the onshore wind energy potential in mainland China—Based on GIS modeling and EROI analysis. Resources, Conservation and Recycling, 152, 104484.

GB/T 18451.1. (2012). Wind turbine generator systems - Design requirements, Standards Press of China, Beijing, China. (in Chinese)

GB/T 31519-2015. (2015). Wind turbine generator system under typhoon condition, Standards Press of China, Beijing, China. (in Chinese)

GB/T19201. (2006). China meteorology administration, grade of tropical cyclones (GB/T19201-2006), Beijing: China Standards Press. (in Chinese)

Georgiou, P.N., Davenport, A.G., & Vickery, B.J. (1983). Design wind speeds in regions dominated by tropical cyclones. Journal of Wind Engineering and Industrial Aerodynamics. 1983; 13, 139–152.GB/T 18451.1 (2012).

Hallowell, S.T., Myers, A.T., Arwade, S. R., Pang, W., Rawal, P., Hines, E.M., ... & Carswell, W. (2018). Hurricane risk assessment of offshore wind turbines. Renewable Energy, 125, 234-249.

Hong, H. P., Li, S. H., & Duan, Z. D. (2016). Typhoon wind hazard estimation and mapping for coastal region in mainland China. Natural Hazards Review, 17(2), 04016001.

Hong, H. P., Tang, Q., Yang, S. C., Cui, X. Z., Cannon, A. J., Lounis, Z., & Irwin, P. (2021). Calibration of the design wind load and snow load considering the historical climate statistics and climate change effects. Structural Safety, 93, 102135.

IEC International Electrotechnical Commission (2019). IEC 61400-3-1: Wind energy generation systems –Part 3-1: Design requirements for fixed offshore wind turbines.

IEC International Electrotechnical Commission. (2019). IEC 61400-1: Wind turbines part 1: Design requirements. International Electrotechnical Commission.

Jha, A., Dolan, D., Musial, W., & Smith, C. (2010). On hurricane risk to offshore wind turbines in US Waters. Proceedings from the 2010 Offshore Technology Conference. Houston, TX.

Jiang, D., Zhuang, D., Huang, Y., Wang, J., & Fu, J. (2013). Evaluating the spatio-temporal variation of China's offshore wind resources based on remotely sensed wind field data. Renewable and Sustainable Energy Reviews, 24, 142-148.

Jiang, Z., Hu, W., Dong, W., Gao, Z., & Ren, Z. (2017). Structural reliability analysis of wind turbines: A review. Energies, 10(12), 2099.

Jonkman, J., Butterfield, S., Musial, W., & Scott, G. (2009). Definition of a 5-MW reference wind turbine for offshore system development (No. NREL/TP-500-38060). National Renewable Energy Lab. (NREL), Golden, CO (United States).

Jonkman, J.M. (2007). Dynamics modeling and loads analysis of an offshore floating wind turbine (No. NREL/TP-500-41958). National Renewable Energy Lab. (NREL), Golden, CO (United States).

Jonkman, J.M., & Buhl Jr, M.L. (2005). FAST user's guide. National Renewable Energy Laboratory, Golden, CO, Technical Report No. NREL/EL-500-38230.

Li, S. H., & Hong, H. P. (2015a). Observations on a hurricane wind hazard model used to map extreme hurricane wind speed. Journal of Structural Engineering, 141(10), 04014238.

Li, S. H., & Hong, H. P. (2015b). Use of historical best track data to estimate typhoon wind hazard at selected sites in China. Natural Hazards, 76(2), 1395-1414.

Li, S.H., & Hong, H.P. (2016). Typhoon wind hazard estimation for China using an empirical track model. Natural Hazards, 82(2), 1009-1029.

Li, Y., Huang, X., Tee, K. F., Li, Q., & Wu, X. P. (2020). Comparative study of onshore and offshore wind characteristics and wind energy potentials: A case study for southeast coastal region of China. Sustainable Energy Technologies and Assessments, 39, 100711.

Liu, Y., Li, S., Chan, P.W., & Chen, D. (2018). On the failure probability of offshore wind turbines in the China coastal waters due to typhoons: A case study using the OC4-DeepCwind semisubmersible. IEEE Transactions on Sustainable Energy.

Madsen, H.O., Krenk, S., & Lind, N.C. (2006). Methods of structural safety. Courier Corporation.

Mandell, J.F., Samborsky, D.D., Miller, D.A., Agastra, P., & Sears, A.T. (2016). Analysis of SNL/MSU/DOE Fatigue Database Trends for Wind Turbine Blade Materials 2010-2015 (No. SAND-2016-1441). Sandia National Lab. (SNL-NM), Albuquerque, NM (United States).

Martin del Campo, J. O., Pozos‐Estrada, A., & Pozos‐Estrada, O. (2021). Development of fragility curves of land‐based wind turbines with tuned mass dampers under cyclone and seismic loading. Wind Energy.

Melchers, R.E., & Beck, A.T. (2018). Structural reliability analysis and prediction. John Wiley & Sons.

Myers, A. T., Arwade, S. R., Valamanesh, V., Hallowell, S., & Carswell, W. (2015). Strength, stiffness, resonance and the design of offshore wind turbine monopiles. Engineering structures, 100, 332-341.

Nessim, M. A., Hong, H. P., & Jordaan, I. J. (1995a). Environmental load uncertainties for offshore structures. ASME Journal of Offshore Mechanics and Arctic Engineering, Vol. 117.

Nessim, M. A., Hong, H. P., Swail, V. R., and Henderson, C. A., (1995b). Design Criteria for Offshore Structures Under Combined Wind and Wave Loading, ASME Journal of Offshore Mechanics and Arctic Engineering, Vol. 117.

Nie, B., & Li, J. (2018). Technical potential assessment of offshore wind energy over shallow continent shelf along China coast. Renewable Energy, 128, 391-399.

Pokhrel, J., & Seo, J. (2019). Natural hazard vulnerability quantification of offshore wind turbine in shallow water. Engineering Structures, 192, 254-263.

Ronold, K.O., & Larsen, G.C. (2000). Reliability-based design of wind-turbine rotor blades against failure in ultimate loading. Engineering Structures, 22(6), 565-574.

CCS China Classification Society. (2012). Specification for certification of offshore wind turbines. (in Chinese)

Sheng, C. & Hong, H.P. (2020). On the joint tropical cyclone wind and wave hazard, Structural Safety, 84, 101917.

Sheng, C., & Hong, H. P. (2021). Reliability and fragility assessment of offshore floating wind turbine subjected to tropical cyclone hazard. Structural Safety, 93, 102138.

Sørensen, J.D., & Berzonskis, A. (2017). Probabilistic design and estimation of life of wind turbine components. In 12th International Conference on Structural Safety & Reliability: ICOSSAR 2017 (pp. 2889-2898). TU Verlag.

Sørensen, J.D., & Tarp-Johansen, N.J. (2005). Reliability-based optimization and optimal reliability level of offshore wind turbines. International Journal of Offshore and Polar Engineering, 15(02).

Tarp-Johansen, N. J. (2005). Partial safety factors and characteristic values for combined extreme wind and wave load effects. Journal of Solar Energy Engineering, 127(2), 242-252.

Tarp-Johansen, N.J., & Clausen, N-E. (2006). Design of Wind Turbines in Typhoon area: A first study of Structural Safety of Wind Turbines in Typhoon prone areas. EC-ASEAN Energy Facility.

Tarp-Johansen, N.J., Sørensen, J.D., & Madsen, P.H. (2002). Experience with acceptance criteria for offshore wind turbines in extreme loading. In Workshop on reliability based code calibration.

Valamanesh, V., Myers, A. T., Arwade, S. R., Hajjar, J. F., Hines, E., & Pang, W. (2016). Wind-wave prediction equations for probabilistic offshore hurricane hazard analysis. Natural Hazards, 83(1), 541-562.

Vickery, P.J., Wadhera, D., Powell, M.D., & Chen, Y. (2009a). A hurricane boundary layer and wind field model for use in engineering applications. Journal of Applied Meteorology and Climatology, 48(2), 381-405.

Vickery, P. J., Wadhera, D., Twisdale Jr, L. A., & Lavelle, F. M. (2009b). US hurricane

wind speed risk and uncertainty. Journal of structural engineering, 135(3), 301-320.

Vorpahl, F., Schwarze, H., Fischer, T., Seidel, M., & Jonkman, J. (2013). Offshore wind turbine environment, loads, simulation, and design. Wiley Interdisciplinary Reviews: Energy and Environment, 2(5), 548-570.

Wei, K., Arwade, S. R., & Myers, A. T. (2014). Incremental wind-wave analysis of the structural capacity of offshore wind turbine support structures under extreme loading. Engineering Structures, 79, 58-69.

Wilkie, D., & Galasso, C. (2020). Site-specific ultimate limit state fragility of offshore wind turbines on monopile substructures. Engineering Structures, 204, 109903.

Wu, F., Huang, G., & Zhou, X. (2021). Enhanced Circular Subregion Method in Typhoon Hazard Analysis. Journal of Structural Engineering, 147(6), 06021003.

Xiao, Y. F., Duan, Z. D., Xiao, Y. Q., Ou, J. P., Chang, L., & Li, Q. S. (2011). Typhoon wind hazard analysis for southeast China coastal regions. Structural Safety, 33(4-5), 286-295.

Ying, M., Zhang, W., Yu, H., Lu, X., Feng, J., Fan, Y., ... & Chen, D. (2014). An overview of the China Meteorological Administration tropical cyclone database. Journal of Atmospheric and Oceanic Technology, 31(2), 287-301.

Young, I.R. (1988). Parametric hurricane wave prediction model. Journal of Waterway, Port, Coastal, and Ocean Engineering, 114(5), 637-652.

Young, I.R. (2003). A review of the sea state generated by hurricanes. Marine structures, 16(3), 201-218.

Young, I.R. (2017). A review of parametric descriptions of tropical cyclone wind-wave generation. Atmosphere, 8(10), 194.

Zhang, R., Zhao, Z., & Dai, K. (2019). Seismic response mitigation of a wind turbine tower using a tuned parallel inerter mass system. Engineering Structures, 180, 29-39.

Zhou, W., & Hong, H. P. (2001). Statistical analyses of strength of slender RC columns. Journal of Structural Engineering, 127(1), 21-27.

Chapter 6

6 Conclusions and recommendations for future work

6.1 Conclusions

This study evaluated the stochastic track model parameters by considering different best track databases; assessed the joint TC wind and wave hazard by combining the TC wind hazard model and wave hazard model; presented a database-driven simulation-based (DDSB) procedure to assess the wind turbine reliability subjected to TC hazards; and calibrated required design TC wind and wave loads and load companion factors for design onshore and offshore monopole wind turbine. The major conclusions that can be drawn from the studies are:

1) The annual number of genesis based on the TC best-track dataset given by CMA is about 7% greater than that by JTWC. The statistics of the TC tracks from the two datasets differ in terms of landfalling TC for southwest China and of the TC heading and translation velocity for northeast China. In general, the mapped *T*-year return period value of the annual maximum TC wind speed based on the beta-advection model (BAM) developed using the dataset from CMA is greater than that developed using the dataset from JTWC. For a few selected major cities, the former is greater than the latter by about 3% and 6% for *T* equal to 50 and 100 years. A comparison of various return period values of the annual maximum TC wind speed is presented by considering two stochastic track models: an available autoregressive type of model in the literature and BAM that is developed using the historical track dataset from CMA. The comparison indicates that their differences are up to 10% and 12% for return periods equal to 50 and 100 years. Part of this difference is due to the fact that the periods of the historical track used in the two models differ; the one developed in the present study uses historical TC tracks that are more up-to-date and cover a longer period.

2) A simulation-based framework to estimate TC-induced wind and wave hazards is presented. The simulation results indicate that the generalized extreme value distribution

for both the annual maximum and event-based values at a site is preferable to the Gumbel distribution. Also, the Kendall's τ of wind speed and wave height ranges from about 0.4 to 0.7 for both annual maximum and event-based data. The statistics based on paired samples TC wind speed and significant wave height for both annual maximum and event-based data indicate that the Gumbel copula could be adopted to model the joint probability distribution of these two quantities.

3) The simulated wind and wave were used to assess the companion load combination factor for the offshore regions in China. By considering that the wave load is dominated by inertial force, it shows that a load companion factor of 0.85 for wave action could be recommended if the wind action is the primary load action, and a companion load factor of 0.75 for the wind action could be suggested if the wave action is the principal load action. The suggested companion load combination factors are based on an annual exceedance probability of 0.02 for the combined wind and wave load effects. Also, the sensitivity analysis indicates that these suggested values are not very sensitive to return periods equal to 50 or 500 years.

4) Results of TC wind hazards indicate that the TC wind and wave hazards vary geographically. The hazard deaggregation results indicate that the identified TC events contributing to a specified quantile of the wind speed differ from those identified for the quantile of the significant wave height. In general, the identified events based on the former are associated with a larger Holland B parameter than those based on the wave height.

5) An overall database-driven simulation-based (DDSB) framework is proposed to assess the fragility and reliability of offshore WTs. The estimated 50-year return period values of the TC wind speed for five considered sites indicate that they can exceed the design values stipulated in the GB/T 31519 (2015) for wind turbine design under typhoon conditions. The application of the proposed (DDSB) procedure for reliability analysis is shown by a numerical example, where a semi-submersible WT from NREL is adopted. The results show that if this floating WT is placed in the coastal region of mainland China, the failure probability is spatially varying because of the spatially varying

statistics of TC wind and wave hazards. Also, it is shown that failure mode is dominated by the buckling of the tower, followed by the overturning of the floating platform. The obtained relatively large failure probability could be attributed to the large coefficient of variation of the annual maximum TC wind speed and significant wave height and to the fact that the considered wind turbine is not designed for the considered sites with the applicable design codes. The sensitivity analysis implies that if the design is carried out based on the site-specified 50-year return period value of TC wind or significant wave height, the uncertainty in the transformation from environmental parameters to load effects is considered, and the failure probability in the operation wind regime is neglected, the annual failure probability is about less than 2×10^{-3}, which is deemed small.

6) The reliability-based design code calibration considering the site-specific TC wind and wave loads for designing offshore and onshore WTs located in the coastal region of China was carried out for selected target reliability indices. The calibration takes into account the correlated TC wind speed and significant wave height during the passage of TC events. The calibration results show that, for specified target reliability index, the return period or the annual exceedance probability that is required for evaluating the design wind speed and wave height is geographically varying due to the space-varying statistical characteristics of the annual maximum TC wind speed and significant wave height.

7) Simple to use empirical equations are developed to evaluate the required return periods for evaluating the design TC wind and wave loads. These equations depend on the COV values of the annual maximum TC wind speed and significant wave height, and the selected target reliability index. Also, maps of the required return periods for the design wind load and wave load are given. Provided that wave force is dominated by the drag force component, it recommends that if the TC wind load is taken as the principal load, the companion load factor of 0.9 is to be considered for the wave load. Alternatively, the companion load factor of 0.85 is to be considered for the wind load if the TC wave load is taken as the principal load. The verification analysis results by considering the onshore and offshore versions of NREL 5MW wind turbine indicate that using the calibrated

geographically varying TC wind and wave loads is adequate and can aid structural design code making.

6.2 Recommendations for future work

1) The quantification of the uncertainty in the TC wind field models is important for probabilistic wind hazard assessment. The uncertainty assessment should be carried out based on measured wind speed (when available) and should take into account the intraevent as well as interevent variability and spatial correlation.

2) The 3-D TC wind field models are presented in the literature, although their calibration using measured wind records or fields seems to be missing. The use of a well-calibrated 3-D wind field model for TC wind hazard analysis would be valuable to provide a more accurate and reliable approach for TC hazard analysis.

3) Risk-informed and reliability-constrained design for the WT structure should be explored. This should include benefit and loss models at present value and risk attitude of decision-makers.

Curriculum Vitae

Name: Chao Sheng

Post-secondary Education and Degrees:

Hunan University
Changsha, Hunan, China
2010-2014 B.Sc.

Tongji University
Shanghai, China
2014-2017 M.Sc.

Western University
London, Ontario, Canada
2018-2022 Ph.D.

Related Work Experience

Teaching and Research Assistant
Western University
2018-2022

Publications:
Journal

Sheng, C., & Hong, H. P. (2021). Reliability and fragility assessment of offshore floating wind turbine subjected to tropical cyclone hazard. Structural Safety, 93, 102138.

Sheng, C., & Hong, H. P. (2020). On the joint tropical cyclone wind and wave hazard. Structural Safety, 84, 101917.

Gu, J. Y., Sheng, C., & Hong, H. P. (2020). Comparison of tropical cyclone wind field models and their influence on estimated wind hazard. Wind and Structures, 31(4), 321-334.

Zhao, Z., Dai, K.S., Camara, A., Bitsuamlak, G., & Sheng, C. (2019). Wind turbine tower failure modes under seismic and wind loads. Journal of Performance of Constructed Facilities, 33(2), 04019015.

Dai, K.S., Sheng, C., Zhao, Z., Yi, Z., Camara, A., & Bitsuamlak, G. (2017). Nonlinear response history analysis and collapse mode study of a wind turbine tower subjected to tropical cyclonic winds. Wind and Structures, 25(1), 79-100.

Dai, K.S., Zhao, Z., Yi, Z., & Sheng, C. (2017). Seismic analyses of a wind turbine tower under operational conditions. Chinese Journal of Engineering, 39(10), 1598-1605. (In Chinese)

Dai, K.S., & Sheng, C., (2015). Wind turbine tower structural responses under typhoon loads. Structural Engineer, 6. (In Chinese)

Conference

Sheng, C., He, P.P., Hong, H.P., & Newson T. Fatigue Damage Estimation for Wind Turbine Service Lifetime Extension. Western Geotechnical Centrifuge Opening & Symposium. 2-3th, May 2019, Geotechnical Research Centre (GRC), The University of Western Ontario. (Poster presentation)

Other Publications

Hong, H.P., Xiao, M.Y., Cui, X.Z., Liu, Y.X., & Sheng, C. (2021). Development of Guideline to Calibrate Resistance Factors for Designing Connections: with Application to Bolted Connections. Report to National Research Centre (NRC), Western University.

Hong, H.P. (with contributions of authors in alphabet order from Cannon, A., Cui, X.Z., Huang, Q., Jarrett, P., Jiang, W.J., Lounis, Z., Sheng, C., Tang, Q., & Yang, S.C.) (2020). Hazard Mapping and Reliability-based Calibration for Canadian Highway Bridge Design Considering the Historical Climate Statistics and Climate Change Effects: Wind and Ice Accretion. Report to National Research Centre (NRC), Western University, 2020.

He, P.P., Sheng, C., Newson, T., & Hong, H.P. (2019). Estimation of Time-varying Fatigue Reliability of Wind Turbine. Report to YR21 Energy Investment Decision Support System, Western University.